Microanalytical Constraints on the Geometry and Chemical Evolution of Kīlauea's Volcanic Plumbing System



UNIVERSITY OF CAMBRIDGE

Penelope Elaine Wieser

Jesus College

University of Cambridge

This thesis is submitted for the degree of Doctor of Philosophy

Supervisors: Marie Edmonds, John Maclennan and Frances Jenner

Submission Date: October 2020

Declaration

"No one is as smart as all of us" – Ken Blachard

I, Penelope Wieser, declare that this is the result of my own work and includes nothing which is the outcome of work done in collaboration except as declared in the Preface and specified in the text. It is not substantially the same as any that I have submitted, or, is being concurrently submitted for a degree or diploma or other qualification at the University of Cambridge or any other University or similar institution except as declared in the Preface and specified in the text. I further state that no substantial part of my thesis has already been submitted, or, is being concurrently submitted for any such degree, diploma or other qualification at the University of Cambridge or any other University or similar institution except as declared in the Preface and specified in the text. It does not exceed the prescribed word limit of 225 pages as stipulated by the Degree Committee of Earth Sciences.

Chapters 3-6 in this thesis represent published manuscripts so have received inputs from coauthors and reviewers. Chapter 7 has been submitted to G^3, so has received input from coauthors. In all cases except those laid out below, I collected and processed the data, wrote the relevant models, the manuscript, and the supplementary information, made all the figures, and responded to reviewer comments.

- Chapter 3 looking at crystal aggregation represents a collaborative effort with Zoja Vukmanovic (a postdoc at Cambridge), Rudiger Kilian, Emilie Ringe, and Marian Holness (as well as my supervisors Marie Edmonds and John Maclennan). It became apparent from conversions at coffee time that the research Zoja was conducting on the origin of chromite chains in the Bushveld complex were very similar to my investigations of olivine aggregates at Kīlauea Volcano. Marian Holness suggested that we address both topics in a single paper, to demonstrate the power of EBSD to quantitatively discriminate different hypothesis in igneous petrology. Zoja processed the chromite EBSD data following numerous discussions with Rudiger and I to ensure that we were producing comparable datasets for the two mineral phases. I produced the final chromite figures.
- Frances Jenner collected the Lōi‘hi major, volatile and chalcophile element data presented in Chapter 6
- John Maclennan ran the bubble growth model in Chapter 7 as the code is not published. I directed him towards the model inputs I wanted, and interpreted and plotted up the outputs.

Abstract

Kīlauea Volcano is an outstanding natural laboratory in which to investigate basaltic volcanism, owing to over a century of extensive study. In the last decade, there has been a paradigm shift in our understanding of volcanic plumbing systems, moving away from a model where large vats of melt are stored in the crust, to a model dominated by extensive piles of settled crystals. This thesis examines the petrological evidence for this 'mush-dominated' model at Kīlauea Volcano, using a variety of state-of-the-art microanalytical techniques. Chapters 3 and 4 demonstrate the power of electron backscatter diffraction (EBSD) to investigate the processes leading to the formation of crystal aggregates and deformed crystals, which are observed in a wide variety of basaltic systems worldwide. Chapter 4 applies microstructural techniques developed through the study of experimentally- and naturally-deformed mantle peridotites to erupted volcanic crystals, demonstrating that mush piles have vertical extents of ∼200–700 m. Chapter 5 shows that relatively primitive Kīlauean olivines and their melt inclusions are out of major and trace element equilibrium with their carrier melts, with broad-reaching implications for the interpretation of melt inclusion records in mush-rich volcanic systems. Specifically, this work demonstrates that inclusions record processes happening over centuries to millennia, rather than those specific to an individual eruption (e.g., volatile fluxes, triggering mechanisms). Chapter 6 capitalizes on recent advances in LA-ICP-MS, permitting analyses of chalcophile elements within melt inclusions and matrix glasses. This dataset provides new constraints on the behaviour of these poorly-understood elements during mantle melting, crustal storage and fractionation, and low pressure degassing. Chapter 7 quantifies the CO_2 budget of melt inclusions from the 2018 eruption using SIMS and Raman Spectroscopy. These paired analyses, combined with detailed evaluation of different CO_2-H_2O solubility models, yield storage depths which align remarkably well with reservoir depths inferred from geophysical inversions. Overall, this thesis demonstrates that the integration of different data streams obtained from state-of-the-art microanalysis has the potential to further our understanding of magmatic processes, even at extremely well-studied volcanic systems.

This thesis is dedicated to my late grandfather Brian Nolan
One day I hope to be as calm as you when things don't quite go to plan

An extra special shout out must also go to the Cambridge Degree Committee for deciding that reformatting published papers into a thesis (rather than thesis by publication) is a valuable use of the finite amount of time PhD students have to do research

Acknowledgements

Firstly, I thank my lead supervisor Marie Edmonds for giving me a huge amount of academic freedom throughout my PhD to pursue the rather eclectic selection of topics that make up this thesis, and to work with a wide range of collaborators, both within and outside Cambridge (Emilie Ringe, Marian Holness, Zoja Vukmanovic, John Wheeler, Rudiger Kilian, Hector Lamadrid, and the awesome USGS/HVO and UH Hilo scientists). In particular, I am very grateful for how supportive Marie was of my struggle with my long term GI condition throughout my PhD. Thanks to my co-supervisor, John Maclennan, for always pushing me to think harder about my hypotheses; while countering his scepticism always required more modelling than I would have liked, it always drastically improved the quality of my science. Finally, to Fran Jenner, for adopting me into the world of chalcophile elements at a really challenging point in my PhD, and providing a huge amount of scientific and emotional support, and numerous opportunities to collaborate on interesting side projects. This research has been made possible by funding from the Natural Environment Research Council of the U.K for my PhD studentship as well as SIMS time. I am also very grateful for two grants from the Fieldwork Fund.

In such a microanalysis-based project, I could not have collected high quality data without the help of the amazingly talented lab technicians I have been lucky enough to work with. Firstly to Iris Buisman and Giulio Lampronti; I have lost count of how many hours I spent on the EPMA and SEM (although regardless of what Giulio will have people believe, I never actually moved into or slept in the lab!). They were both always so happy to help when I wanted to try strange analytical protocols, when something wasn't quite working correctly, or when I just needed a chat! Barbara Kunz and Frances Jenner at the Open University were both instrumental to the collection of the chalcophile element data presented in Chapter 5 and 6. I learnt so much from the various lab visits about LA-ICP-MS analysis, and they have definitely set a gold standard for what makes a great lab. For my SIMS work at Edinburgh, I am hugely grateful to Cees-Jan de Hoog and John Craven. For the sulfide work, I thank Sally Gibson and John Craven for providing sulfide standards, and Giulio and Iris for helping me characterize them.

The EBSD work presented in Chapter 3 and 4 benefited from the amazing community on the MTEX google forum, with a particular shout out to Rudiger Kilian and Ralf Hielscher for their help. I hope such community-driven data processing tools become more and more common place so that comparable results can be produced by groups using a wide range of instrument hardware, rather than relying on black-box proprietary software.

The Raman work presented in Chapter 7 would not have been possible without the help of Hector Lamadrid. Hector not only supplied me with the CO_2 standards required to produce a calibration line for the Cambridge Raman Spectrometer, but also a huge amount of information and support to ensure that the analyses were high quality.

The 2018 eruption of Kīlauea changed the course of my PhD drastically. I am extremely grateful to Evgenia Ilyinskaya for introducing me to the world of aerosol monitoring, and giving me an opportunity to participate in the eruption response. Being part of this large collaborative project has been one of the most rewarding parts of my time at Cambridge, and I have made great friends in the process (Evgenia herself, Rachel Whitty, Em Mason and Emma Liu).

I also am very thankful to my academic friends Marian Holness and Owen Weller for much needed words of encouragement and advise. Additionally, my office mates Euan Mutch, Charlotte Jackson, Fiona LB, Callum Reekie and Pip Liggins for keeping me sane, and all my other department friends for all their help, support, and much-needed coffee breaks (Nick Barber, Victoria Honour, Luke Grinham). Also, my mum for a near-constant supply of cakes and time with my family cat, and my dad for help with tricky software installation. Of course, my biggest thanks go to my husband Matt Gleeson. As well as bringing me dinners to the department after long days in the EPMA/SEM/Raman lab, and putting up with the fact that I spent my PhD (and really, every aspect of my life) in a constant state of stress, you were my sounding board for new scientific ideas.

Of course, Chapters 3-6 of this thesis would not have been possible without the amazing set of Hawaiian samples collected by Isobel Sides, along with her meticulous field and laboratory notes. Frank Trusdell's incredible lava fishing provided some extremely well quenched samples from the Fissure 8 channel that form the basis of Chapter 7. A massive thanks also has to go to Rod Kindel (a resident in Leilani Estates) who took me on a serious bush-whack through his acre of jungle to be able to sample Fissures 11 and 12 in 2019. I am also very grateful to Cheryl Gansecki and Lopaka Lee for supplying samples from the early fissures of the 2018 eruption, and Lotte Larsen for kindly sharing the dendritic olivines from West Greenland. Thanks also to Pele (but not always Delta airlines...) for letting me transport some of her rocks half way across the world)!

Finally, I owe my sanity to Cam and Hunts Sailing Club, the Cambridge University Sailing Team, and most importantly my Laser Radial, for getting me out the lab and into the cold/rain/wind (and sometimes even the sun)!

"It's remarkable how quickly a good and favourable wind can sweep away the maddening frustrations of shore living." - Ernest K. Gann

"Believe me, my young friend, there is nothing - absolutely nothing - half so much worth doing as simply messing about in boats." - Kenneth Grahame, The Wind in the Willows

Publications

"If you think information shouldn't cost anything, go to Wikipedia" – Elsevier

"What's the difference between Elsevier and Wikipedia? Wikipedia is free. What's the same with Elsevier and Wikipedia? They both received their content for free" – Bernhard Mittermaier

Publications arising from this thesis:

1. **Wieser, P.E.**, Vukmanovic, Z., Kilian, R., Ringe, E., Holness, M.B., Maclennan, J. and Edmonds, M., 2019. To sink, swim, twin, or nucleate: A critical appraisal of crystal aggregation processes. Geology, 47(10), pp.948-952. `https://doi.org/10.1130/G46660.1` - **Chapter 3**
2. **Wieser, P.E.**, Edmonds, M., Maclennan, J. and Wheeler, J., 2020. Microstructural Constraints on Magmatic Mushes at Kīlauea Volcano, Hawai'i. Nature Communications. `https://doi.org/10.1038/s41467-019-13635-y-` **Chapter 4**
3. **Wieser, P.E.**, Edmonds, M., Maclennan, J., Jenner, F.E., Kunz, B.E., 2019. Crystal scavenging from mush piles recorded by melt inclusions. Nature Communications. `https://doi.org/10.1038/s41467-019-13518-2` - **Chapter 5**
4. **Wieser, P.E.**, Jenner, F.E., Edmonds, M., Maclennan, J. and Kunz, B., 2020, December. Chalcophile elements track the fate of sulfur at Kīlauea Volcano, Hawai'i. GCA. `https://doi.org/10.1016/j.gca.2020.05.018` - **Chapter 6**
5. **Wieser, P.E.** and Jenner, F.E, (2020). Chalcophile Elements: Systematics and Relevance. Invited article for Elsevier's Encyclopedia of Geology. `https://doi.org/10.1016/B978-0-08-102908-4.00092-8` - **Chapters 1 and 8**
6. **Wieser, P.E**., Lamadrid, H., Maclennan, J., Edmonds, M., Matthews, S., Iacovino, K., Jenner, J., Gansecki, C., Trusdell, F., Lee, L., and Ilyinskaya, E. Reconstructing Magma Storage Depths for the 2018 Kīlauean Eruption from Melt inclusion CO_2 Contents: The Importance of Vapor Bubbles. In review, G^3. - **Chapter 7**

Other publications produced during my time as a PhD student:

7. **Wieser, P.E.**, et al., 2019. New constraints from Central Chile on the origins of enriched continental compositions in thick-crusted arc magmas. Geochimica et Cosmochimica Acta, 267, pp.51-74. `https://doi.org/10.1016/j.gca.2019.09.008`
8. Whitty, R., Ilyinskaya, E., Mason, E., **Wieser, P.E.**, et al., (2020). Spatial and temporal variations in SO_2 and $PM_{2.5}$ levels from 2007-2018 Kīlauea Volcano, Hawaii. Frontiers. `doi:10.3389/feart.2020.00036`

9. Jenner, F.E., **Wieser, P.E.**.... et al. (in revision). Distinguishing between mantle depletion, fertilization and crustal contamination events using oceanic basalts. Nature Communications.
10. Ilyinskaya, E., Mason, E., **Wieser, P.E.**.... et al. (in review). Self-limiting lifetime of environmentally reactive elements in volcanic plumes. Communications Earth and Environment.
11. Mason, E., **Wieser, P.E.** ... et al. (in review). Volatile metal emissions from volcanic degassing and lava-ocean interactions at Kīlauea Volcano, Hawaii. Communications Earth and Environment. `https://www.researchsquare.com/article/rs-53034/v1`
12. Iacovino, K., Matthews, S., **Wieser,. P**... et al. (in prep). VESIcal: An open-source model engine for mixed volatile (H_2O-CO_2) solubility in silicate melts. `https://github.com/kaylai/VESIcal`
13. Liu, E., Edmonds, M., **Wieser, P.E.** ... et al. (in prep). Sulfide saturation and breakdown during the 2014–2015 Holuhraun eruption, Iceland.

Supplementary Data

The data presented in this thesis is supplied as an Electronic Appendix, along with pdfs of relevant published papers. There is a folder for each chapter, which contains an excel spreadsheet with all the data, and relevant MATLAB/Python scripts. There is a ReadMe.txt file within each folder explaining the materials.

Contents

List of Figures **xiii**

List of Abbreviations **xvi**

1 Introduction **1**
1.1 Motivation . . . 1
1.2 The Volcanic Plumbing System of Kīlauea Volcano . . . 2
1.3 Rift-Summit Connections During the Mauna Ulu Period . . . 7
1.4 The 2018 Lower East Rift Zone Eruption . . . 9

2 Methods **14**
2.1 Sample Collection . . . 14
2.2 Sample Preparation . . . 17
2.3 Electron Backscatter Diffraction (ESBD) . . . 20
2.4 Electron Probe Micro-Analyser (EPMA) . . . 20
2.4.1 Olivine Transects . . . 21
2.4.2 WDS Minor Element Maps . . . 21
2.4.3 Olivine Spot Analyses . . . 21
2.4.4 Glass Spot Analyses . . . 23
2.5 Laser Ablation Inductively Coupled Plasma Mass Spectrometry (LA-ICP-MS) 26
2.6 Sulfide Identification and Bulk Analysis . . . 29
2.7 Raman Spectroscopy . . . 30
2.7.1 Theory . . . 30
2.7.2 Analytical Procedure . . . 31
2.7.3 Peak Fitting . . . 31
2.7.4 Calibration . . . 32
2.7.5 Instrument Drift . . . 37
2.7.6 Precision and Accuracy . . . 41
2.8 Secondary Ion Mass Spectrometry (SIMS) . . . 42

3 To sink, swim, twin or nucleate: A critical appraisal of crystal aggregation processes **47**
3.1 Introduction . . . 47
3.2 Sample Details and Methods . . . 50
3.3 Results . . . 53
3.4 Physical Aggregation of Crystals . . . 55
3.5 Crystal Growth Processes . . . 56

3.6 Conclusions . . . 59
3.7 Additional Information . . . 59
3.7.1 Identifying Twin Laws . . . 59
3.7.2 Calculating Surface Energies . . . 60

4 Microstructural Constraints on Magmatic Mushes under Kīlauea Volcano, Hawai'i 62
4.1 Introduction . . . 62
4.2 Methods . . . 65
4.2.1 Sample Preparation and Analysis . . . 65
4.2.2 Comparison of Optical and EBSD Observations . . . 66
4.2.3 Slip System Identification . . . 68
4.3 Results and Discussion . . . 69
4.3.1 Incidence of Lattice Distortions . . . 69
4.3.2 Evaluating the Dendritic Growth Hypothesis . . . 70
4.3.3 Collisions of Crystals . . . 74
4.3.4 Generating Differential Stresses within Volcanic Plumbing Systems . 76
4.3.5 Assessing the Conditions of Deformation . . . 78
4.3.6 Mush Pile Geometry . . . 83
4.3.7 Mush Pile Location . . . 85
4.4 Conclusions . . . 88

5 Crystal scavenging from mush piles recorded by melt inclusions 89
5.1 Introduction . . . 89
5.2 Methods . . . 94
5.3 Results and Discussion . . . 94
5.3.1 Constraints from Olivine-Liquid Disequilibrium . . . 94
5.3.2 Constraints from Melt–Inclusion Liquid Disequilibrium . . . 97
5.3.3 Centurial Storage Times Within Mush Piles . . . 102
5.3.4 Disequilibrium Affects Melt Inclusion CO_2 Systematics . . . 104
5.3.5 Pre–eruptive History of Evolved Crystal Cargoes . . . 106
5.3.6 Pre–eruptive history of primitive crystal cargoes . . . 107
5.4 Conclusions . . . 108

6 Chalcophile elements track the fate of sulfur at Kīlauea Volcano, Hawai'i 110
6.1 Introduction . . . 111
6.2 Methods and Sample Details . . . 114
6.3 Results . . . 115
6.3.1 Glass and Melt Inclusion Chemistry . . . 115
6.3.2 Sulfide Occurrence . . . 120
6.4 Discussion . . . 123

6.4.1 Sulfides in Kīlauea's Mantle Source . . . 123
6.4.2 Sulfide Systematics During Magma Ascent and Fractionation . . . 134
6.4.3 Sulfide Saturation in Lava Lakes . . . 142
6.4.4 Degassing of Chalcophile Elements . . . 143
6.4.5 Sulfide Resorption During Magma Degassing . . . 146
6.5 Conclusions . . . 152

7 Reconstructing Magma Storage Depths for the 2018 Kīlauean Eruption from Melt Inclusion CO_2 Contents 155
7.1 Introduction . . . 156
7.2 Melt Inclusion Entrapment Pressures . . . 158
7.2.1 The Importance of Vapour Bubbles . . . 158
7.2.2 Reconstructing Vapour Bubble CO_2 . . . 159
7.3 Materials and Methods . . . 163
7.3.1 Sample Details and Preparation . . . 163
7.4 Results . . . 165
7.5 Discussion . . . 171
7.5.1 Mineral-melt disequilibrium drives the growth of a CO_2-rich bubble . 171
7.5.2 PEC and melt-vapour CO_2 partitioning . . . 174
7.5.3 Analytical versus theoretical constructions of vapour bubble CO_2 . . 179
7.5.4 Reconstructing Magma Storage Depths . . . 184
7.5.5 Summit-Rift Connectivity . . . 188
7.6 Conclusion . . . 191

8 Conclusions and Future Work 193
8.1 Future Work . . . 197

Works Cited 199

List of Figures

1.1 Map of the Hawaiian islands and Kīlauea Volcano 2
1.2 Schematic of Kīlauea's plumbing system 5
1.3 Pb isotope trends 6
1.4 Changes at Kīlauea's summit 9
1.5 2018 field campaign 10
1.6 Chalcophile elements 11

2.1 Lava sampling during the 2018 LERZ eruption 15
2.2 Lava sampling in 2019 15
2.3 Epoxy mounting techniques 18
2.4 Melt inclusion mounting technique 19
2.5 Se-As line scans 28
2.6 Example Raman spectra of melt inclusion vapour bubbles 31
2.7 Gaussian peak fitting routine in MATLAB 32
2.8 Literature densimeters 33
2.9 Compilation of CO_2 densities in the Literature 35
2.10 Fluid inclusion standards 36
2.11 Calibration line for the Cambridge Raman 36
2.12 Spectral emission of Ne 38
2.13 Ne line correction routines 40
2.14 Monitoring Raman drift with synthetic standards 41
2.15 Analytical uncertainties 42
2.16 SIMS calibration lines 44
2.17 Corrections for SiO_2 contents 45

3.1 Chromite aggregates 48
3.2 Olivine aggregates 49
3.3 Cartoon definition of misorientation 51
3.4 Example misorientation method 52
3.5 Misorientation signatures of olivine aggregates 53
3.6 EPMA profiles across olivine aggregates 54
3.7 Misorientation signatures of chromite aggregates 54
3.8 Crystal geometries used for energy calculations 57
3.9 Olivine and chromite twin laws 59

4.1 Comparison of optical and EBSD observations (1) 66
4.2 Comparison of optical and EBSD observations (2) 67

4.3 Comparison of optical and EBSD observations (3) . . . 67
4.4 Comparison of optical and EBSD observations (4) . . . 68
4.5 Sample locations . . . 70
4.6 Relationship between minor element enrichments and lattice distortions . . . 72
4.7 Crystallographic signatures of branching dendrites. . . . 73
4.8 Crystallographic signatures of lattice distortions within Kīlauean olivines. . 74
4.9 Chemical differences between deformed and undeformed Kīlauean olivines . . 75
4.10 Textural evolution of mush piles . . . 77
4.11 Slip system identification method . . . 79
4.12 Quantifying the conditions of deformation . . . 81
4.13 Adapted linear intercept method . . . 83
4.14 Schematic cross section showing the generation of deformed grains within the SC reservoir . . . 85
4.15 Estimating mush pile accumulation rates using a simple box model . . . 87

5.1 Map of sample locations examined in this study and the literature . . . 93
5.2 Olivine-liquid relationships . . . 95
5.3 Nb/Y vs. MgO . . . 98
5.4 Melt inclusion–liquid disequilibrium . . . 99
5.5 Trace element ratios vs. Fo content . . . 101
5.6 Assessing trace element re–equilibration . . . 103
5.7 Correlations between melt inclusion and glass MgO . . . 104
5.9 Schematic diagram of Kīlauea's plumbing system highlighting the crystal scavenging process . . . 109

6.1 Chalcophile element systematics of the Kīlauea Iki lava lake . . . 114
6.2 Cu, S and MgO systematics of Hawaiian melts . . . 116
6.3 Chalcophile element volatility . . . 118
6.4 Fractionation-corrected trace element systematics . . . 119
6.5 Chemistry and textures of Kīlauean sulfides . . . 120
6.6 Sulfides in matrix glass vesicles . . . 121
6.7 Sulfides in melt inclusion vapour bubbles . . . 122
6.9 Modelling sulfide saturation during mantle melting . . . 125
6.10 S and Fe redox during fractionation . . . 128
6.11 Modelling Cu and Ba during mantle melting . . . 133
6.12 Modelling sulfide solubility during ascent . . . 135
6.13 Comparing calculated and measured sulfide compositions . . . 137
6.14 Sulfide solubility using calculated sulfide compositions . . . 138
6.15 Modelling sulfide solubility during fractionation . . . 141
6.16 Calculating emanation coefficients . . . 145
6.17 Emanation coefficients vs. sulfide-liquid partition coefficients . . . 148

6.18 Chemical trajectories of sulfide resorption 151
6.19 Schematic diagram of chalcophile behaviour at Kīlauea 153

7.1 Map of 2018 eruption site 156
7.2 Sensitivity of saturation pressures to melt inclusion H_2O contents 160
7.3 PEC corrections 165
7.4 Olivine chemistry and olivine-melt relationships at Fissure 8 166
7.5 EDS map of high-Fo olivine 167
7.6 Major element systematics of F8 melt inclusions and glasses 168
7.7 Vapour bubble and melt inclusion CO_2 systematics 170
7.8 H_2O systematics of F8 melt inclusions 171
7.9 Evaluating the compositional sensitivity of CO_2 solubility 175
7.10 Histograms of melt inclusion CO_2 contents from F8 and the literature 177
7.11 Comparison of EOS methods and Raman spectroscopy 181
7.12 Models of CO_2 partitioning between melt and bubble phases 183
7.13 Cumulative distribution functions of entrapment pressures 187
7.14 Schematic diagram of Kīlauea's plumbing system feeding the 2018 eruption . 190

List of Abbreviations

ERZ . . . . . East Rift Zone

LERZ . . . . . Lower East Rift Zone

SWRZ . . . . . South West Rift Zone

SSWRZ . . . . Seismic South West Rift Zone

VSWRZ . . . . Volcanic South West Rift Zone

HMM . . . . . Halema'uma'u

SC . . . . . South Caldera

HVO . . . . . Hawaiian Volcano Observatory

USGS . . . . . United States Geological Survey

F8, 9, 10, 17 . Fissure 8, Fissure 9, Fissure 10, Fissure 17...

EPMA . . . . Electron Probe Microanalyser

EBSD . . . . . Electron Backscatter Diffraction

SIMS . . . . . Secondary Ion Mass Spectrometry

LA-ICP-MS . (Laser Ablation) Inductively Coupled Plasma Mass Spectroscopy

FTIR . . . . . Fourier Transform Infrared spectroscopy

InSAR . . . . . Interferometric synthetic aperture radar

IPF . . . . . Inverse Pole Figure

WBVD . . . . Weighted Burgers Vector Direction

{**012**} . . . . . A plane or face in crystal coordinates.

[012] . . . . . A crystallographic direction

KS test . . . . Kolmogorov-Smirnov test

1 Introduction

1.1 Motivation

Constraining the geometry of magma storage and transport regions beneath active volcanic centres is crucial for the interpretation of volcanic monitoring data (e.g., differentiating magmatic and hydrothermal activity from precursory signals; Pritchard et al., 2019), accurate estimates of volatile fluxes (Poland et al., 2015), and to further our understanding of the chemical evolution of the Earth's crust (Thybo and Artemieva, 2013). Many volcanoes around the world have not experienced an eruption or a significant period of unrest since historical records began. For example, Chaiten Volcano erupted after ∼9000 years of dormancy in 2008 (Major and Lara, 2013). Additionally, more than half of the world's volcanoes have no ground-based monitoring sensors (Valade et al., 2019). In these systems, erupted lava flows, tephra, spatter and ash provide invaluable constraints on the geometry of the magmatic plumbing system, as well as information on repose periods, eruption styles, and eruptive volumes to inform long-term volcanic hazard assessment (Molist, 2017). Developing, testing and groundtruthing these techniques on well studied volcanoes is essential to ensure that petrological archives are interpreted correctly in poorly-constrained systems.

Over the last decade, there has been a paradigm shift from the century-old model of magmatic systems consisting of large bodies of melt within the crust to a "mush-dominated" model, where plumbing systems predominantly consist of extensive piles of settled crystals with low enough melt fractions to form rigid frameworks (Cashman et al., 2017). Crystals may be stored in mush piles for hundreds to thousands of years, before their eruption in unrelated carrier melts. The mush paradigm challenges the common assumption that careful petrological examinations of erupted crystals can be used to investigate specific eruption episodes (e.g., controls on eruption style, eruption triggering; Sides et al., 2014a; Stock et al., 2016). This thesis interrogates erupted crystals and melts from Kīlauea Volcano, Hawaii, using a wide variety of microanalytical techniques, to re-evaluate the utility of petrological archives to assess the geometry and chemical evolution of mush-dominated magmatic plumbing systems.

1.2 The Volcanic Plumbing System of Kīlauea Volcano

Kīlauea Volcano is an outstanding natural laboratory in which to investigate basaltic volcanism, resulting from over a century of careful observation and detailed study following the founding of Hawaii Volcano Observatory (HVO) in 1912 (Poland, 2015). Kīlauea is the youngest of 5 volcanic centres on the island of Hawai'i, located at the south-eastern end of the >6,000 km long Hawaiian-Emperor volcanic chain (Fig. 1.1a). Volcanism on the Hawaiian-Emperor chain is driven by melt generation within a thermochemical "hotspot" extending into the lower-most mantle (Morgan, 1972; Ballmer et al., 2013; Dannberg and Sobolev, 2015). The pseudo-stationary position of this hotspot relative to the motion of the Pacific plate at 9 cm/yr to the NW over >70 Myrs has generated the archetypal example of a hotspot track, with volcanic islands forming a linear chain with clear age progression away from the site of active volcanism (Eaton and Murata, 1960; Tilling and Dvorak, 1993; Tarduno et al., 2003). Topographically, Kīlauea is a relatively low (1,243 masl) and elongate (~80×20 km) tholeiitic shield volcano (Holcomb, 1987), perched on the SE flank of Mauna Loa Volcano. Eruptions are mostly restricted to the area around the summit caldera, and the two prominent rift zones stretching to the east and south west (Fig 1.1b).

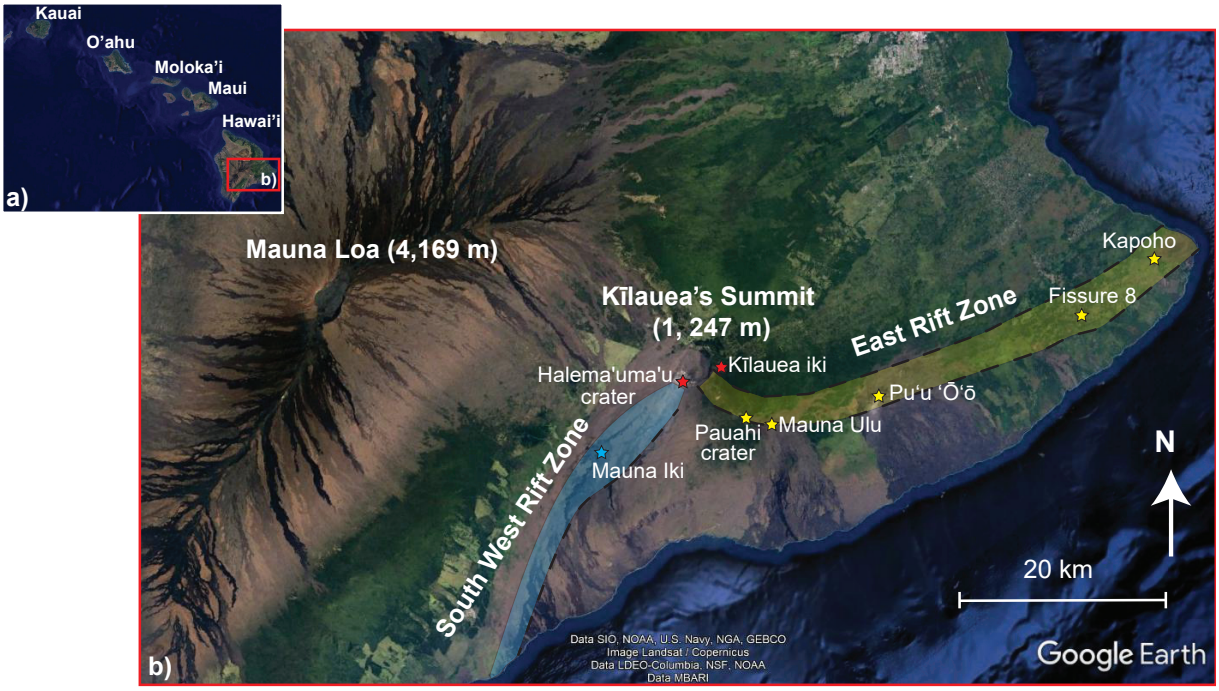


Figure 1.1: a) Map of the Hawaiian Island chain, with the red rectangle expanded in **b)**. **b)** Map of Kīlauea Volcano, which perches on the SE flank of Mauna Loa Volcano. Two prominent rift zones radiate to the east and south-west of the summit caldera. Key eruption sites discussed in this thesis are indicated with coloured stars.

The summit area of Kīlauea is dominated by a number of arcuate blocks bounded by caldera faults (Holcomb, 1987). The most prominent topographic features is a large collapse structure (Kīlauea Caldera; ∼3×5 km) thought to have formed between 300 and 500 years ago (Neal and Lockwood, 2003). In the south western region of this larger caldera lies the smaller, Halema'uma'u (HMM) pit crater, which had a diameter of ∼1 km prior to the 2018 summit collapse. This crater contained the smaller Overlook Crater, which was the site of a persistently-active lava lake between 2008–2018. The East Rift Zone (ERZ) consists of a ∼55 km long subaerial portion dominated by "chains of craters" (Eaton and Murata, 1960), fissures, faults and grabens, and a prominent submarine ridge which can be traced ∼70 km offshore (Holcomb, 1987). The South West Rift Zone (SWRZ) has less topographic prominence than the ERZ, and lacks any obvious offshore extension (Holcomb, 1987; Fig. 1.1b). The upper portion of the SWRZ is commonly subdivided into two separate strands. The southern, seismic strand (SSWRZ) is characterized by significant earthquake activity, while the northern volcanic strand (VSWRZ) has a clearer surface expression, with numerous fissures and eruptive vents (Poland et al., 2015).

The broad details of the prevailing model of Kīlauea's volcanic plumbing system have remained remarkably similar to that proposed by Eaton and Murata based on observations of ground deformation and seismicity accompanying the 1959 Kīlauea Iki and 1960 Kapoho eruptions (Eaton and Murata, 1960). Swarms of minor earthquakes originating from ∼40–60 km depths were interpreted to mark the feeder conduit from the mantle into the volcanic edifice, and inflation of the caldera between 1958 and 1959 was inferred to represent the accumulation of magma in a reservoir located at a depth of a few kilometres beneath the southern part of the caldera (Eaton and Murata, 1960). Eaton and Murata's observations following the initiation of the Kīlauea Iki eruption on November 14th, 1959 (located just east of the summit caldera), and the resultant shift in activity to Kapoho Village on the Lower ERZ (Fig. 1.1) on January 13th, 1960, were vital to understand the connection between Kīlauea's summit reservoir and the rift zones. Similarities between the volume of summit subsidence and the volume erupted at Kapoho, as well as the similar chemistry and petrology of erupted products at Kīlauea Iki and Kapoho, demonstrated that rift eruptions were supplied from the main summit reservoir via a hydraulically-connected, relatively shallow transport pathway (Eaton and Murata, 1960; Tilling, 1987; Patrick et al., 2019a; Patrick et al., 2019b). Interestingly, long before the arrival of Europeans on the Hawaiian islands, Native Hawaiians had developed a basic understanding of summit-rift connectivity, stating that Pele (their goddess of volcanoes) *"went by a road under ground from her house in the crater to the shore"* (Ellis, 1826).

Numerous petrological and geophysical studies in the 60 years following the seminal paper of Eaton and Murata (1960) have refined our understanding of the geometry of magma storage beneath Kīlauea's summit. Levelling surveys during a period of inflation

preceding the 1967–1968 eruption showed that the centre of uplift repeatedly migrated between the centre and southern portion of the summit caldera. These complex geodetic signals were interpreted to arise from the inflation of a "plexus of sills and dykes" at ∼2–3 km depth[1](Fiske and Kinoshita, 1969). Inversion of data from levelling surveys and global positioning system (GPS) measurements between 1996 and 2002 for a single point source indicates an area of magma storage beneath the southern part of Kīlauea's caldera centred no deeper than 3.5 km (hereafter the "SC reservoir"; Cervelli and Miklius, 2003). Probabilistic modelling of electronic borehole tiltmeter measurements collected over a similar time period (1998–2002) detected a second inflation source located just east of HMM crater (hereafter the "HMM reservoir") at ∼500–700 m depth (Cervelli and Miklius, 2003). Models of ground deformation measured with Interferometric Synthetic Aperture Radar (InSAR) between 2000 and 2008 inferred that the HMM reservoir is centred at ∼1.9 km depth (Baker and Amelung, 2012), and that the SC reservoir may consist of three vertically stacked sills at ∼2.9, 3.4 and 3.6 km depth (Baker and Amelung, 2012). Inversion of GPS and InSAR data of summit subsidence associated with an eruption in 2011 on the ERZ placed the 95% confidence interval on the depth of the HMM reservoir at 1.0–1.9 km (Poland et al., 2015). Probabilistic modelling of GPS measurements, InSAR, and ground tilt during the early phases of the 2018 summit collapse determined that the HMM reservoir was centred at ∼2 km (Anderson et al., 2019). In summary, studies considering deformation, gravity and seismic data from a variety of eruptions are consistent with magma storage in two main reservoirs: the HMM reservoir at ∼1–2 km depth, and the SC reservoir at ∼3–5 km depth (Poland et al., 2015, Fig. 1.2). Variable inflation of these two long-lived reservoirs can account for the complex spatial patterns of uplift centres identified by Fiske and Kinoshita (1969) without the need for a complex network of dykes and sills (Poland et al., 2015).

Despite extensive study, several aspects of Kīlauea's volcanic plumbing system are still subject to debate. Firstly, it is generally accepted, based on earthquake depths and InSAR observations, that the SSWRZ is fed from the SC reservoir (Poland et al., 2015), while the VSWRZ is a more surficial feature fed by shallow dykes from the HMM reservoir (Holcomb, 1987; Pietruszka et al., 2018; Fig. 1.2). However, the depth of the connection between the summit reservoir system and the ERZ conduit is less certain. This connection has been variably described as:

1. A Γ-shaped feeder system with a vertical conduit between the HMM and the SC reservoir, and a single, near-horizontal conduit from the HMM reservoir into the ERZ (Cervelli and Miklius, 2003; Fig. 1.2).
2. A Y-shaped feeder system with the SC reservoir feeding both the HMM reservoir and the ERZ conduit with two discrete conduits (Poland et al., 2015; Pietruszka et al., 2018; Fig. 1.2).

[1]For consistency, throughout this thesis, depths represent the vertical distance between the feature of interest and Kīlauea's caldera floor prior to the 2018 collapse event (∼1100 m above sea level)

Cervelli and Miklius (2003) suggest that the Γ-shaped model is more plausible because a shallow conduit (which is subject to less lithostatic pressure) is more likely to remain open during pauses in eruptive activity than a deep conduit, and because shallow intrusions into the upper ERZ influence both the HMM reservoir and activity at Pu‘u ‘Ō‘ō. However, Poland et al. (2015) favour the Y-shaped model based on earthquake and InSAR observations that dyke intrusions into the ERZ in 2007 and 2011 ascended from a depth of ∼3 km.

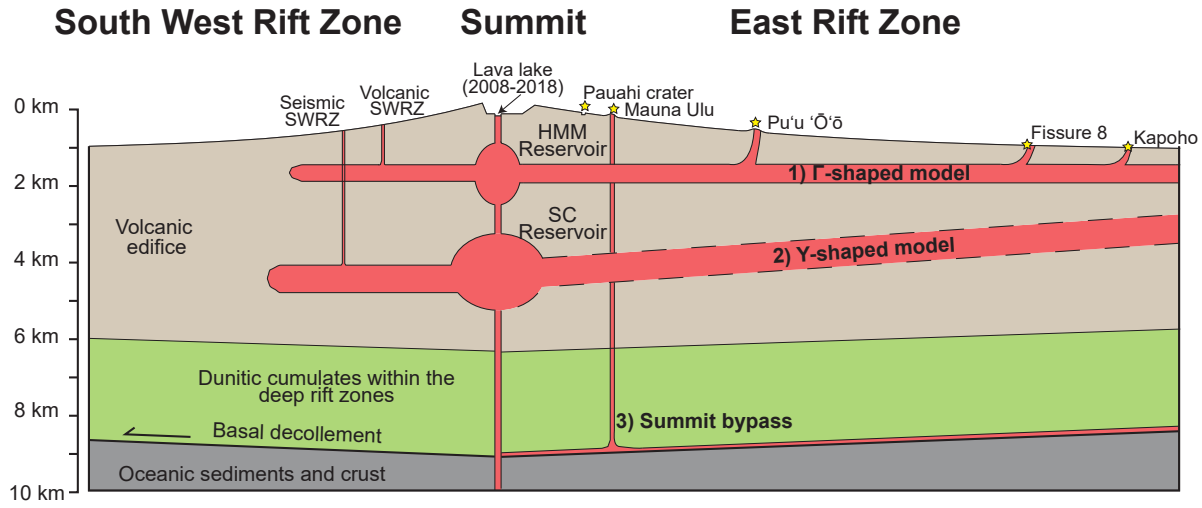


Figure 1.2: Schematic diagram of Kīlauea's plumbing system, showing the three different geometries for the summit-rift connection that have been proposed in the literature. In the Γ-shaped model, ERZ eruptions are supplied from a near-horizontal conduit supplied from the HMM reservoir **(1)**. In the Y-shaped model, ERZ eruptions are supplied from the SC reservoir **(2)**. The degree to which magma bypasses the summit along a conduit within the deep rift zones **(3)** is also uncertain.

Detailed geochemical work on erupted lavas has shown significant potential to supplement geophysical observations, and to help differentiate between the Γ-shaped and Y-shaped model. Pietruszka et al. (2015) show that summit lavas erupted between 1971 and 1983 follow two distinct mixing trends of decreasing $^{206}Pb/^{204}Pb$ ratios, providing strong evidence that magma must be stored within two discrete reservoirs beneath Kīlauea's summit. The "upper trend" with higher isotope ratios is defined by summit eruptions located on the caldera floor with relatively low whole-rock MgO contents (∼7–8 wt%), and has been attributed to magma supply from the upper HMM reservoir. The "lower trend" is defined by summit eruptions located on the easternmost edge of the caldera floor or the caldera rim with higher whole-rock MgO contents (∼9–11 wt%; Fig. 1.3), and has been attributed to magma supply from the deeper SC reservoir (Pietruszka et al., 2018). Analyses of Pb isotopes in rift eruptions during the same time period by Pietruszka et al. (2018) reveals that lavas from the volcanic SWRZ lie on the upper trend, consistent with magma supply from the HMM reservoir (Pietruszka et al., 2018; Poland et al., 2015; Holcomb, 1987),

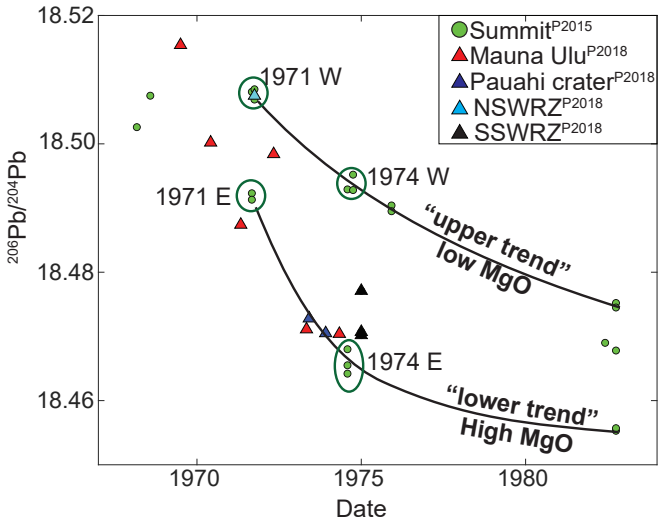


Figure 1.3: Whole-rock $^{206}Pb/^{204}Pb$ in summit lavas from 1971–1982 follow two distinct trends. The upper trend is characterized by low MgO lavas erupted on the centre and western regions of the summit caldera. The lower trend is characterized by high MgO lavas erupted on the easternmost edge and rim of the caldera, and along extracaldera faults (Pietruszka et al., 2015). Lavas from Mauna Ulu and Pauahi crater on the ERZ and lavas on the SSWRZ (Fig. 1.1) plot on the lower trend, while lavas erupted on the NSWRZ plot on the upper trend (Pietruszka et al., 2018).

while lavas erupted at Mauna Ulu on the ERZ from predominantly fall on the lower trend, with some complexities due to mixing with an additional end member. These observations support the Y-shaped model where the ERZ is connected to the SC reservoir (Pietruszka et al., 2018). However, the most recent geodetic measurements associated with the early phases of the 2018 summit collapse (triggered by the effusion of large volumes of magma on the lower ERZ) are best recreated by emptying of the HMM reservoir, with an uncertain contribution from the SC reservoir (Anderson et al., 2019). This may lend support to the Γ model, although it is not implausible that lava drained from the HMM reservoir into the SC reservoir, and out into the ERZ conduit.

A second source of debate is the extent to which mantle-derived melts bypass the summit reservoir system via transport through Kīlauea's deep rift zones at ∼6–9 km depth (Ryan, 1988; Garcia et al., 1996; Vinet and Higgins, 2010; Poland et al., 2015; Fig. 1.2). This model was proposed based on the presence of olivine phenocrysts with prominent lattice distortions in lavas from Mauna Ulu and Kīlauea's submarine ERZ (Trusdell, 1991; Garcia et al., 1996; Vinet and Higgins, 2010), which were thought to be derived from creeping dunitic bodies within Kīlauea's deep rift zones (Clague and Denlinger, 1994). Their presence in erupted lavas has been attributed to magma transport along the basal decollement (allowing melts to pick up these distorted olivines), followed by vertical ascent to the eruption site (Vinet and Higgins, 2010; Fig. 1.2). Similarly, Trusdell (1991) attribute the extremely high MgO contents of the 1840 lava flow on the Lower ERZ to the summit bypass model. However, positive residual gravity anomalies, elevated seismic velocities, and low V_p/V_s ratios within Kīlauea's deep rift zones are consistent with the presence of low melt fraction dunitic/gabbroic cumulates (Poland et al., 2015; Park et al., 2007; Hansen et al., 2004), rather than a melt-rich conduit. Furthermore, during a magma supply surge in 2003–2007,

there was no change in the rate of deep rift zone opening, which would have been expected if considerable volumes of magma bypassed the summit reservoir (Poland et al., 2015).

In this thesis, the summit bypass model is evaluated through detailed microanalytical observations of olivine crystals and matrix glasses erupted over five years between May 1969 and December 1974, hereafter known as the "Mauna Ulu period". Additional insight into the nature of the summit-rift zone connection is provided by melt inclusion barometry on basaltic samples from the lower ERZ eruption of 2018 presented in Chapter 7. Collectively, this work demonstrates the complex, pre-eruptive processes experienced by Kīlauean crystal cargoes.

1.3 Rift-Summit Connections During the Mauna Ulu Period

At the time, the Mauna Ulu eruption was the most voluminous and long-lasting rift eruption at Kīlauea in recorded history (Swanson et al., 1979). However, just nine years later (in 1983), the onset of the 35-year Pu‘u ‘Ō‘ō eruption rapidly demoted its longevity. As a result of a shift in research interest to the Pu‘u ‘Ō‘ō eruption, there have been relatively few detailed petrological studies on lavas from the Mauna Ulu period. However, this five-year period offers a unique opportunity to assess summit-rift connections, because eruptions took place almost simultaneously on both rift zones and at discrete sites within the summit caldera (Lockwood et al., 1999; Duffield et al., 1982). Activity predominantly focused at a site on the ERZ, now marked by the Mauna Ulu shield. However, in June 1971, activity declined at Mauna Ulu, and the summit area began to inflate (Duffield et al., 1982), followed by eruptions within the summit caldera and on the volcanic SWRZ in Sept 1971. Following shifting of the activity back to Mauna Ulu, a blockage of the Mauna Ulu conduit in 1973 resulted in an eruption ∼2 km up-rift at Pauahi Crater (Fig. 1.1). Finally, in July 1974, activity shifted back to the summit area once more, and in December 1974, an eruptive fissure opened on the SSWRZ. In additional to the interesting spatial and temporal relationships between rift and summit eruptions, another significant advantage of working on this time period is that lavas from very similar eruption sites to those examined here were the focus of the Pb-isotope work of Pietruszka et al. (2018), providing insights into which reservoir each eruption was supplied from. Finally, the presence of distorted olivines in Mauna Ulu lavas is commonly cited as evidence for summit bypass (Vinet and Higgins, 2010), so further interrogation of these features is crucial to reconcile the disparate views of geophysical and petrological communities working on Kīlauea Volcano.

In addition to prominent lattice distortions, olivine crystals erupted during the Mauna Ulu period exhibit prominent clusters of 2–17 individual crystals. Both these textural features have been noted in a variety of basaltic systems, but there is little consensus on the mechanisms leading to their formation. In this thesis, an integrative approach combining

major element data collected using an electron microprobe (EPMA), and crystallographic data collected using electron backscatter diffraction (EBSD) was used to critically evaluate the different hypotheses proposed in the literature. In particular, two recent studies attributing both features to an early dendritic growth phase has gained considerable traction (Welsch et al., 2012; Welsch et al., 2014; 152 citations). To quantitatively assess this hypothesis, the crystallographic signatures of dendritic olivines from West Greenland picrites were measured using EBSD, allowing direct comparisons to the crystallographic signatures of Kīlauean aggregates and distorted olivines.

Chapter 3 focuses on the formation of crystal aggregates. To demonstrate the versatility of EBSD to differentiate hypotheses in volcanology in a variety of igneous systems, measurements of Kīlauean olivines are considered alongside EBSD measurements of chromite aggregates from the Bushveld complex (in collaboration with Zoja Vukmanovic). The wide variety of attachment geometries in both cases is indicative of a physical aggregation process, rather than growth or nucleation, which would favour very specific geometric relationships.

Chapter 4 assesses the spatial distribution, chemical composition, and microstructural character of distorted olivines from the Mauna Ulu period. This chapter concludes that lattice distortions are likely generated through prolonged crystal storage in gravitationally-loaded cumulate piles at the base of the SC reservoir, rather than in Kīlauea's deep rift zones. An origin from the SC reservoir invalidates petrological arguments for deep rift zone magma transport paths, and supports the overall shift within igneous communities in the last decade towards a "mush-dominated" view of magmatic plumbing systems.

The prolonged storage of crystals in plastically-deforming mush piles before their eventual eruption in unrelated carrier melts challenges the common assumption that erupted crystals and melt inclusions can be used to investigate specific eruptive episodes (Sides et al., 2014a; Stock et al., 2016). Chapter 5 assess the validity of this assumption by evaluating the extent of trace element disequilibrium between carrier melts and melt inclusions, as well as Fe-Mg disequilibrium between carrier melts and erupted olivine crystals. The remarkable similarity of melt inclusion populations in multiple different eruptive episodes, despite chemically distinct carrier melts, provides support for the model proposed in Chapter 4 where high forsterite olivines are stored in mushes for prolonged periods. These results indicate that extreme care must be used to link melt inclusion records to eruption specific measures (such as volatile fluxes, or eruption styles) in mush-dominated systems.

1.4 The 2018 Lower East Rift Zone Eruption

The focus of the remainder of thesis, which had planned to investigate deposits from a series of paired summit and rift eruptions from the 1950–1970s, was diverted by the onset of the lower East Rift Zone (LERZ) eruption on May 3rd, 2018. This activity marked the most significant change in eruptive character at Kīlauea Volcano in the last 35 years, terminating the long-lived Pu‘u ‘Ō‘ō eruption. Twenty four fissures opened in the Leilani Estates subdivision between May 3rd and 27th, 2018, with activity localizing at Fissure 8 (F8) by the end of May (Fig. 1.1b). The summit area of Kīlauea also changed dramatically over this period (Fig. 1.4), making the deposits from many summit eruptions inaccessible.

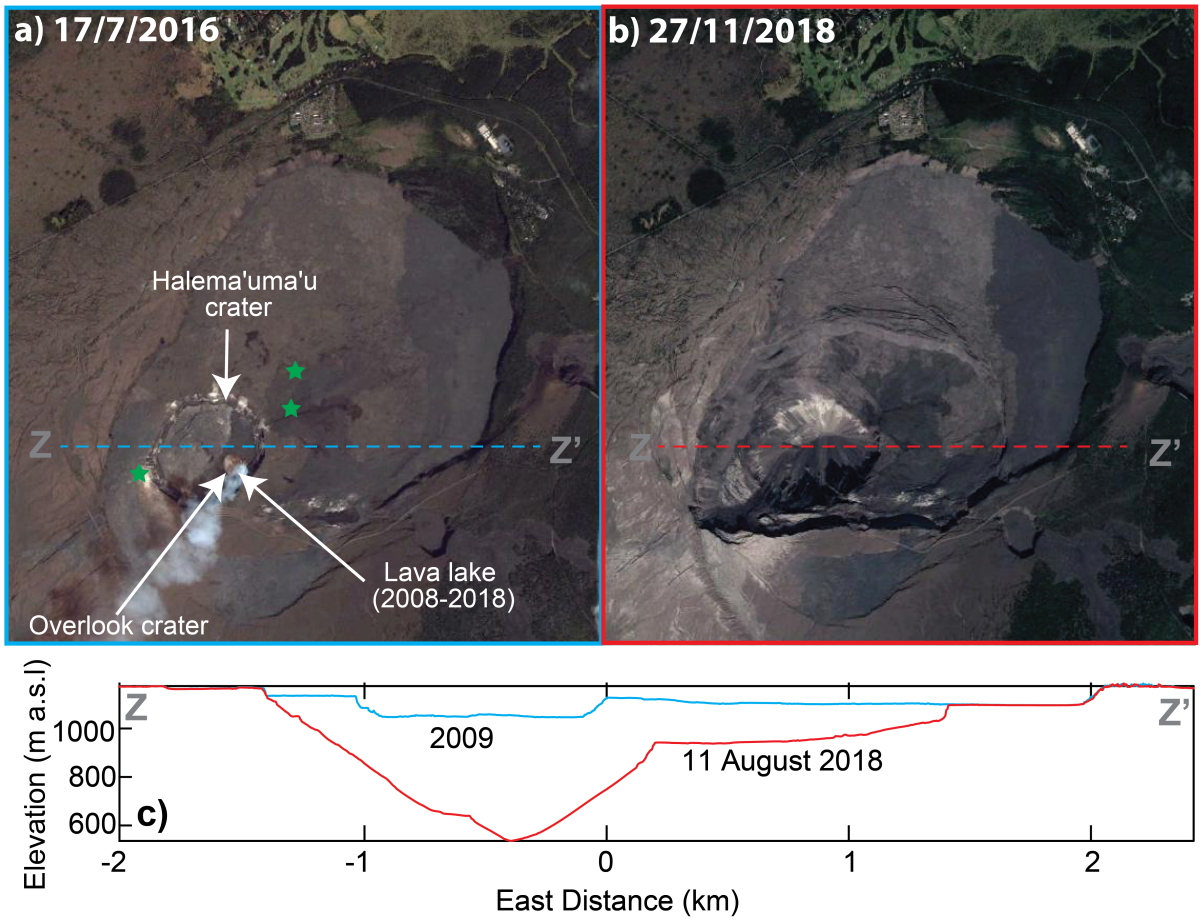


Figure 1.4: a-b) Comparison of Google Earth images taken before and after the 2018 caldera collapse. **c)** Topographic profile across the profile Z-Z' (adapted from Neal et al., 2019). The location of eruption sites that were planned targets for a field campaign in the fall of 2018 are shown with green stars (fissure eruptions from 1954, 1971, 1975 which have paired ERZ eruptions). These deposits now lie on the highly unstable block that subsided several hundred metres.

The level of the lava lake within the Overlook Crater began to drop on May 6th, 2018, disappearing after dropping >325 m by May 10th. Following a large rock fall which trigged an ash plume to rise to 6,000 ft on May 9th, 2018, HVO issued an alert stating that the lowering

of the lava lake could lead to steam-driven explosions, producing ballistic projectiles and ashfall (USGS, 2019b). Rock falls throughout May, 2018 created ash plumes reaching ∼12,000 ft (USGS, 2019a). Progressive widening of the HMM crater due to lava lake withdrawal and explosive activity was followed by large-scale subsidence of approximately half of the caldera floor (Fig. 1.4). The caldera collapse drastically changed the topography of Kīlauea's summit, with the deepest parts of the new caldera having subsided ∼500 m (Fig. 1.4).

Although access to the summit area within Hawai'i Volcanoes National Park was severely restricted throughout the eruption, by June, the LERZ had become more accessible. The focusing of activity at F8 led to the development of a lava channel with relatively stable levees. At this point, the most significant hazard to the residents of Hawai'i was the release of unprecedented quantities of SO_2 and other environmentally-reactive volatile elements to the lower troposphere (Kern et al., 2020). Following an invitation from HVO in late June, a field team from Leeds and Cambridge University was rapidly assembled to quantify the elemental composition of the F8 plume, and to trace downwind changes in chemistry in a number of exposed communities around the island of Hawai'i (#PlumeTeam; Evgenia Ilyinskaya (PI), Emma Liu, Emily Mason, Rachel Whitty, and myself).

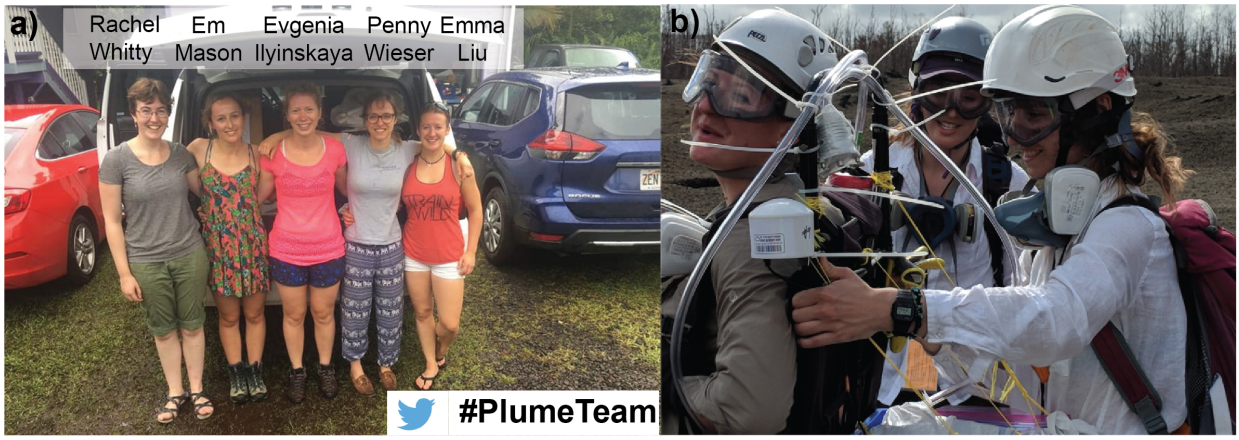


Figure 1.5: a) Team photo at the end of the 2018 aerosol sampling campaign. **b)** Collecting aerosol samples with filter packs and cascade impacts behind the F8 cone with Emma Liu and Emily Mason.

Following this dramatic initiation into the world of volcanic aerosol sampling, I became fascinated by the petrological processes controlling the concentration of environmentally-reactive elements in Kīlauean melts, and their influence on the elemental signatures of volcanic plumes. Traditionally, many of these environmentally-reactive elements have been classified by petrological and mineral exploration communities as "chalcophile", based on their affinity for sulfide phases (e.g., Se, As, Cd, Bi, Cu; Fig. 1.6; Wieser and Jenner, 2020). This classification is used throughout this thesis for continuity with previous geochemical studies, and for brevity when discussing analyses of these elements

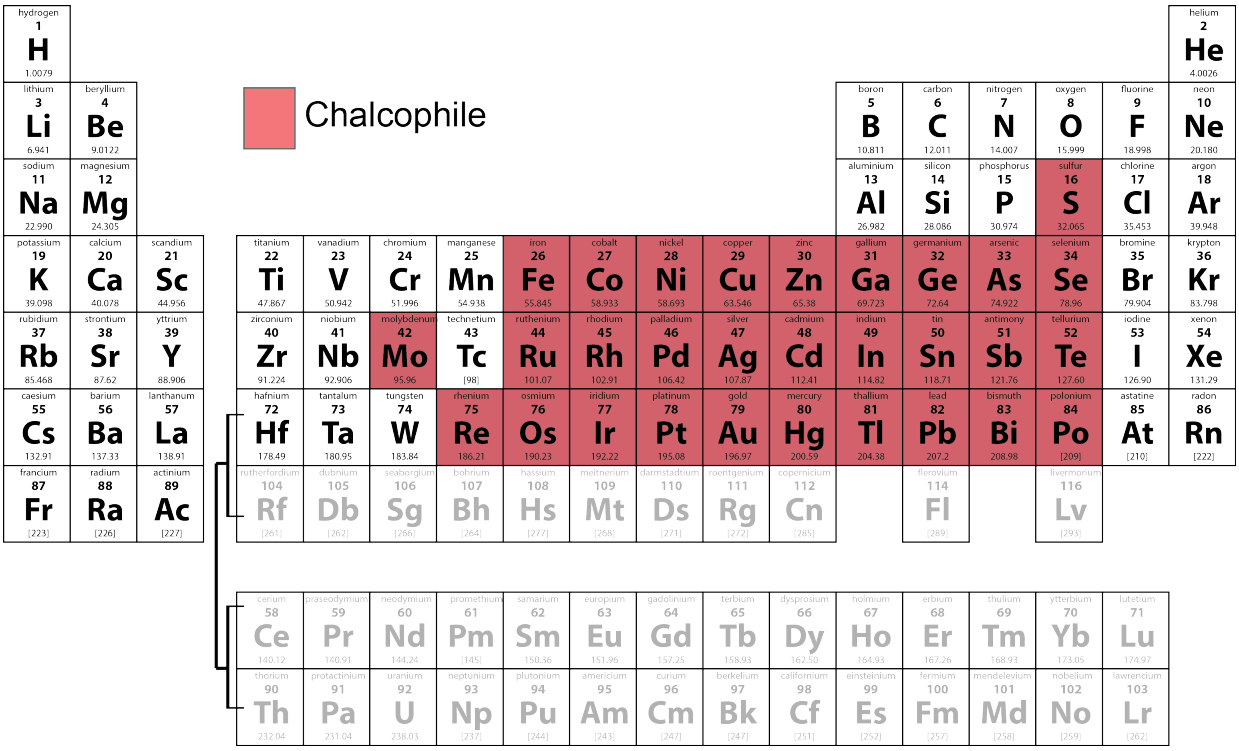


Figure 1.6: Periodic table, where elements displaying chalcophile behaviour are coloured red. Many chalcophile elements also display siderophile behaviour (e.g., Co, Ni, Ru, Rh, Pd, Re, Os, Ir, Pt, Au), lithophile behaviour (e.g., Ru, Rh, Ir), or atmophile behaviour (e.g., S, Se, Re). Periodic table adapted from Coudert (2014) and Kiseeva et al. (2017).

compared to the more routinely-analysed suite of lithophile elements (E.g. Mg, Si, Fe, Nb, Ta, La, Yb; Chapter 5).

Our understanding of the behaviour of chalcophile elements in magmatic systems lags behind that of lithophile elements, largely due to analytical complexities associated with their measurement. Until the introduction of modern inductively coupled plasma mass spectrometry (ICP-MS) instruments, the concentration of many chalcophile elements were below the detection limits of available analytical techniques (e.g., EPMA, INAA, SIMS; Ertel et al., 2008). Furthermore, the in-situ analysis of these elements through the coupling of a laser ablation (LA) system to an ICP-MS has been held back by the paucity of reference materials with homogenous and well constrained concentrations of chalcophile elements (Jochum et al., 2006). Well characterized standards are crucial for instrument calibration and assessment of the accuracy and precision of data collection methods. A further limitation is the fact that many LA-ICP-MS instruments only have unit mass resolution, while naturally abundant chalcophile element isotopes suffer from competing signals from elemental interferences (where a series of atomic or molecular ions have the same mass to charge ratio as the element of interest). For example, $^{107}Ag^{+}$ suffers from interferences with $^{91}Zr^{16}O^{+}$ (Jenner and Arevalo Jr, 2016), $^{80}Se^{+}$ with $40Ar_2^{+}$, $70Ge^{+}$ with $^{54}Fe^{16}O^{+}$ and $^{30}Si^{40}Ar^{+}$ (Arevalo et al., 2011). This problem has been effectively circumvented in

recent years by utilizing instruments with reaction or collision cells. Reaction cells shift the mass of the ion of interest to an interference-free position (e.g., adding oxygen shifts $^{80}Se^{+}$ to $^{86}SeO^{+}$ and $^{75}As^{+}$ to $^{91}AsO^{+}$; Reekie et al., 2019), while collision cells use kinetic energy discrimination to remove polyatomic interferences based on their larger size compared to the target ion. An alternative approach uses mass spectrometers with increased mass resolution, allowing better separation of peaks with similar mass to charge ratios (e.g., $^{71}Ga^{+}$ from $^{142}Nd^{2+}$; Arevalo et al., 2011).

The concentrations of lithophile elements in melt inclusions and matrix glasses presented in Chapter 5 were collected by LA-ICP-MS at the Open University. This laboratory is also optimized for the analysis of chalcophile elements, possessing well characterized standards (Jenner et al., 2009), as well as significant expertise regarding the use of a reaction cell to resolve elemental interferences for As and Se. To address the paucity of chalcophile element concentrations in the literature, a number of elements (Cu, Zn, Mo, Cd, In, Sn, Sb, W, Tl, Bi) were added into the analytical routine during data collection of the lithophile elements discussed in Chapter 5. Additionally, Se and As were analysed in a subset of the same inclusions utilizing laser line scans and the reaction cell. These analyses of melt inclusions and matrix glasses from the Mauna Ulu Period represents the first comprehensive dataset of a large suite of chalcophile element concentrations measured using modern analytical techniques at a hotspot volcano.

This dataset is evaluated in Chapter 6 in the context of a number of uncertainties regarding the behaviour of chalcophile elements during ocean-island magma genesis and evolution, spanning melting processes in the mantle source, through crustal differentiation, to magmatic degassing at low pressures. For example, although S is present in low concentrations in the Earth's mantle, residual sulfide phases almost entirely control the concentration of many chalcophile elements in mantle melts. Recently, chalcophile element signatures in erupted lavas have been used to infer the presence of terrigenous sediments and recycled crust in the Hawaiian mantle source (Greaney et al., 2017; Ding and Dasgupta, 2018). However, such interpretations rely on assumptions regarding the presence or absence of sulfide throughout the melting interval which are still subject to debate (both at Hawai'i, and globally). The onset of sulfide saturation during fractional crystallization at Kīlauea is also uncertain, with Wallace and Anderson (1998) suggesting that melts with relatively high MgO contents are sulfide saturated (>10 wt%), while Greaney et al. (2017) infer that sulfides only saturate in very evolved melts (∼2 wt% MgO). Assessing when Kīlauean magmas saturate in a sulfide phase is vital to assess the processes controlling the elemental compositions of volcanic plumes. For example, it has been suggested based on broad correlations between sulfide-silicate melt coefficients in volcanic plumes, and observations of sulfides attached to bubbles, that chalcophile elements held within sulfides are directly transferred to the gas phase during sulfide resorption (Mungall et al., 2015; Edmonds et al., 2018; Nadeau et al., 2010).

The analyses of lithophile, chalcophile, and volatile elements (H_2O, CO_2, F, Cl) conducted on the basaltic-dacitic melt inclusions and matrix glasses from the 2018 eruption builds on Chapters 5 and 6. To stay within the page limit, and due to COVID-induced analytical delays, Chapter 7 focuses on the CO_2 budget of basaltic melt inclusions erupted during the later phases of the 2018 activity. This represents the first extensive dataset of CO_2 measurements in both the melt and bubble phase of Kīlauean melt inclusions, allowing investigation of the partitioning of CO_2 into vapour bubbles during post-entrapment crystallization. This chapter also capitalizes on a side project I have been involved in, coding up a number of different H_2O-CO_2 solubility models into Python3 (VESIcal, `https://github.com/kaylai/VESIcal`). Prior to the production of this code, most studies calculated saturation pressures by manually entering the major and volatile element concentrations of every single melt inclusion into macro-enabled excel workbooks (e.g, VolatileCalc; Newman and Lowenstern, 2002), or web-hosted calculators (e.g., Magmasat; Ghiorso and Gualda, 2015). The extremely labour-intensive nature of these tools has meant that very few studies have critically evaluated the differences between saturation pressures calculated using different model parametrizations. Through the careful choice of solubility models based on comparisons of calibration datasets to the compositions of Kīlauean melt inclusions, as well as coupled Raman and SIMS measurements on individual inclusions, this study provides the first petrological barometric estimates that align with the depths of the main magma storage reservoirs inferred from geophysical studies at Kīlauea.

2
Methods

This chapter describes the sample preparation and microanalytical techniques used in this thesis. Unless stated otherwise, all facilities were located within the Department of Earth Sciences at the University of Cambridge.

2.1 Sample Collection

The spatter, scoria and reticulite samples examined in Chapters 3 to 6 were collected by Isobel Sides during her PhD. Samples examined in Chapter 7 were collected in 2018 and 2019 (Table 2.1). Sample LL7 was fished directly from the F8 channel ∼500 m downstream of the F8 vent on August 1st, 2018 by Frank Trusdell (Fig. 2.1a-b) using a long metal rod with a chain attached to it. The chain was dipped into the channel, and then the clump of lava that stuck to it was swung onto the channel levee and rapidly quenched using a few litres of water. Once the outside had solidified, a geological hammer was used to punch holes in the lava to allow water to quench the interior. Sample LL8 was collected from a glassy proximal overflow from the F8 channel on July 21st, 2018 (Fig. 2.1c). Based on the silvery colour of the flow, it was likely less than one week old (pers. comms. Dave Schneider, USGS). Additional samples were collected in 2019 with the help of Rod Kindel, a Leilani resident who owns the land where F10, F11 and F12 opened. Samples LL11 (F11) and LL12 (F12) were collected from the spatter mounds around the centre of each fissure system (Fig. 2.2b). Care was taken to collect the glassiest spatter to mitigate the effects of H^+ diffusion (Lloyd et al., 2013). These samples were supplemented by material from the HVO archives from F4, F5, F10, F13, F17, and F20, as well as samples collected in the early stages of F8 in May, 2018 (Table 2.1).

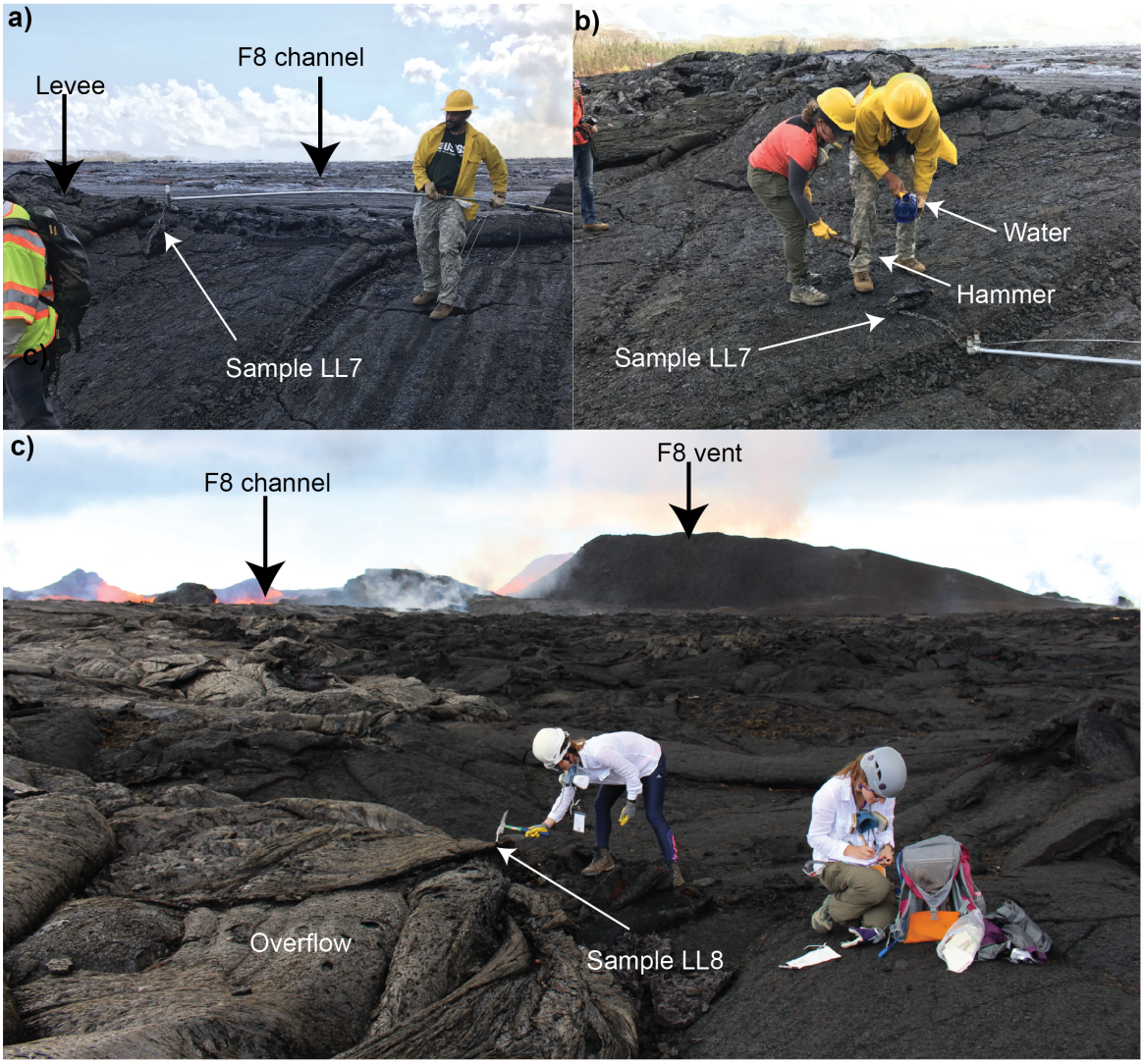


Figure 2.1: a-b) Accompanying Frank Trusdell on his lava fishing mission of the F8 channel on August 1st, 2018. **c)** Sampling a proximal overflow with Emily Mason on July 21st, 2018 (see Table 2.1).

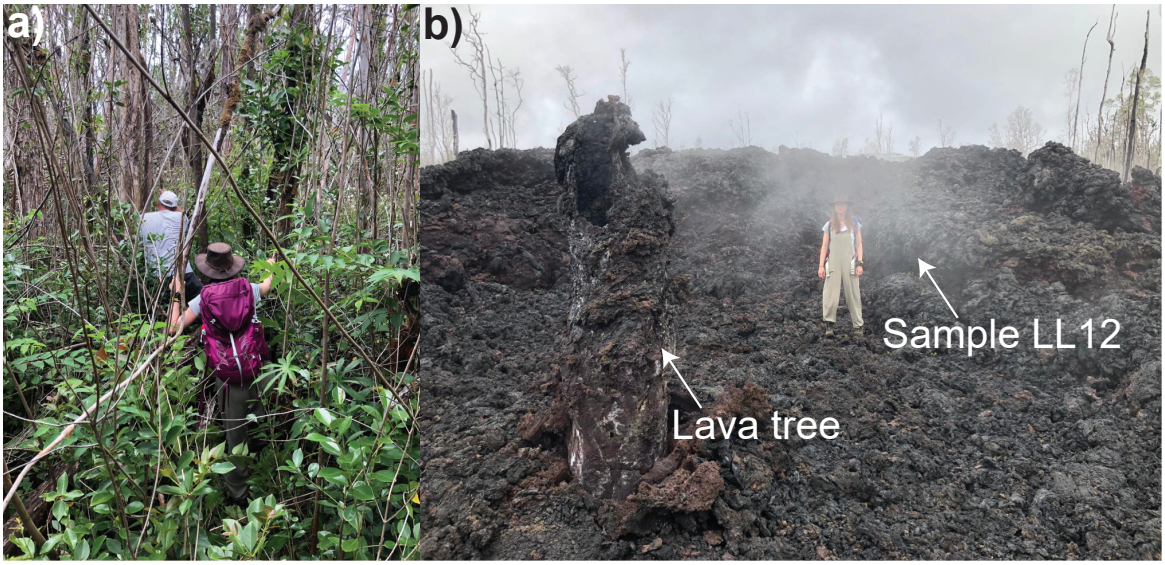


Figure 2.2: a) Being led into the jungle by Leilani Resident Rod Kindel, owner of F10, F11 and F12. Rapid regrowth of the jungle over rotting trees felled by the volcanic plume in 2018 made access extremely challenging. **b)** Out of the forest in the centre of F12. Glassy spatter was collected from the raised bluff at the back of the photo.

Table 2.1: Samples analysed in this thesis. The official USGS sample codes as well as laboratory abbreviations are shown for the LERZ samples. Samples indicated with a * were examined for sulfide occurrence only in Chapter 6. The exact eruption date of samples indicated with ** are unknown. Classification abbreviations are as follows: EC - Extracaldera (eruption site located on the rim of Kīlauea's caldera), IC - Intracaldera (eruption site located on the floor of Kīlauea's caldera), ERZ - East Rift Zone, SSWRZ - Seismic South West Rift Zone, VSWRZ - Volcanic South West Rift Zone, LERZ - Lower East Rift Zone.

Sample #	Date (CE)	Location	Classification	GPS coordinate	Chapter
Collected by I.Sides					
KL0905	July 19-22nd, 1974	Lua Manu Crater	EC	19 23.935‘ N, 155 15.337‘ W	6*
KL0909	May 24th, 1969	Ep. 1 Mauna Ulu	ERZ	19 21.826‘ N, 155 12.877‘ W	3, 4
KL0908	Dec 30th, 1969	Ep. 12 Mauna Ulu	ERZ	19 20.839‘ N, 155 12.518‘ W	3, 4, 5, 6
KL0910	Nov 10th, 1973	Pau'ahi Crater	ERZ	19 22.313‘ N, 155 13.510‘ W	3, 4, 5, 6
KL0914	Sept 24-29th, 1971		IC	19 24.580‘ N, 155 16.631‘ W	4, 6*
KL0916	Aug 14th, 1971		IC	19 24.137‘ N, 155 16.644‘ W	3, 4, 5, 6
KL0917	Late July, 1974		IC	19 24.061‘ N, 155 16.653‘ W	3, 4
KL0919	Late Dec, 1974	Ka'u Desert	SSWRZ	19 22.649‘ N, 155 17.609‘ W	3, 4, 5, 6
KL0920	Late Dec, 1974	Ka'u Desert	SSWRZ	19 22.603‘ N, 155 17.713‘ W	3, 4, 6*
KL0921	∼1700 AD	Circumferential flow, Ka'u Desert	SSWRZ	19 22.989‘ N, 155 17.464 ‘W	3, 4
KL0922	Sept 1974		IC	19 24.201' N, 155 17.502' W	4 , 6*
KL0924	Late July, 1974		EC	19 24.142' N, 155 16.896' W	3, 4
KL0930	1919-1920	Mauna Iki	VSWRZ	19 21.230' N, 155 23.892' W	3, 4
KL0931	Sept 24-29th, 1971		VSWRZ	19 20.625' N, 155 21.659' W	3, 4
Collected by P.Wieser/HVO					
LL1 (KE62-3242s)	May 15th, 2018	Fissure 13 (reactivated)	LERZ	19 28.2468' N, 154 53.5992' W	7
LL2 (KE62-3240s)	May 14th, 2018	Fissure 17	LERZ	19 29.0184' N, 154 52.4376' W	7
LL3 (KE62-3231s)	May 7th, 2018	Fissure 8	LERZ	19 27.6642'N, 154 54.5406' W	7
LL4 (KE62-3293s)	May 30th, 2018	Fissure 8	LERZ	19 27.7486' N, 154 54.8636' W	7
LL5 (KE62-3243s)	May 16th, 2018	Fissure 20	LERZ	19 28.6746' N, 154 52.7472 W	7
LL6 (KE62-3219s)	May 4th, 2018	Fissure 5	LERZ	19 28.2226' N, 154 53.6167' W	7
LL7	Mid July, 2018**	Fissure 8	LERZ	19 27.879' N, 154 54.645' W	7
LL8	Aug 1st, 2018	Fissure 8	LERZ	19 28.31508'N, 154 54.51426' W	7
LL9 (KE62-3227)	May 5-6th, 2018	Fissure 10	LERZ	19 27.2994' N, 154 55.2852' W	7
LL10 (KE62-3224)	May 5th, 2018	Fissure 4	LERZ	19 28.0183' N, 154 53.9709' W	7
LL11	Early May, 2018**	Fissure 11	LERZ	19 27.2018' N, 154 55.4556' W	7
LL12	Early May, 2018**	Fissure 12	LERZ	19 27.2328' N, 154 55.3946' W	7

2.2 Sample Preparation

The vesicular lava, spatter, tephra and reticulite samples examined in this thesis were not amenable to extensive thin section making, due to difficulties ensuring complete epoxy impregnation into unconnected vesicles. Additionally, due to the high modal proportion of vesicles, very few olivines were found in each thin section. Instead, samples were crushed using a jaw crusher, with care taken to clean the crusher thoroughly before and after each sample (∼10 minutes) to avoid contamination. Crushed samples were then sieved into fractions >2 mm, 1–2 mm, 1000–840 µm, 840–250 µm, and <250 µm. Olivines and glass fragments were picked from the four largest size fractions using a binocular microscope and fine tweezers. Olivines examined in Chapters 3–4, and all matrix glasses, were mounted on double-sided sticky tape overlain on the base of 1" stub holders (Fig. 2.3a). Olivines were mounted in groups based on the size fraction they were found in, allowing stubs to be variably ground down to ensure that the cores of crystals were exposed. For the melt inclusion analyses presented in Chapters 5, 6, and 7, crystals were individually mounted on glass slides in Crystalbond^{TM} resin warmed using a hotplate. After allowing the Crystalbond^{TM} resin to set for a few minutes, individual melt inclusions were exposed by progressive grinding with 250–5000 grade wet and dry paper with frequent observations using a reflected and transmitted light microscope. This method allowed embayments (melt inclusions with a connection to the outside of the crystal) to be identified and discarded. For the melt inclusions examined in Chapter 7, care was taken to identify whether inclusions contained vapour bubbles, allowing bubble-bearing crystals to be ground down with 3000–8000 grade wet and dry paper to within ∼10–30 µm of the top of the bubble for analysis by Raman spectroscopy. In some instances, depending on the crystallographic orientation of the olivine, a few minutes of polishing on a cloth pad with 9 µm diamond paste was needed to remove larger scratches prior to Raman analysis.

Once a target melt inclusion was selected (and following Raman analyses for the study presented in Chapter 7), the host crystal was ground down with progressively finer wet and dry paper until the middle of the inclusion was exposed. The glass slides were placed on a hotplate at ∼100°C (Fig. 2.4a), and crystals were carefully picked out of the molten Crystalbond^{TM} resin using tweezers. To dissolve any remaining residue, each crystal was placed into a small beaker containing acetone for ∼1-2 minutes (Fig. 2.4b). Individual crystals were removed from the acetone, and placed onto a thin layer of tissue paper within a small petri dish to absorb residual acetone. Careful examination of each crystal using a microscope with reflected and transmitted light allowed identification of the flat, polished face containing the target melt inclusion (Fig. 2.4c). Fine tweezers were used to place the crystal with its polished face down onto a mount consisting of a square of flat plastic covered in three parallel strips of double-sided sticky tape, overlain with a layer of parcel tape (sticky side up; Fig. 2.4d). Care was taken to ensure there were no creases in the parcel tape, and crystals were placed on top of the central strip of the double-sided sticky tape to avoid the crease associated with the join between the strips of tape. The top half of epoxy pots used to produce 1" mounts were placed on top of the tape, and secured by wrapping the base in Blu-tac to prevent leakage of epoxy (Fig. 2.3b). All epoxy stubs were made using Bueller Epothin2 resin poured in an evacuated chamber. After 24–48 hours of curing, epoxy stubs were polished with 9, 6, 3, 1 and 0.25 µm diamond pastes.

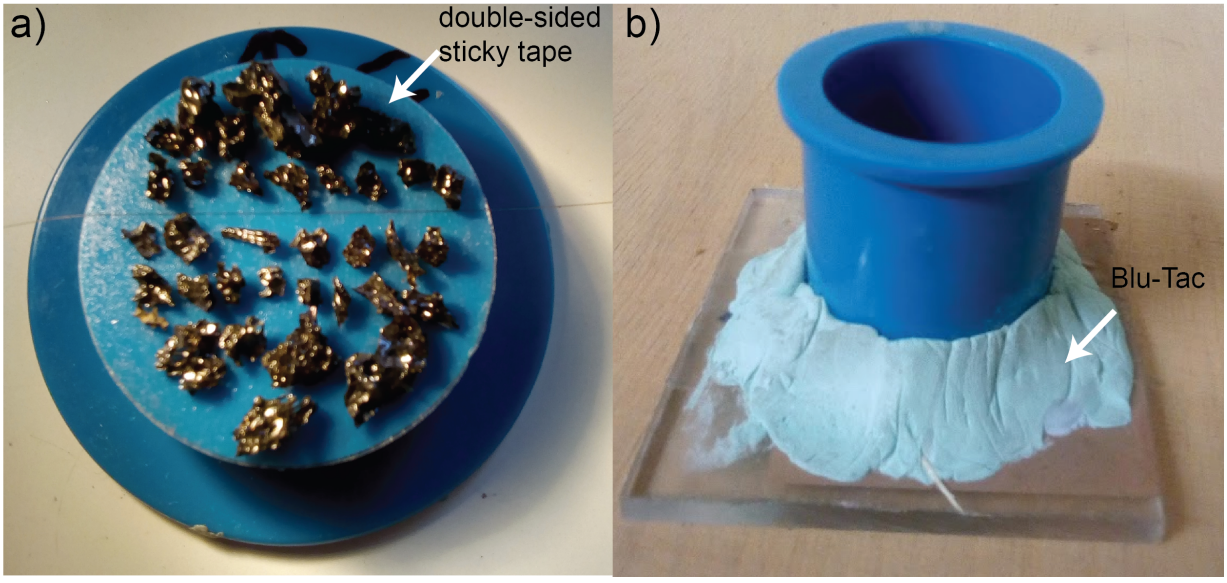


Figure 2.3: a) All matrix glasses, and olivines examined in Chapters 3–4, were mounted on top of double-sided sticky tape on the base of 1" stub moulds, and epoxy was poured into the assembled mould. **b)** Melt inclusions were mounted by pressing the top of a 1" mould onto double-sided sticky tape overlying a piece of plastic, and securing it with a blue-tac dam to prevent leakage of epoxy.

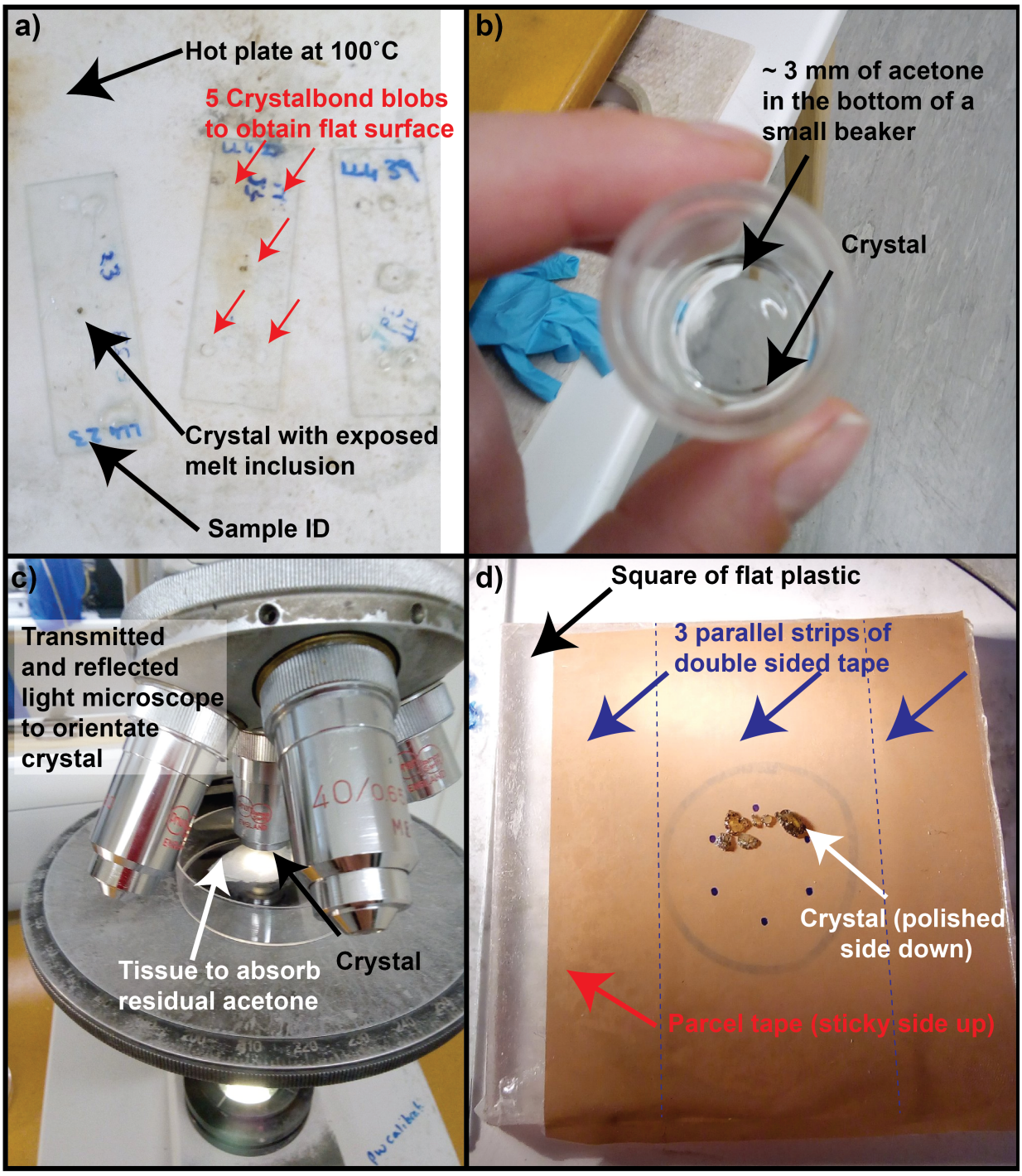


Figure 2.4: Method used to transfer crystals from glass slides onto a flat surface to allow mounting in epoxy resin. **a)** Following grinding down to the middle of the target inclusion, slides were placed on a hotplate at ~100°C. Crystals were extracted from the molten Crystalbond^{TM} and individually placed into small beakers containing a few ml of acetone **b)**. After a few minutes to allow the remaining Crystalbond^{TM} residue to dissolve, crystals were placed into a petri dish with a thin layer of tissue to absorb residual acetone (**c**). **c)** An optical microscope with reflected and transmitted light was used to identify the face containing the exposed melt inclusion. **d)** Crystals were carefully manipulated with tweezers such that the melt inclusions had their polished faces stuck on the parcel tape.

2.3 Electron Backscatter Diffraction (ESBD)

EBSD maps of Kīlauean olivines (in epoxy stubs) and West Greenland dendrites (in thin section) were collected on a FEI Quanta 650FEG SEM equipped with a Bruker e-Flash HR EBSD detector. Epoxy stubs and thin sections were polished prior to analysis with colloidal silica for 90 minutes using a VibroMet 2 Buehler Vibratory Polisher, followed by the application of a thin carbon coat. Data collection and indexing was performed with Bruker QUANTAX CrystaAlign. Step size was varied depending on the size of the olivine such that each map took ∼15–20 minutes to collect. EBSD data for chromite aggregates was collected by Zoja Vukmanovic on a FEI sFEG XL30 SEM with an Oxford Nordlys HKL detector in the Department of Physics, University of Cambridge (Table 2.3). EBSD data clean up and post-processing was performed in MTEX v5.0.4 and v5.1.0, an open-source toolbox for MATLAB (Bachmann et al., 2010). Single misindexed pixels were removed, and grain boundaries were identified using the CalcGrains function.

Table 2.2: EBSD acquisition settings for Kīlauean olivines and West Greenland dendrites.

SEM settings		SEM settings	
Aperture	3	Background (frames)	2
Voltage	20 kV	Gain	10–30
Beam size	5.5	Hough resolution	60
Working distance	17–14 mm	Band detection (min/max)	6/7
Step size	3–15 µm	EBSP resolution	340×240 pixels

Table 2.3: EBSD acquisition settings for chromite aggregates. Chromite.cry (Aztec database) was used as the reference.

SEM settings		SEM settings	
Aperture	3	Background (frames)	64
Voltage	20 kV	Gain	10
Beam size	5	Hough resolution	60
Working distance	20 mm	Band detection (min/max)	6/7
Step size	15 µm		

2.4 Electron Probe Micro-Analyser (EPMA)

Electron microprobe transects, maps and spot analyses presented in this thesis were obtained using a Cameca SX100 electron probe microanalyser (EPMA). Acquisition parameters, calibration materials, and estimates of precision and accuracy calculated from repeated measurements of secondary standards are presented below. Precision is defined as the standard deviation of repeated analyses of a secondary standard in a given analytical session divided by the mean composition of that standard in a given session. Accuracy is defined as the mean composition measured in a given analytical session divided by the long-term laboratory preferred value for that standard.

2.4.1 Olivine Transects

Chemical profiles across olivine aggregates presented in Chapter 3 were collected using line transects consisting of individual spots spaced ∼13–18 µm apart, with a beam size of 1 µm and beam conditions of 15 kV and 20 nA. Calibration materials, crystals, count times and estimates of precision and accuracy calculated from repeated measurements of a San Carlos Olivine secondary standard are shown in Table 2.4.

Table 2.4: Analytical conditions, precision and accuracy for EPMA transects across olivine aggregates.

Element	Calibration material	Crystal	Peak count (s)	Precision (%)	Accuracy (%)
Al	Corundum	LTAP	60	12.3	97.7
Ca	Diopside	PET, LPET	60, 60	6.4	93.6
Si	Diopside	TAP	10	0.9	99.6
Mg	SJ Olivine	TAP	20	0.8	99.1
Fe	Fayalite	LIF	20	1.8	99.6

2.4.2 WDS Minor Element Maps

WDS maps of phosphorus presented in Chapter 4 were collected at 15 kV, 200 nA, with a dwell time of 400 ms, and a spot size of 1 µm. The pixel size was varied between 3–6 µm depending on the size of the olivine. The total acquisition time for each map varied between 3–17 hours. Al was measured on the LTAP, Ca on the PET, P on the LPET, Al on the TAP, and Fe on the LIF spectrometer. WDS maps were plotted in ImageJ using false colouring based on the number of counts per pixel.

2.4.3 Olivine Spot Analyses

Olivine spot analyses presented in Chapters 4–7 were measured in a number of different analytical sessions. In all sessions, precision and accuracy was calculated from repeated measurements of a San Carlos Olivine secondary standard. As the focus of Chapter 4 was to assess the Fe, Mg and Ca concentrations in a large number of olivine crystals from many different eruptions, a relatively short analytical routine was chosen. Calibration materials, crystals, count times and estimates of precision and accuracy are shown in Table 2.5. Olivines containing melt inclusions (Chapters 5–7) were analysed in a longer dual condition routine to obtain precise measurements of minor element concentrations. Si, Mg and Fe were analysed in the first condition, at 15 kV, 20 nA, using a 1 µm spot, while Al, Ti, Ca, Ni, Cr and Mn were analysed in the second condition, at 15 kV, 100 nA, using a 1 µm spot. Calibration materials, crystals, count times and estimates of precision and accuracy are shown in Tables 2.6 and 2.7.

Table 2.5: Acquisition parameters and estimates of precision and accuracy for the olivine EPMA analyses presented in Chapter 4 and the olivine forsterite compilation presented in Chapter 5. Some instrument drift occurred in Session 2. Only forsterite contents are reported from this session, as repeated analyses of forsterite within the San Carlos Olivine secondary standards showed consistent enough drift that a linear correction could be applied. The drift was less coherent for Si and Ca, so these elements were not reported. Ca contents for Session 1 and 3 were internally corrected to the values measured in the San Carlos Olivine standard (factors of 1.3 and 1.05 respectively). Session 1 used a single condition routine, at 30 nA, 15 kV, with a 1 µm spot. Session 2 used a dual condition routine, with condition 1 at 30 nA, 15 kV, using a 1 µm spot, and condition 2 at 100 nA, 15 kV with a 1 µm spot. Session 3 used a single condition routine at 40 nA, 15 kV, with a 1 µm spot.

Element	Calibration material	Crystal	Peak count (s)	Order	Condition	Precision (%)	Accuracy (%)
Session 1 - Nov 2017							
Si	Diopside	TAP	10	1st	N/A	0.5	99.0
Mg	SJ Olivine	TAP	20	2nd	N/A	1.2	97.7
Fe	Fayalite	LIF	20	1st	N/A	1.1	99.3
Ca	Diopside	LPET	60	1st	N/A	9.3	130.7
Session 2 - Feb 2018							
Si	Diopside	TAP	10	1st	1	1.1	99.3
Mg	SJ Olivine	TAP	20	2nd	1	2.4	100.3
Fe	Fayalite	LIF	20	1st	1	1.1	98.5
Ca	Diopside	LPET	10	1st	2	12.3	118.0
Session 3 - March 2018							
Si	Diopside	TAP	10	1st	N/A	0.7	100.7
Mg	SJ Olivine	TAP	20	2nd	N/A	0.7	99.9
Fe	Fayalite	LIF	20	1st	N/A	0.9	99.3
Ca	Diopside	PET, LPET	30, 20	1st	N/A	0.93	105.4

Table 2.6: Acquisition parameters and estimates of precision and accuracy for the olivine EPMA analyses presented in Chapters 5 and 6 (collected September, 2018). Condition 1 was at 15 kV, 20 nA, using a 1 µm spot, and condition 2 was at 15 kV, 100 nA, using a 1 µm spot.

Element	Calibration	Crystal	Peak count (s)	Condition	Order	Precision (%)	Accuracy (%)
Si	Diopside	TAP	10	1	1st	0.7	100.2
Mg	SJ Olivine	TAP	20	1	2nd	0.5	99.8
Fe	Fayalite	LIF	20	1	1st	1.0	99.8
Al	Corundum	LTAP	120	2	1st	7.7	97.9
Ti	Rutile	PET	120	2	1st	76.2	132.7
Ca	Diopside	LPET	10	2	1st	6.2	89.5
Ni	Nickel oxide	LIF	60	2	1st	3.1	102.1
Cr	Cr metal	LIF	30	2	2nd	48.7	118.1
Mn	Mn metal	LIF	30	2	3rd	8.4	100.3

Table 2.7: Acquisition parameters and estimates of precision and accuracy for the olivine EPMA analyses presented in Chapter 7. Both analytical sessions utilized a dual condition routine, with condition 1 at 15 kV, 20 nA, using a 1 µm spot, and condition 2 at 15 kV, 100 nA, using a 1 µm spot.

Element	Calibration	Crystal	Peak count (s)	Condition	Order	Precision (%)	Accuracy (%)
Session 1 - Aug 2019							
Mg	SJ Olivine	TAP	20	1	1st	0.9	98.9
Si	Diopside	TAP	10	1	2nd	1.0	99.3
Fe	Fayalite	LIF	20	1	1st	1.2	98.6
Al	Corundum	LTAP	120	2	1st	4.8	93.5
Ca	Diopside	LPET	120	2	1st	5.6	121.3
Mn	Mn metal	LIF	60	2	1st	6.2	101.3
Ni	Nickel oxide	LIF	60	2	2nd	3.7	101.0
Session 2 - Jan 2020							
Mg	SJ Olivine	TAP	20	1	1st	1.3	98.5
Si	Diopside	TAP	10	1	2nd	1.3	97.9
Fe	Fayalite	LIF	20	1	1st	1.4	98.4
Al	Corundum	LTAP	120	2	1st	8.6	93.1
Ca	Diopside	LPET	120	2	1st	11.8	113.4
Mn	Mn metal	LIF	60	2	1st	7.1	90.7
Ni	Nickel oxide	LIF	60	2	2nd	4.5	95.1

2.4.4 Glass Spot Analyses

Matrix glasses from the 10 eruption sites examined in Chapter 4 (samples KL0908, KL0909, KL0910, KL0914, KL0916, KL0917, KL0919, KL0920, KL0922, KL0931) were analysed in a single analytical session at 15 kV, 6 nA, using a 5 µm spot. Glass compositions for samples KL0921, KL0930 and KL0924 were taken from Sides et al. (2014a). Calibration materials, crystals and count times are shown in Table 2.8. Estimates of precision and accuracy from repeated measurements of VG2 and Basalt 113716-1 are shown in Table 2.9.

EPMA analyses of matrix glasses and melt inclusions presented in Chapters 5–7 were conducted using a dual condition routine, allowing precise determination of the concentrations of S and Cl. Na, Al, P, Ca, K, Ti, Si, Mg, Fe and Mn were analysed in the first condition, at 15 kV, 10 nA, using a 10 µm spot. S and Cl were analysed in the second condition on both the PET and LPET crystal at 15 kV, 40 nA, using a 10 µm spot (Table 2.10). Small melt inclusions (<30 µm diameter) were analysed manually to ensure that the beam was in the centre of the melt inclusions. Precision and accuracy for each analytical session were calculated from repeated measurements of VG2 and A99 secondary standards (Table 2.11).

Table 2.8: Calibration materials, spectrometer crystals, count times and analysis order for EPMA analyses of matrix glasses presented in Chapter 4.

Element	Calibration material	Crystal	Peak count (s)	Analysis order
Na	Jadeite	LTAP	10	1^{st}
Al	Corundum	LTAP	20	2^{nd}
Ca	Diopside	PET	20	1^{st}
P	Apatite	PET	60	2^{nd}
K	K feldspar	LPET	10	1^{st}
Ti	Rutile	LPET	60	2^{nd}
Si	Diopside	TAP	10	1^{st}
Mg	SJ Olivine	TAP	20	2^{nd}
Fe	Fayalite	LIF	20	1^{st}
Cr	Cr spinel	LIF	40	2^{nd}
Mn	Manganese	LIF	40	3^{rd}

Table 2.9: Estimates of precision and accuracy for matrix glass EPMA analyses presented in Chapter 4.

Element	Accuracy (%, BCR-2G)	Precision (%, BCR-2G)	Accuracy (%, 13716-1)	Precision (%, 13716-1)
Si	98.3	1.5	99.2	1.4
Mg	98.3	1.6	98.5	2.2
Al	101.5	1.1	101.7	1.7
Ca	99.2	1.7	99.0	1.8
Ti	101.2	2.3	103.6	1.8
Fe	100.7	2.7	101.3	2.8
Cr	279.5	115.8	108.8	66.2
Mn	85.1	15.8	125.8	15.4
Na	101.9	6.4	100.5	2.2
K	99.8	11.6	91.0	17.1
P	84.9	20.6	104.3	23.4

Table 2.10: Calibration materials, spectrometer crystals, count times and analysis order for EPMA analyses of matrix glasses and melt inclusions presented in Chapters 5, 6, and 7.

Element	Calibration material	Crystal	Peak count (s)	Condition	Analysis order
Na	Jadeite	LTAP	10	1	1^{st}
Al	Corundum	LTAP	30	1	2^{nd}
P	Apatite	PET	30	1	1^{st}
Ca	Diopside	PET	30	1	2^{nd}
K	K feldspar	LPET	10	1	1^{st}
Ti	Rutile	LPET	60	1	2^{nd}
Si	Diopside	TAP	10	1	1^{st}
Mg	SJ Olivine	TAP	30	1	2^{nd}
Fe	Fayalite	LIF	20	1	1^{st}
Mn	Manganese	LIF	40	1	2^{nd}
S	Pyrite	PET, LPET	60, 60	2	1^{st}, 1^{st}
Cl	Halite	PET, LPET	60, 60	2	2^{nd}, 2^{nd}

Table 2.11: Precision and accuracy for EPMA analyses of matrix glasses and melt inclusions presented in Chapters 5, 6, and 7. Cl and Mn concentrations in Session 1 were consistently higher than long-term laboratory preferred values (bold values). Their concentrations were divided by 1.15 and 1.65 respectively to correct for this offset.

Element	Accuracy (%, A99)	Precision (%, A99)	Accuracy (%, VG2)	Precision(%, VG2)
Session 1 - Sept 2018 (Chapter 5–6)				
Na	95.6	6.21	98.2	2.71
Al	98.7	0.9	98.1	0.6
P	97.6	6.93	92.8	17.76
K	101.2	0.91	101.2	0.99
Ca	99.6	2.3	99.2	9.39
Ti	100.6	0.56	99.3	0.83
Si	98.6	0.48	99.3	0.58
Mg	99.9	2.25	101.1	2.26
Fe	98.8	1.12	99.2	1.21
Mn	**159.4**	10.22	**175.1**	5.54
S	91.1	18.5	98	1.83
Cl	**115.8**	16.48	**112.9**	6.84
Session 2 - Aug 2019 (Chapter 7)				
Na	99.7	3.7	99.9	2.5
Al	98.0	0.9	96.9	1.1
P	97.9	8.9	94.3	14.9
Ca	100.5	0.9	100.2	1.1
K	100.9	3.0	95.9	9.1
Ti	100.1	0.7	98.1	0.9
Si	98.7	1.0	98.6	1.0
Mg	97.1	1.7	96.7	1.4
Fe	99.3	1.7	98.7	1.5
Mn	86.8	17.7	89.4	18.6
S	91.2	10.3	100.6	1.8
Cl	98.7	12.8	104.5	8.6
Session 3 - Dec 2019 (Chapter 7)				
Na	102.6	6.3	102.9	2.6
Al	100.8	0.6	99.5	0.5
P	99.8	10.5	113.0	11.9
Ca	100.1	0.9	99.3	0.8
K	99.6	4.3	113.3	11.2
Ti	100.1	0.7	99.6	1.1
Si	98.9	0.5	99.6	0.5
Mg	99.9	1.5	99.8	1.3
Fe	99.7	1.8	101.0	1.7
Mn	75.7	20.3	105.2	18.4
S	94.1	14.5	102.6	2.0
Cl	101.9	10.7	109.4	6.8
Session 4 - Jan 2020 (Chapter 7)				
Na	103.9	3.0	104.3	3.5
Al	100.3	3.0	98.7	2.1
P	98.9	11.7	100.5	16.9
Ca	99.5	1.2	100.0	0.9
K	102.3	7.2	106.7	9.8
Ti	100.1	0.5	98.2	0.8
Si	97.8	0.8	98.0	0.6
Mg	98.2	1.2	97.9	1.3
Fe	98.5	2.2	98.5	2.1
Mn	84.2	16.1	100.0	16.4
S	92.1	13.8	100.8	2.0
Cl	107.5	7.7	107.0	7.7

2.5 Laser Ablation Inductively Coupled Plasma Mass Spectrometry (LA-ICP-MS)

Trace elements in matrix glasses and melt inclusions presented in Chapters 5 and 6 were analysed by LA-ICP-MS at the School of Environment, Earth and Ecosystem Sciences at The Open University. Analyses were performed using a Photon Machines G2 193 nm excimer laser system, equipped with a HelEx II 2-volume cell coupled to an Agilent 8800 ICP-MS/MS) following the techniques described by Jenner et al. (2015) (Table 2.12). Run conditions utilized a 10 Hz repetition rate, a fluency of 3.63 J/cm^2 on the sample surface, and an ablation cell He gas flow of 0.9 l/min. Backgrounds were measured for 30 seconds prior to each analysis, followed by 20 seconds of signal and 50 seconds of washout. NIST-SRM 612 was used for external calibration and ^{43}Ca for internal calibration for all elements except P, where BCR-2G was used for external calibration of data, and ^{29}Si for internal calibration. For all elements except P, BCR-2G was used as the secondary standard to monitor precision and accuracy (see Electronic Appendices).

Table 2.12: Conditions for spot and line LA-ICP-MS analyses

	Background (s)	Signal length (s)	Repetition rate (Hz)	Scan speed	Oxygen flow
Spot analyses (trace elements)	30	20	10	N/A	N/A
Spot analyses (Se+As)	30	20	20	N/A	N/A
Line scans (Se+As)	30	N/A	50	50 µm/sec	0.47 l/min

Matrix glasses erupted during the Mauna Ulu Period (1969-1974; Chapters 5 and 6) were extremely glassy, so could be analysed with a spot size of 110 µm. Melt inclusions were analysed at various spot sizes (65, 50, 40, 30, 25 and 20 µm) depending on the diameter of the inclusion. The surface of melt inclusions was pre-ablated with three laser shots prior to analysis to remove surface contamination. Analyses were performed manually if the laser spot was similar in size to the inclusion, to ensure that spots did not overlap with the host olivine or vapour bubbles below the surface. Ni signals were monitored during each analysis to determine whether the laser had ablated through the inclusion into the underlying olivine. Signals were carefully selected in Iolite to only include the signal from the melt inclusion. The run order for melt inclusions consisted of two spots of NIST-SRM 612, two spots on San Carlos Olivine (to help "wash out" the high concentrations of some elements in NIST-SRM 612), two analyses of BCR-2G, analyses of 10-20 inclusions, followed by two spots on BCR-2G and two on NIST-SRM 612. Matrix glasses were analysed in longer runs (50–70 analyses), with the same start and end bracket described above, with additional brackets of 2×NIST-SRM 612, 2×San Carlos Olivine, and 2×BCR-2G inserted every ∼15–20 spots.

Se and As are both affected by polyatomic and doubly charged interferences, and therefore require a different analytical protocol from the other trace elements. Analyses

were performed in oxygen mode using MS/MS mode, mass shifting $^{80}Se^{+}$ and $^{75}As^{+}$ to $^{96}SeO^{+}$ and $^{91}AsO^{+}$. This allowed effective elimination of interferences, monitored by comparing analyses of in-house Se and As standards to preferred values (measured using isotope dilution ICP-MS). NIST-SRM 612 was used for external calibration of data, with ^{29}Si used for internal calibration. NIST-SRM 612 has considerably higher contents of some elements compared to volcanic materials (e.g., NIST-SRM 612 has 15.2 ppm Se, Jenner et al., 2009). As for spot analyses, two line scans of olivine crystals were run after each analysis of NIST-SRM 612 to help "wash out" the system (Jenner and O'Neill, 2012b).

Se and As were analysed in Kīlauean matrix glasses using a spot size of 110 µm. Melt inclusions were analysed using lines scans with a width of 50 µm. Line scans across melt inclusions were placed such that they started and ended in the olivine crystal surrounding the melt inclusion. Concurrent analysis of ^{43}Ca and ^{60}Ni, which are highly sensitive to ablation of small quantities of olivine, allowed careful selection of the unmixed signal from the melt inclusion (Fig. 2.5). Accuracy was ±10% relative to in-house standards (see Jenner et al., 2015) with Se and As concentrations close to those in Kīlauean melt inclusions and matrix glasses.

Estimates of precision and accuracy are reported in the Electronic Appendices. Repeated analyses of secondary standards for lithophile elements were within ±5% of long-term (>2 years) Open University laboratory preferred values and preferred values for BCR-2G reported in Jenner et al. (2012). Repeated analyses of secondary standards for the chalcophile element concentrations were predominantly within ±5% for Ni, Cu, Zn, ±10% for Mo, Sb, W, As, and ±20–30% for Cd, In, Bi, Tl, Sn, Se of preferred values. Some of the variability in the latter elements may be attributed to standard heterogeneity (Jenner and Arevalo, 2016). Precision, calculated from the standard deviation of 55 repeated analyses of BCR-2G divided by the mean analysis of BCR-2G, is <5% for most lithophile elements, and between 5–10% for most chalcophile elements (12% for Tl, 13% for Sn, 19% for Bi, 29 % for In, 44% for Cd).

Lōihi matrix glass compositions reported in Chapter 6 were analysed by Frances Jenner, using the EPMA at the Smithsonian Institution (see Jenner et al., 2015 or further details), SIMS at the Carnegie Institution of Washington, and LA-ICP-MS analyses at the Australian National University and the Open University (Se and As only).

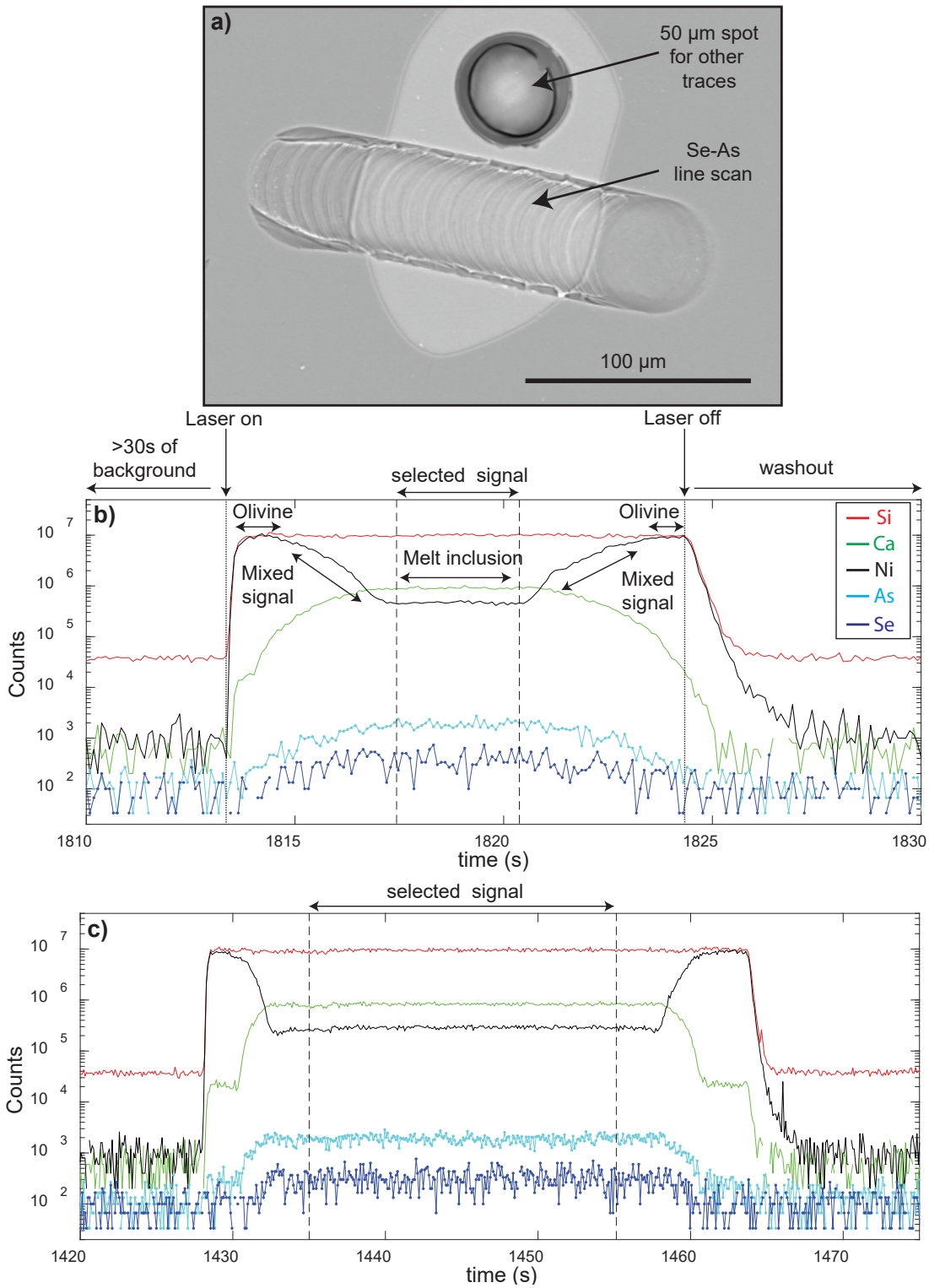


Figure 2.5: Examples of Se-As line scans. **a)** BSE image of melt inclusion with a 50 µm laser spot and a Se-As line scan. **b)** Raw signal for the Se-As line scan shown in **a)**. The line scan starts in the host olivine crystal (which has high Ni, and low Ca contents). The rapid drop in Ni, and increase in Ca occurs as the signal from the melt inclusion and host olivine mix, with a flat plateau in these elements once the signal derives from just the melt inclusion. The selected signal in this instance was relatively short (2.04 s) due to the relatively small size of the melt inclusion. **c)** Line scan signals from a significantly larger melt inclusion (selected signal = 20.1 s).

2.6 Sulfide Identification and Bulk Analysis

Sulfides are commonly identified based on their distinctive gold-yellow colour in reflected light. However, optical observations are biased towards larger sulfides, and are extremely time consuming. A new approach was developed to identify sulfides in Kīlauean samples using concurrent backscatter electron (BSE) and secondary electron (SE) imaging on a FEI Quanta 650FEG SEM. BSE maps of epoxy mounts were collected with the brightness and contrast of the image adjusted such that sulfides appeared white, and silicate mineral, glasses and epoxy appeared black. Maps2.1 software allows concurrent collection of SE maps at normal brightness and contrast conditions. Following acquisition of the two maps (∼45 minutes), the opacity of the SE layer in MAPS2.1 software was set at 10%. This allowed the outlines of crystals and glasses to be identified, such that large areas of epoxy resin could be ignored. The BSE map inside the outline of each grain was used to identify bright spots, and drive the stage to their position. Rapid (∼10 s) EDS maps of Ni, Fe, Cu and S allowed assessment of whether the bright spot was a sulfide grain, or another source of high BSE intensity such as small pieces of lint, or residual flecks of gold coat. This method successfully identified sulfides with diameters as small as ∼0.1 µm.

Determining bulk sulfide compositions is crucial to accurately model the solubility of S in basaltic magmas (see Chapter 6). Traditionally, bulk sulfide compositions have been obtained by EPMA using a defocused beam (e.g., Stone and Fleet, 1991). However, the fine scale exsolution features of naturally-quenched sulfides result in highly imprecise analyses. It is also very difficult to ensure that the beam is defocused to the exact diameter of the sulfide, and that the centre of the beam is placed in the centre of the sulfide. These problems are particularly acute for sulfides with irregular outlines, or ellipsoidal morphologies. Instead, bulk sulfide compositions were quantified using energy dispersive x-ray spectroscopy (EDS). EDS maps were collected using two 3|60 Bruker flash detectors (90 kcps) at 20 kV, with a spot size of 4.5, and acquisition times of 15–20 minutes. To assess the precision and accuracy of EDS analyses in each analytical session, a pyrite (UWPy-1), chalcopyrite (Nifty) and pentlandite (GLAHM) standard kindly supplied by John Craven and Sally Gibson were characterized using the Cameca SX100 EPMA. Ni, Cu, Se and Fe were analysed at 20 kV, 20 nA, using a 5 µm spot. Crystals, calibration materials and count times are shown in Table 2.13.

Table 2.13: Analytical conditions for characterization of in-house sulfide standards.

Element	Crystal	Calibration material	Peak count (s)
S	PET	Pyrite	10
Cu	LLIF	Cu metal	30
Ni	LIF	Ni metal	30
Fe	LIF	Pyrite	10

EDS maps of small (10–30 µm) areas of these three in-house standards were collected using the same analytical conditions as maps of unknown Kīlauean sulfides during each analytical session. The spectra from all mapped areas were quantified in Esprit2.1 software, using a P/B ZAF model. Comparison of EPMA and EDS data for the sulfide standards demonstrated that the automatic background fit in Esprit2.1 resulted in a significant underestimation of S concentrations, due to an anomalous background window close to the low energy Skα peak. Deletion of this background window resolved this discrepancy, and was performed during quantification of each spectra. For Kīlauean sulfides, maps were quantified for a hand-drawn area to exclude the outer rim of each sulfide (which exhibited a mixed spectrum with significant contributions from the host olivine/glass, assessed by quantifying the Si, Mg and Ca peak). Based on repeated maps of in-house sulfide standards, precision for EDS quantification was <1%, and the accuracy relative to EPMA measurements of these standards was within ±5%. EDS results were corrected for consistent offsets from EPMA measurements by a factor of 0.96 for Fe, and 1.025 for Ni and Cu.

2.7 Raman Spectroscopy

Raman spectroscopy may be used to measure the density of CO_2 in pockets of fluid trapped within crystals (e.g., fluid inclusions, melt inclusion vapour bubbles). Recently, vapour bubbles have been shown to contain significant proportions of the total CO_2 budget of melt inclusions (Steele-MacInnis et al., 2011; Moore et al., 2015; Aster et al., 2016; Hartley et al., 2014; Taracsák et al., 2019; Moore et al., 2018; Esposito et al., 2011). However, few labs (e.g., Virginia Tech, WHOI) have optimized their Raman systems for analysis of low density CO_2 vapour bubbles. As part of this thesis, significant method development was undertaken to produce precise and accurate measurements of CO_2 density using a confocal LabRAM 300 (Horiba Jobin Yvon) Raman spectrometer.

2.7.1 Theory

The Raman spectrum of CO_2 consists of two relatively strong, well-defined peaks at approximately 1285–1286 cm^{-1} and 1388–1389 cm^{-1}. These peaks result from the interaction of a symmetrical stretching mode and an active bending mode in the CO_2 molecule by a process known as Fermi resonance (Lamadrid et al., 2017; Rosso and Bodnar, 1995; Fermi, 1931). Hence, collectively, these strong CO_2 peaks are referred to as the Fermi diad. The Fermi diad is flanked by low intensity "hot bands" (Fig. 2.6), which arise from molecules populating the first excited vibron due to their thermal energy at room temperature, and are also perturbed by a Fermi resonance effect. The peak height of the hot bands relative to the Fermi diad increases with increasing temperature (Rosso and Bodnar, 1995).

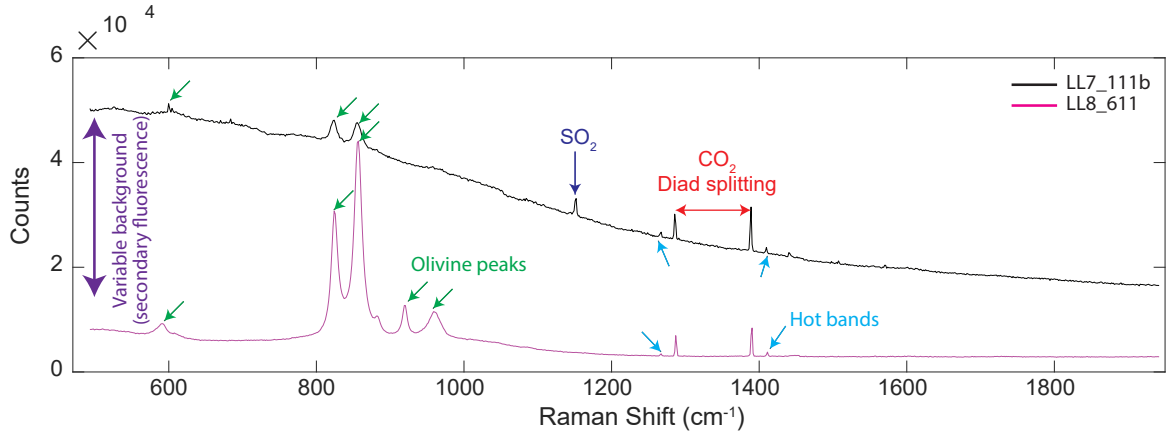


Figure 2.6: Raman spectra for two melt inclusion vapour bubbles showing the dominant peaks in the spectral window of interest. As well as the prominent Fermi diad and hot bands resulting from the presence of gaseous CO_2, there are also strong peaks from the olivine host. In some bubbles (e.g., LL7_111b), there is a peak at $\sim$ 1150 cm^{-1} indicating the presence of gaseous SO_2 (Gerding and Nijveld, 1936).

2.7.2 Analytical Procedure

The Raman spectrometer was calibrated at the start of every day with the Labspec 6 autocalibration function, which uses the zero position (laser line) and the Koeff value defined by the peak from a Si wafer (520.7 cm^{-1}) to set the linearity of the spectral region between 0 and 520.7 cm^{-1}. The Ventus laser source (532.05 nm; Laser Quantum) was set to a power of 100 mW (filter=100%), and focused on the sample using an Olympus LMPLFLN 50× long working distance objective. Raman spectra were collected with a Peltier front illuminated CCD detector (1024×256 pixels) using a holographic grating of 1800 gr/mm, a 300 µm hole and a 100 µm slit. Spectra were collected within a single spectral window centred on 1250 cm^{-1}, spanning ∼439–1942 cm^{-1}. Acquisition times were varied between 30–90 s depending on the strength of the diad, and between 3–6 accumulations were averaged for each acquisition (total analysis time of ∼90–360 s). Each vapour bubble was analysed three times. Between each of these repeated analyses, the focus and position of the laser within the bubble was adjusted slightly to obtain three distinct spectra.

2.7.3 Peak Fitting

Peaks were fitted using scripts written in MATLAB. Firstly, a region of the spectrum within ± 10 cm^{-1} of the peak was extracted (Fig. 2.7a). Then, the number of points comprising the peak was assessed visually, and the remaining points were allocated as background. For many spectra, an initial peak fit was performed, and then the points comprising the background and peak were adjusted iteratively to produce better fits. Polynomials of 3rd and 4th order were used to fit the points allocated as background (Fig. 2.7b). The predicted

y values from this polynomial at all measured x values were subtracted from measured y values to yield background-subtracted data (Fig. 2.7c). Gaussian peaks were then fitted to this corrected data using an iterative regime minimising errors by least squares (Fig. 2.7d).

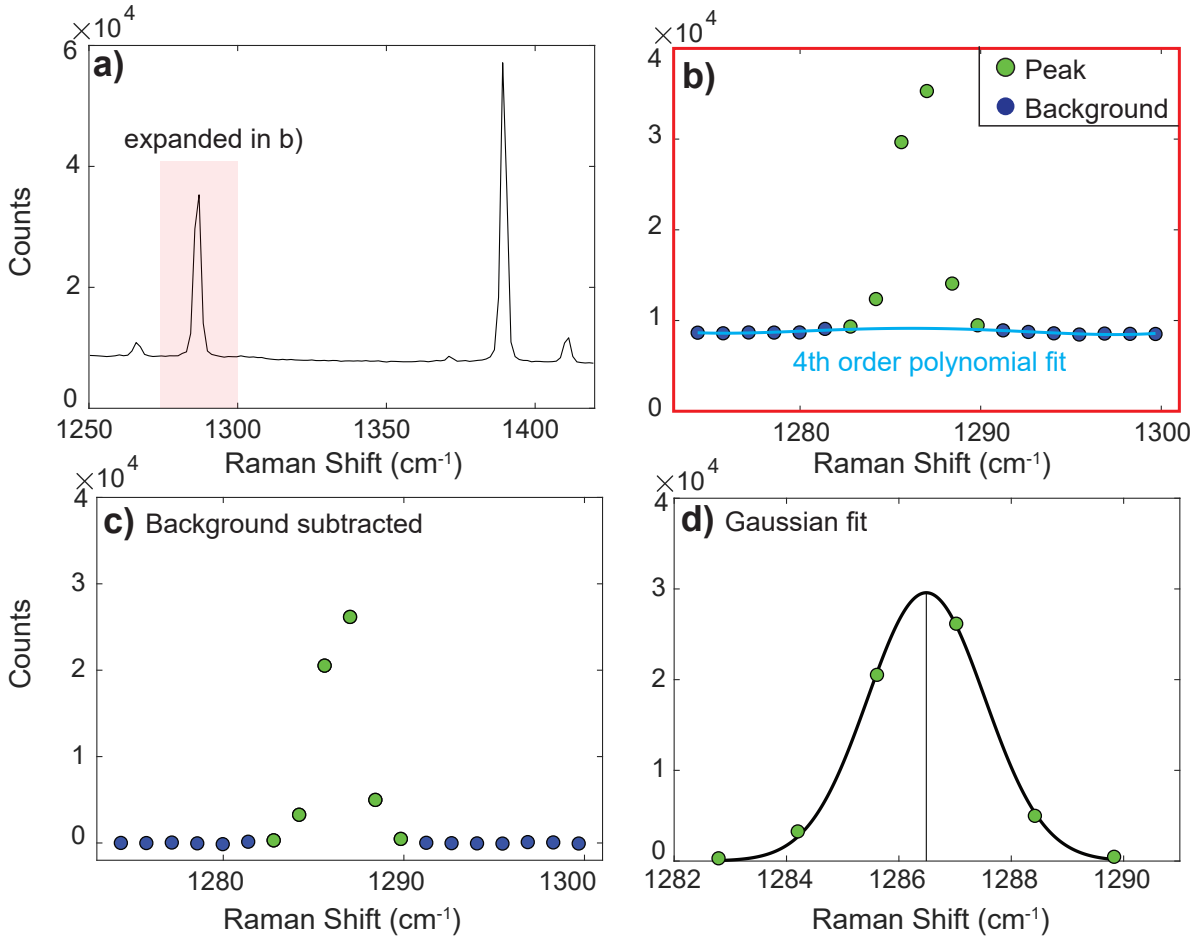


Figure 2.7: a) The spectral region of interest around each peak was cropped. For CO_2 peaks, the cropping window was visually adjusted to ensure that the hot bands were not included in the background. **b)** Following the selection of a number of points comprising the peak by the user, polynomials of 3^{rd} or 4^{th} order were fitted to background data. **c)** This polynomial fit was used to subtract the background from the data. **d)** A Gaussian peak was fitted iteratively to background-subtracted data using a least squares minimisation procedure in MATLAB (adapted from `https://www.youtube.com/watch?v=8eHYx5RYfMk`).

2.7.4 Calibration

It is well accepted that the distance between the two strong CO_2 peaks (diad splitting, or Δ) correlates with the density of CO_2 vapour. However, there are a number of different parameterizations for this relationship in the literature (Fig. 2.8; Rosso and Bodnar, 1995; Fall et al., 2011; Yamamoto et al., 2007; Wang et al., 2011; Wang et al., 2019; Kawakami et al., 2003), resulting from differences in instrument hardware as well as the choice of

analytical conditions (e.g., laser power, laser wavelength, grating; Lamadrid et al., 2017). The absolute differences in CO_2 densities for a given diad splitting calculated using different published densimeter equations are very large; a splitting of 102.8 cm^{-1} yields a density of 0.0281 g/cm^3 using the densimeter of Wang et al. (2019), but a density of 0.1397 g/cm^3 using the densimeter of Kawakami et al. (2003) (Fig. 2.8). For a bubble volume of 5% (typical for Hawaiian melt inclusions; Tucker et al., 2019), these different densimeters predict vapour bubble CO_2 contents of ∼520 ppm and ∼2590 ppm respectively. For an inclusion with SiO_2=49 wt%, and H_2O=0.5 wt%, these bubble CO_2 contents correspond to entrapment pressures of 1.1 and 4.7 kbar using the solubility model of Dixon (1997). Thus, the approach used by a number of studies, where a densimeter is chosen from the literature for use on an different Raman instrument (e.g., Hartley et al., 2014; Taracsák et al., 2019; Venugopal et al., 2020) yields large systematic uncertainties for CO_2 densities, and, by extension, magma storage depths.

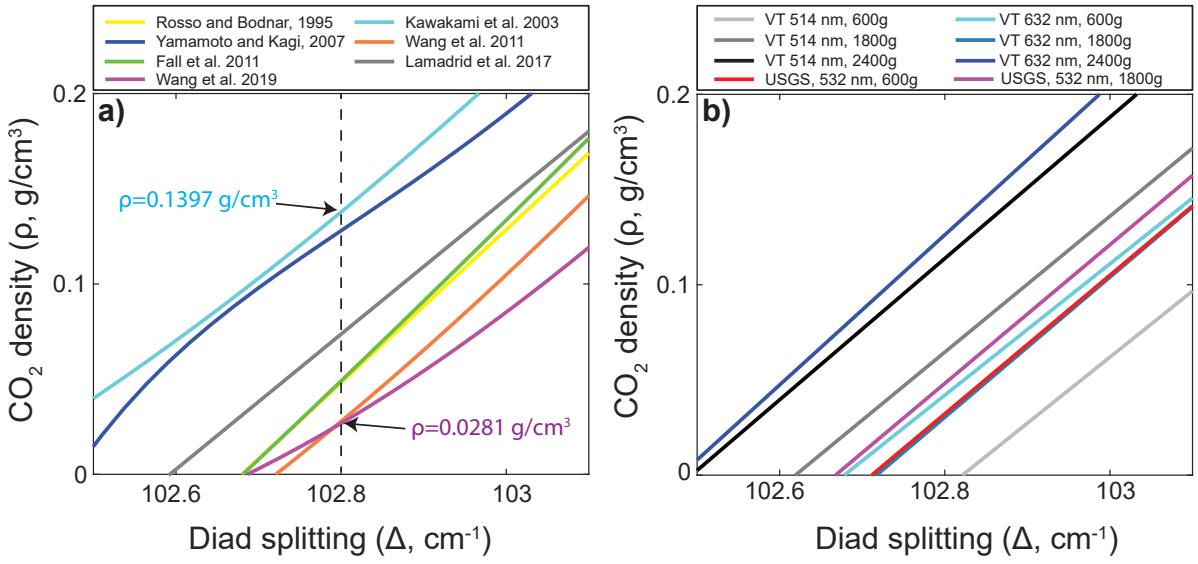


Figure 2.8: a) Published densimeters from the literature predict very different CO_2 densities for a given diad splitting. **b)** Variation in the relationship between diad splitting and CO_2 density resulting from changes in acquisition parameters (e.g., laser wavelength, grating) for two different Raman systems at Virginia Tech (VT) and the United States Geological Survey (USGS) (see Lamadrid et al., 2017).

The problems associated with the use of calibrations from the literature, rather than instrument-specific calibrations, are best demonstrated by comparing published CO_2 densities to the CO_2 phase diagram (Fig. 2.9a). At room temperature (∼22°C), the maximum possible density for a CO_2 vapour is ∼0.21 g/cm^3 (Moore et al., 2018; Rosso and Bodnar, 1995; Fig. 2.9). Thus, trapped pockets of CO_2 fluid with bulk densities between ∼0.21–0.75 g/cm^3 will consist of a vapour with a density of ∼0.21 g/cm^3, and a high density liquid (∼0.75 g/cm^3) at room temperature, while those with bulk densities >0.75 g/cm^3 will be a single phase CO_2

liquid. However, studies using densimeters from the literature have routinely reported CO_2 densities between 0.21–0.75 g/cm^3, despite the fact that it is thermodynamically impossible for a CO_2 phase to possess these densities at room temperature (Fig. 2.9b). For example, 17 (4%) of the vapour bubble densities reported by Hartley et al. (2014) exceed 0.21 g/cm^3, with a maximum reported density of 0.57 g/cm^3. Similarly, 19 (76%) of the vapour bubble densities reported by Taracsák et al. (2019) are >0.21 g/cm^3, with a maximum density of 0.4 g/cm^3. Finally, Venugopal et al. (2020) report 18 vapour bubbles (78%) with densities >0.21 g/cm^3, with a maximum density of 0.44 g/cm^3. These authors attribute these high densities to laser-induced heating, raising the temperature of the vapour bubble above the CO_2 critical point (31°C) such that the inclusion homogenizes to a higher density supercritical fluid (S. Venugopal and Z. Taracsak, written comm.).

Dubessy et al. (2012) perform simple calculations to investigate the maximum amount of laser heating samples may experience during Raman analyses. They show that in the absence of heat loss through convection or conduction, a laser power at the sample of 1 mW can raise the temperature of a volume equal to the laser irradiated volume (∼1 µm^3) by >666°C for typical mineral heat capacities and volumes. However, the median vapour bubble radii for inclusions with CO_2 densities >0.21 g/cm^3 in the studies of Taracsák et al. (2019) and Venugopal et al. (2020) are 9.5 and 5.5 µm respectively (Fig. 2.9), corresponding to bubble volumes of ∼697 and 3591 µm^3. Using the parameters of Dubessy et al. (2012), these bubbles would experience less than 1°C of heating. Additionally, the absorption coefficient of CO_2 in the visible light region is extremely low (as is the fundamental tenet of the greenhouse effect), especially compared to the silicate minerals used in the calculations of Dubessy et al. (2012). Large vapour bubbles will also experience significant heat dissapation, further reducing the temperature rise (Dubessy et al., 2012). Rosso and Bodnar (1995) investigate the effects of laser heating in CO_2 fluids experimentally, utilizing the strong temperature dependence on the intensities of the CO_2 hot bands relative to the strong CO_2 Fermi diad. They demonstrate that there are no significant differences between the peak intensity ratios calculated using a Boltzman factor relationship for the temperature of the sample set by the heating stage, and those measured in the laser-excited gas. Thus, it seems highly improbable that laser heating raises the temperature of melt inclusion vapour bubbles by ∼ 9°C from room temperature to the CO_2 critical point of 31°C, allowing a single CO_2 phase with densities between 0.21 and 0.75 g/cm^3 to exist. It would be a very unlikely coincidence that only vapour bubbles in studies using literature calibrations would experience laser heating (yielding densities >0.21 g/cm^3), while studies using an instrument-specific densimeter all report densities within error of this thermodynamic limit at room temperature (Fig. 2.9b). Thus, it seems very probable that the publication of densities between 0.21–0.75 g/cm^3 results from the choice of an unsuitable literature densimeter, and the carbon contents of inclusions in these studies, and therefore magma storage depths, will have been systematically overestimated.

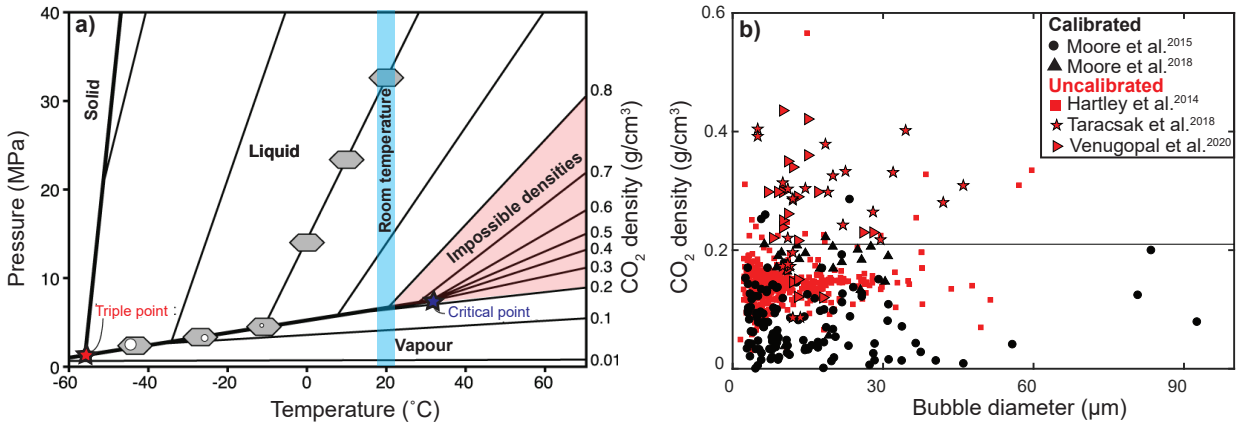


Figure 2.9: a) Phase diagram of pure CO_2 (adapted from Yamamoto et al., 2015). **b)** CO_2 densities measured in the literature vs. the diameter of the vapour bubble. Studies which use a calibration line developed for their specific instrumental set up have measured very few densities >0.21 g/cm^3 (black symbols). In contrast, studies using a densimeter from the literature calibrated on a different Raman instrument (red symbols) report large numbers of vapour bubbles with densities >0.21 g/cm^3 for a wide range of bubble diameters.

This discussion emphasizes the importance of developing a calibration line for each Raman instrument, and each set of analytical conditions. Precise calibration over a wide range of densities can be achieved using a high pressure optical cell, which allows the diad splitting of pure CO_2 gas at varying pressures to be measured (e.g., Lamadrid et al. 2017). However, as the different calibrations are nearly parallel for CO_2 densities <0.21 g/cm^3, only a small number of samples with known densities are required to make a calibration line. As no high pressure optical cell was available in Cambridge, the Raman was calibrated using 16 synthetic CO_2 - H_2O fluid inclusions hosted in quartz with a range of densities (∼0.04 g/cm^3, 0.08 g/cm^3 and 0.14 g/cm^3), as well as three Kīlauean melt inclusion vapour bubbles. The quartz fluid inclusion standards were supplied by Hector Lamadrid (University of Missouri). The densities of all 19 primary standards were measured using the Virginia Tech Raman spectrometer, which has been calibrated using a high pressure optical cell (see Lamadrid et al., 2017).

All 19 primary standards were analysed within a single analytical session ('Run 1'). A subset of 6 synthetic fluid inclusions ('Run 6') were analysed 4 weeks later to check the stability of the calibration line following installation of a new laser unit. Additionally, at the start of every analytical session, fluid inclusion 10mol%_FIE (Fig. 2.10) and melt inclusion LL8_404A (which bracket either end of the calibration line) were analysed. Due to difficulties constraining instrument drift during each session using conventional methods (see Section 2.7.5) it was not possible to (retrospectively) account for small differences between analytical sessions. Thus, the final regression line was generated from all these analyses of primary standards (Fig. 2.11). This approach means that the confidence interval on the regression incorporates the uncertainty caused by slight differences between sessions.

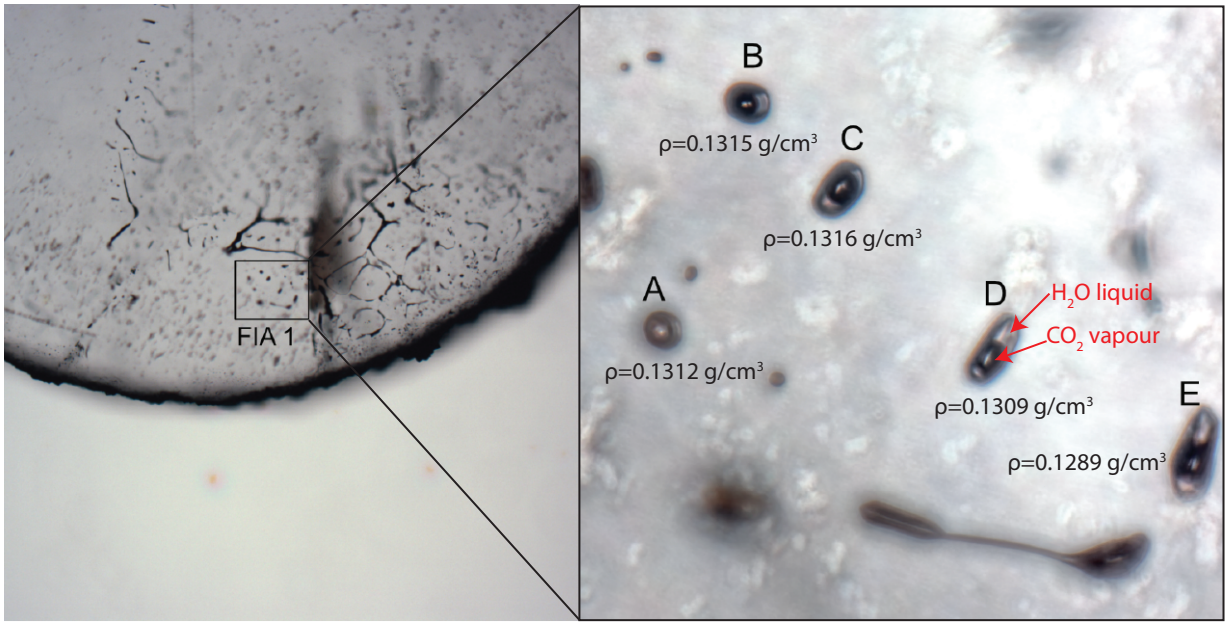


Figure 2.10: Transmitted light photographs of the quartz-hosted fluid inclusion standard provided by Hector Lamadrid (standard 10mol%). Thin quartz standard wafers were mounted in Crystalbond^{TM} on a glass slide in Cambridge for ease of regular analysis.

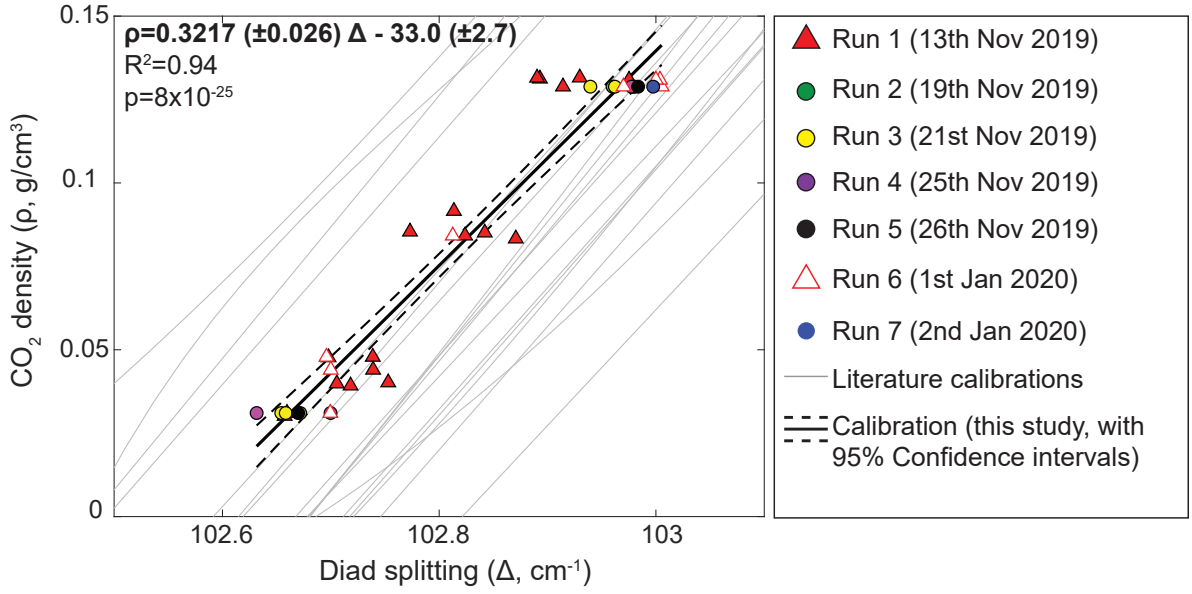


Figure 2.11: Calibration line for the Cambridge Raman spectrometer, showing analyses of primary standards in 7 separate runs. The 95% confidence intervals are significantly smaller than the uncertainty associated with picking a literature calibration (grey lines).

One possible method of calibration for laboratories which do not have access to well-characterized standards or a high pressure optical cell would be to utilize the fact that the maximum measured density of CO_2 vapour at room temperature is ~0.21 g/cm^3. As the different calibration lines in the literature are almost parallel for low CO_2 densities,

analysis of the inner vapour phase of a two-phase fluid inclusion could be used to fix the calibration line, using the gradient from literature densimeters.

2.7.5 Instrument Drift

Non-linearity of the spectrometer within the spectral region containing the Fermi diad is often assessed by monitoring the emission spectrum of Ne. The Ne spectrum has a number of distinctive "lines", several of which lie close to the position of the CO_2 Fermi diad. The wavelength of the different Ne lines in air (λ_1) are converted into Raman shifts (Δ_v) in cm^{-1} using the excitation wavelength of the laser (λ_0=532.05 nm; Lin et al., 2007):

$$\Delta_v = \left(\frac{1}{0.1 \times \lambda_0(\text{Å})} - \frac{1}{\lambda_1(\text{nm})} \right) \times 10^7 \tag{2.1}$$

Table 2.14: Positions of Ne lines that lie close to the CO_2 Fermi diad. Wavelengths in air were taken from `https://physics.nist.gov/PhysRefData/Handbook/Tables/neontable2.htm`, with Raman shifts calculated using Equation 2.1. The observed Ne line at $\sim$ 1220 cm^{-1} does not have a reported value in published compilations of the atomic spectrum of Ne. The theoretical position of this line was estimated at 1219.95±0.03 cm^{-1} using correlations between the observed and measured peaks for 18 separate acquisitions of the other 5 Ne lines.

Wavelength in air (Å)	Raman shift (cm^{-1})
5656.659	1116.946
5719.225	1310.339
5748.299	1398.774
5764.419	1447.423
5804.450	1567.064
5820.156	1613.555

Modern Raman instruments are set up so that the emission spectrum of Ne and the spectrum from a sample can be acquired simultaneously. The measured distance between any two Ne lines ($\Delta_{\text{Ne}}^{\text{Measured}}$) can be compared to the theoretical distance ($\Delta_{\text{Ne}}^{\text{Theoretical}}$) using the Ne line positions in Table 2.14, allowing any stretching or contraction of the spectrum to be quantified in terms of a correction factor:

$$\text{Correction Factor} = \frac{\Delta_{Ne}^{Theoretical}}{\Delta_{Ne}^{Measured}} \tag{2.2}$$

Diad splittings corrected for instrument drift, $\Delta_{\text{CO}_2}^{\text{Corrected}}$, are obtained by multiplying this correction factor by the measured diad splitting ($\Delta_{\text{CO}_2}^{\text{Measured}}$; Lamadrid et al., 2017):

$$\Delta_{CO_2}^{Corrected} = \text{Correction Factor} \times \Delta_{CO_2}^{Measured} \tag{2.3}$$

Unfortunately, the Cambridge Raman system cannot measure Ne lines at the same time as samples. Instead, Ne lines were collected before and after each set of three repeated measurements on a given vapour bubble by removing the sample, and placing the Ne lamp under the objective.

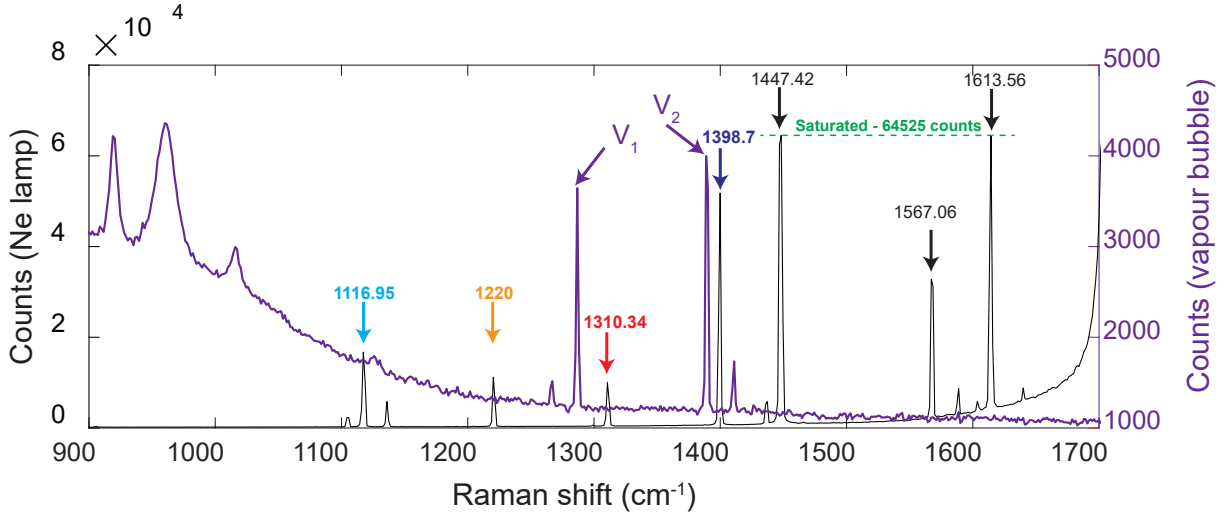


Figure 2.12: Relative positions of the Ne lines compared to the Fermi diad for the 532.05 nm laser used in Cambridge.

The Ne lines at ∼1117, 1220 and 1310 cm^{-1} are significantly weaker than the lines at ∼1399, 1447, 1567 and 1614 cm^{-1}. This made it difficult to obtain sufficient counts to get good peak fits on the former lines without saturating the detector for the latter lines (Fig. 2.12). Once the detector is saturated (64,525 counts), it is no longer possible to accurately fit a gaussian curve to a peak. Additionally, the presence of a small peak on the shoulder of the 1447.42 line meant that it was not possible to make a suitable background correction for this line.

Monitoring the position of Ne lines relative to the theoretical value throughout a given run shows that peak positions shift progressively with time (Fig. 2.13). However, the distance between peaks (spectral stretching) is considerably less than the amount of peak motion, as the position of all the peaks move in the same direction (Fig. 2.13a). The amount of spectral stretching was calculated using the theoretical and measured splitting between different Ne line combinations (1399 vs. 1310 cm^{-1}, 1399 vs. 1220 cm^{-1}, 1399 vs. 1117 cm^{-1}, 1320 vs. 1220 cm^{-1}, 1310 vs. 1117 cm^{-1}, 1220 vs. 1117 cm^{-1}; Equation 2.2; Fig. 2.13b). Interestingly, both the absolute value of the correction factor, and the apparent direction of drift (contraction or expansion of the spectra) was highly sensitive to the choice of Ne lines. The reliability of the correction factors calculated from Ne lines were assessed by comparing the raw data for four repeated measurements of a synthetic fluid inclusion with ρ=0.1289 cm^{-1} (10mol%_FIE) at the start and the end of a given run with data corrected using different Ne line combinations. The drift in the uncorrected data (yellow squares) was significantly less than that observed for fluid inclusion densities calculated using correction factors (Fig. 2.13c). The lack of agreement between correction factors obtained from different Ne line combinations likely results from the limited spectral resolution of the Cambridge Raman Spectrometer (∼1.4 cm^{-1} in the spectral window of interest vs.

$\sim$0.47 cm^{-1} for the instrument used by Lamadrid et al. 2017, and 0.1 cm^{-1} for the newest instruments). The Ne peaks are very narrow, yielding only 3 data points convincingly above background, which introduces large errors in fitting Gaussian peaks. Thus, applying correction factors introduces more error than leaving the data uncorrected. Instead, after recognising that Ne line measurements were not a viable option on the Cambridge Raman, repeated measurements were made of a synthetic fluid inclusion (10mol%_FIE). Only two runs (#5 and 7) showed significant drift outside the standard deviation of the 3–4 back-to-back measurements of this inclusion. In these two runs where drift was coherent (e.g., Fig. 2.14a), the correction factor for each measurement was calculated by dividing the mean density of fluid inclusion 10mol%_FIE calculated from the regression line shown on Fig. 2.11 by the measured density, and a linear regression of this correction factor versus time was used to correct measurements of vapour bubbles throughout the run. Overall, this analysis demonstrates that for instruments with a spectral resolution of the order of $\sim$1–2 cm^{-1}, Ne lines are not suitable to monitor instrument drift. Although more time consuming, the broader peaks of the diads produced by fluid inclusions relative to Ne lines means that this method of drift correction is more accurate for instruments with low spectral resolution.

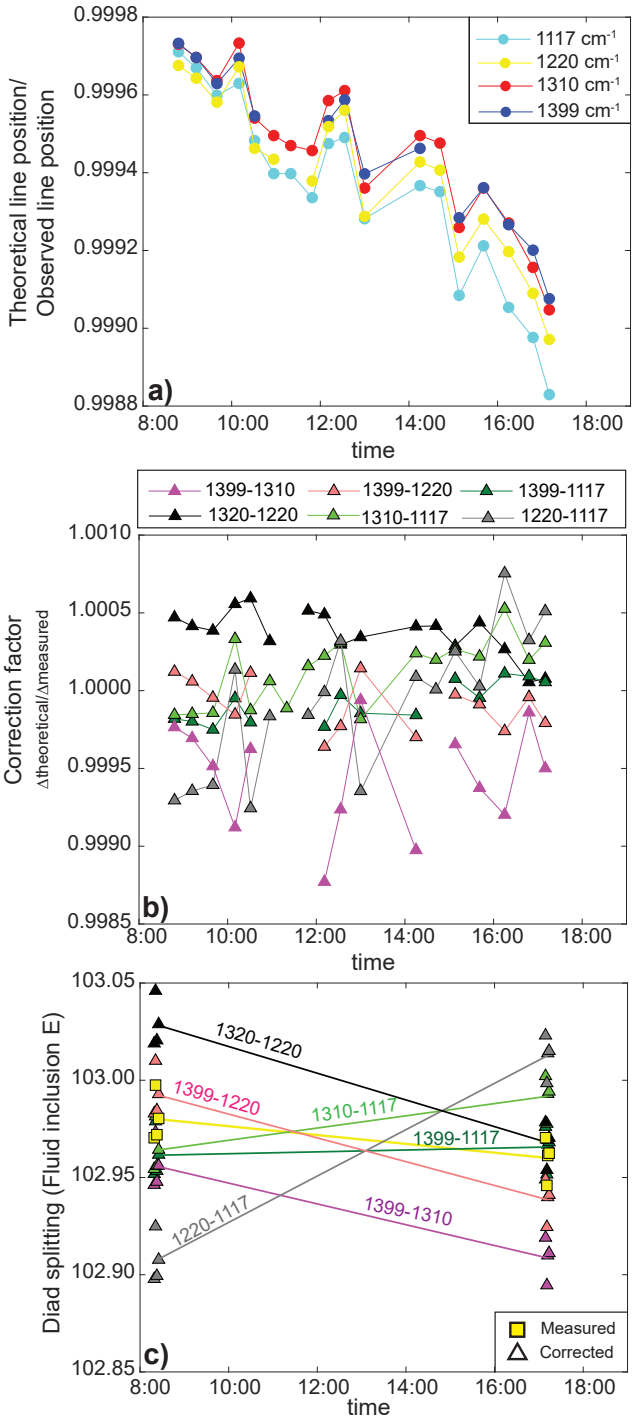


Figure 2.13: **a)** Changes in the absolute position of the Ne peaks with time, plotted by taking the theoretical line position from Table 2.14, and dividing by the measured position so that all lines could be shown on the same y axis. **b)** Correction factors calculated using Equation 2.2 for different Ne line combinations. Data points where the spectrometer was saturated are not shown. While the distance between the Ne lines at 1320 cm^{-1} and 1220 cm^{-1} (black triangles) suggest that the spectrum was expanding during the run, the changes between the lines at 1220 cm^{-1} and 1117 cm^{-1} (grey triangles) suggest that the spectrum was contracting. **c)** Diad splitting for 10mol%_FIE using correction factors from different line combinations. This fluid inclusion standard was analysed 4 times at the beginning of the run and 4 times at the end of the run. The yellow squares show the measured diad splitting without any corrections, and the other colours match the lines shown in **b)**. Densities corrected for "drift" from Ne lines show more variation than the measured splittings, which overlap.

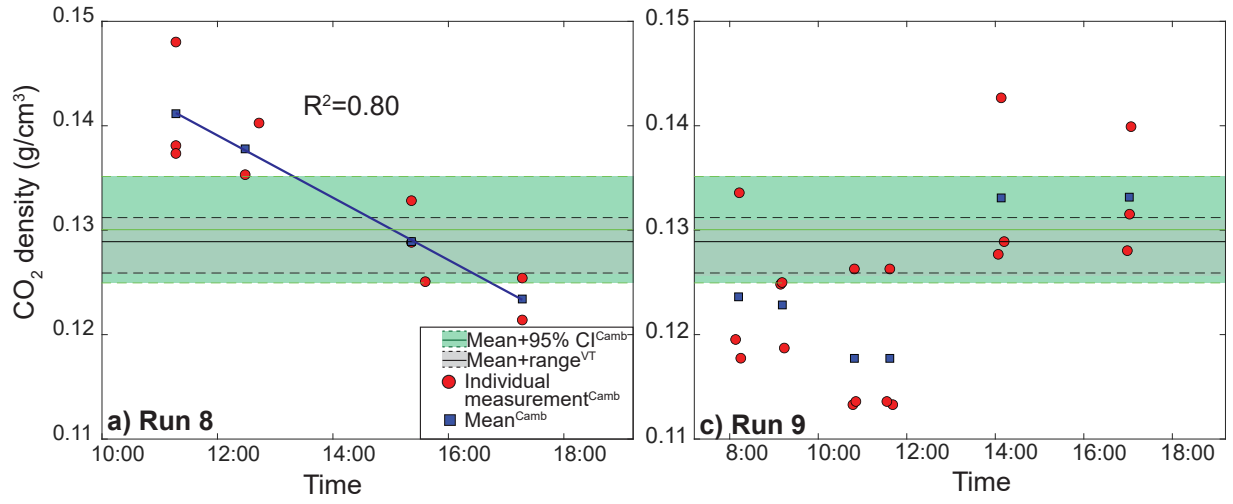


Figure 2.14: a-b Monitoring drift during each run using repeated measurements of fluid inclusion 10mol%_FIE. The green bar shows the mean CO_2 density of all the repeated measurements of 10mol%_FIE used to produce the calibration line in Fig. 2.11. The 95% CI on this calibration line is also shown. This overlaps with measurements of this fluid inclusion's density from the Virginia Tech laboratory (black lines and grey bar). Drift in Run 8 was coherent, while drift in Run 9 was incoherent, with repeated measurements lying just within analytical error of each other and the 95% confidence interval on the calibration.

2.7.6 Precision and Accuracy

The precision of Raman analyses were assessed from the standard deviation of three repeated measurements of each vapour bubble (termed analytical noise). While these standard deviations are small relative to the spectral resolution of the instrument, due to the effective increase in spectral resolution achieved through least squares fitting of Gaussian peaks ($\sim$ 0.02 vs. $\sim$ 1.4 cm^{-1}), they are still relatively large compared with the range of diad splittings reported in Chapter 7 (Fig. 2.15a). As measured diad splittings are converted into densities using a densimeter (Fig. 2.11), the confidence interval on the regression line is another source of error when assessing the precision of Raman measurements. The percentage error from using the upper and lower 67% confidence interval of the regression varies from 59% at 102.63 cm^{-1}, to 9.3% at 102.8cm^{-1}, and 8.3% at 103 cm^{-1} (Fig. 2.15b). However, this source of error is not independent from that estimated from the standard deviation of repeated measurements, as calibration standards are also affected by analytical noise. Due to the difficulty in deconvolving these sources of error, and the fact that the standard deviations calculated for repeated analyses of vapour bubbles are mostly larger than the confidence interval on the regression, error bars in Chapter 7 use only the standard deviation of repeated measurements to quantify instrument-induced error. This is permissable because analytical errors are largely overwhelmed by the -47 to +37% error associated with estimating bubble proportions from 2D images (Tucker et al., 2019). Due to large uncertainties on the magnitude of these different errors, and the interrelated nature of

calibration errors and analytical noise, estimates of bubble volume errors from Tucker et al. (2019) were simply combined with the standard deviation of repeated measurements of each bubble (not in quadrature) to give a reasonable upper estimate of the total error on the amount of CO_2 held within vapour bubbles.

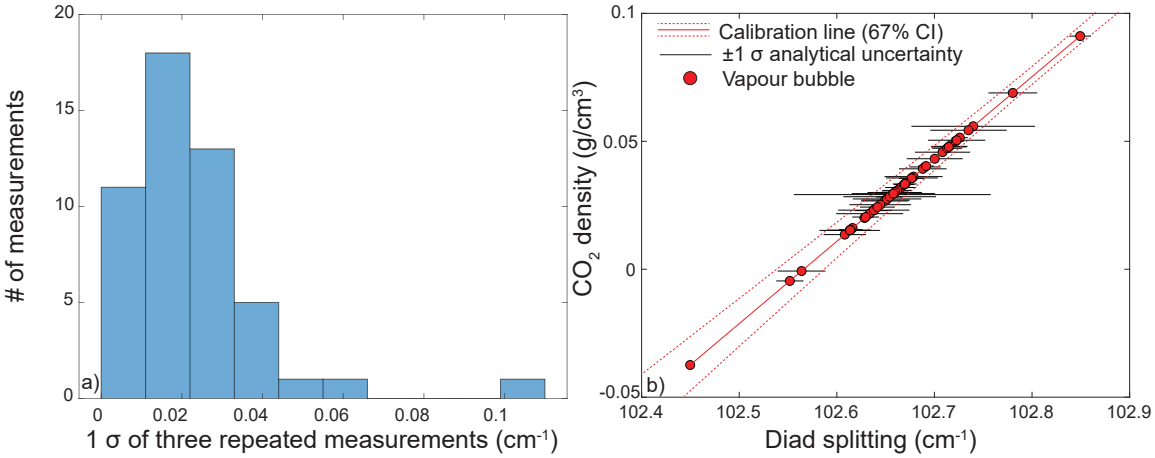


Figure 2.15: a) 1σ errors calculated from three repeated measurements of a single vapour bubble. **b)** 1σ errors shown on the density vs. splitting diagram. There is no obvious correlation between the analytical uncertainty, and the density of the bubble.

The accuracy of CO_2 densities measured using Raman Spectroscopy relies on the calibration line being correct, rather than systematically offset as inferred for literature studies publishing densities >0.21 g/cm^3. The fact that the average density for 10mol%_FIE calculated from the calibration line in Fig. 2.11 defined by 19 primary standards overlaps within error of the density of this inclusion measured at Virginia Tech (Fig. 2.14) provides strong support for the Cambridge calibration. Additionally, the average measurements of 10mol%_FIE in runs which were not used to define the calibration line also lie within analytical error of densities measured at Virginia Tech (Fig. 2.14). Of course, these tests rely on the Virginia Tech calibration being accurate, but given the expertise of this lab with calibration protocols involving high pressure optical cells, there is no reason to doubt their measurements (Lamadrid et al., 2017). The final line of evidence that the Cambridge calibration line is accurate is the fact that no vapour bubbles have yielded densities >0.21 g/cm^3 at room temperature, and a significant number of bubbles from the East African Rift possess densities within error of this upper limit (Kevin Wong, Pers. Comms).

2.8 Secondary Ion Mass Spectrometry (SIMS)

The concentrations of H_2O and CO_2 (as well as MgO and SiO_2 for normalization) presented in Chapter 7 were determined using the Cameca IMS-7f GEO at the NERC Ion Microprobe Facility at the University of Edinburgh in two analytical sessions (July 2019, January

2020). Volatile data for the more evolved samples from earlier fissures (and all F data) are not presented in this thesis due to page limits, and COVID-induced delays collecting LA-ICP-MS data. However, the analytical details for these more evolved samples are discussed below, as small corrections were also applied to the more primitive melt inclusions and glasses from Fissure 8 to produce a single, self-consistent dataset. This other work will be published once LA-ICP-MS data can be collected.

Epoxy stubs were gold-coated at the University of Edinburgh. SIMS analysis was performed prior to EPMA analysis to avoid volatile migration under the electron beam, and to avoid contamination of measured carbon concentrations by a carbon coat (a carbon coat was only applied to the sample after SIMS analyses were completed). Epoxy stubs were placed in the sample chamber at vacuum for a minimum of 6 hours before analysis to allow them to outgas.

A primary beam of $^{16}O^-$ ions with a beam current of 5 nA and an impact energy of 18 kV was focused on the sample resulting in a spot size of ∼10 µm. An image field of 100 µm, and a field aperture with an effective size of 8 µm was used to avoid contamination from the edges of the sputtering pit. Positive secondary ions sputtered from the sample surface were accelerated at 5 keV. Only ions with an energy of 50±20 eV were allowed into the mass spectrometer. Before each analysis the analytical area was pre-sputtered for 3 minutes using a 15 µm beam raster. The secondary beam was centred in the field aperture prior to each analyses and peak positions were automatically updated using a mass scan of the ^{30}Si peak. The mass spectrometer was set to a mass resolution of 2000 ($M/\Delta M$) to avoid interference of $^{24}Mg^{2+}$ on $^{12}C^+$. Peak positions of all measured isotopes and instrument calibration were performed each morning and checked several times each day. Estimates of precision were calculated for both session from repeated analyses of standards (Table 2.15).

Each analysis consisted of 10 cycles, ^{12}C and ^{19}F were counted for 10 s on peak, ^{30}Si for 2 s, ^{26}Mg for 3 s, and $^{24}Mg^{2+}$ and ^{1}H for 5 s. For H and C, the first 4 cycles of each measurement were discarded because the signal sometimes dropped during the first few cycles for glasses with low volatile contents due to small remnants of surface contamination. Instrument backgrounds for H_2O and CO_2 were assessed for each epoxy stub by analysing clean olivine crystals (assumed to be volatile-free). Measurements of F concentrations in olivines were ∼1–3 ppm, indicating that the F background was negligible. In some runs, the volatile backgrounds continued to decline while the sample was in the chamber. In these cases, repeated olivine measurements were used to create a linear fit for the drop in the background as a function of time.

Raw count rates for ^{1}H, ^{12}C, ^{19}F, and ^{26}Mg were normalized to the count rate of ^{30}Si. Normalized count rates for ^{1}H were converted into H_2O concentrations using a calibration curve of H_2O vs. $^{1}H/^{30}Si$ produced from repeated analyses of well-characterized glass standards (N71, M10, 519-4-1, M5, M40, M36, M21, M47, M36; Shishkina et al., 2010;

Hauri, 2002; Fig. 2.16a). Note that no correction for the SiO_2 content was applied as it has been shown that matrix effects for $^{1}H/^{30}Si$ scale with the SiO_2 content of the samples (for the SiO_2 range of these basaltic standards). Normalized counts for ^{12}C were converted into CO_2 concentrations using a calibration curve of CO_2 vs. $^{12}C/(^{30}Si \times SiO_2)$ for the same standards (Fig. 2.16b). SiO_2 concentrations in LERZ samples needed to calculate concentrations were determined using EPMA. Normalized counts of ^{19}F were converted into F concentrations using a 2-point calibration line between (0,0), and the composition of Rick5 (Fig. 2.16c; Guggino and Hervig, 2011). Drift was monitored by repeated analysis every ~12 hours of N72, N5, N40 for H_2O and CO_2, and Rick5 and Lipari for F. In the first 24 hours of Session 1 (July, 2019), the peak position of ^{1}H drifted quite substantially (Fig. 2.16d), resulting in a coherent drop in H_2O in both M5 and M40. This drift was corrected using a linear correction with time (hollow circles), and the ^{1}H peak was re-aligned. After this, peak positions were verified, and re-adjusted if necessary every 12 hours.

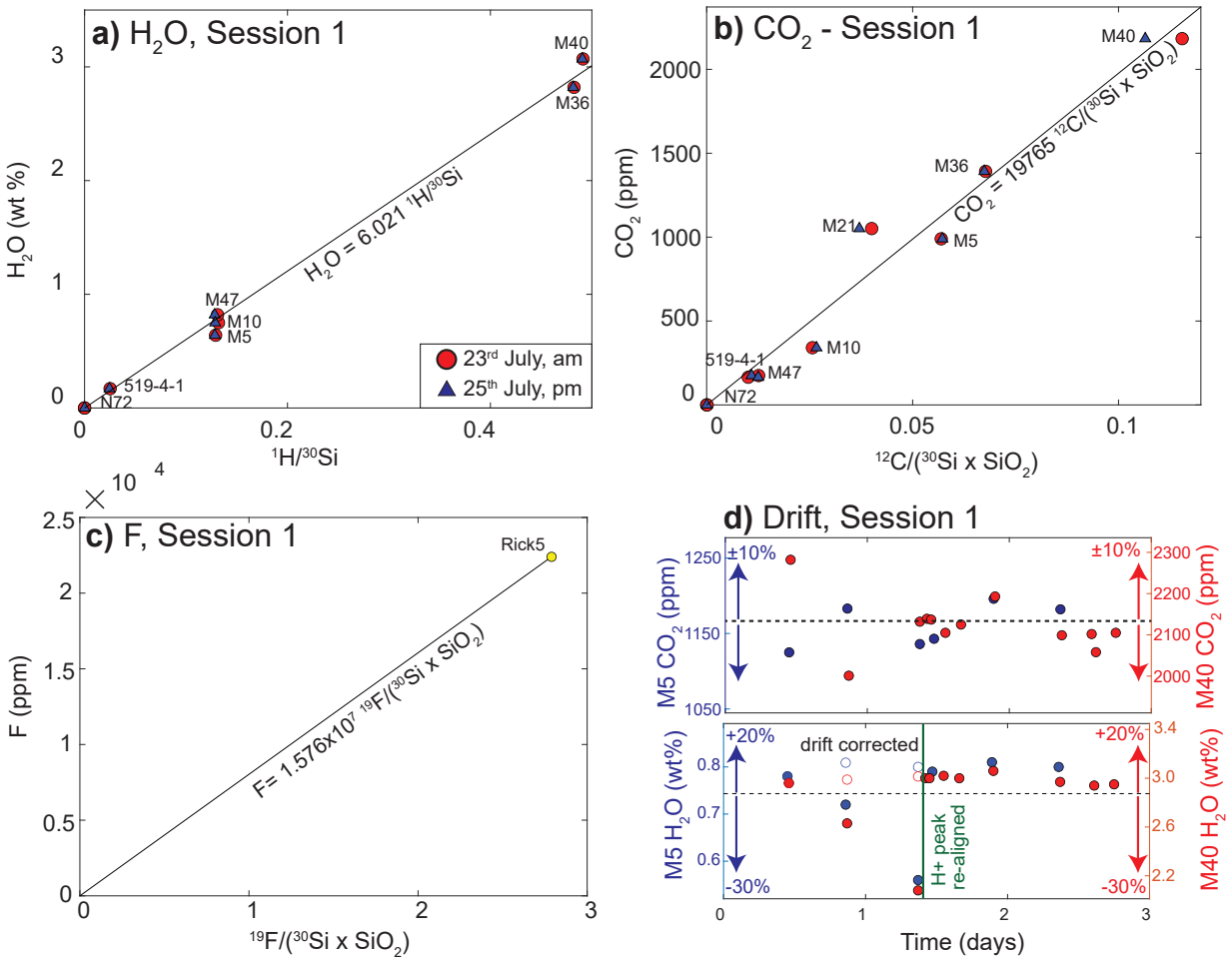


Figure 2.16: a-c) Calibration lines for basaltic-andesite standards for Session 1 used to convert measured counts of ^{1}H, ^{12}C and ^{19}F into concentrations. **d)** Monitoring drift in Session 1 using repeated measurements of M40 (red dots) and M5 (blue dots). In the first 24 hours, coherent drift of ^{1}H was seen in both standards, due to shifting of the ^{1}H peak. The peak was re-centred, and this drift was corrected using a linear model (corrected values shown as hollow circles).

Glasses and melt inclusions from the LERZ eruption span a wide range of SiO_2 contents (48–68 wt%), while the H_2O and CO_2 glass standards used to produce the calibration lines shown in Fig. 2.16 have basaltic-andesitic compositions. As there is a strong matrix effect on the ion yield for H_2O and F (and to a lesser extent CO_2) relative to ^{30}Si, a correction factor as a function of glass SiO_2 content must be applied to obtain accurate concentrations. The extent of this matrix effect was quantified by measuring a variety of more silicic glasses: Sisson51 (73.5 wt% SiO_2), Run84 (58.1 wt% SiO_2), MC84-66-46-b2 (74.0 wt% SiO_2), RB_480 (73.6 wt% SiO_2) and Lipari (74.6 wt% SiO_2). The concentrations of H_2O, CO_2 and F in high-Si standards obtained using the calibration lines developed from the basaltic-andesite glasses were compared to preferred values to calculate the correction factor as a function of SiO_2 content (Fig. 2.17). Note that for ^1H the matrix effect is partially negated by using $^1H/^{30}Si$ for calibration (instead of $^1H/^{30}Si$ x SiO_2), but a small residual matrix effect remained. As expected, the matrix effect for CO_2 was small ($\sim$ 10% between rhyolite and basalt) but for F it was very large (nearly a factor 4 between rhyolite and basalt). High-Si H_2O and CO_2 standards were only analysed in Session 2, when the vast majority of the more evolved samples from 2018 were analysed. Correction factors obtained from this run were used to correct concentrations for the more evolved samples run in Session 1. Rick 5 and Lipari were analysed in both session 1 and 2, and the correction factors derived from the two runs for F were within error of one another across the range of SiO_2 contents in glasses and melt inclusions from the LERZ eruption.

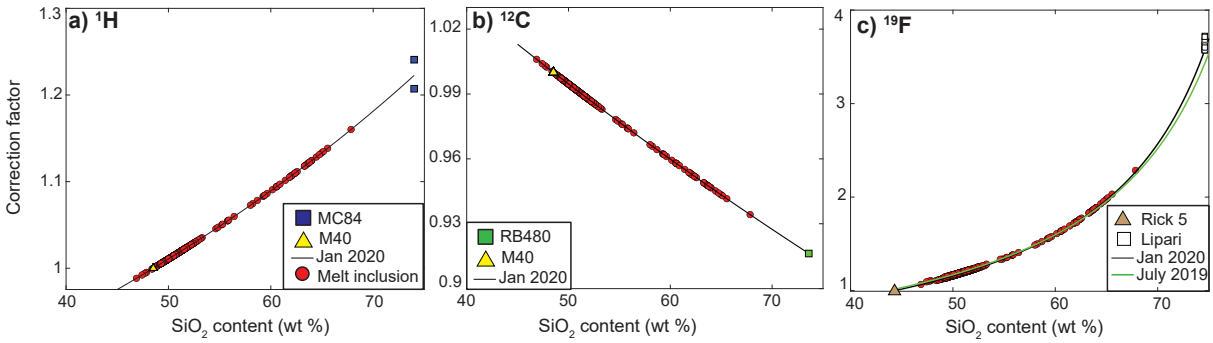


Figure 2.17: Corrections factors for H, C and F based on the SiO_2 content of the sample. MC84 is MC84-66-4b-b2 from Newman et al. (1986), and RB480 is from Brooker et al. (1999).

Table 2.15: Estimates of precision (%) for SIMS measurements. Concentrations marked with a star are those calculated from the average of measurements performed in this study, as the concentrations of these elements in these standards were not reported in the original publication.

Element	Concentration	Run 1 (%)	Run 2 (%)
M5 (N=3 for Run 1, N=8 for Run 2)			
H_2O	0.64 (wt%)	1.1	3.6
CO_2	990 (ppm)	1.9	4.0
F	57.1* (ppm)	1.1	4.6
M4O (N=7 for Run 1, N=8 for Run 2)			
H_2O	3.07 (wt%)	1.4	3.1
CO_2	2183 (ppm)	1.8	2.3
F	53.7* (ppm)	5.0	5.6
M36 (N=2 for Run 1, N=3 for Run 2)			
H_2O	2.82 (wt%)	0.1	0.9
CO_2	1392 (ppm)	0.2	4.6
F	49.7* (ppm)	8.6	2.8
M21 (N=2 for Run 1, N=3 for Run 2)			
H_2O	7.56 (wt%)	0.8	9.0
CO_2	1051 (ppm)	3.9	4.6
F	47.7* (ppm)	2.7	3.3
M47 (N=2 for Run 1, N=2 for Run 2)			
H_2O	0.82 (wt%)	1.1	8.7
CO_2	175 (ppm)	7.3	9.4
F	51.9* (ppm)	1.8	5.2
M10 (N=2 for Run 1, N=2 for Run 2)			
H_2O	0.75 (wt%)	1.2	10.1
CO_2	341 (ppm)	1.9	9.1
F	54.2* (ppm)	6.7	5.3
519-4-1 (N=2 for Run 1, N=2 for Run 2)			
H_2O	0.17 (wt%)	1.3	10.0
CO_2	165 (ppm)	10.8	9.7
F	78.2* (ppm)	0.1	2.6
Lipari (N=5 for Run 1, N=7 for Run 2)			
H_2O	0.58* (wt%)	4.5	15.6
CO_2	18.7* (ppm)	43.9	55.0
F	1700 (ppm)	2.0	1.4
Rick 5 (N=9 for Run 1, N=7 for Run 2)			
CO_2	18.1* (ppm)	33.1	35.2
F	22400 (ppm)	0.0	2.4

Published as: *Wieser, P.E., Vukmanovic, Z., Kilian, R., Ringe, E., Holness, M.B., Maclennan, J. and Edmonds, M., 2019. To sink, swim, twin, or nucleate: A critical appraisal of crystal aggregation processes. Geology, 47(10), pp.948-952. https://doi.org/10.1130/G46660.1.*
Figures reproduced under CC-BY licence.

3

To sink, swim, twin, or nucleate: A critical appraisal of crystal aggregation processes

Abstract

Crystal aggregates in igneous rocks have been variously ascribed to growth processes (e.g., twinning, heterogeneous nucleation, epitaxial growth, dendritic growth), or dynamical processes (e.g., synneusis, accumulation during settling). These hypotheses were tested by quantifying the relative orientation of adjacent crystals using Electron Backscatter Diffraction. Both olivine aggregates from Kīlauea Volcano (Hawai'i, USA) and chromite aggregates from the Bushveld Complex (South Africa) show diverse attachment geometries inconsistent with growth processes. Near-random attachments in chromite aggregates are consistent with accumulation by settling of individual crystals. Attachment geometries and prominent geochemical differences across grain boundaries in olivine aggregates are indicative of synneusis.

3.1 Introduction

Despite the abundance of crystal aggregates in a diverse range of igneous rocks, no consensus has been reached on their origin (Day and Taylor, 2007; Jerram et al., 2003; Schwindinger and Anderson, 1989). As early as 1921, Vogt suggested that crystal aggregates form by synneusis, the swimming together and attachment of previously isolated crystals in a fluid medium. More recently, aggregates have been attributed to growth twinning (Welsch et al., 2012), the nucleation and growth of a daughter crystal via epitaxial growth/heterogeneous nucleation (Dowty, 1980b; Hammer et al., 2010; Kirkpatrick, 1977; Špillar and Dolejš, 2015), or the textural maturation of dendrites (Welsch et al., 2012; Welsch et al., 2014). Previous attempts at distinguishing these hypotheses have utilized optical observations of chemical zoning (Dowty, 1980b), assessments of crystallographic orientation using a universal stage (Ross, 1957), and observations of 3D aggregate morphology (Schwindinger and Anderson,

1989; Welsch et al., 2012). In this study, changes in crystallographic orientation across grain boundaries were quantified using Electron Backscatter Diffraction (EBSD; e.g., Prior et al., 1999). This allows direct comparison between observed aggregate geometries and those predicted by each hypothesis, even in optically isotropic or chemically homogeneous minerals. To demonstrate the versatility of this method, the origin of crystal aggregation in chromite crystals from the UG2 chromitite layer of the Bushveld Complex, South Africa (Fig. 3.1), and olivine aggregates from rapidly quenched scoria from several eruptions at Kīlauea Volcano, Hawai'i, USA were investigated (∼1700 CE, hereafter CE omitted for brevity, 1920, and 1969–1975; Fig. 3.2).

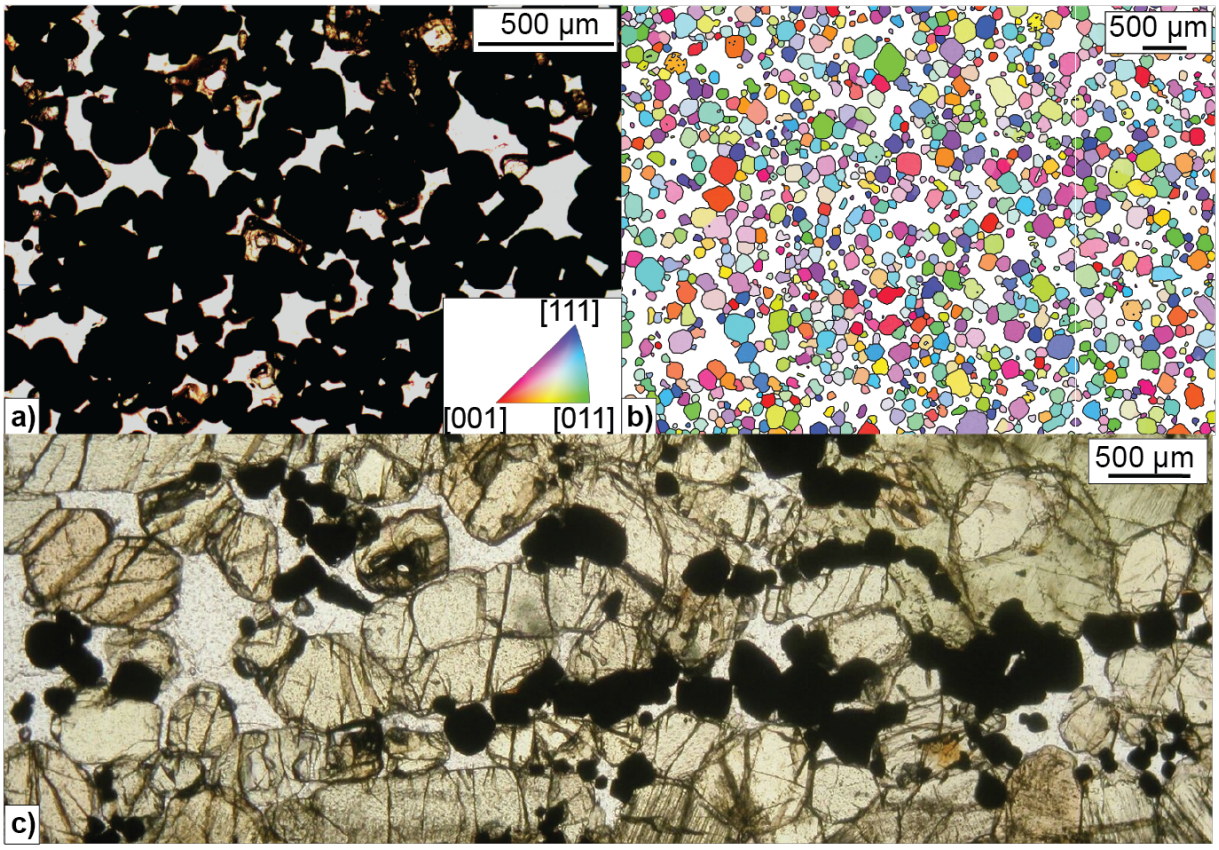


Figure 3.1: a) Transmitted light image of a small region of a thin section from the UG2 chromitite layer. The chromites (black) form a prominent touching network. **b)** EBSD map of a larger area of the thin section coloured using an Inverse Pole Figure (IPF) key. Pixels are coloured with respect to their crystallographic direction. For example, chromites with vertical [111] axes appear blue. The wide range of colours points to an absence of crystallographic preferred orientation. **c)** Transmitted light image of a chromite-poor pyroxenite, lying 0.5 m above the UG2 chromitite layer. Touching frameworks of chromite crystals are relatively scarce compared to the chromitite layer itself (**a-b**), and separated and attached chromite crystals rest on the underlying pyroxene grains. This indicates that chromites settle as isolated grains (accounting for their random orientations), with aggregates only forming when sufficient grains settle in one place.

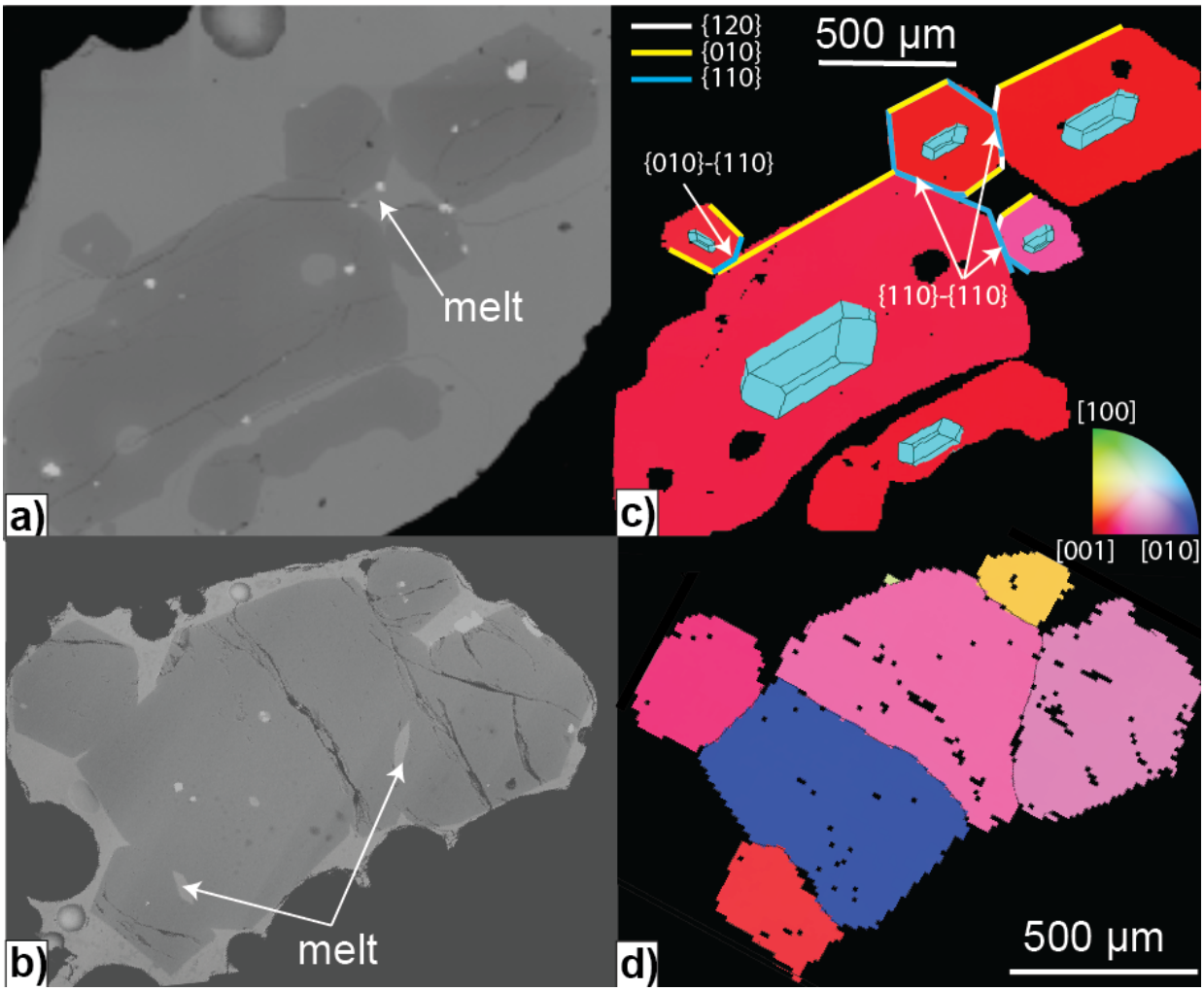


Figure 3.2: a-b) Backscatter electron (BSE) images of olivine aggregates consisting of 3 to 5 crystals. Prominent areas of melt are trapped between neighbouring crystals. **c-d)** EBSD-derived inverse pole figure maps (IPF) of olivine aggregates, colour-coding the crystal direction as in Fig. 3.1. For example, the crystals in **c)** are coloured red because their [001] axes are close to vertical. Olivine shapes in **c)** were computed using the crystalShape MTEX class, allowing assessment of facial attachments. In this case, crystals are predominantly attached along {110}-{110} faces. Note the presence of crystal in **c)** at the top left displaying a {010}-{110} attachment to the main crystal, despite the rest of the aggregate being formed of crystals with very similar orientations. If the well-aligned parts of this aggregate formed by dendritic growth, synneusis would also have to be operating. The more parsimonious explanation is that attached crystals with both high and low misorientations formed by synneusis.

Unravelling the magmatic processes responsible for aggregation has important implications. At Kīlauea, olivine constitutes the principal record of pre-eruptive processes in primitive lavas. Understanding the formation and evolution of chromitite layers such as the Bushveld UG2 is crucial to advance our understanding of how platinum group elements are concentrated into economically viable ore deposits (Naldrett, 2013). The timing and mechanism of aggregate formation also influences crystal re-distribution and accumulation in layered intrusions (Campbell, 1978; Holness et al., 2017b), and the

interpretation of quantitative textural measurements such as crystal size distributions (CSDs), which frequently record kinked CSDs, and an over-abundance of larger crystal sizes in volcanic rocks (Marsh, 1998).

3.2 Sample Details and Methods

The UG2 chromitite sample (kindly provided by Ilya Veksler) was collected from the Rustenburg layered suite at Khuseleka mine (25°37'26.73"S, 27°15'22.11"E; Veksler et al., 2018). Olivine dendrites were examined in West Greenland picritic samples to evaluate the dendritic growth hypothesis (see Larsen and Pedersen, 2000 for more details). Samples from the UG2 chromitite layer and West Greenland Picrites were made into thin sections. Olivine aggregates were identified from the external morphology of crystals mounted in epoxy stubs (following the methods in Chapter 2) using backscatter electron (BSE) maps. EBSD maps were collected for 93 aggregates from a variety of subaerial eruption sites on Kīlauea's summit region, East Rift Zone (ERZ), and the volcanic and seismic strand of the South West Rift Zone (VSWRZ; SSWRZ;Table 3.1).

Table 3.1: Table showing sample locations for Kīlauean aggregates. The number of aggregates examined is indicated.

Sample	# of aggregates	Eruption Date (CE)	Location	GPS coordinate
KL0909	4	May 24th, 1969	ERZ	19° 21.826′ N, 155° 12.877′ W
KL0908	29	Dec 30th, 1969	ERZ	19° 20.839′ N, 155° 12.518′ W
KL0910	13	Nov 10th, 1973	ERZ	19° 22.313′ N, 155° 13.510′ W
KL0916	1	Aug 14th, 1971	Intracaldera	19° 24.137′ N, 155° 16.644′ W
KL0917	2	Late July, 1974	Intracaldera	19° 24.061′ N, 155° 16.653′ W
KL0919	5	Late Dec, 1974	SSWRZ	19° 22.649′ N, 155° 17.609′ W
KL0920	5	Late Dec, 1974	SSWRZ	19° 22.603′ N, 155° 17.713′ W
KL0921	7	∼1700 CE	SSWRZ	19° 22.989′ N, 155° 17.464 ′W
KL0924	10	Late July, 1974	Extracaldera	19° 24.142′ N, 155° 16.896′ W
KL0930	15	1919-1920	VSWRZ	19° 21.230′ N, 155° 23.892′ W
KL0931	2	Sept 24-29, 1971	VSWRZ	19° 20.625′ N, 155° 21.659′ W

The crystallographic relationships between touching grains in aggregates were quantified in terms of their misorientation. This describes the coordinate transform from one crystal orientation to that across the grain boundary, displayed as an axis-angle pair (Fig. 3.3). Misorientations were calculated using MTEX V5.0.4 (Bachmann et al., 2010), an open-source toolbox for MATLAB. Slightly different methods were used to calculate the misorientation between adjacent grains within olivine and chromite aggregates, reflecting the fact that thousands of chromites were present within a single thin section, whereas olivines aggregates were mounted separately in epoxy, and mapped individually.

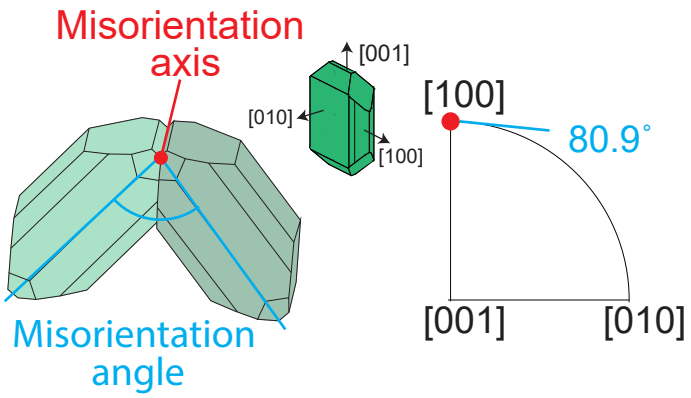


Figure 3.3: Schematic diagram showing the misorientation angle (80.9°) and axis ([100]) for a hypothetical olivine aggregate displayed on an inverse pole figure.

For a single EBSD map of an olivine aggregate, grains were calculated using the MTEX calcGrains function with a threshold angle of 0.5°. The positions of the resulting grain boundaries were then compared to BSE images, and only those separating morphologically distinct grains were selected, discarding low angle boundaries in the interior of grains (see Chapter 4). Misorientations were calculated by comparing the mean orientation of adjacent grains selected by the user (Fig. 3.4). The traditional approach of calculating misorientations along grain boundaries was not used due to the common presence of residual melt along boundaries (Fig. 3.2b). For each map, the resulting misorientation axis and angle were saved as a MATLAB variable. These variables were combined for 203 touching grains within 93 aggregates. The same methodology was used to assess the misorientation signature of olivine dendrites (see Chapter 4). The crystalShape MTEX class was used to superimpose 3D olivine crystals on 2D EBSD maps (`https://mtextoolbox.github.io/files/doc/crystalShape_index.html`). This, alongside examination of the external outlines of grains in BSE images, allowed assessment of facial attachments in approximately ∼50% of aggregates (those with euhedral-subhedral crystal shapes; Figs. 3.2, 3.4).

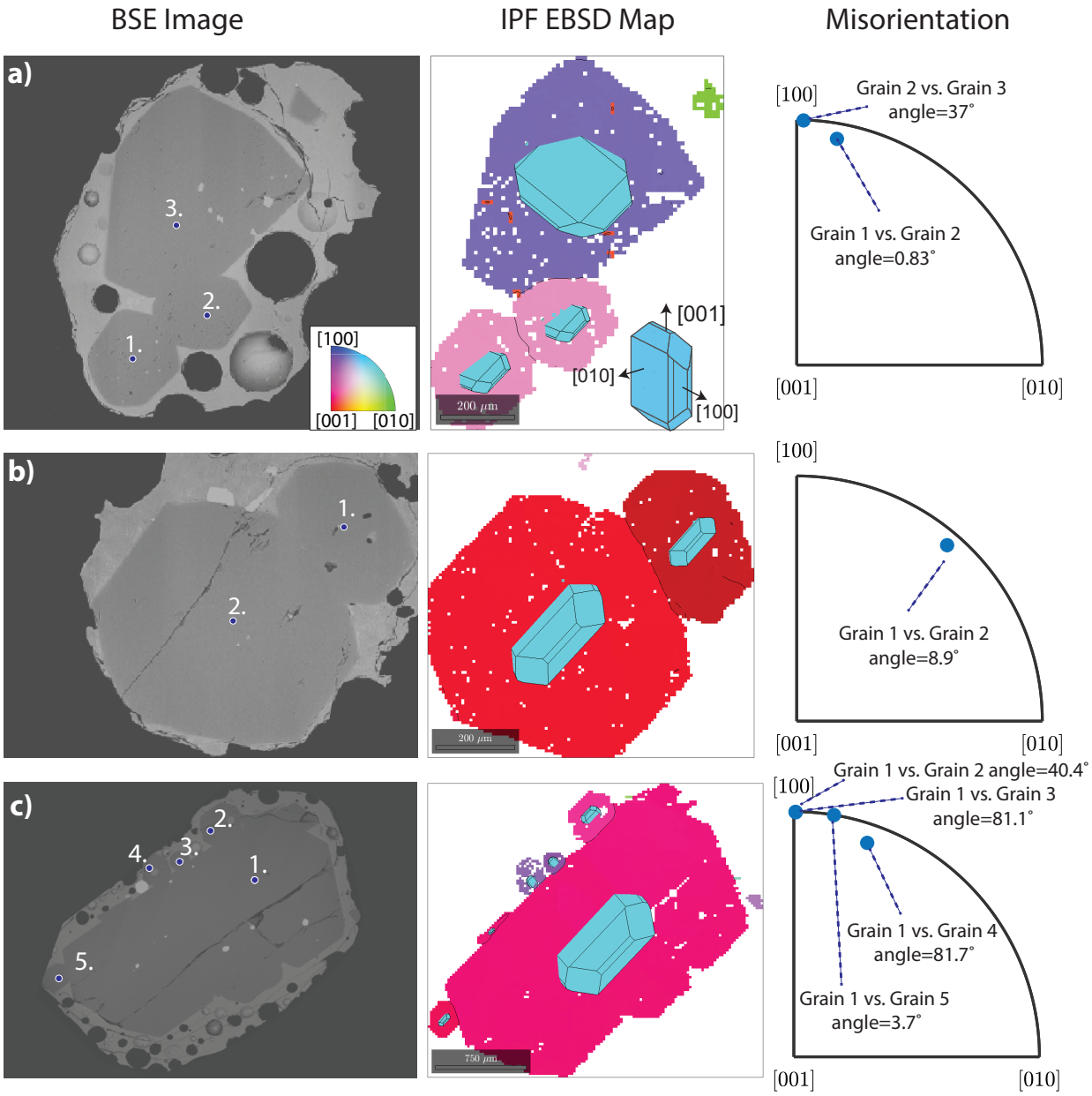


Figure 3.4: Example of the misorientation axes and angles for neighbouring grains in olivine aggregates. EBSD maps (middle) are coloured with respect to their orientation using an IPF key. The orientation of each crystal can also be visualized from the 3D olivine shape superimposed in MTEX. BSE images (LHS) were used to identify boundaries between morphologically distinct crystals. Misorientations for each pair of touching grains are shown as axis-angle pairs (RHS).

In contrast, chromite neighbour pair misorientation measurements were calculated automatically in MTEX from a single EBSD map of the entire thin section. Due to the presence of thousands of individual chromites in a single EBSD map, a higher threshold for the grain segmentation was used (8°), to automatically separate high and low angle grain boundaries (rather than visually inspecting BSE images as for olivine aggregates).

3.3 Results

Olivine aggregates, consisting of 2-17 individual crystals (Fig. 3.2), show misorientation axes strongly clustered about [100], and broad peaks in misorientation angles at <5°, ∼40° and ∼80° (Fig. 3.5). EPMA transects across attached olivine crystals reveal flat compositional profiles in the cores of crystals, with sharp gradients across grain boundaries (Fig. 3.6; sections X-X', Z-Z'). The distribution of chromite misorientation angles is very close to the theoretical random distribution (Fig. 3.7c), with the only prominent peak at 60°. Chromite misorientation axes exhibit weak clustering about [111] and [011] (Fig. 3.7a). Removal of the {111} twins responsible for the 60° peak results in a nearly uniform distribution of misorientation axes and angles (Fig. 3.7b-c).

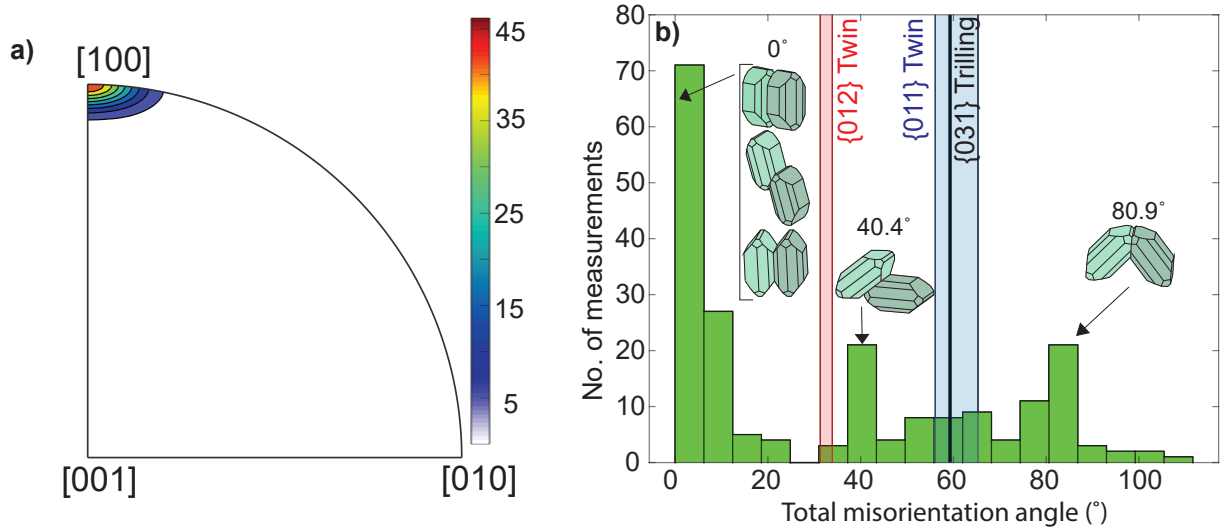


Figure 3.5: Misorientation axes and angles for 203 touching olivine crystals within 93 aggregates. **a)** Misorientation axes cluster strongly at [100]. **b)** Misorientation angles exhibit prominent peaks centred around the angles predicted for perfect attachment along different crystal faces (crystal aggregates drawn in SHAPE7.4; Dowty, 1980b). The colour scale shown in **a)** has units of 'multiples of uniform distribution'

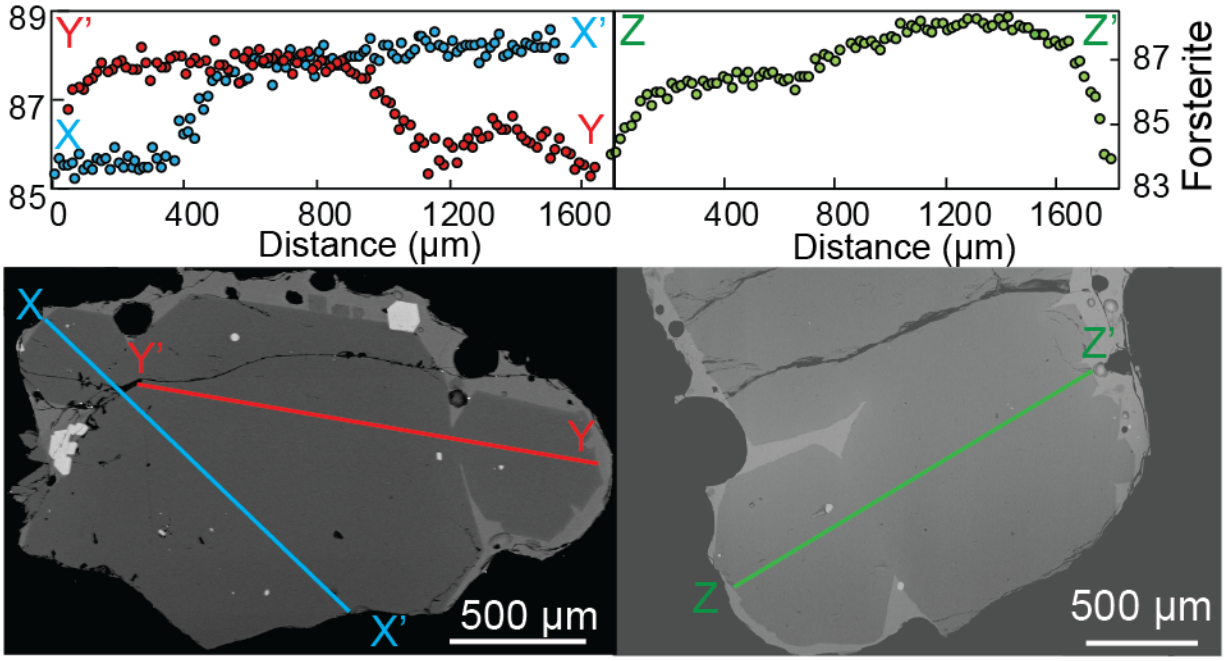


Figure 3.6: BSE images of two olivine aggregates, showing the locations of EPMA transects. Attached grains show different forsterite contents [Fo=100×Mg/(Mg+Fe), atomic]. The presence of flat plateaus within profiles X-X' and Z-Z' demonstrates that these transects cut across grain cores, which must have grown in different conditions. These profiles are not consistent with a scenario whereby compositionally homogeneous aggregates (formed by growth processes) are altered by diffusion or late-stage growth. The presence of steep gradients in forsterite content between crystals indicates that limited diffusive re-equilibration occurred following aggregation.

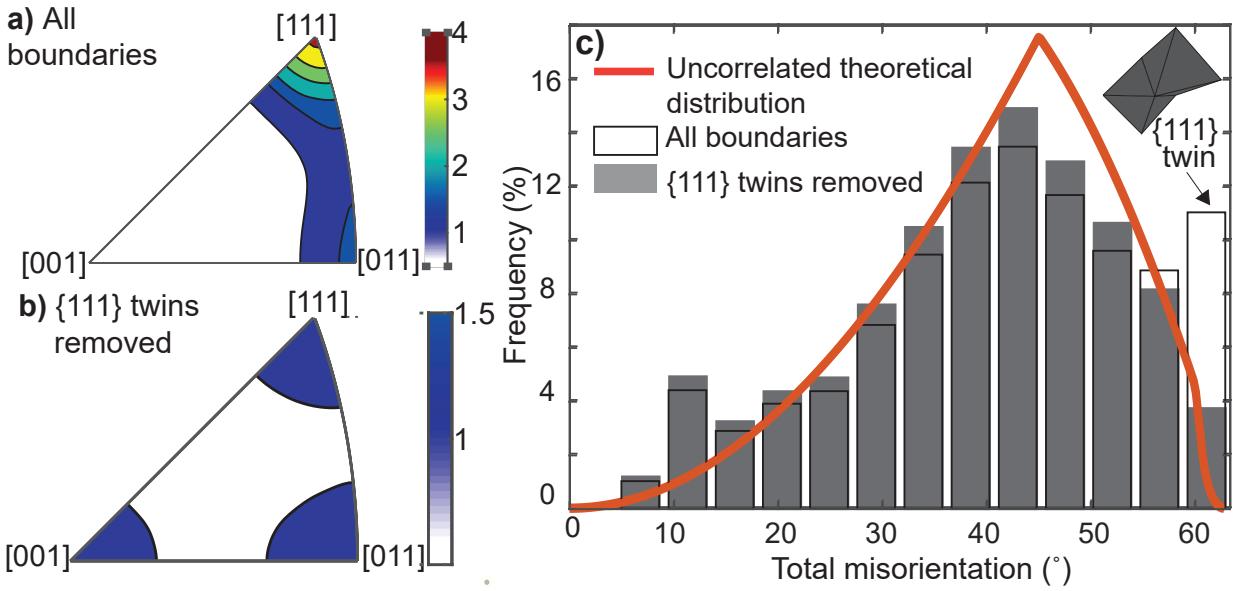


Figure 3.7: **a)** Chromite misorientation axes show moderate clustering about [111] (for ∼3500 chromite grains within one thin section). **b)** Removal of {111} twins and normalization to the theoretical axis distribution leaves a near-uniform axis distribution. The colour scales shown in **a)** and **b)** have units of 'multiples of uniform distribution' **c)** Chromite aggregates show a wide range of misorientation angles. Removal of the prominent peak at 60° caused by {111} twins results in a distribution similar to the uncorrelated theoretical distribution resulting from crystal symmetry.

3.4 Physical Aggregation of Crystals

Hydrodynamic processes within magmatic systems can drive the aggregation of preformed crystals (McIntire et al., 2019). One such process is synneusis (Vogt, 1921; Vance, 1969). While the driving forces associated with interfacial energy minimisation during synneusis are too localized to drive crystals together (Dowty, 1980b), crystals may be aligned while suspended in convecting magma (Holness et al., 2017a), or during settling (Schwindinger, 1999; Schwindinger and Anderson, 1989), resulting in their attachment in specific orientations. Once sufficiently close, reductions in interfacial energy associated with particular crystallographic orientations can drive small readjustments in aggregate geometry (Dowty, 1980b), before further crystal growth cements the crystals together.

To assess the synneusis hypothesis in Kīlauean olivine aggregates, the faces of attachment between adjacent crystals were assessed by superimposing 3D olivine shapes onto EBSD maps (Figs. 3.2; 3.4), and these were compared to the predicted hydrodynamical alignments during settling. Oblate olivines align their axis of symmetry vertically during settling, while prolate olivines align their axis of symmetry horizontally (Leal, 1980). This creates mostly {010} attachments in oblate olivines, and {110} and {010} attachments in prolate olivines, with occasional {021} attachments in both cases (Schwindinger and Anderson, 1989). It is anticipated that similar alignments would also occur during convection.

Attachments on {110}-{110} faces were the most commonly observed geometry in Kīlauean aggregates (Fig. 3.2), followed by {010}-{010} or parallel {021}-{021} attachments (difficult to distinguish in 2D). Crystals which are perfectly attached along parallel {110}-{110}, {010}-{010} and {021}-{021} faces would have identical orientations, while perfect attachments along {021}-{010} and perpendicular {021}-{021} faces would generate misorientations about [100] of 40.4° and 80.9° respectively. The presence of broad misorientation angle peaks centred about these angles is strong evidence for synneusis (Fig. 3.5b). Unlike crystal growth processes, which favour specific crystallographic relationships, attachment by synneusis can easily generate slight misalignments from these ideal attachment geometries, through the mechanical hindrance to re-orientation driven by the reduction of interfacial energies (Nespolo and Ferraris, 2004; Vance, 1969), or near-random attachment under conditions of high supersaturation (Schwindinger and Anderson, 1989). Imperfect attachment by synneusis also accounts for the presence of discontinuous melt films between adjacent olivine crystals (Fig. 3.2a-b). If formed during growth, such films would impose high energy penalties.

Finally, EPMA transects support the hypothesis that the olivine aggregates formed by synneusis (Fig. 3.6). While synneusis can bring together crystals with different core compositions that formed in disparate environments (Schwindinger and Anderson, 1989), aggregates produced by twinning or dendritic growth share a common history, so the cores of attached crystals should have identical chemistry (Philpotts et al., 1998). The

sharp gradients in forsterite contents (which dissipate rapidly by diffusion) suggest that the aggregation event occurred shortly before eruption. Crystal aggregation may occur following a disturbance to the magmatic system triggering their eruption, or during transport of the magma to the eruption site.

Evaluating the role of physical aggregation in the formation of chromite aggregates is complicated because attachment along the only crystal face, {111}, produces misorientation axes indistinguishable from primary twinning (60° rotation about [111]; Deer, 1966). However, this geometric relationship is relatively uncommon, and the removal of misorientations corresponding to the chromite twin law (and effects induced by crystal symmetry) produces a near-uniform misorientation axis distribution, and an angle distribution resembling the theoretical random distribution induced by crystal symmetry (Fig. 3.7c). This implies that chromite grains are randomly aggregated by a mechanism which is not selective to crystallographic orientation; this is inconsistent with the attachment of {111} faces by synneusis, or various growth processes. This suggests that the randomly-oriented touching frameworks of chromite grains formed during the settling of individual grains through the overlying magma column to the top of the cumulate pile (Jackson, 1961). This hypothesis is consistent with microstructures in the cumulates overlying UG2, in which individual chromite grains apparently rest on underlying pyroxene primocrysts (Fig. 3.1c).

3.5 Crystal Growth Processes

Crystal aggregates attached along specific planes have also been attributed to primary twinning (Welsch et al., 2012). However, neighbouring chromite grains displaying twin relations are relatively rare (<10% of neighbouring grains, based on deviations from ideal twin laws; Brandon, 1966, Section 3.9). Similarly, <7% of neighbouring olivines are related by the three olivine twin laws (twinning on {011}, {012} and {031}, corresponding to misorientations about [100] of 60.7°, 32.6° and 59.3° respectively; Azevedo and Nespolo, 2017; Dodd and Calef, 1971; Fig. 3.5b). Thus, twinning is not the dominant cause of grain aggregation in the samples investigated here.

Dowty (1980a) suggested that the textural and chemical characteristics of crystal aggregates could result from epitaxial growth or heterogeneous nucleation. These processes, driven by the reduction of the activation barrier to nucleation by the presence of an existing crystalline substrate in the melt (Lofgren, 1983; Mithen and Sear, 2014), are well-documented in multiphase aggregates (Hammer et al., 2010; Hammer et al., 2010). However, in monomineralic aggregates, nucleation and growth of a daughter crystal are associated with energy penalties. The increased surface area per unit volume (and increased interfacial energy) caused by the growth of a daughter crystal was assessed by comparing an individual crystal of a given volume with an aggregate with the same total volume composed

of two identical crystals (volumes and areas calculated in SHAPE7.4; Dowty, 1980a; Fig. 3.8). For olivine, forsterite unit cell parameters were used (a=4.756, b=10.195, c=5.981 Å). The shape ratio was set at a:b:c=1.5:1:2, with the central distance ratios used by Welsch et al. (2012). For cubic chromite, only {111} faces were expressed. Central distances were adjusted in SHAPE7.4 to produce a crystal with a volume of 1 mm^3 (Fig. 3.8).

The interfacial energy for a single crystal with a volume of 1 mm^3 was calculated by multiplying the area of each face by the interfacial energy of that face. Central distances were then adjusted in SHAPE7.4 to yield a crystal with a volume of 0.5 mm^3. The total interfacial energy of two attached 0.5 mm^3 crystals was calculated by multiplying the area of each face by its energy, minus the energies of the two attached faces (see Section 3.7.2).

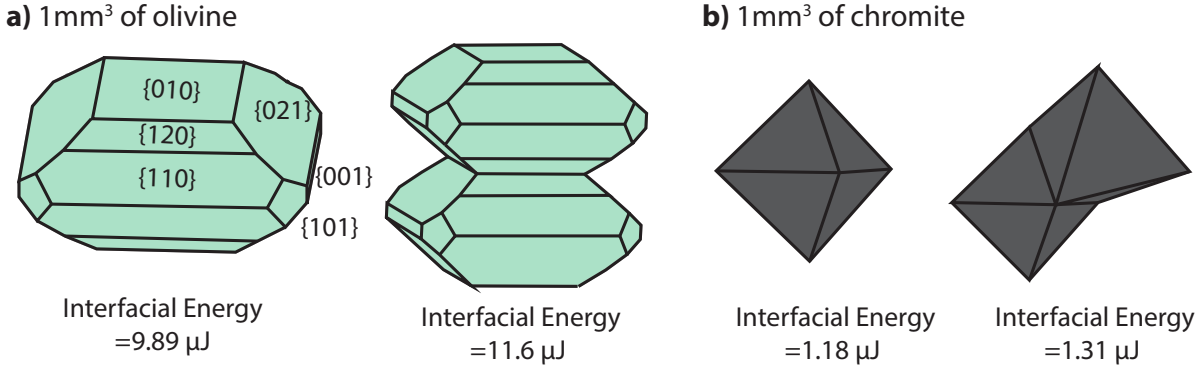


Figure 3.8: Crystal geometries used for interfacial energy calculations (produced in SHAPE V7.4).

For chromites, the increase in interfacial energy for aggregates compared to individual crystals of the same volume is 11%. Surface energies for $NiFe_2O_4$ spinel were used in the sample calculations shown in Section 3.7.2 (Mishra and Thomas, 1977). However, as chromite crystals express only {111} faces, the calculated percetange increase in interfacial energy is not dependent on the choosen value for the surface energy of this face. For olivine, ab initio surface energies of forsterite in a vacuum at 0 K were used (Bruno et al., 2014). As surface adsorption on olivine in basaltic melt is anisotropic (Wanamaker and Kohlstedt, 1991; De Leeuw et al., 2000), calculated energy differences are reliant on the assumption that the relative magnitudes of facial energies are not affected by surface adsorption. However, regardless of the attachment face, the growth of a daughter crystal in olivine is accompanied by significant energy penalties (13–24%; Section 3.7.2). Thus, the conclusion that heterogeneous nucleation is energetically unfavourable is not sensitive to the exact choice of facial energies.

Energy penalties for heterogenous nucleation are even greater. While epitaxial growth describes the nucleation of crystals in a specific crystallographic orientation with respect to the host crystal (identical or twin orientations in single phase aggregates; Mithen and

Sear, 2014), heterogeneous nucleation has no such orientation constraints. The large lattice mismatches and associated energy penalties generated by heterogeneous nucleation may drive the detachment of a poorly-orientated unit, followed by reattachment in a more favourable orientation (Buerger, 1945). In certain cases, it may even be more energetically favourable for the components of the misaligned daughter crystal to remain in the liquid state (Brugger and Hammer, 2015).

The larger energy penalties for heterogeneous nucleation than for epitaxial growth, alongside lower nucleation rates for mismatching parent and daughter lattices (Turnbull and Vonnegut, 1952), means that heterogeneous nucleation should occur less frequently than epitaxy in monomineralic aggregates. Olivine and chromite aggregates show little evidence for epitaxy; twin relationships are rare (Figs. 3.5, 3.7), and no crystals with uniform orientations show external morphologies indicative of aggregation. Given the limited evidence for epitaxial growth, it is improbable that the less energetically favourable process of heterogeneous nucleation was the dominant cause of grain aggregation in this study.

Welsch et al. (2012) propose that polyhedral aggregates are produced during an early period of dendritic growth, followed by textural ripening. This hypothesis is based on observations that attached olivine crystals have identical orientations, are in continuous contact, and are superimposed in chains of decreasing crystal size elongated along [100] (Welsch et al., 2012). However, crystallographic branching in dendrites (Cody and Cody, 1995; Faure et al., 2003b; Faure et al., 2003a) is associated with misorientations lower than $\sim 3^\circ$ (Faure et al., 2003a), so cannot account for the 86% of olivine aggregates with misorientations $>3^\circ$ (Fig. 3.5). Additionally, neighbouring crystals in the subset of olivine aggregates displaying small misorientations ($<5^\circ$) are often separated by pockets of melt, and show no preferential elongation direction or size ordering (Fig. 3.2, cf. Welsch et al., 2012). While the textural maturation of non-crystallographic branching dendrites (Donaldson, 1976; Keith and Padden, 1963) could produce the 86% of aggregates with large misorientation angles, the crystallographic signatures of branching olivine dendrites from West Greenland picrites differ from those of olivine aggregates (see Chapter 4; Fig. 4.7). While olivine dendrites and aggregates both display a misorientation angle peak at $<20^\circ$, dendrites show no peaks at higher angles. The differences between these distributions are statistically significant ($p=0.013$; Kolmogorov-Smirnov test). Additionally, misorientation axes in branching dendrites form a bimodal distribution, with a primary maximum at [010] (Donaldson, 1976) and a minor secondary maximum at [100] (Fig. 4.7). In contrast, the misorientation axes for Kīlauean aggregates are strongly clustered about [100] (Fig. 3.5). Overall, the crystallographic and textural signatures of olivine aggregation are inconsistent with an origin from non-crystallographic branching during dendritic growth.

3.6 Conclusions

The large range of misorientations in chromite and olivine aggregates cannot be explained by crystal growth processes, which favour specific crystallographic relationships. Observed facial attachments and compositional profiles across adjacent olivines are consistent with crystal aggregation by synneusis shortly before eruption. In crystal populations affected by synneusis, textural investigations such as crystal size distributions must be constructed from measurements of individual grains within an aggregate. Consideration of the total size of an aggregate is only justified if aggregation can be attributed to twinning or dendritic growth. To distinguish between these cases routinely, a workflow could be developed whereby the origin of grain aggregation is assessed using EBSD maps, which are subsequently used to generate "informed" CSDs. The random crystallographic relationships between adjacent chromite grains in our sample of the UG2 chromitite layer are best explained by the formation of touching networks following crystal settling. Settling as individual crystals rather than aggregates has implications for initial mush porosity and accumulation timescales, with relevance to the formation of economically-viable platinum group element deposits.

3.7 Additional Information

3.7.1 Identifying Twin Laws

To identify potential twins in aggregates, a criterion was required to specific the permitted deviation from the ideal twin laws for olivine and chromite (Fig. 3.9).

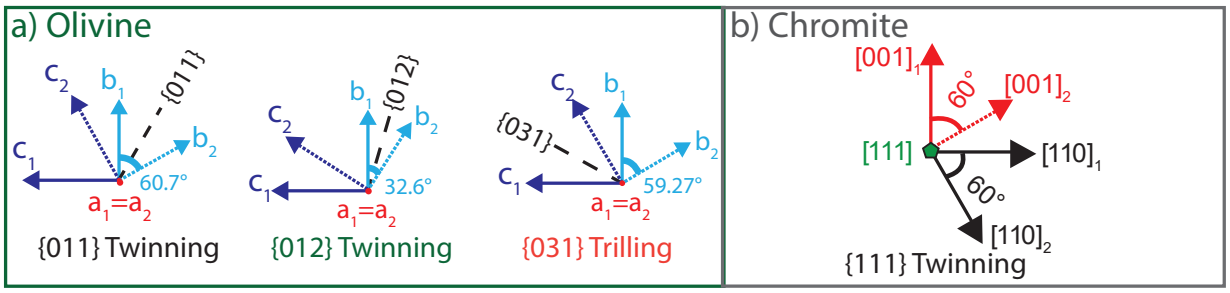


Figure 3.9: Twin laws in olivine and chromite, after Dodd and Calef (1971) and Deer (1966) respectively

Crystals of cubic minerals such as chromites exhibit a special type of low energy boundary called coincidence site lattices (CSLs), where a finite number (Σ) of lattice points coincide along the boundary (Randle and Engler, 2000). The chromite twin law is the most common CSL with $\vartheta = 3$ (Garbacz and Grabski, 1989). The permitted deviation from these ideal CSLs (or twins) was calculated using Brandon's Law:

$$\vartheta = \vartheta_0(\Sigma)^{-0.5} \tag{3.1}$$

Where ϑ is the permitted deviation, ϑ_0 is the angle used to differentiate subgrain and true grain boundaries (8°), and ϑ is the CSL number. For the {111} twin in chromites (CSL3), the permitted deviation is 4.61°. The application of Brandon's law (and thus CSL numbers) to systems with lower symmetry such as olivine is less well established. As an approximation, CSL numbers can be calculated based on the hexagonal cubic sublattice for planes of oxygen within olivine (Poirier, 1975). Using Σ=3 for {011} twinning, and Σ=39 for {012} twinning (Faul and Gerald, 1999), this permits angular deviations of 4.6° and 1.3° respectively from the idea twin laws (when ϑ_0=8°).

3.7.2 Calculating Surface Energies

Example calculations of surface energies for chromite and olivine individual crystals and aggregates.

Table 3.2: Interfacial energy calculations for single olivine crystal with a volume of 1 mm^3 (morphology shown in Fig. 3.8). Total face area was calculated as the area of each face (mm^2) multiplied by the number of faces of that type. The total energy (in µJ) of a given face was calculated by multiplying the facial energy (J/m^2) by the area (mm^2)

Face	Energy (J/m^2)	# of faces	Total face area (mm^2)	Total energy per face type (µJ)
{010}	1.22	2	1.109	1.353
{021}	1.90	4	2.023	3.843
{110}	2.18	4	1.438	3.135
{101}	1.78	4	0.179	0.319
{001}	1.78	2	0.176	0.313
{120}	1.36	4	0.683	0.928
Total interfacial energy (sum of all 6 faces)				9.89 µJ

Table 3.3: Calculation of the interfacial energy for an olivine aggregate consisting of two identical crystals (each with a volume of 0.5 mm^3) joined along the {010} face. The total interfacial energy of the aggregate was calculated as 2 × the energy of a single crystal minus the interfacial energies of the two touching faces.

Face	Energy (J/m^2)	# of faces	Total face area (mm^2)	Total energy per face (µJ)
{010}	1.22	2	0.699	0.853
{021}	1.9	4	1.274	2.421
{110}	2.18	4	0.906	1.975
{101}	1.78	4	0.113	0.201
{001}	1.78	2	0.111	0.197
{120}	1.36	4	0.43	0.585
Total interfacial energy (sum of all 6 faces)				6.23 µJ
Interfacial energy of 2 {010} faces				0.853 µJ
Total interfacial energy of aggregate				11.6 µJ
Energy increase vs. single crystal of same volume (%)				17%

Table 3.4: Interfacial energy penalties for different facial attachments of olivine crystals.

Attached faces	{110}	{120}	{010}	{021}	{001}	{101}
Energy penalty (%)	16%	23%	17%	14%	24%	25%

Table 3.5: Interfacial energies for a single chromite crystal with a volume of 1 mm^2 (morphology shown in Fig. 3.8)

Face	Energy (J/m^2)	# of faces	Total face area (mm^2)	Total energy per face type µJ
{111}	0.207	8	5.719	1.184
Total interfacial energy (sum of all 6 faces)				1.18 µJ

Table 3.6: Interfacial energy for a chromite aggregate consisting of two identical crystals, each with a volume of 0.5 mm^2 (morphology shown in Fig. 3.8)

Face	Energy (J/m^2)	# of faces	Total face are (mm^2)	Total energy per face type µJ
{111}	0.207	8	3.603	0.746
Total interfacial energy per crystal				0.746 µJ
Total interfacial energy of two {111} faces				0.186 µJ
Total interfacial energy of aggregate				1.31 µJ
Energy increase vs. single crystal of same volume (%)				11%

Published as: *Wieser, P.E., Edmonds, M., Maclennan, J. and Wheeler, J., 2020. Microstructural constraints on magmatic mushes under Kīlauea Volcano, Hawaii. Nature Communications, 11(1), pp.1–14. https://doi.org/10.1038/s41467-019-13635-y.*
Figures reproduced under CC-BY licence.

4

Microstructural Constraints on Magmatic Mushes under Kīlauea Volcano, Hawai'i

Abstract

Distorted olivines of enigmatic origin are ubiquitous in erupted products from a wide range of volcanic systems (e.g., Hawai'i, Iceland, Andes). Investigation of these features at Kīlauea Volcano, Hawai'i, using an integrative crystallographic and chemical approach places quantitative constraints on mush pile thicknesses. Electron backscatter diffraction (EBSD) reveals that the microstructural features of distorted olivines, whose chemical composition is distinct from undistorted olivines, are remarkably similar to olivines within deformed mantle peridotites, but inconsistent with an origin from dendritic growth. This, alongside the spatial distribution of distorted grains and the absence of adcumulate textures, suggests that olivines were deformed within melt-rich mush piles accumulating within the summit reservoir. Quantitative analysis of subgrain geometry reveals that olivines experienced differential stresses of ∼3–12 MPa, consistent with their storage in mush piles with thicknesses of a few hundred metres. Overall, this study demonstrates that microstructural analysis of erupted crystals provides novel insights into mush-rich magmatic systems.

4.1 Introduction

Studies of the textural and geochemical characteristics of olivine crystals have revealed significant complexity in basaltic volcanic plumbing systems, including the timescales of eruptive triggering from diffusion profiles (Rae et al., 2016), storage times from crystal chemistry (Thomson and Maclennan, 2012), and depths of magma storage from melt inclusion geochemistry (Tuohy et al., 2016). Olivines with prominent lattice distortions are commonplace in olivine-rich basalts from a range of tectonic settings (Thomson and Maclennan, 2012; Vinet et al., 2015; Welsch et al., 2012). As the magmatic processes

producing distorted olivines are poorly understood, these features represent a previously unexploited source of information.

At Kīlauea Volcano, distorted olivines are commonly attributed to ductile creep within dunitic bodies located around the central conduit (Helz, 1987) or within the deep rift zones (∼5–9 km depth; Clague et al., 1995; Vinet and Higgins, 2010). However, a recent suggestion that lattice distortions are produced by an early phase of branching dendritic growth, followed by textural ripening and the merging of misoriented crystal buds, has gained considerable traction (Welsch et al., 2012; Welsch et al., 2014). Lattice distortions have also been attributed to collisions between crystals during magma flow through constricted or irregular conduits (Natland, 2003; Wilkinson and Hensel, 1988).

Establishing the magmatic processes producing distorted olivines is vital to further our understanding of basaltic plumbing systems. Extracting the information held within these features is particularly crucial at Kīlauea, where olivine is the only silicate phase in magmas containing >6.8 wt% MgO (Wright and Fiske, 1971) so provides the main record of pre-eruptive storage. Furthermore, Kīlauean primary melts have ∼15–17 wt% MgO (Clague et al., 1991), yet erupted lavas contain 5–10 wt% MgO, and few crystals (1–3 vol%; Garcia et al., 2003). This disparity in MgO contents requires fractionation and storage of considerable volumes of olivine within the volcanic edifice (Clague and Denlinger, 1994).

Materials with high seismic velocities (interpreted as dunitic bodies) have been imaged within the summit region and deep rift zones of Kīlauea Volcano (Park et al., 2007). Large earthquakes, slow slip events, and landslides have been attributed to the presence of these weak dunitic bodies separating the south flank of Kīlauea from the rest of the island of Hawai'i (Clague and Denlinger, 1994; Denlinger and Morgan, 2014). Yet, the relationship between distorted olivines in erupted products and seismically-imaged dunites remains unresolved. If lattice distortions are created within dunitic bodies, microstructural interrogation of these features may provide insights into the instability of the south flank. However, if distortions are in fact formed during crystal growth, the association between dunitic bodies and edifice instability at ocean islands (e.g., Hawai'i, Reunion) may have been overestimated from petrological observations of distorted grains (Welsch et al., 2012). Finally, the hypothesis that distorted olivines originate from dunitic bodies has fuelled suggestions that Kīlauea's deep rift zones allow magma to bypass the summit reservoir (Vinet and Higgins, 2010). Re-assessing the petrological evidence for summit bypass is vital for accurate estimates of magma supply rates and CO_2 fluxes at Kīlauea (Poland et al., 2015).

If distorted olivines record plastic deformation, rather than crystal growth processes, their microstructures can be evaluated within the conceptual framework developed through the extensive study of naturally- and experimentally-deformed mantle peridotites. The movement of dislocations is one of the main mechanisms accommodating plastic deformation within crystals. Dislocations can be characterized in terms of a Burgers vector ($\overrightarrow{b}$) and a

line direction ($\overrightarrow{u}$). The plane containing these vectors defines the slip plane (Cordier, 2002). The angle between $\overrightarrow{b}$ and $\overrightarrow{u}$ determines whether the dislocation is an edge dislocation ($\overrightarrow{b} \perp \overrightarrow{u}$) a screw dislocation ($\overrightarrow{b} \parallel \overrightarrow{u}$), or a mixed dislocation ($\overrightarrow{b}$ and $\overrightarrow{u}$ neither parallel or perpendicular). A slip system is described in terms of a set of slip planes, and a Burgers vector direction on which dislocation motion occurs. For example, the olivine slip system (010)[100] denotes the movement of edge dislocations along the (010) plane with a [100] Burgers vector direction. Previous work has identified five olivine fabric types (A to E-types) from different crystallographically preferred orientations (CPOs), and determined the role that pressure, temperature, differential stress and hydration exert on their formation (Ave'Lallemant and Carter, 1970; Katayama et al., 2004; Zhang and Karato, 1995). However, unlike thin sections of mantle peridotites, the orientations of erupted olivines in tephra and spatter deposits have been randomised upon eruption and again during sample preparation, so CPOs cannot be used to infer deformation conditions in volcanic olivines. Fortunately, CPOs are macroscopic features resulting from the activities of different dislocation types, which can be classified in terms of slip systems (Jung and Karato, 2001, Karato et al., 2008, Katayama et al., 2004, Lloyd et al., 1997, Prior et al., 1999).

Until now, most assessments of lattice distortion in volcanic olivines have used optical microscopy (Bradshaw et al., 2018, Helz, 1987, Vinet and Higgins, 2010). This method is largely qualitative, and optical evidence for distortion is often ambiguous in small grains, or across subgrain boundaries with small misorientations (Vinet et al., 2011; Figs. 4.1–4.4). A few studies have employed more quantitative methods, but these have been restricted to visual examination of dislocation structures and densities following oxidation decoration of dislocations (Kohlstedt et al., 1976; Sakyi et al., 2012), and examination of lattice strain using in situ X-ray diffraction (Vinet et al., 2011). In this study, low angle boundaries in individual olivine crystals within basaltic spatter and scoria from Kīlauean eruptions were mapped using electron backscatter diffraction (EBSD). This method not only offers significant improvements in spatial and angular resolution compared to optical observations (see Figs. 4.1–4.4; Humphreys, 2001), it also provides sufficient crystallographic information to quantify the Burgers vector and slip plane, and thus the dominant slip system.

As many deformation experiments on mantle-derived olivines were conducted at pressures and temperatures similar to those found within igneous plumbing systems (e.g., 250–300 MPa, 1200°C; Hansen et al., 2014), assessment of the activities of different slip systems in erupted olivine crystals places constraints on the conditions of deformation, using established links between slip systems, CPOs and fabric types, and between fabric types and deformation conditions (Jung and Karato, 2001, Karato et al., 2008, Katayama et al., 2004, Lloyd et al., 1997, Prior et al., 1999). Finally, to evaluate the suggestion that lattice distortions result from the textural maturation of olivine dendrites, the crystallographic signatures of branching dendritic growth in olivine dendrites from West Greenland picrites were examined (Larsen and Pedersen, 2000), and compared to the microstructures of distorted Kīlauean olivines.

4.2 Methods

4.2.1 Sample Preparation and Analysis

Electron microprobe spot analyses, wavelength-dispersive spectroscopy (WDS) maps, and EBSD maps of Kīlauean olivine crystals from a variety of eruption sites (Fig. 4.5) were collected using the methods discussed in Chapter 2. EBSD maps were also collected of dendritic olivines from West Greenland. One Kīlauean epoxy grain mount was made into a thin section to allow comparison of EBSD and optical observations (Figs. 4.1–4.4). Data processing was performed in MTEX v5.0.4. Single misindexed pixels were removed, and data was denoised using a 5 neighbour Kuwahara filter. Subgrains were identified using the calcGrains MTEX function, with a threshold misorientation angle of 0.5°. Boundaries with misorientation angles >10° were classified as high angle boundaries. Interior and exterior low-angle boundaries were combined into a single variable. The use of threshold angles smaller than 0.5° results in imprecise estimates of misorientation axes and angles, due to the finite angular resolution of conventional EBSD (Brough et al., 2006; Prior, 1999). Furthermore, utilization of smaller threshold angles can result in inaccurate stress estimates from microstructural methods such as subgrain piezometry (Hansen and Warren, 2015).

In Chapter 3, pixels in EBSD maps were coloured using an IPF key with respect to their absolute orientation (e.g., pixels with their [001] axes vertical were coloured red; Fig. 3.2). In this Chapter, to emphasize small misorientations, EBSD maps were coloured using an adaptation of the Inverse Pole Figure (IPF) key. A colour reference direction for each map is defined as the mean orientation of a user-selected grain. Pixels with the same orientation as this reference direction are coloured white. Pixels which are misorientated with respect to this reference direction are coloured based on the misorientation angle and axis using a IPF key scaled to a given misorientation. In Fig. 4.1, the IPF key is scaled to 2°, so pixels misorientated by more than 2° from the reference direction are coloured black. This means the other colours are available to emphasize small changes in misorientation. For example, pixels coloured green are misorientated from the reference direction by 2° about the [100] direction. The lighter the green colour, the smaller the misorientation angle. This colouring method, along with the calcGrains function, was very successful at identifying low angle boundaries with small misorientations. The shape of low-angle boundaries and relation to external morphological features in BSE images were visually assessed to ensure that grains with low misorientations resulting from grain aggregation (Chapter 3) were not considered further (e.g., the boundaries between euhedral grains in Fig. 4.6d).

In order to assess the occurrence and character of lattice distortions, a definition of what constitutes a "distorted grain" is required. Such classifications are somewhat arbitrary, particularly based on optical observations (Sakyi et al., 2012; Vinet et al., 2011). Here, an olivine was classified as distorted if at least 1 low-angle boundary calculated using the

CalcGrains function stretching across approximately a third of the crystal was identified. The same detector resolution was used for all EBSD acquisitions, and pixel spacings were significantly smaller than the microstructure features of interest (3–10 µm vs. ∼100 µm), resulting in a consistent definition of a distorted crystal.

4.2.2 Comparison of Optical and EBSD Observations

To allow comparison between the definition of distortion used in this study, and previous observations in the literature which have predominantly relied on optical observations (Bradshaw et al., 2018, Helz, 1987, Vinet and Higgins, 2010), EBSD maps were collected for 20 grains within a ∼40 µm thick section produced from an epoxy stub. Low angle boundaries with misorientations <1° were extremely difficult to see even with a high specification optical microscope (Zeiss Axioscope A1; Figs. 4.1–4.4). Low-angle boundaries identified with EBSD were only visible optically when the crystal was within 2–4° of its extinction position. In particular, the ability to optically resolve subgrain boundaries depended on the sharpness of the misorientation contrast, and the orientation of the crystal within the thin section. In some instances, subgrain boundaries with misorientations up to 2.5° were invisible. In many cases, these features could only be seen if the brightness and contrast of the microscope image was adjusted. Based on the small subset of grains examined here, even if previous studies using optical microscopy examined each grain individually, and rotated it through 90° while adjusting the brightness and contrast, they may have underestimated the proportion of distorted grains by ∼45%. This observation is similar to the conclusions of Sakyi et al. (2012), who observe dislocation textures in optically undeformed grains.

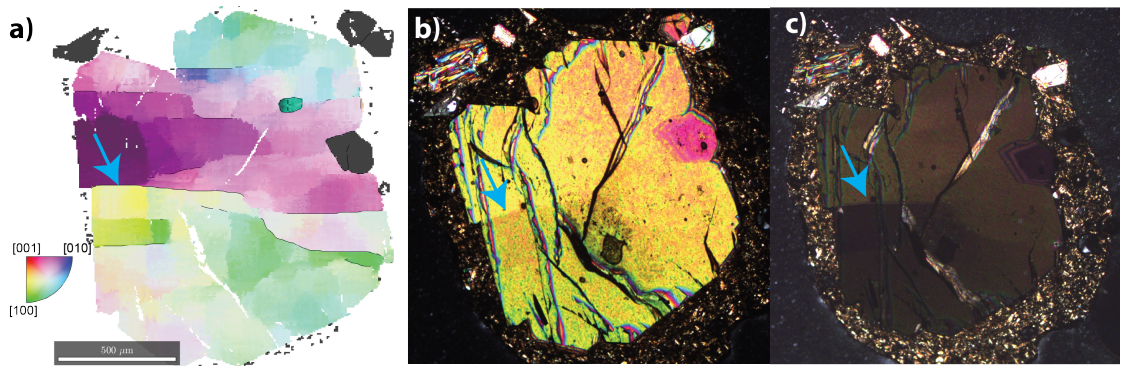


Figure 4.1: Comparisons of EBSD-derived IPF maps scaled to 2° (panel **a**) with photos taken using a high specification optical microscope (panels **b-c**) for grain IZ_592.

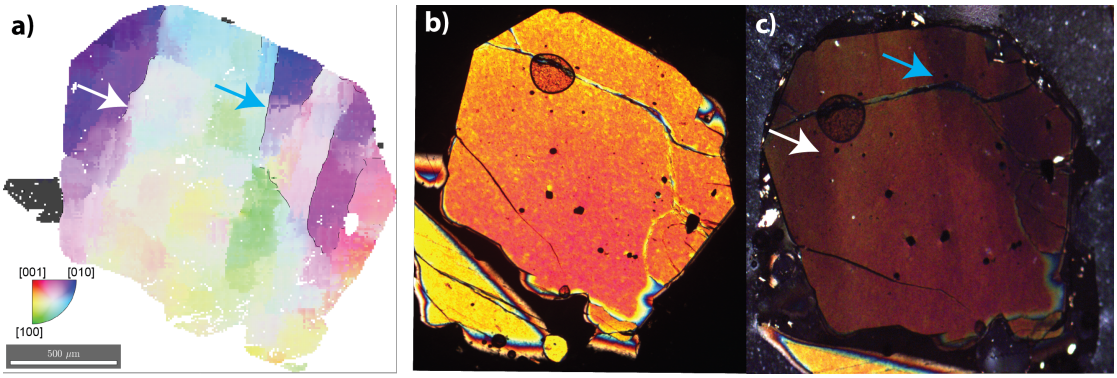


Figure 4.2: Comparisons of EBSD-derived IPF maps scaled to 2° (panel **a**) with photos taken using a high specification optical microscope (panels **b-c**) for grain IZ_574).

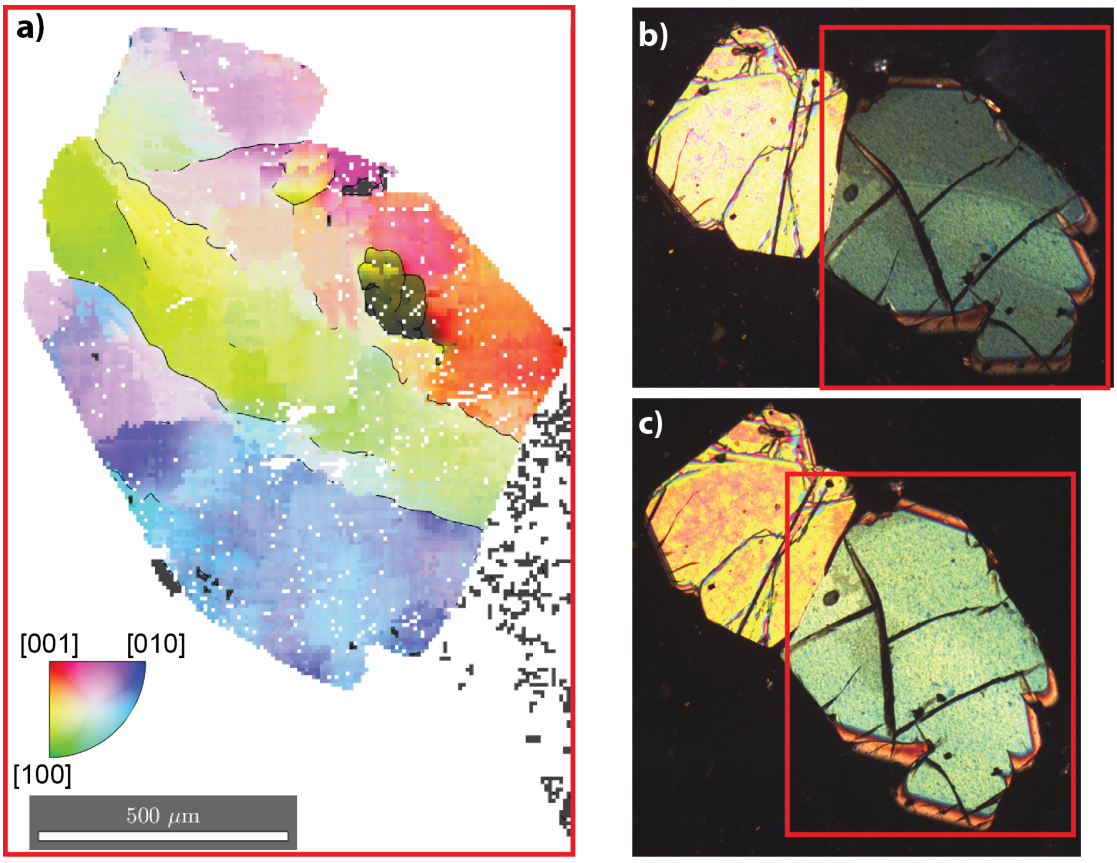


Figure 4.3: Comparisons of EBSD-derived IPF maps scaled to 2° (panel **a**) with photos taken using a high specification optical microscope (panels **b-c**) for grain IZ_571).

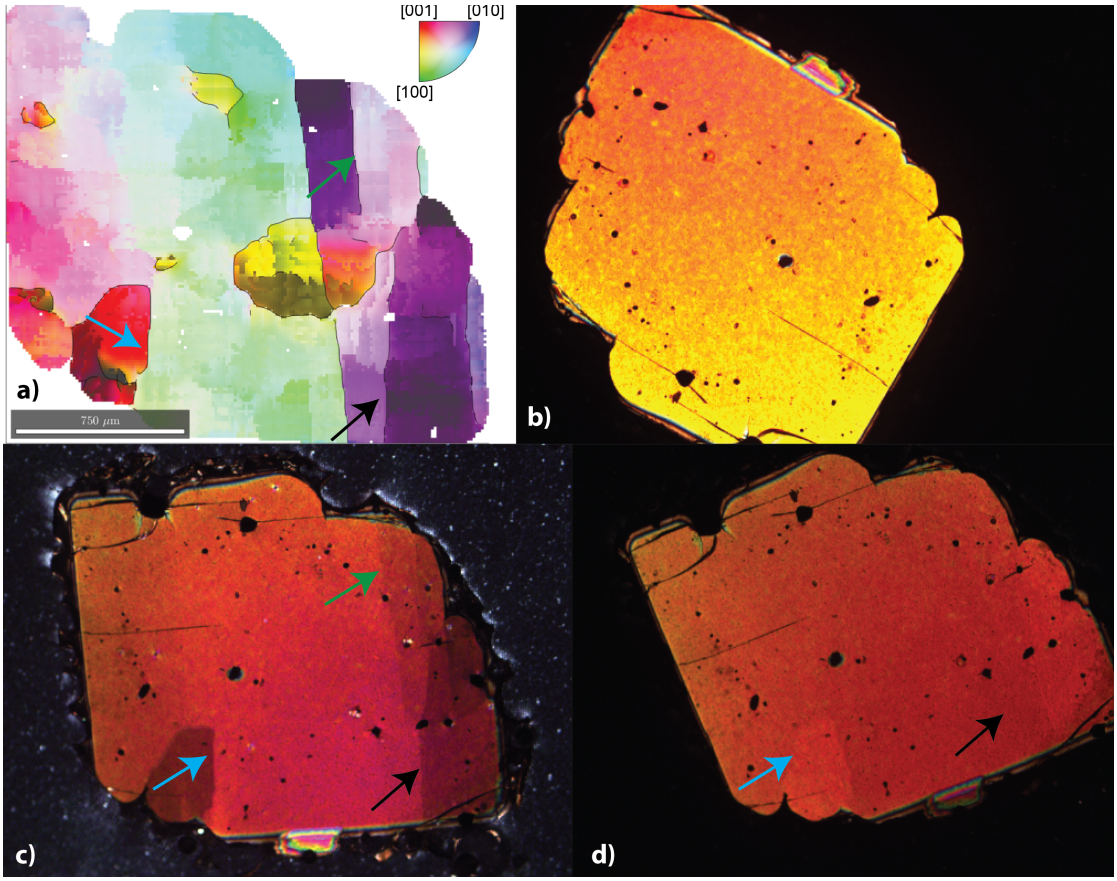


Figure 4.4: Comparisons of EBSD-derived IPF maps scaled to 2° (panel **a**) with photos taken using a high specification optical microscope (panels **b-c**) for grain IZ_573.

4.2.3 Slip System Identification

The dislocations present (and thus the dominant slip systems) within distorted olivine crystals were assessed using two metrics that can be obtained from EBSD maps; the misorientation across a boundary, and the Weighted Burgers Vector Direction (WBVD). The misorientation describes the axis-angle pair of the coordinate transform from the crystallographic orientation on one side of the boundary to that across the boundary. Misorientations are stated in terms of a misorientation axis and the minimum angle of rotation about this axis (Wheeler et al., 2001; Fig. 3.3). For example, a misorientation of 3° about [010] shows that the orientation of the crystal lattices of two adjacent subgrains can be superimposed by a rotation of 3° about the olivine b axis.

The Weighted Burgers Vector direction (WBVD) quantifies the weighted mean of the Burgers vectors of all types of geometrically necessary dislocation in a local region, assessed using 2D orientation gradients in EBSD maps (Wheeler et al., 2009). This is also expressed in terms of a crystallographic direction (e.g., [100]). The WBVD depends on the dislocation density for each type, and is weighted towards dislocation lines at a high angle to the map. Specifically, the WBVD samples the Burgers vectors of dislocations in low-angle

boundaries and cannot introduce any illusory directions which are not present in the actual microstructure. For discrete boundaries, the apparent dislocation density and hence the Weighted Burgers Vector magnitude depends on pixel spacing, but the WBVD does not, and provides sufficient crystallographic information to assess slip system occurrence.

Crucially, EBSD allow assessment of the misorientation and WBVDs for lots of neighbouring pixels along a given low angle boundary, and large numbers of individual low angle boundaries in relatively short acquisition times (15–20 minutes per grain), and processing times (∼2 minutes per grain). The large datasets generated using these methods are crucial for the precise characterisation of microstructures in volcanic olivines which show only subtle distortions.

4.3 Results and Discussion

4.3.1 Incidence of Lattice Distortions

Olivine crystals from a wide range of eruptions temporally associated with activity at Mauna Ulu (May 1969 to December 1974) were examined. During this five year period eruptions occurred almost simultaneously on the ERZ, summit and SWRZ (Fig. 4.5; Lockwood et al., 1999), providing a unique opportunity to decipher the spatial distribution of distorted olivines within a single eruptive period at Kīlauea. Additionally, two further SWRZ eruptions were investigated; the circumferential lava flow on the SSWRZ (∼1700; Lynn et al., 2017) and the Mauna Iki eruption on the VSWRZ (1919–1920; Rowland and Munro, 1993).

Optical observations have led to the suggestion that distorted olivines are reasonably rare in subaerial eruptions compared to submarine eruptions at Kīlauea (Clague and Denlinger, 1994, Garcia et al., 1996, Helz, 1987). However, in this study, EBSD reveals that abundant distorted grains are present in subaerially erupted products from all ERZ eruptions (Pauahi crater, Episode 1 and 12 of Mauna Ulu) and SSWRZ eruptions (∼1700, 1974; Fig. 4.5). Spatter from Mauna Iki on the VSWRZ also contains a significant number of distorted grains. In contrast, erupted products from four intracaldera summit eruptions and the 1971 VSWRZ eruption contain very few distorted grains. In almost all eruption products, distorted grains are more abundant in sieved fractions >1 mm (Sakyi et al., 2012; Fig. 4.5). Spatter from the 1971 VSWRZ eruption contain very few grains >1 mm (4 in ∼150 g), but all are distorted, whereas no grains <1 mm show distortion. Intracaldera summit eruptions (August, 1971, September 1971, July 1974, September 1974) contain no grains >1 mm, but all distorted grains are >840 µm.

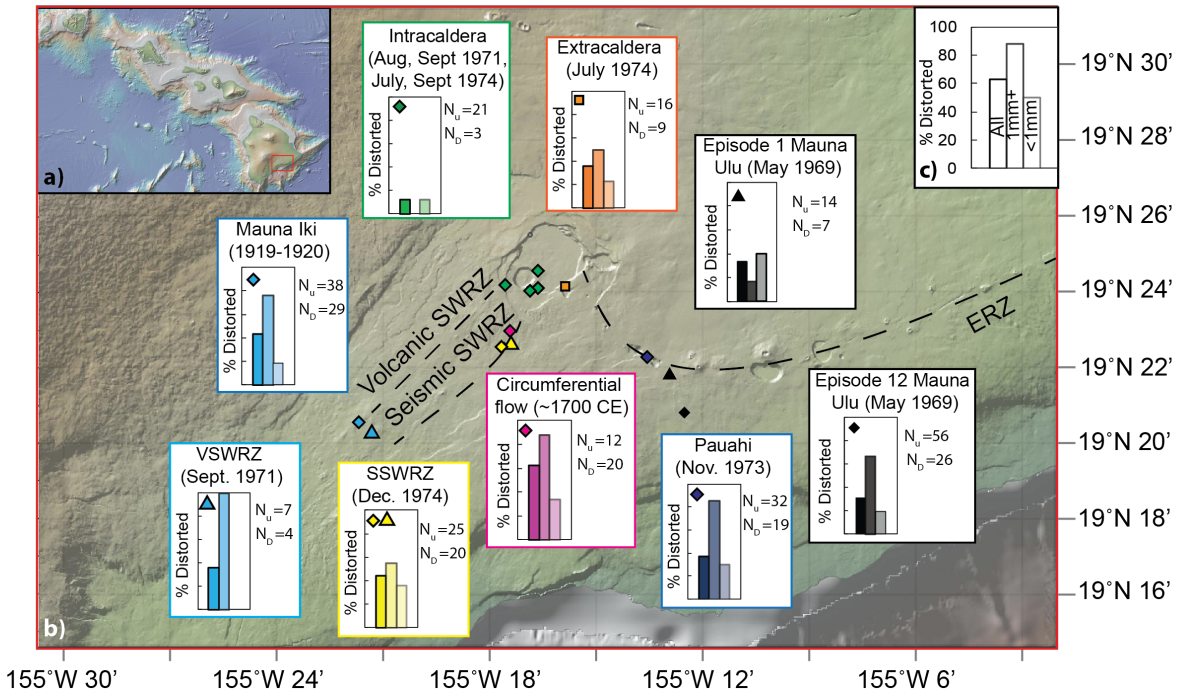
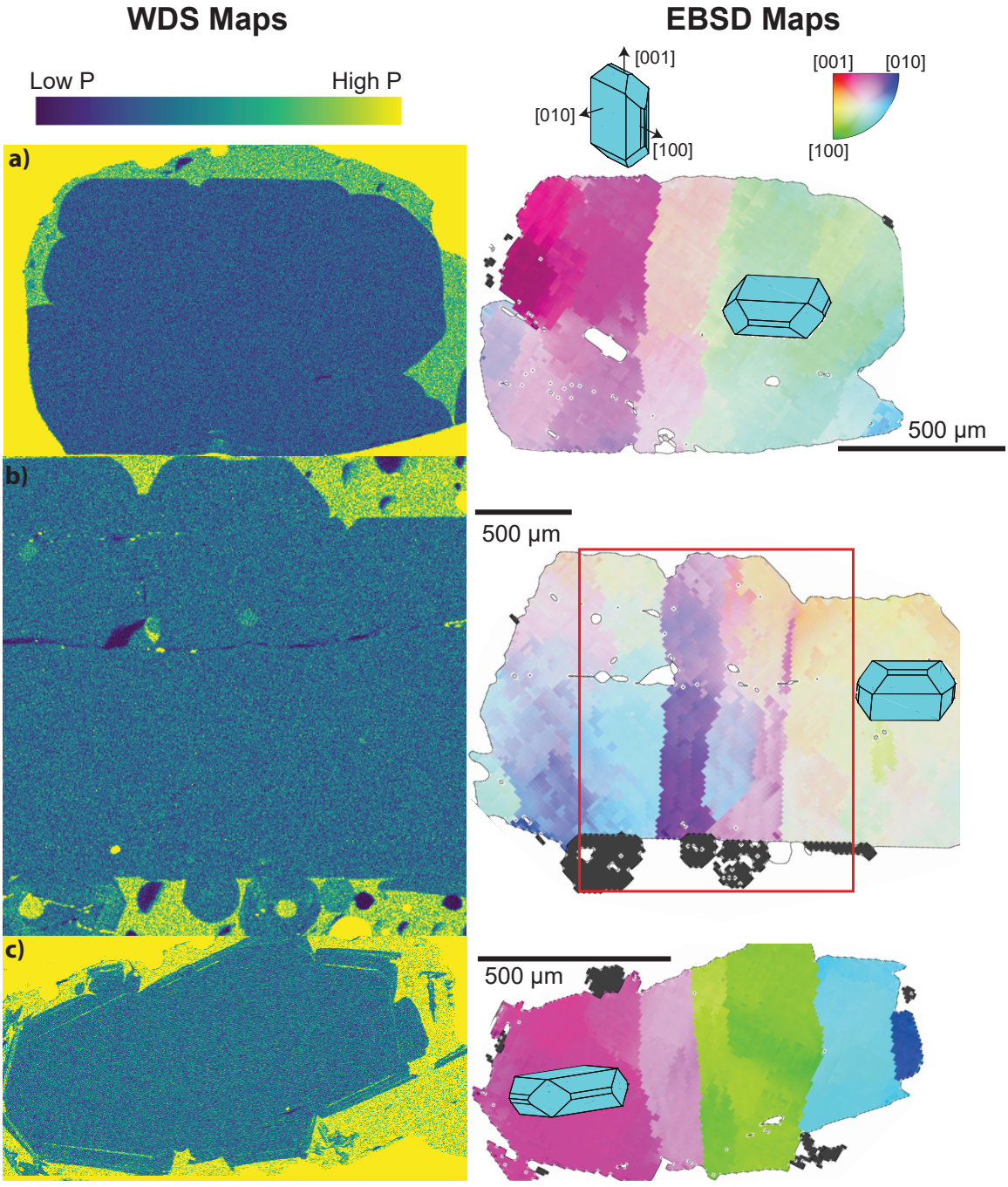


Figure 4.5: a) Topographic map of the Hawaiian Islands, with the red rectangle showing the location of Kīlauea Volcano on the island of Hawai'i (expanded in **b**). **b)** Expanded map of Kīlauea Volcano, with coloured symbols showing the location of eruption deposits examined in this study (symbol colours and shapes are the same as those used in Fig. 4.9). The East Rift Zone (ERZ), and volcanic and seismic strand of the South West Rift Zone (VSWRZ and SSWRZ respectively) are shown with black dashed lines. **c)** Schematic histogram representing the proportion of distorted grains in 3 size categories (all grains, grains >1 mm and <1 mm based on sieved size fractions). For each eruption site, a coloured histogram following this schematic shows the proportion of distorted grains in each size category. The number of distorted (N_D) and undistorted (N_U) grains is also shown, along with the symbol used on the basemap. Basemap from GeoMapApp (Ryan et al., 2009), showing the topography of Kīlauea before the onset of the 2018 summit collapse.

4.3.2 Evaluating the Dendritic Growth Hypothesis

First, the hypothesis that lattice distortions are produced during an early phase of branching dendritic growth, followed by textural re-equilibration during periods of reduced undercooling, was assessed (Welsch et al., 2012). Due to a change in olivine-melt partitioning during rapid dendritic growth, high concentrations of phosphorous (P) are incorporated into the crystal structure (Shea et al., 2019). While the external morphology of dendritic crystals evolves during subsequent textural re-equilibration to obscure this early growth phase, slow diffusion rates preserve internal P enrichments (Spandler et al., 2007). The presence of P-rich zones passing across extinction discontinuities is one of the main lines of evidence supporting the dendritic growth hypothesis (Welsch et al., 2012; Welsch et al., 2014). However, wavelength-dispersive spectroscopy (WDS) maps collected by electron microprobe reveal homogenous cores within almost all distorted grains (Fig. 4.6). Similar findings

have been reported for olivines from Kīlauea Iki (Bradshaw et al., 2018). One P-rich zone terminates against a subgrain boundary (Fig. 4.6d), suggesting that P enrichments and subgrains did not form during the common process of dendritic growth. Instead, the rapid growth episode generating the P zoning may have preceded the distortion of the crystal lattice, perhaps separated by a dissolution episode (c.f., Welsch et al., 2012). Thus, while some olivines at Kīlauea may have experienced an early dendritic growth phase, this process appears unrelated to the production of lattice distortions.



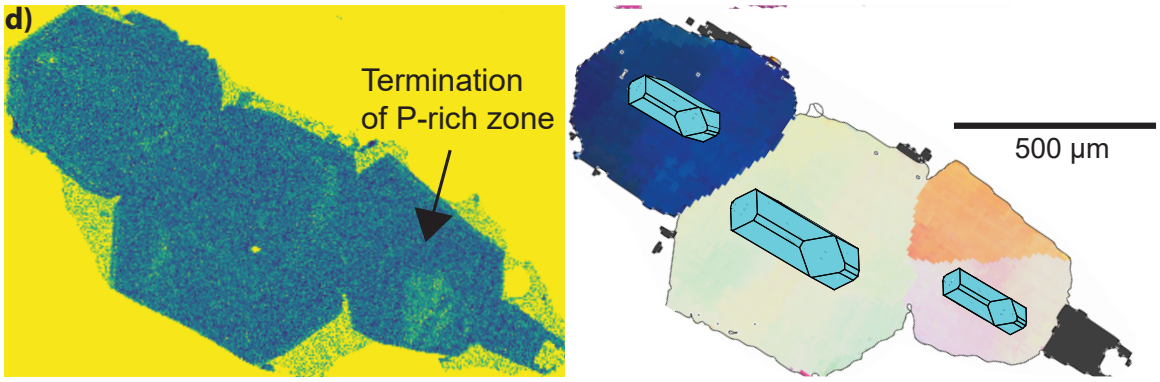


Figure 4.6: Relationship between minor element enrichments and lattice distortions. WDS maps of P enrichment compared to EBSD maps coloured with an IPF key scaled to 3°. Light blue 3D olivine crystals are superimposed (using the MTEX crystalShape package) to allow visualization of the orientation of the three crystallographic axes ([100], [010], and [001]). **a-c)** Grains with internal lattice distortions (revealed by stripes of different colours in EBSD maps) have homogeneous concentrations of P in their cores (see WDS maps). Observed P enrichments in the rim of the crystal shown in **c)** mark a period of rapid growth upon eruption. **d)** Internal P enrichments are truncated against a subgrain boundary. WDS elemental maps are coloured by the number of counts per pixel (in ImageJ).

Furthermore, if distorted olivines represent texturally-matured dendrites, the crystallographic signatures of dendritic growth and lattice distortion should be identical. Low-angle subgrain boundaries were examined in 137 distorted olivine crystals from Kīlauea, and compared to the crystallographic signature of dendritic branching in 61 olivine dendrites from West Greenland (Larsen and Pedersen, 2000). Most branching dendritic buds in the West Greenland olivines show identical crystallographic orientations to the primary crystal; merging of such buds cannot produce lattice distortions. The 125 misorientated crystal buds show a bimodal distribution of misorientation axes, with a strong maximum around [010] and a weaker maximum around [100] (Fig. 4.7c; Donaldson, 1976). Misorientation angles are predominantly <20°, but extend up to 90.5° (Fig. 4.7d). In contrast, lattice distortions in Kīlauean olivines show misorientation axes predominantly between [010] and [100] (Fig. 4.8c), and small (<5°) misorientation angles. The boundary between dendritic buds and the host crystal display [010] and [001] WBVDs (Fig. 4.7b), while lattice distortions show predominantly [100] WBVDs, with some [001] vectors (Fig. 4.8b). Finally, the interior of dendritic olivines display no low-angle boundaries with [100] or [001] Burgers vectors.

These crystallographic differences imply that lattice distortions are not produced by textural maturation of olivine dendrites. Instead, the misorientation axes and WBVDs in distorted olivines are indicative of slip systems similar to those invoked to cause CPOs in olivine deformation experiments at conditions resembling Kīlauea's plumbing system (>1000°C, relatively low stresses and water contents; Bai and Kohlstedt, 1992). Crucially, in contrast to olivine dendrites, Kīlauean olivines exhibit very few [010] WBVDs. This is consistent with experimental observations that slip on [010] is unusual due to the long

length of the b lattice vector (Boioli et al., 2015). Thus, lattice distortions likely represent true deformation of the crystal lattice, rather than growth features.

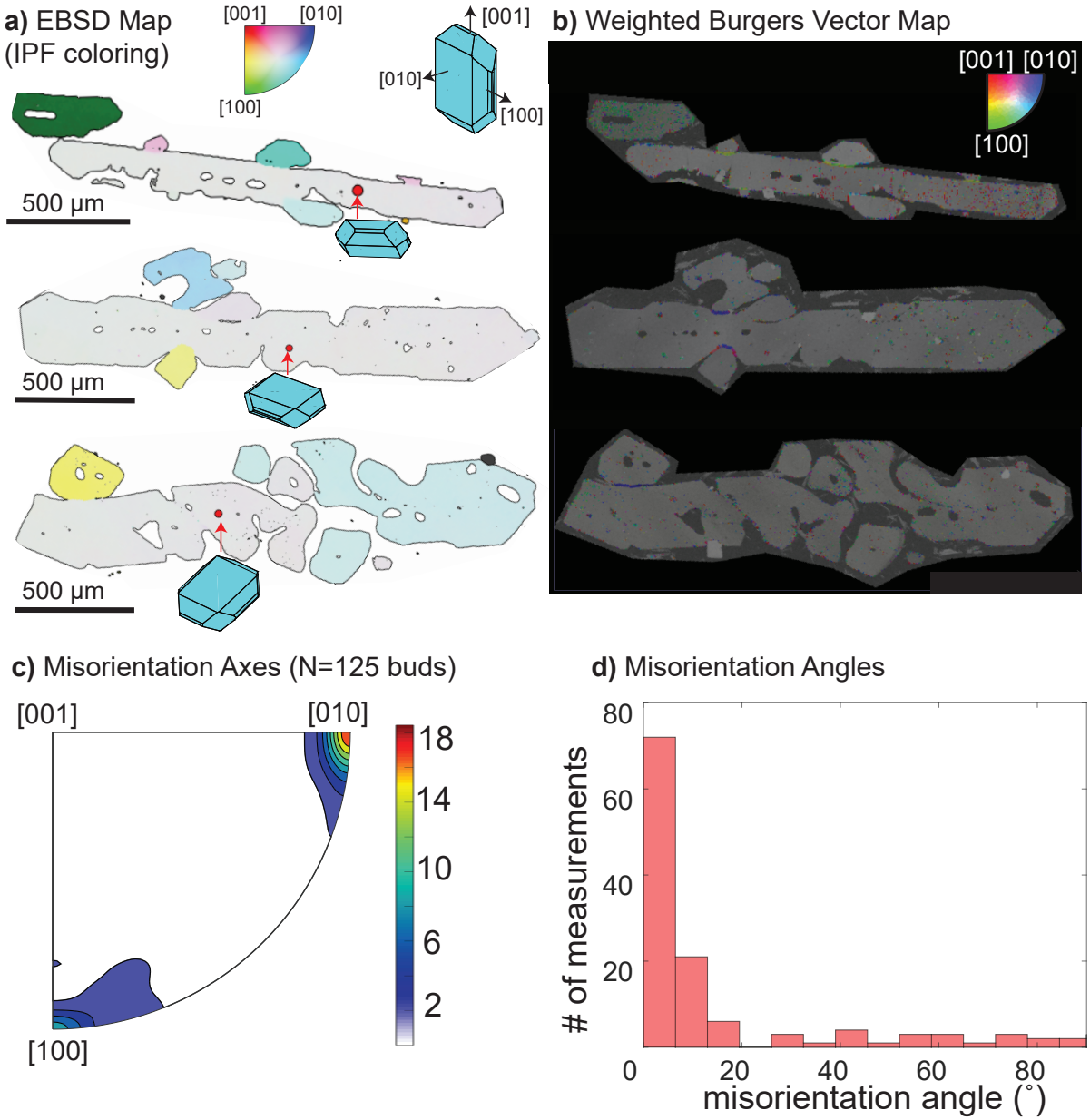


Figure 4.7: Crystallographic signatures of olivine dendrites from West Greenland Picrites. **a)** EBSD maps coloured using the IPF key scaled to 20° to emphasize the larger range of misorientation angles in branching dendrites compared with the distorted olivines in Fig. 4.6. 3D olivine crystals are overlain to allow visualization of the orientation of the dendritic olivines with respect to the three crystallographic directions of olivine. **b)** Weighted Burgers Vector directions (WBVDs) overlain on band contrast maps ([100]=green, [010]=blue, [001]=red]). Scale for both images shown on EBSD map. **c)** Misorientation axes for 125 dendritic buds from West Greenland picrites (misorientation angle >1°). The colour scale has units of 'multiples of uniform distribution'. **d)** Histogram of misorientation angles between adjacent dendrite buds. 70% of dendritic buds are misoriented from the host crystal by >5°.

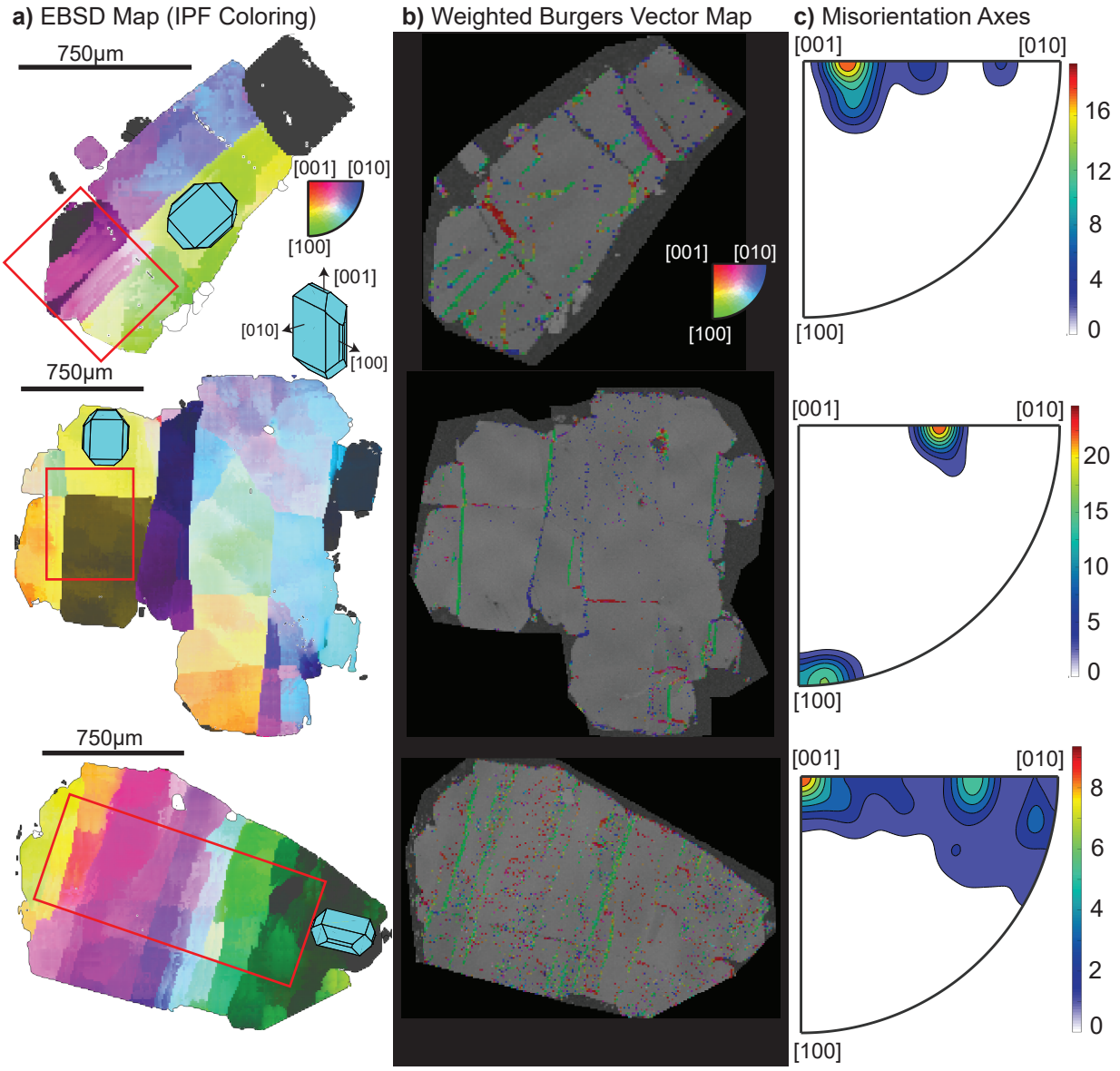


Figure 4.8: Crystallographic signatures of lattice distortions within Kīlauean olivines. **a)** EBSD maps coloured using the IPF key as in Fig. 4.6 (scaled to 3°). 3D olivine shapes are overlain to demonstrate the average orientation of the olivine crystal with respect to the three crystallographic axes. **b)** Weighted Burgers Vector directions (WBVDs) overlain on band contrast maps ([100]=green, [010]=blue, [001]=red]). Scale for both images shown on EBSD map. **c)** Misorientation axes across subgrain boundaries located within the red box indicated in column **a)**. The colour scale has units of 'multiples of uniform distribution'. Subgrain boundaries with [100] WBVDs (green) show misorientation axes between [001] and [010]. Subgrain boundaries with [001] WBVDs (red) show misorientation axes about [100] or [010].

4.3.3 Collisions of Crystals

The indistinguishable major element chemistry of deformed and undeformed grains (Garcia et al., 1996; Helz, 1987), along with euhedral grain outlines, has led to suggestions that deformation results from grain collisions during magma flow through constricted conduits

(Natland, 2003, Wilkinson and Hensel, 1988). However, deformed grains examined in this study have higher forsterite contents than undeformed grains (Fig. 4.9a-b), with statistically significant differences for individual eruptions ($p<0.01$, Kolmogorov-Smirnov test, Fig. 4.9c-f). Within each run, deformed and undeformed grains from each eruption were analysed in roughly equal proportions, so chemical differences between deformed and undeformed grains cannot be attributed to slight variations between analytical sessions.

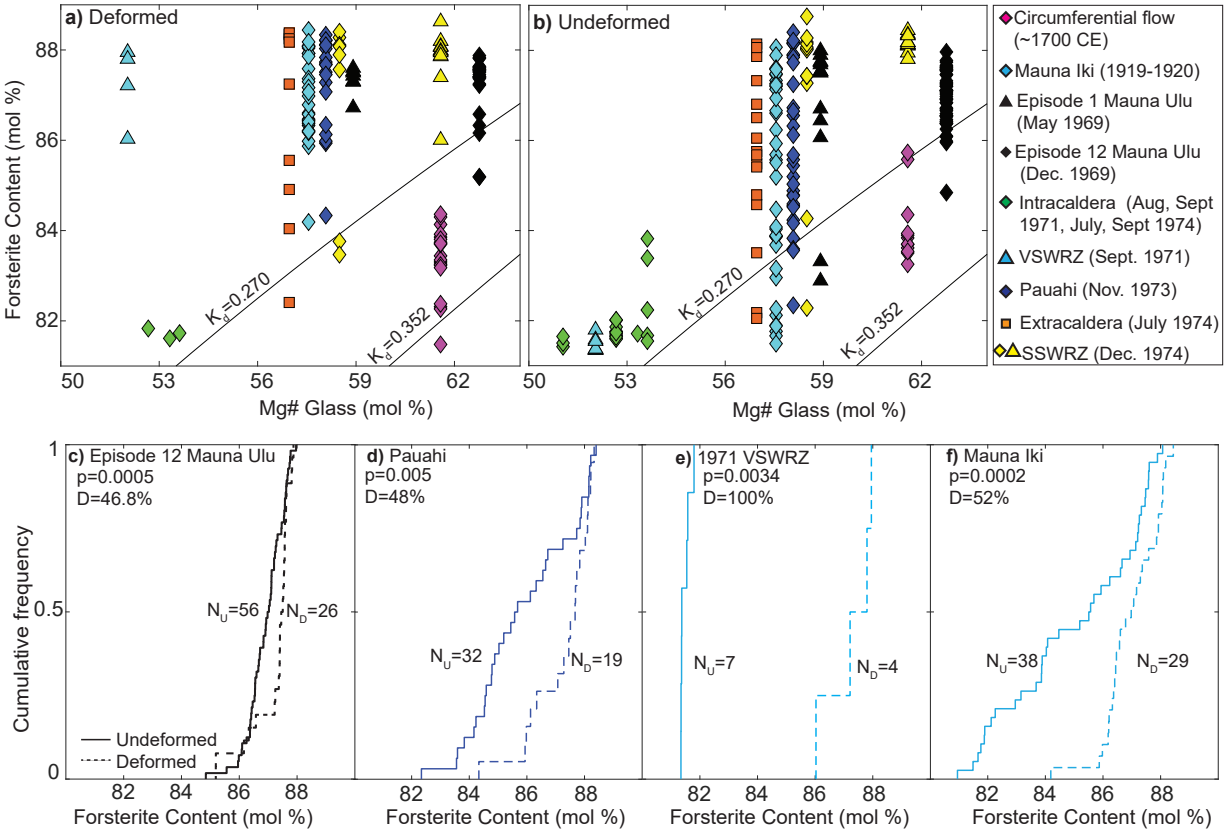


Figure 4.9: Chemical differences between deformed and undeformed Kīlauean olivine grains. **a-b)** Olivine forsterite contents (mol %) versus matrix glass Mg# (Fe^{3+}/Fe_T=0.15; ~QFM; Moussallam et al., 2016). Olivine-liquid equilibrium lines are shown for $K_D^{Mg-Fe^{2+}}$=0.270–0.352 (Matzen et al., 2011, Roeder and Emslie, 1970; hereafter abbreviated as K_D). Both deformed and undeformed grains have higher forsterite contents than the equilibrium olivine composition of their matrix glasses. However, deformed grains show a narrower range of forsterite contents, which lie further from the equilibrium field than undeformed grains. **c–f)** Cumulative distribution functions comparing undeformed (solid lines) and deformed (dashed lines) olivines for 4 eruptions. Deformed grains are more primitive at a statistically significant level ($p<0.01$) using the two sample Kolmogorov-Smirnov test. The test statistic D quantifying the distance between the two distributions is also shown.

Differences in minor element compositions have also been reported for deformed and undeformed grains erupted at Kīlauea Iki (Bradshaw et al., 2018). Finally, deformed olivines in different eruptions have similar forsterite contents, which are significantly out of equilibrium with their matrix glasses. In contrast, undeformed olivines show more chemical

variability, and many plot closer to the equilibrium composition (Fig. 4.9a-b). These observations cannot be reconciled with late stage crystal-crystal collisions, which would result in deformed and undeformed grains having indistinguishable chemistry (Bradshaw et al., 2018), and the same degree of disequilibrium with co-erupted matrix glasses.

4.3.4 Generating Differential Stresses within Volcanic Plumbing Systems

The majority of deformed olivines sampled at the Earth's surface are derived from mantle peridotites. However, deformed Kīlauean olivines are unlikely to be mantle xenocrysts for two principal reasons. Firstly, almost all deformed Kīlauean olivines have high CaO contents (>0.2 wt%), while the deformed olivines in mantle peridotites and plutonic rocks typically have <0.1 wt% CaO (Clague and Denlinger, 1994, Thompson and Gibson, 2000; Fig. 4.10a). Secondly, many deformed Kīlauean olivines have inclusions of melt and euhedral spinels, indicating growth within the volcanic system (Sakyi et al., 2012; Vinet and Higgins, 2010). These observations suggest that these olivines grew, and were subsequently deformed within Kīlauea's plumbing system.

To generate lattice distortions, crystals must be subject to non-hydrostatic stress (Helz, 1987). Previously, olivine deformation has been attributed to differential stresses exerted within Kīlauea's deep rift zone dunites, during the downward flow of olivine from the summit area to the rift zones, or rapid rift zone extension during south flank earthquakes (Clague and Denlinger, 1994). However, mechanisms involving deep rift zone processes require specific magma transport paths to bring deformed crystals to the surface. For example, the presence of deformed grains in lavas from the Mauna Ulu eruption has led to suggestions that magma is transported along the basal decollement (Vinet and Higgins, 2010). However, significant magma transport through the deep rift zones is at odds with geophysical observations, which demonstrate no measurable changes in rift zone opening rates during magma supply surges or rift zone eruptions (Poland et al., 2015) and generally support shallow (<2 km) magma transport (Montgomery-Brown et al., 2011). Given the wide spatial and temporal distribution of deformed grains identified in this study, it seems untenable that every eruption received a significant contribution to its olivine crystal cargo from deep rift zone transport paths.

The textural features of deformed olivines are also inconsistent with an origin from low melt fraction dunites (<5 % melt; Clague and Denlinger, 1994). Olivines derived from such bodies would be expected to show adcumulate textures similar to those found in xenoliths erupted at Kīlauea Iki (Helz, 1987) and post-shield Hawaiian lavas (Kirby and Green, 1980). Instead, most distorted grains have subhedral-euhedral outlines with no internal melt films and high angle grain boundaries (Fig. 4.8). While corrosion followed by overgrowth can produce euhedral crystals from disaggregated dunites (Boudier, 1991), this process would preserve internal melt films.

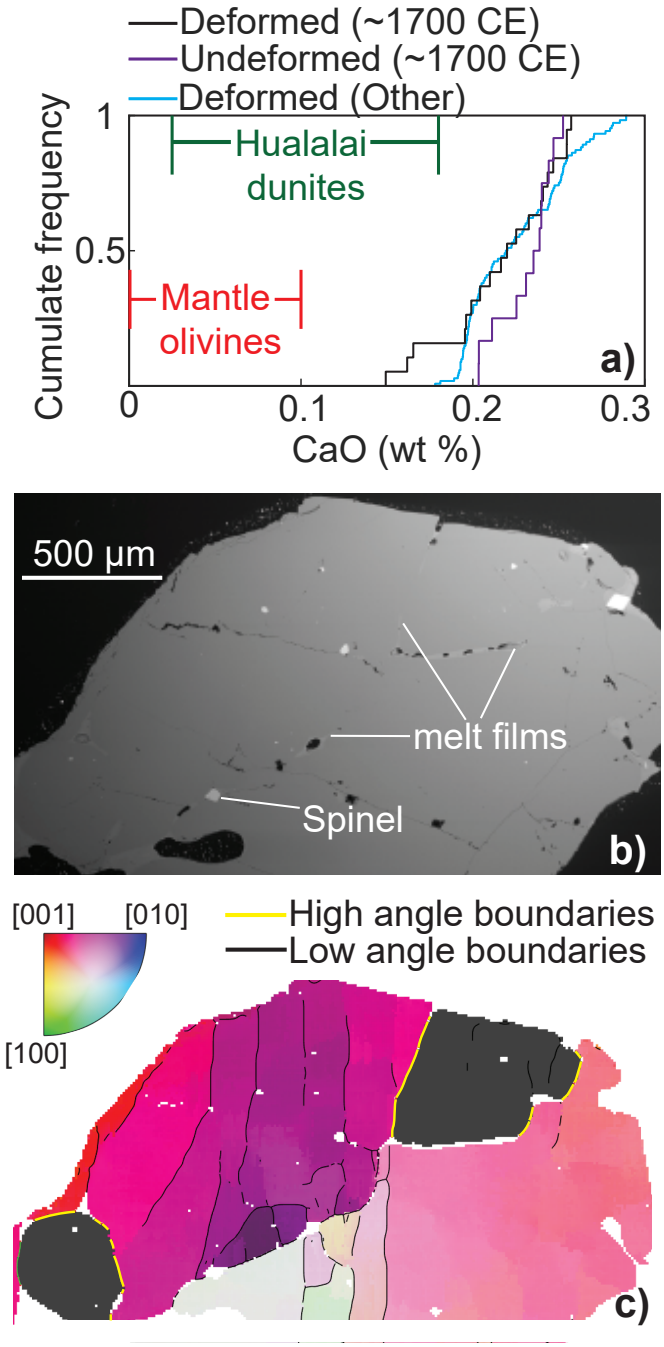


Figure 4.10: Textural and chemical evolution during downslope flow. **a)** CaO contents of deformed Kīlauean olivines (excluding the ~1700 lava flow) plot well outside the field for mantle olivines (Thompson and Gibson, 2000), and have substantially higher CaO contents than olivines from Hualalai dunites (Clague and Denlinger, 1994). Some deformed olivines from ~1700 have lower CaO contents than undeformed olivines in this sample. In fact, three deformed olivines fall within the field of Hualalai dunites. **b)** Backscatter electron image showing prominent melt films along high angle boundaries (yellow lines in **c**) in the interior of a deformed crystal from the ~1700 eruption. **c)** EBSD map coloured with the IPF colour key scaled to 10° about the mean orientation of the central grain. High angle boundaries (misorientation angle >10°) are coloured yellow, and low angle boundaries (misorientation angle <10°) are coloured black. Scale for both images shown on the backscatter image.

A crucial observation is the fact that deformed olivines have been noted in a variety of basaltic systems. Vinet et al. (2015) report their presence in all five of the volcanic centres which they examined in the Andean Southern Volcanic Zone. Deformed olivines have also been noted in the Vaigat formation of West Greenland (Larsen and Pedersen, 2000), the Baffin Bay volcanic province (Francis, 1985), Piton de la Fournaise volcano (Welsch et al., 2012), and the Loch Uisg area, Mull (Westland, 2014). This implies that olivines are deformed by a process which is near-ubiquitous in a wide range of volcanic plumbing systems. One plausible mechanism is gravitational loading within melt-rich cumulate piles with ~40% porosity (Hughes, 2013) produced by crystal settling (Thomson

and Maclennan, 2012). Such an origin accounts for the global distribution of deformed grains, and the absence of adcumulate textures at Kīlauea. To investigate this hypothesis, further constraints were placed on the conditions under which olivines were deformed by classifying the dominant slip systems present in low-angle boundaries.

4.3.5 Assessing the Conditions of Deformation

Dominant slip systems in low-angle subgrain boundaries were identified using misorientation axes, Weighted Burgers Vector directions (WBVDs), and boundary wall geometries extracted from EBSD maps. A new classification algorithm was developed in MTEX v5.0.4 (Bachmann et al., 2010), incorporating WBVD calculations from CrystalScape (Wheeler et al., 2009). Firstly, misorientation axes were calculated for boundary segments with misorientation angles between 0.5–10°. Boundaries were classified as twist walls if they met the following criteria:

(a) Angle between the misorientation axis and the z direction in specimen coordinates >15°

(b) Angle between the misorientation axis and the grain boundary trace in specimen coordinates >75°

Criteria a) accounts for the fact that boundaries with low dips are unlikely to be observed (Wheeler et al., 2009). Crucially, this rules out misidentification of a tilt boundary orientated such that the misorientation axis is near vertical as a twist wall. The second criteria accounts for the theoretical geometry of a twist wall (Fig. 4.11b), where the misorientation axis is perpendicular to the boundary trace (allowing for 15° leniency). Boundaries were classified as tilt walls if:

c) the boundary was not classified as a twist wall

d) the normal to the plane containing the grain boundary trace and misorientation axis (i.e., the normal to the tilt boundary plane) in specimen coordinates was >15° from the z direction (discarding boundaries with low dips).

For example, boundary pixels within the pink rectangle (Fig. 4.11c) meet criteria b) but not a), as the misorientation axes are nearly vertical (blue dots; Fig. 4.11d). Thus, boundary pixels were classified as a tilt walls, as they met condition c) and condition d). This tilt wall is orientated with a near vertical boundary plane and misorientation axis.

This approach resolves the ambiguities involved when using misorientation axes alone to determine slip systems (Cao et al., 2015). For example, tilt walls consisting of (100)[001] or (001)[100] edge dislocations (described in terms of (slip plane)[Burgers Vector]) and twist walls consisting of (010)[100] and (010)[001] screw dislocations all produce misorientation axes about [010].

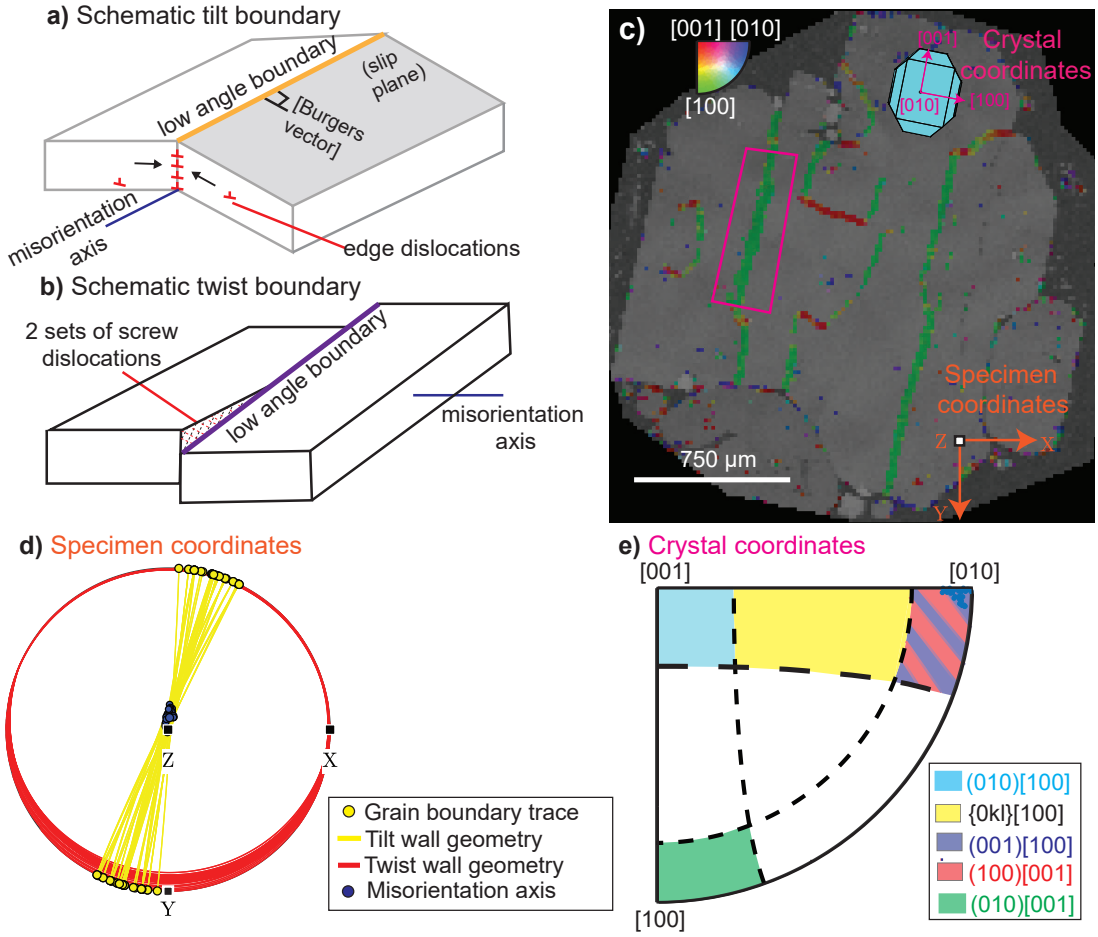


Figure 4.11: Slip system identification method. **a)** A schematic diagram of a tilt boundary, where the misorientation axis lies within the plane of the low angle boundary. **b)** A schematic diagram of a twist boundary, where the boundary plane is perpendicular to the misorientation axis. Two sets of screw dislocations are shown within the twist wall for illustrative purposes; this is just one possible geometry. **c)** Map of Weighted Burgers Vector directions (WBVDs) in a deformed olivine. Specimen coordinates (orange arrows) represent the x, y, and z directions within the SEM. Crystal coordinates (pink arrows) represent the directions of the [100], [010], and [001] axes of the olivine. A 3D olivine crystal is overlain to demonstrate the orientation of the crystal in crystal co-ordinates. Boundaries with [100] WBVDs are almost parallel to the y direction, while those with [001] WBVDs are almost parallel to the x direction in specimen coordinates. A small section of a [100] WBVD boundary is selected for further discussion (pink rectangle). **d)** Ideal tilt (yellow) and twist (red) boundaries calculated for each boundary segment in the pink rectangle based on the trace of the subgrain boundary and direction of the misorientation axis (in specimen coordinates). As the calculated twist wall planes show extremely low dips, the MTEX code classifies all segments along this boundary as tilt walls. **e)** Schematic diagram showing the misorientation axes in crystal coordinates for tilt boundaries built from dislocations types associated with each of the 5 olivine slip systems, written as (slip plane)[Burgers vector], allowing 20° leniency. Misorientation axes of the boundary pixels within the pink rectangle plot near [010]. Along with the [100] WBVDs, this indicates that this tilt wall consists of (001)[100] dislocations.

However, WBVDs (which can be highlighted by colour coding of EBSD maps; e.g., Fig. 4.8, 4.11c) can distinguish between these three boundary types: (100)[001] tilt walls would show [001] WBVDs (red), (001)[100] tilt walls would show [100] WBVDs (green), and twist walls would show mixes of [100] and [001] WBVDs (green via yellow to red). The geometry of the subgrain boundary provides further discriminatory power. Tilt walls contain the misorientation axis within the boundary plane, while twist wall boundary planes are perpendicular to the misorientation axis (Fig. 4.11a-b). For simplicity, it was assumed that subgrain boundaries showed pure tilt or twist character. Within a single grain, tilt boundaries with a given WBVD displayed a narrow range of boundary traces (Fig. 4.11c), allowing isolation of tilt boundaries with [100] and [001] WBVD. For boundaries displaying each WBVD, the direction of the misorientation axis for each boundary segment was compared to the misorientation axis (in crystal coordinates) expected for each slip system (Fig. 4.11e). Slip system proportions were calculated in two ways; by summing the total length of each boundary type, and by calculating the proportion of each boundary type in a single grain, and averaging these values (N=62 grains, Fig. 4.12a).

Approximately 83% and 17% of boundaries were classified as tilt and twist walls respectively, so slip systems proportions were quantitatively assessed in the more prevalent (and geometrically simple) tilt walls. The observed prevalence of tilt walls is consistent with literature observations that olivine subgrain walls with [100] WBVDs tend to have edge character (Boioli et al., 2015), and the fact that the majority of WBVDs are [100] or [001] (Fig. 4.8, 4.11c), rather than mixed directions (e.g., a WBVD parallel to [101] would appear yellow). Boundaries related to (010)[100], {0kl}[100] and (001)[100] slip comprised ∼30%, ∼44% and ∼16% of the total length of tilt boundaries respectively (Fig. 4.12a). These findings imply that [100] slip systems represent the primary slip systems, with the mosaicity of crystallographic orientation in some olivine grains (Fig. 4.8) resulting from secondary (100)[001] and (010)[001] slip (∼6% and ∼3% of boundaries respectively; Fig. 4.12a).

Experimental work shows that (010)[100] slip, producing A-type fabrics in deformed mantle peridotites, dominates in hot, dry, low stress environments (Zhang and Karato, 1995). Slip on (001)[100], producing E-type fabrics, occurs at similar pressure, temperature and stress conditions to A-type fabrics, but is favoured by a higher water content (Fig. 4.12c; Katayama et al., 2004). The strengths of these two slip systems are comparable at pressures of 300 MPa, and olivine water contents of ∼200 $H/10^6Si_{molar}$ (Katayama et al., 2004). The conditions producing D-type fabrics are debated, they may involve high stresses, low temperatures and low water contents favouring slip on {0kl}[100] (Ave'Lallemant and Carter, 1970, Jung and Karato, 2001). Alternatively, crystallographic signatures indicative of {0kl}[100] slip may be produced when (010)[100] and (001)[100] edge dislocations are present within a single subgrain boundary (Hansen et al., 2014). Overall, the dominance of slip systems with [100] WBVDs in Kīlauean olivines is indicative of deformation at

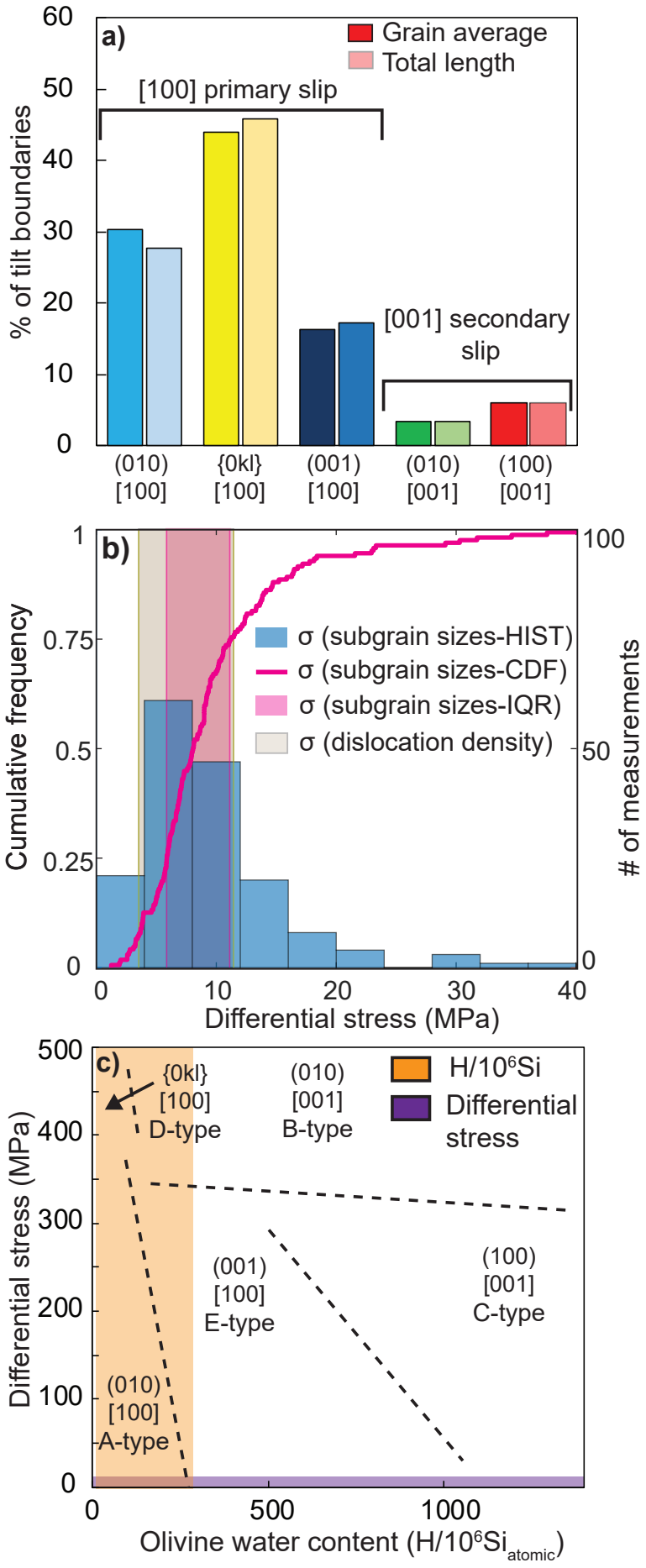


Figure 4.12: Quantifying the conditions of deformation. **a)** Proportions of each slip system calculated by averaging the proportion of each slip system per grain (darker colours; giving equal weight to all grains regardless of their size), and by summing the total length of each boundary type in 62 deformed grains (lighter colours). All deformed grains exhibit low-angle boundaries with [100] Weighted Burgers Vector directions (WBVDs), suggesting that this is the primary slip direction. Only a subset of grains contain low angle boundaries with [001] WBVDs, suggesting that this is a secondary slip direction. **b)** Differential stresses calculated using subgrain piezometery (Toriumi, 1979) applied to linear intercept distances clearly overlap with those estimated from dislocation density piezometery (Bai and Kohlstedt, 1992) on published dislocation densities (Sakyi et al., 2012). Differential stress estimates are shown as a cumulative density function (CDF–magenta) with the interquartile range (IQR-light pink), and as a histogram (darker blue). **c)** Olivine regime diagram (Jung et al., 2006) for T=1470–1570 K with subgrain stress estimates (purple bar) and olivine water contents (orange bar) superimposed.

moderate-high temperatures and low-moderate water contents (Fig. 4.12a, c). To further constrain the deformation conditions, and assess the origin of {0kl}[100] slip, independent constraints were placed on differential stresses and olivine water contents.

Differential stresses were estimated using subgrain and dislocation density piezometry. As both methods apply to steady state microstructures, they likely represent minimum stress estimates. Subgrain piezometry utilizes the empirical relationship between subgrain-size (d) and differential stress (σ; Toriumi, 1979):

$$\sigma = \frac{45\mu b}{d} \tag{4.1}$$

where μ is the shear modulus (65×10^9 Pa), b is the magnitude of the Burgers vector (5×10^{-10} m) and d is the distance between subgrain boundaries in m.

Subgrain sizes were assessed using an adapted linear intercept method suitable for EBSD maps of individual olivines. The distances between boundaries with [100] WBVDs and misorientations >0.5° were measured perpendicular to the mean boundary trace (Figs. 4.13), rather than along predefined directions in specimen coordinates (c.f. Hansen and Warren, 2015). Additionally, distances between the outermost subgrain boundary and the edges of the crystal were not used, as this distance depends on the amount of crystal preserved during jaw crushing, and the extent of crystal growth following entrainment into erupting magmas. It was decided that sectioning effects were negligible compared to the uncertainty stemming from different parameterizations of the relationship between subgrain size and differential stresses (Hansen and Warren, 2015). Subgrain sizes were converted into estimates of differential stress using equation 4.1. Subgrain differential stress estimates show a prominent peak at ∼3–12 MPa, with 95% of the stresses lying between ∼3 and 30 MPa (Fig. 4.12b).

Dislocation-density piezometry utilizes the relationship between dislocation densities (ρ) and differential stress (σ; Bai and Kohlstedt, 1992):

$$\sigma = \sqrt[s]{\frac{pb^2}{B}} \times \mu \tag{4.2}$$

Where B=1.74×10^{-3} and s=1.37.

Sakyi et al. (2012) report dislocation densities measured using the oxidative decoration technique in a variety of picritic basalts from Kīlauea and Mauna Loa (including some from Mauna Ulu). While they do not report dislocation densities for specific eruptions, their textural descriptions of "blocky olivines" are very similar to observations of distorted grains examined in this study. Blocky olivines have dislocation densities of 1–5 x 10^{10} m^{-2}, yielding differential stress estimates of ∼4–11 MPa. Despite estimates pertaining to different samples, and the large uncertainties associated with each method, stress estimates from subgrain piezometry and dislocation densities are in close agreement (Fig. 4.12b). Olivine water contents of $H/10^6Si_{molar}$ = 20–280 were calculated from H_2O measurements in olivine-hosted

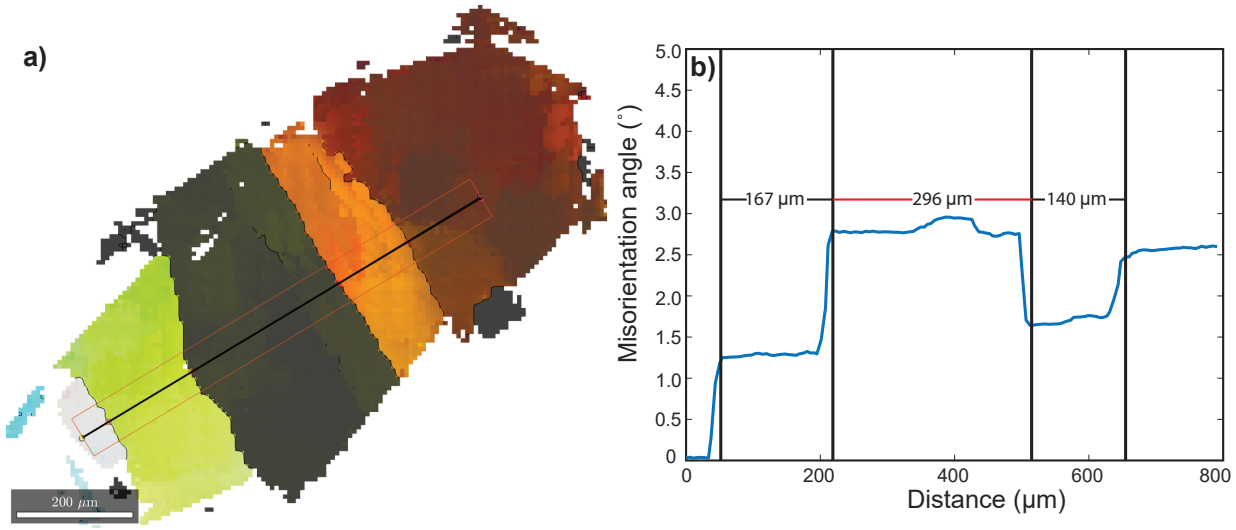


Figure 4.13: Example of the linear intercept method. **a)** The black line on the IPF-coloured EBSD map denotes the user-selected profile perpendicular to the trace of subgrain boundaries. **b)** Misorientations along the profile, averaged laterally over 5 pixels either side of the profile line to remove noise (red rectangle; code adapted from `https://gist.github.com/kilir/410bab7e3e2777200c5e509f1906d225`). The black lines mark the point at which the low angle boundary is crossed at the centre of the profile.

melt inclusions from multiple Kīlauean eruptions (Sides et al., 2014a) and olivine-melt partition coefficients (K_D = 0.0013–0.0021; Hauri et al., 2006; orange bar; Fig. 4.12c).

The low differential stresses estimated from linear intercept distances and dislocation densities are difficult to reconcile with the conventional interpretation that misorientation axes lying between [001] and [010] represent slip on the relatively high stress {0kl}[100] system. Instead, stress estimates from subgrain and dislocation density piezometry support the hypothesis that a {0kl}[100]-like misorientation axis distribution is generated by the presence of (010)[100] and (001)[100] edge dislocations within a single subgrain boundary (Hansen et al., 2014). Slip on (010)[100] dominates at low-moderate stresses and low-moderate water contents, while (001)[100] slip dominates is favoured by higher water contents (Jung et al., 2006; Fig. 4.12c). These independent estimates of olivine water contents and differential stresses lie at this transition where the strengths of (010)[100] and (001)[100] slip are comparable (Katayama et al., 2004). Thus, it is highly probable that subgrain walls in Kīlauean olivines apparently relating to {0kl}[100] slip are actually made from mixtures of (010)[100] and (001)[100] type dislocations. This reconciles independent estimates of deformation conditions from subgrain piezometry and the microstructural analysis of slip system proportions in this study.

4.3.6 Mush Pile Geometry

The distribution of differential stress estimates from subgrain and dislocation density piezometry (predominantly ∼3–12 MPa) allows assessment of the hypothesis that volcanic

olivines are deformed by gravitational loading within melt-rich mush piles. Differential stresses (σ_D) in mush piles scale as a function of the density difference between crystals and host melts ($\Delta\rho$), and the thickness (H):

$$H = \frac{\sigma_D}{g\Delta\rho} \tag{4.3}$$

Where g=9.8 m/s^2, and $\Delta\rho$=567 kg/m^3, using ρ=3282 kg/m^3 for Fo_{86} olivine at 1230°C (Neave et al., 2014), and ρ=2715 kg/m^3 for the interstitial basaltic liquid (Lange and Carmichael, 1987; Sides et al., 2014a).

Using this simple equation, the measured differential stresses may be generated at the bottom of mush piles ∼540–2160 m thick. However, centuries of observations have demonstrated that a near-ubiquitous feature of granular materials is the arrangement of solid particles into force chains, resulting in unequal transmission of load (e.g., corn in silos, stacked fruit, poppy seeds; photoelastic particles; Antony, 2007, Bergantz et al., 2017, Sperl, 2006, Tordesillas et al., 2010). Highly stressed chains of primary members transmit most of the force, while a larger group of secondary members experience less than the mean force, and a few spectator particles experience no force (Fig. 4.14b; Estep and Dufek, 2012). The settling of dense olivine crystals into mush piles creates a crystal framework with ∼40% porosity (Hughes, 2013), which constitutes a granular medium. Thus, it is highly probable that mush piles contain force chains. Simulations of mush piles show that the proportion of particles experiencing more than the mean force has an exponential distribution, with forces on certain grains exceeding 6× the mean force (Bergantz et al., 2017). Dynamical phenomena within magma chambers (e.g., magma injection) drive the migration of force chains, resulting in a large proportion of olivines experiencing greater than the mean force (Bergantz et al., 2017). This process could reduce the required mush pile thickness by a third, to ∼180–720 m.

More precise constraints on mush pile thicknesses in igneous systems from investigations of deformed volcanic crystals will require several conceptual advances. Numerical simulations of granular mush piles are computationally expensive, despite only considering spherical particles in 2D (Bergantz et al., 2017). In reality, the force applied at contacts between angular crystals will be amplified into very high stresses by small contact areas (Gallagher et al., 1974). Such highly heterogenous stress distributions within individual grains (Wheeler, 2018) complicate piezometric estimates. An increased understanding of how heterogenous stresses within individual grains are translated into subgrain sizes and dislocation densities is needed, alongside discrete-element models accounting for force chain geometry in three dimensions, using realistic crystal shapes. Finally, transitions between a predominantly frictional regime (with force chains) to a lubricating regime may occur within mush piles, affecting the amount of stress amplification (Bergantz et al., 2017). An alternative research direction would be to perform EBSD on olivines at the base of mush piles of known thickness in extinct volcanic systems (where intrusions outcrop at the surface), to produce a calibration between deformation intensity and mush pile thickness.

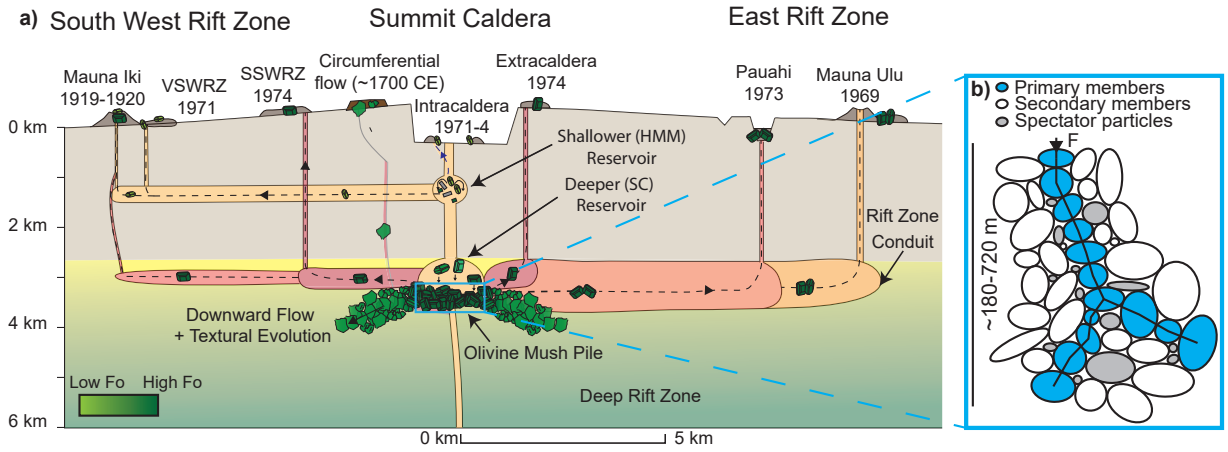


Figure 4.14: Schematic cross section along the magmatic plumbing system of Kīlauea Volcano showing the formation of deformed olivines within the SC reservoir. **a)** Olivine crystals in intracaldera eruptions thought to tap the shallower reservoir based on Pb isotope compositions (Pietruszka et al., 2015; Pietruszka et al., 2018) are largely undeformed. These crystals have evolved forsterite contents, close to the equilibrium composition of their matrix glasses. Extracaldera and rift eruptions, thought to tap the deeper SC reservoir based on Pb isotopes (Pietruszka et al., 2015; Pietruszka et al., 2018), entrain deformed crystals from melt-rich olivine mush piles at the base of the deeper reservoir just prior to eruption. The Mauna Iki eruption taps a mixed crystal cargo, from the upper and lower reservoir (Rowland and Munro, 1993). The ∼1700 eruption and the Kīlauea Iki eruption (Helz, 1987) may tap olivine bodies that have begun their descent into the deep rift zones. **b)** Schematic diagram of force chains within granular olivine mush piles (adapted from Bergantz et al., 2017). Primary members can experience forces ∼6× the mean force, secondary members experience less than the mean force, while spectator particles experience no force.

4.3.7 Mush Pile Location

The spatial distribution of deformed grains across the Kīlauean edifice provides insights into the location of the mush piles from which they are sourced. Geophysical and geochemical observations at Kīlauea have led to a model in which magma is stored at two distinct depths (Cervelli and Miklius, 2003; Pietruszka et al., 2015; Pietruszka et al., 2018). The largest proportion of deformed olivines were found in eruptions derived from the deeper South Caldera (SC) reservoir (based on Pb isotopes; Pietruszka et al., 2015; Pietruszka et al., 2018). In contrast, there are few deformed grains in intracaldera and volcanic SWRZ eruptions which tap the upper, more evolved Halema'uma'u reservoir. The different sources of these eruptions is also evident from the higher Mg# of co-erupted glasses in eruptions containing abundant deformed grains (Fig. 4.9a-b), consistent with the storage of more primitive melts in the deeper SC reservoir (Helz et al., 2015; Pietruszka et al., 2018). Interestingly, unlike the 1971 SWRZ eruption, the 1919–1920 Mauna Iki eruption contains abundant deformed grains (both eruptions occurred on the volcanic SWRZ). This supports the hypothesis that the Mauna Iki eruption tapped magma from multiple reservoirs based on the decoupling of E-W and N-S tilt components (Rowland and Munro, 1993).

Crucially, the commonality between eruptions containing deformed grains is that a significant proportion of their magma supply (and thus crystal cargo) was derived from the SC reservoir. An origin for deformed grains within mush piles at the base of this reservoir is a simpler explanation for their abundance in a wide variety of subaerial eruptions than invoking magma transport paths along the basal decollement (Vinet and Higgins, 2010). The narrow range of forsterite contents in deformed grains in this study ($\sim Fo_{87}$; Fig. 4.9) may result from diffusive re-equilibration of Mg and Fe during prolonged mush pile storage (Thomson and Maclennan, 2012; see Chapter 5). The scavenging of deformed grains from mush piles just before eruption also explains the high degree of major element disequilibrium between deformed grains and their host melts (Fig. 4.9; see Chapter 5). As the HMM reservoir is thought to be recharged from the SC reservoir (Pietruszka et al., 2018), entrainment of a small number of deformed grains during recharge events can account for their occasional occurrence in intracaldera eruptions, and the more extreme difference in forsterite contents between deformed and undeformed grains in these eruptions (Fig. 4.9e).

To further assess the hypothesis that deformed grains form in mush piles accumulating at the base of the SC reservoir, the timescales required to generate the mush piles thicknesses indicated by subgrain piezometry (∼180–720 m) were explored using a simple box model informed by available geophysical and geochemical constraints at Kīlauea. Primary melts with 16.5 wt% MgO enter a cylindrical reservoir at a rate of 0.1 km^3/yr (Anderson and Poland, 2016; 4.15a). Within the reservoir, olivine crystals form and settle into cumulate piles (∼40% porosity), causing the remaining liquid to evolve to lower MgO contents. This liquid leaves the reservoir, and is either erupted, or stored within the deep rift zones (Anderson and Poland, 2016). Fractionation from primary liquids to the average whole rock MgO contents of erupted lavas (∼10 wt% MgO) requires removal of ∼14 vol% olivine cumulate (Clague and Denlinger, 1994). The thickness of the cumulate pile in the sill is a play off between reservoir radius and accumulation time (Fig. 4.15b). Geodetic observations of surface displacements from InSAR can be modelled as a magma chamber represented by penny-shaped cracks with radii of ∼2–4 km (Baker and Amelung, 2012). This geometry permits accumulation of ∼180–720 m of mush with ∼40% porosity in just a few centuries (Fig. 4.15). This is consistent with the diverse range of trace element ratios within melt inclusions in any given eruption, which indicate minimum mush pile residence times of >170 yrs (Chapter 5). Thus, the hypothesis that deformed grains are generated by gravitational loading within mush piles accumulating within the SC reservoir is supported by available geometric and temporal constraints. Under this framework, deformed olivines are not archives of processes occurring within Kīlauea's deep rift zones. However, the absence of petrological evidence for dunitic bodies does not imply their absence (c.f. Welsch et al., 2012). Many deep processes within igneous systems are not manifested in erupted products (Davidson et al., 2007), but still play a crucial role in the evolution of volcanic systems.

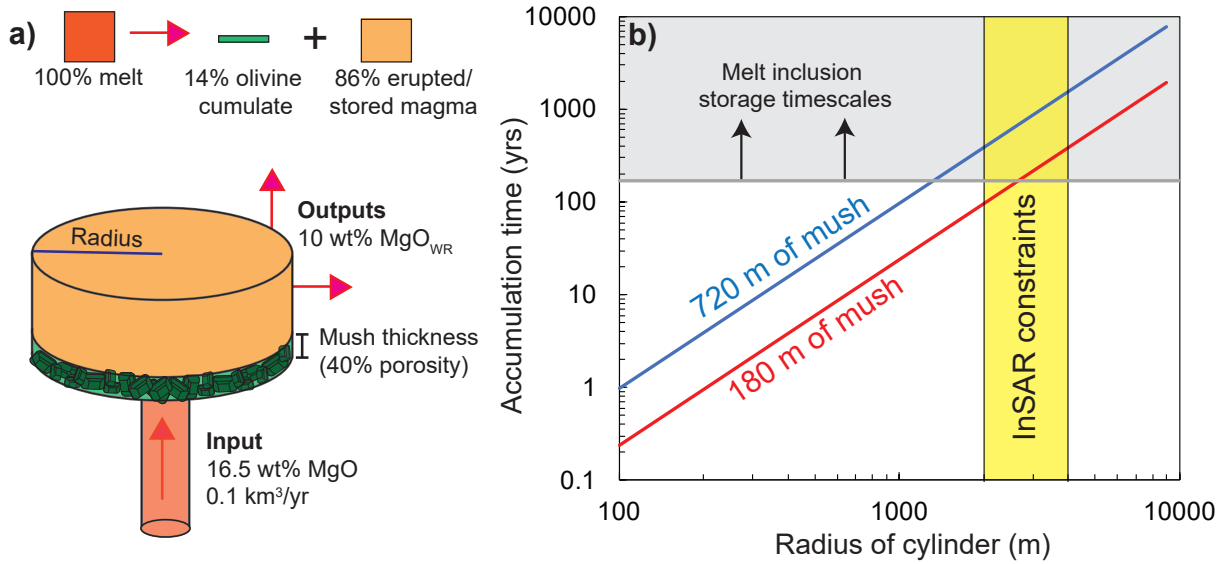


Figure 4.15: Estimating mush pile accumulation rates using a simple box model. **a)** A cylinder is supplied with primary melt (16.5 wt% MgO) at a rate of 0.1 km^3/yr (Anderson and Poland, 2016). Fractionation of these primary melts to the average whole-rock MgO contents of erupted lavas (∼10 wt %) requires the removal of 14 vol % olivine crystals (Clague and Denlinger, 1994). **b)** The play off between cylinder radius and accumulation time is shown for mush piles with thicknesses of 180 m and 720 m (assuming 40% porosity). Available constraints on reservoir radius from interferometric synthetic aperture radar (InSAR) are shown in yellow (Baker and Amelung, 2012). Melt inclusion trace element diversity at Kīlauea indicates that crystals are stored in mush piles for >170 years (grey line; Chapter 5). These geometric and temporal constraints bracket the range of mush thicknesses estimated in this study.

The temporal evolution of mush piles at the base of the deeper SC reservoir is uncertain. To resolve space problems, olivine must eventually migrate downslope to form the seismically imaged dunitic bodies (Clague and Denlinger, 1994; Fig. 4.14a). It seems probable that the amount of interstitial melt gradually reduces during this process, leading to the generation of true adcumulate textures, with internal melt films and high angle grain boundaries. Additional stress imposed during downslope flow accounts for the higher differential stresses estimated from subgrain piezometry in dunitic xenoliths from Hualalai (40±20 MPa vs. 3–12 MPa; Kirby and Green, 1980). Deformed olivines from the ∼1700 eruption may record the first stages of this process; they contain prominent low and high angle boundaries (misorientations <10° and >10° respectively; Fig 6b-c). The latter are decorated with thin films of melt (Fig. 4.10b), indicating derivation from low melt fraction bodies. These olivines also show trails of secondary fluid inclusions, similar to those observed in Hawaiian xenoliths (Clague and Denlinger, 1994). Finally, these olivines have substantially lower forsterite contents than other deformed olivines (∼Fo_{82-83} vs. ∼Fo_{86-88}; Fig. 4.9a-b), and several have Ca contents overlapping with values measured in Hualalai dunites (Kirby and Green, 1980; Fig. 4.10a). These chemical differences may reflect cooling during transport away from the main magma storage region at Kīlauea. Texturally similar olivines have

also been identified in the Kīlauea Iki eruption (Helz, 1987). Eruptions sampling these more consolidated dunitic bodies are clearly uncommon, and may be restricted to those ascending along infrequently utilized pathways to the surface (Helz, 1987).

4.4 Conclusions

A quantitative examination of microstructures in distorted olivines erupted at Kīlauea Volcano by electron backscatter diffraction reveals striking similarities to deformed mantle peridotites, but significant differences to the crystallographic signatures of dendritic growth. This suggests that lattice distortions record the application of differential stresses at high temperatures within the magmatic plumbing system, rather than rapid crystal growth. Previous petrological work has concluded that differential stresses are applied during the creep of dunitic bodies within Kīlauea's rift zones. Crucially, this has fuelled suggestions that significant quantities of magma bypass the summit reservoir and travel along the deep rift zones, despite the paucity of geophysical evidence for this process. In contrast, this study suggests that olivine crystals are deformed in gravitationally-loaded olivine mush piles at the base of the deeper South Caldera reservoir, explaining the spatial distribution of grains at Kīlauea, and the absence of adcumulate textures. Moreover, the mechanism proposed here accounts for the occurrence of deformed grains in a wide variety of basaltic systems worldwide, which lack deep rift zones.

Application of piezometers developed for mantle peridotites reveals that deformed olivines experienced differential stresses of ∼3–12 MPa. Assuming that olivine mush piles behave as granular materials, and form force chains, the vertical extent of mush piles at Kīlauea can be estimated (∼180–720 m). Based on available constraints on the magma supply rate, and the geometry of Kīlauea's summit reservoir, these thicknesses accumulate in a few centuries.

Overall, microstructural investigations of erupted olivine crystals by EBSD generates rich datasets which provide quantitative insights into crystal storage within mush piles. Under the increasingly prevalent view that crustal magmatic systems are mush-dominated (Cashman et al., 2017), constraining the geometry and dynamics of crystal storage regions is crucial to further our understanding of magmatic plumbing systems. The presence of deformed olivines in many different volcanic settings highlights the global applicability of the methods developed in this study. Furthermore, assessments of deformation conditions using EBSD need not be restricted to olivine-bearing samples. Microstructural fabrics types in natural and experimental samples have been established for a wide variety of igneous phases: diopside (AvéLallemant, 1978), plagioclase (Stünitz et al., 2003) and hornblende (Ko and Jung, 2015), extending the applicability of this study to more evolved igneous systems.

Published as: *Wieser, P.E., Edmonds, M., Maclennan, J., Jenner, F.E. and Kunz, B.E., 2019. Crystal scavenging from mush piles recorded by melt inclusions. Nature Communications, 10(1), pp.1–11. https://doi.org/10.1038/s41467–019–13518–2.*
Figures reproduced under CC-BY licence.

5

Crystal scavenging from mush piles recorded by melt inclusions

Abstract

Olivine-hosted melt inclusions are commonly used to assess pre-eruptive storage conditions, melt volatile contents, and eruption triggering mechanisms. However, this approach relies on the assumption that co-erupted olivines have a simple association with their carrier melts. This chapter shows that primitive olivine crystal cargoes and their melt inclusions display a high degree of geochemical disequilibrium with their carrier melts at Kīlauea Volcano, Hawai'i. Within a given eruption, melt inclusions trapped in primitive olivine crystals exhibit compositional diversity exceeding that in erupted lava compositions since 1790. This demonstrates that erupting liquids scavenge crystal cargoes from mush piles accumulating diverse melt inclusion populations over timescales of centuries or longer. Entrainment of hot primitive olivines into cooler, evolved carrier melts drives post-entrapment crystallization and sequestration of CO_2 into vapour bubbles, producing spurious barometric estimates. While scavenged melt inclusion records may not be suitable for the investigation of eruption-specific processes, they record timescales of crystal storage and remobilization within magmatic mush piles.

5.1 Introduction

The utility of melt inclusions, pockets of silicate melt trapped in growing crystals, is well established in igneous petrology and volcanology. Olivine-hosted melt inclusions are commonly used to investigate pre-eruptive processes in basaltic volcanoes, including magma storage depths (Tuohy et al., 2016), magma mixing (Maclennan, 2019), and the factors controlling eruption style (Sides et al., 2014b; Spilliaert et al., 2006). However, it is becoming increasingly apparent that melt inclusions are not a perfect archive of magmatic processes occurring at depth. The post-entrapment crystallization (PEC) of olivine on the walls of the

melt inclusion during cooling of the host crystal with progressive fractional crystallization, or upon eruption, changes the major and trace element composition of the remaining melt (Danyushevsky et al., 2000; Steele-MacInnis et al., 2011). The concentration of elements that are compatible in olivine decrease (e.g., MgO, Ni), while the concentration of incompatible elements increase (e.g. Nb, La, Sm, H_2O, CO_2; Maclennan, 2017). These changes, combined with a drop in inclusion pressure, favour the formation of a CO_2-rich vapour bubble (Aster et al., 2016; Maclennan, 2017; Steele-MacInnis et al., 2011). Unless the CO_2 content of the bubble is quantified (e.g., using Raman spectroscopy), melt inclusion analyses using techniques such as secondary ion mass spectrometry (SIMS) or fourier transform infra red spectroscopy (FTIR) will underestimate the CO_2 content at the time of entrapment (Aster et al., 2016; Hartley et al., 2014; Moore et al., 2015). Furthermore, global compilations of melt inclusion data demonstrates that the process of decrepitation, where the host olivine ruptures and releases CO_2 due to a large pressure difference between the inclusion and the host melt, may account for the significantly lower entrapment pressures recorded by melt inclusions than independent petrological barometers (e.g., clinopyroxene-liquid; Maclennan, 2017).

Rapid diffusion rates of H^+ in olivine mean that melt inclusion water contents are vulnerable to diffusional re-equilibration (Bucholz et al., 2013). This process may produce anomalously low water contents if the sample is not quenched rapidly upon cooling, allowing the melt inclusion to equilibrate with the degassed carrier melt (Chen et al., 2011; Gaetani et al., 2012), or anomalously high water contents due to entrainment into a water-rich carrier melt, or the mixing of compositionally diverse melts (Hartley et al., 2015). Finally, a recent study at Llaima Volcano, combining melt inclusion volatile data with diffusive modelling of major element zoning in host olivines, demonstrated that melt inclusions record the progressive mixing of melts stored at various levels in the plumbing system for months to years prior to their eventual eruption (Ruth et al., 2018).

In addition to the processes discussed above which alter melt inclusion geochemistry pre- and post-entrapment, the increasingly prevalent view of magmatic systems as mush-dominated (Cashman et al., 2017) raises more fundamental questions regarding the utility of melt inclusions. Settled crystals may be stored at a wide range of depths within extensive crustal cumulate piles for many millennia (Cashman et al., 2017; Jackson et al., 2018; Sparks et al., 2019). The re-entrainment of these crystals into unrelated magma batches challenges the common assumption that melt inclusions and matrix glasses (the solidified carrier melt) are related (Sides et al., 2014a), such that inclusions provide a record of the pre-eruptive storage and evolution of the erupted melt. Instead, a significant proportion of erupted crystals may be antecrysts; commonly defined as crystals which formed in a separate magma batch to the one in which they were erupted (Davidson et al., 2007; Jackson et al., 2018; Tuohy et al., 2016). Here, crystal-melt relationships were investigated using olivine-hosted melt inclusions from Kīlauea Volcano, Hawai'i, to assess the utility of melt inclusion records in a mush-dominated volcanic system.

Kīlauea Volcano provides the ideal test site to assess the influence of long-lived mush piles on melt inclusion records. It is one of the most extensively-studied volcanoes in the world; geophysical monitoring data collected over the last century, combined with numerous geochemical studies, have led to a well-constrained model of the plumbing system. Primitive basaltic magmas supplied from the Hawaiian hotspot at >100 km depth (Li et al., 2004) ascend through the lithosphere into two main crustal storage reservoirs situated beneath the summit of Kīlauea (Anderson et al., 2015; Cervelli and Miklius, 2003; Poland et al., 2015). Geophysical observations indicate that the deeper, South Caldera (SC) reservoir is located at ∼2–6 km depth (Cervelli and Miklius, 2003; Wright and Klein, 2014), while the shallower Halemaumau (HMM) reservoir is located at ∼1 km depth (Poland et al., 2015). The presence of two distinct mixing trends in Pb isotope ratios of lavas erupted since the 1970s corroborates geophysical evidence that magma is stored in two main reservoirs (Pietruszka et al., 2015; Pietruszka et al., 2018). A combination of geophysical and geochemical observations suggests that the SC reservoir supplies magma to extracaldera and rift zone eruptions (Pietruszka et al., 2015; Pietruszka et al., 2018), while the HMM reservoir supplies intracaldera summit eruptions and summit lava lakes (Cervelli and Miklius, 2003; Wright and Klein, 2014).

It is well accepted that extensive olivine mush piles are located in close proximity to magma storage reservoirs. For example, localized regions with P-wave velocities of 6.5–7 km/s (indicative of dunitic cumulate bodies) are located at ∼5 km depth beneath the summit, close to the inferred base of the SC reservoir (Park et al., 2007). Mass balance constraints indicate that these bodies form through the settling of olivine from fractionating melts. Primary melts have >16 wt% MgO (Clague et al., 1991; Matzen et al., 2011), yet the average bulk-rock composition of erupted melts is ∼10 wt% MgO. This difference in MgO content requires the removal of >14 vol% olivine between the intrusion of primary melts into the plumbing system, and their eruption at the surface (Clague and Denlinger, 1994). In just a century, ∼1.4 km^3 of olivine must accumulate from fractionating melts (for magma supply rates of ∼0.1 km^3/yr; Anderson et al., 2015).

Erupted products from Kīlauea Volcano exhibit prominent changes in primary melt composition over decades and centuries, offering a means of fingerprinting specific time periods. Ratios of elements with similar incompatibility during crystal fractionation (e.g. Nb/Y, La/Yb) and isotopic ratios (e.g. $^{206}Pb/^{204}Pb$, $^{87}Sr/^{86}Sr$) show pronounced changes over decadal to centurial timescales, resulting from heterogeneity in the mantle source (Marske et al., 2007), conditions of melting (Hofmann et al., 1984), and incomplete melt mixing during magma ascent and storage (Jennings et al., 2017; Pietruszka et al., 2015; Pietruszka et al., 2018). For example, Nb/Y increases from ∼0.4 to 0.7 between ∼1800 and 1930, before falling again to ∼0.49 in 1982 (Pietruszka and Garcia, 1999b). Concurrently, $^{206}Pb/^{204}Pb$ rises from ∼18.40 to 18.65 and back to ∼18.40 (Pietruszka and Garcia, 1999a).

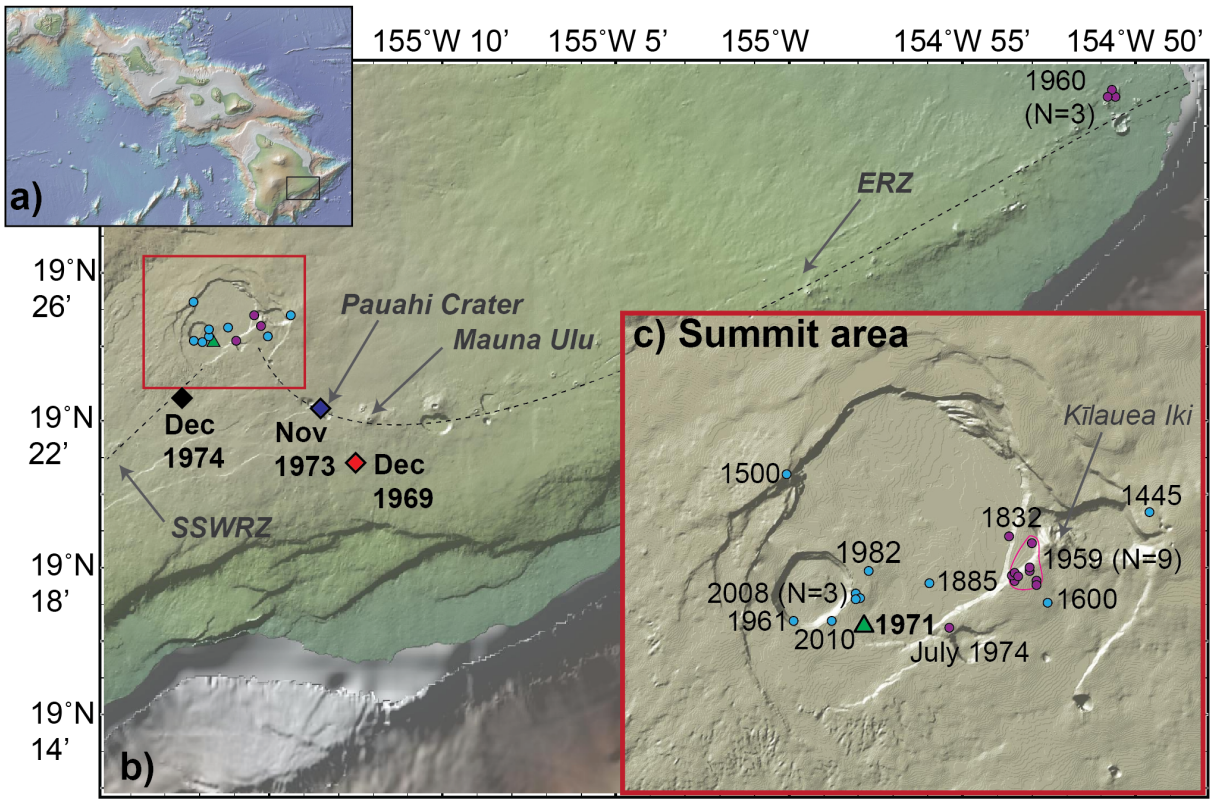
The presence of extensive olivine mush piles provides numerous opportunities for carrier melts to entrain crystal cargoes that formed in previous magma batches, while changes in

melt chemistry with time allows assessment of crystal-melt relationships and crystal residence times. Melt inclusions trapped within olivine phenocrysts should track the changes in carrier melt compositions with time. However, melt inclusions hosted within olivine 'antecrysts' plucked from mush piles by an intruding magma should record the compositional range of historic magma batches in which these olivines crystallized, rather than the carrier melt in which they were erupted (Maclennan, 2019; Tuohy et al., 2016). The relationship between melt inclusions and carrier melts may also be assessed using experimentally determined Fe-Mg partitioning between olivine and melt (Matzen et al., 2011; Roeder and Emslie, 1970). Comparison of olivine forsterite contents to the equilibrium olivine composition that would crystallize from their carrier melts provides a first assessment of the degree of major element equilibrium. The forsterite contents of phenocrystic olivines should lie close to the equilibrium olivine composition, except in the case of delayed fractionation (Maaløe et al., 1988) or prolonged storage in close proximity to their host melts (Thomson and Maclennan, 2012). In contrast, antecrystic olivines may show deviations from equilibrium substantially exceeding the experimental uncertainty in olivine-liquid K

To investigate the degree of equilibrium between erupted melts and their crystal cargoes, matrix glasses, melt inclusions and their host olivine crystals were analysed from four eruptions temporally associated with activity at Mauna Ulu on the upper ERZ (Fig. 5.1). These tephra and spatter samples were erupted during the highest fountaining phase of the Mauna Ulu eruption in December, 1969 on the ERZ, the intracaldera fissure eruption of August, 1971, the Pauahi Crater eruption of November, 1973 on the ERZ, and the fissure eruption of December, 1974 on the SSWRZ (Fig. 5.1; Poland et al., 2015). This new dataset of 126 melt inclusions and 40 matrix glass chips was supplemented with melt inclusion analyses from the literature where trace elements were reported in ≥8 inclusions and co-erupted matrix glasses from a given eruptive episode (Fig. 5.1d, Table 5.1). The combined dataset of 27 eruptive episodes and 384 melt inclusions spans ∼600 years of eruptive history at Kīlauea (Fig. 5.1), and incorporates large variations in matrix glass and whole rock compositions (Pietruszka and Garcia, 1999b).

Table 5.1: Literature melt inclusion data used in this study.

Reference	Eruptions used
Sides et al. (2014)	1445, 1500, 1832, 1885B, 1959 (Episode 1, 2, 3, 5, 6, 7, 8, 15, 16), 1960, 1961, 1974–J2, 1982, 2008 (×3), 2010
Tuohy et al. (2016)	1960 Kapoho (Kap6 and Kap8)



d)

	Date	Mean Fo (mol %)	Location	Reference	# of MI
Fo > Fo_{84}	1832	86.0	Extracaldera	Sides et al.	9
	1959 (episodes 1, 2, 3, 5, 6, 7, 8, 15, 16)	87.5, 86.8, 86.1, 87.2, 87.1, 85.9, 86.8, 86.4, 86.0	Extracaldera	Sides et al.	10, 11, 13, 8, 9, 12, 10, 10, 15
	1960	85.7	ERZ	Sides et al.	17
	1960 (2 episodes)	85.5, 88.4	ERZ	Tuohy et al.	10, 19
	Dec 1969	86.7	ERZ	This study	37
	Nov, 1973	85.6	ERZ	This study	27
	July, 1974	85.4	Extracaldera	Sides et al.	8
	Dec, 1974	87.3	SSWRZ	This study	42
Fo < Fo_{84}	1445	80.6	Intracaldera	Sides et al.	12
	1500	83.3	Intracaldera	Sides et al.	9
	1885	81.5	Intracaldera	Sides et al.	10
	1961	82.4	Intracaldera	Sides et al.	9
	Aug, 1971	82.8	Intracaldera	This study	20
	1982	82.2	Intracaldera	Sides et al.	9
	2008 (3 episodes)	82.6, 82.6, 82.9	Intracaldera	Sides et al.	9, 20, 9
	2010	81.7	Intracaldera	Sides et al.	10

Figure 5.1: a) Map of Kīlauea Volcano showing the locations of eruptions analysed in this study (bold text), alongside eruptions in the literature with melt inclusion and glass trace element data. Multiple episodes were examined from the 1959, 1960 and 2008 eruptions. **c)** An expanded map of Kīlauea's summit area (red rectangle in **b**). Maps were produced in GeoMapApp (Ryan et al., 2009), and show the topography of Kīlauea before the onset of the 2018 summit collapse. **d)** Key data on the samples analysed in this study, and those compiled from the literature.

5.2 Methods

Matrix glasses, melt inclusions and their host olivine crystals from the 1969, 1971, 1973 and 1974 eruptions were analysed by EPMA and LA-ICP-MS following the methods described in Chapter 2. An additional 689 olivine core compositions from 12 different eruptions distributed across the Kīlauean edifice were determined by EPMA in three separate analytical sessions (see Chapter 2). These measurements were supplemented with 2121 measurements from the literature. A GEOROC search (January 2018) was conducted for all shield stage olivines from Kīlauea. As this database was compiled to gain insight into magma storage at depth, olivines from lava lakes and experimental studies were discarded, as were analyses specified as rim compositions. Finally, any olivines without locations were discarded, in case they represented lake or experimentally-grown olivines. This dataset was supplemented with publications missing from GEOROC (Lynn et al., 2017; Sides et al., 2014b; Sides et al., 2014a; Thornber et al., 2015; Vinet and Higgins, 2010).

Fractional crystallization models were run in Petrolog3 (Danyushevsky and Plechov, 2011) using the primary melt composition of Clague et al. (1991) at 1 kbar, QFM (using the model of Kress and Carmichael, 1988). The FeO_T for the primary melt composition was increased by a factor of 3.2% to provide a better match with glass data. Mineral melt models of Danyushevsky (2001) were used for olivine, clinopyroxene and plagioclase. Olivine K_D was set at 0.3. The amount of post-entrapment crystallization experienced by each melt inclusion was calculated with the Petrolog3 "Olivine MI" tool (Danyushevsky et al., 2000; Danyushevsky and Plechov, 2011) at QFM using the model of Kress and Carmichael (1988). Host forsterite contents were determined from EPMA analyses of olivine crystals close to the inclusion of interest, and the initial melt inclusion FeO content (FeO*) was set at 11.33 wt% based on observed liquid lines of descent (and for consistency with previous studies; Sides et al., 2014b; Sides et al., 2014a).

5.3 Results and Discussion

5.3.1 Constraints from Olivine-Liquid Disequilibrium

Olivine forsterite contents in Kīlauean magmas show a strongly bimodal distribution (Helz et al., 2015; Fig. 5.2b), which is readily apparent in the compilation of 2810 erupted olivine core compositions from this study and the literature. The two distinct peaks are centred at $\sim Fo_{87-88}$ and $\sim Fo_{80-82}$, with a dearth of olivines with $\sim Fo_{84}$ (Fig. 5.2b). Within a given eruption, olivine forsterite contents fall mostly within one peak (Fig. 5.2a), permitting classification of eruptions based on mean forsterite contents ($\overline{Fo}$) into those with primitive ($\overline{Fo}$>Fo_{84}) and evolved crystal cargoes ($\overline{Fo}$<Fo_{84}).

Primitive crystal cargoes were observed in the three rift eruptions analysed in this study (1969, 1973, 1974; red, blue and black diamonds in Figs. 5.1 and 5.2), and in 14 eruptive

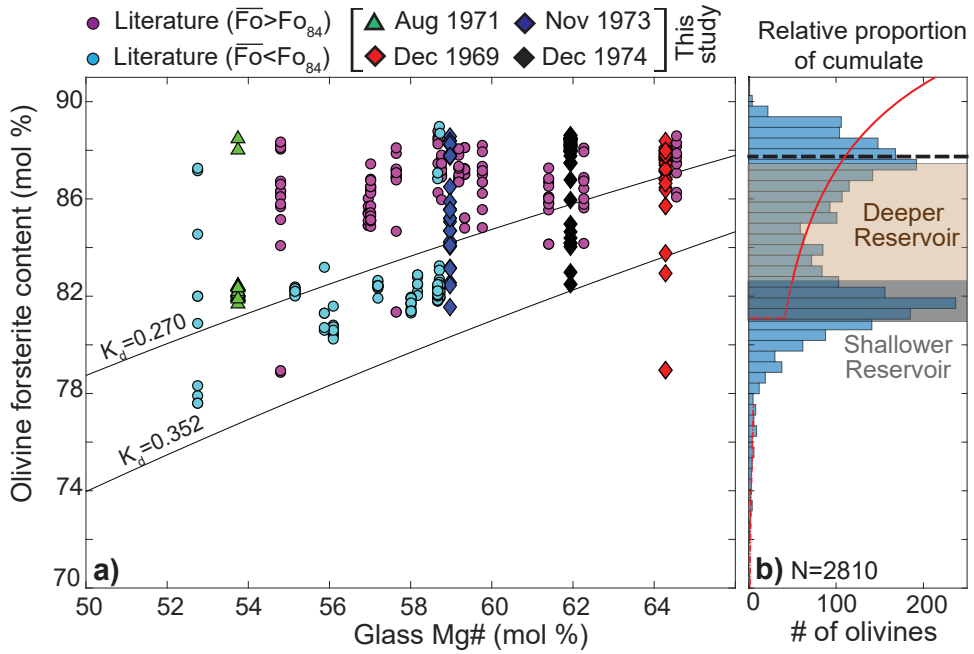


Figure 5.2: a) Olivine forsterite contents versus matrix glass Mg# (Fe^{3+}/Fe_T=0.15; Moussallam et al., 2016). Olivine-liquid equilibrium lines are shown for K_D=0.270–0.352; Matzen et al., 2011; Roeder and Emslie, 1970). Eruptions with evolved crystal cargoes ($\overline{Fo}$<Fo_{84}; cyan circles and green triangles) contain olivines lying closer to olivine-liquid equilibrium lines than eruptions with primitive crystal cargoes ($\overline{Fo}$>Fo_{84}; magenta circles, blue, black and red diamonds). **b)** Histogram of 2810 Kīlauean olivine core compositions. The red line shows the expected distribution of forsterite contents following fractional crystallization within a single reservoir from a primary melt composition (17.1 wt% MgO; Clague et al., 1991). The solid section of the line represents the composition of olivines that would crystallize from primary melts, down to the composition of the most evolved melts present within the SC reservoir. The dashed section of the line represents the olivine compositions that would crystallize from more evolved melts. The beige box shows the range of olivine compositions that would crystallize from the observed distribution of glass compositions in eruptions thought to originate in the SC reservoir (~10±2 wt% MgO), while the grey box shows the olivine compositions that would crystallize from the observed distribution of glass compositions in eruptions thought to originate in the shallower, HMM reservoir (~7±1 wt% MgO; Pietruszka et al., 2015). The black dashed line shows the mean olivine composition produced by the fractionation trajectory indicated by the solid red line (17.1 wt% MgO to 8 wt% MgO). Models run in Petrolog3 at QFM, K_D=0.3.

episodes from the literature (1832 and July 1974 eruption, 9 episodes of the 1959 Kīlauea Iki eruption, and 3 episodes of the 1960 Kapoho eruption; magenta circles; Sides et al., 2014b; Sides et al., 2014a). Evolved olivine compositions are observed in the intracaldera eruption of 1971 (this study; green triangles), and 9 eruptive episodes from the literature (1445, 1500, 1885, 1961, 1982 and 2010 eruptions, and 3 episodes of the 2008 summit eruption, cyan circles). Primitive crystal cargoes are significantly out of major element equilibrium with their matrix glasses, while evolved crystal cargoes lie close to the equilibrium composition (Fig. 5.2a). In addition to bimodal forsterite contents, lavas erupted around Kīlauea's summit also show bimodal whole-rock MgO contents (Helz et al., 2015), centred

at ∼7±1 wt% and ∼10±2 wt% MgO (Pietruszka et al., 2018). This bimodality has been attributed to magma storage in two distinct reservoirs, as eruptions between 1969–1982 thought to have tapped the HMM reservoir based on Pb isotopes (Pietruszka et al., 2015; Pietruszka et al., 2018) have whole-rock MgO contents aligned with the evolved peak, while extracaldera and rift eruptions thought to have tapped the SC reservoir align with the primitive peak (Pietruszka et al., 2018). The spatial distribution of olivine compositions is similar (Helz et al., 2015); historic and prehistoric intracaldera eruption products host evolved olivines ($\overline{Fo}$<Fo_{84}) while extracaldera and rift eruption products host more primitive olivines ($\overline{Fo}$>Fo_{84}; Figs. 5.1 and 5.2). Thus, it seems probable that bimodality in olivine forsterite contents is also generated, in part, by fractionation within two separate reservoirs, as progressive fractional crystallization within a single reservoir would produce steadily declining amounts of olivine with a given forsterite content between ∼Fo_{90-81} (red line, Fig. 5.2b). Although the geometry of magma storage at Kīlauea may undergo changes following caldera-collapse events (e.g. 1924, 2018; Neal et al., 2019; Pietruszka et al., 2015), the fact that prehistoric tephra and lava show a similar, bimodal distribution of glass and olivine compositions suggests that variably evolved melts were stored at two distinct depths over the time period evaluated in this study (Helz et al., 2015; Pietruszka et al., 2018).

A fractional crystallization model over the suggested range of melt compositions present in the HMM reservoir (∼7±1 wt% MgO; Pietruszka et al., 2018) produces olivine compositions overlapping with the low forsterite olivine peak (red dashed line in grey box; Fig. 5.2b). This, combined with the high degree of major element equilibrium between olivine crystals and their matrix glasses (Fig. 5.2a), implies that these crystals grew in equilibrium with their carrier liquids. The narrow range of evolved liquid (and therefore olivine) compositions in the HMM reservoir (Pietruszka et al., 2015) likely results from an increase in the enthalpy of crystallization, and a decrease in the rate of change of Mg# for a given amount of crystallization as clinopyroxene joins the liquidus assemblage (Garcia et al., 2003; Pietruszka et al., 2018). However, fractional crystallization over the range of melt compositions erupted from the SC reservoir (∼10±2 wt% MgO; Pietruszka et al., 2018) produces a distribution of olivine forsterite contents which steadily declines between ∼$Fo_{87.4-82.6}$ (section of red line within beige box; Fig. 5.2b). Crucially, compared with the observed distribution of forsterite contents, the modelled distribution shows no peak, and is shifted to substantially lower forsterite contents (Fig. 5.2b). Producing the peaked distribution of primitive olivine compositions with fractional crystallization alone is problematic. Unlike the evolved HMM reservoir, it is difficult to envisage an efficient thermal or chemical buffering process operating in the small-volume (0.1–0.3 km^3; Pietruszka et al., 2015) SC reservoir fractionating only olivine and chromite. Similar peaks at high forsterite contents in Icelandic lavas have been attributed to diffusive re–equilibration of Fe and Mg within crystal mush piles, which produces a peaked distribution of forsterite contents centred on the mean composition of

the mush pile (Thomson and Maclennan, 2012). Fractionation from estimated primary melt compositions (∼17.1 wt% MgO; Clague et al., 1991) to the most evolved liquid composition in the SC reservoir (∼8 wt% MgO; solid section of red line; Pietruszka et al., 2018) produces an olivine mush pile with a mean olivine composition of $\sim Fo_{87.7}$ (black dashed line; Fig. 5.2b). Thus, the random scavenging of olivines stored in diffusively re–equilibrating mush piles by subsequent carrier melts accounts for the high degree of major element disequilibrium (Fig. 5.2a), and the strongly peaked distribution of primitive forsterite contents in many different eruptions (Fig. 5.2b).

Assessing storage timescales from peaked forsterite distributions requires knowledge of the initial distribution, and the mush pile height. Thomson and Maclennan (2012) explored this parameter space for Icelandic lavas assuming that a sill of variable thickness underwent progressive fractional crystallization in a closed system. However, the SC reservoir is an open system, with primitive melts entering at the base, and variably evolved melts leaving the reservoir to be erupted, or stored within the rift zones (Anderson and Poland, 2016). Repeated injection of more primitive melts likely produces cyclic variations in forsterite content with height. Clearly, an alternative approach is required to assess the residence times of primitive olivine crystals in open (and therefore highly unconstrained) systems such as Kīlauea.

5.3.2 Constraints from Melt–Inclusion Liquid Disequilibrium

To test the hypothesis that evolved olivines are phenocrysts forming within the HMM reservoir, while primitive olivines represent antecrysts scavenged from extensive mush piles at the base of the SC reservoir, the trace element compositions of matrix glasses and olivine–hosted melt inclusions were compared. Phenocrystic olivines from the HMM reservoir should contain melt inclusions with trace element signatures overlapping those of their carrier melts (matrix glasses), while antecrystic olivines from the SC reservoir should host melt inclusions with no obvious geochemical affinity to their carrier melts. Matrix glasses from the four eruptions investigated in this study have distinct trace element signatures. Matrix glass trace element ratios which are relatively insensitive to crystal fractionation of predominantly olivine (and minor chromite), or post-entrapment crystallization (e.g., Nb/Y, La/Yb, Zr/Y and Nb/Yb, Fig. 5.3), follow similar temporal trends to whole-rock measurements from summit lavas (Fig. 5.4a). This chapter specifically focuses on Nb/Y ratios for consistency with previous work at Kīlauea (Pietruszka et al., 2018; Pietruszka and Garcia, 1999b; Pietruszka and Garcia, 1999a; Tuohy et al., 2016), and because this ratio shows the largest percent variation in historic lavas (Table 5.2).

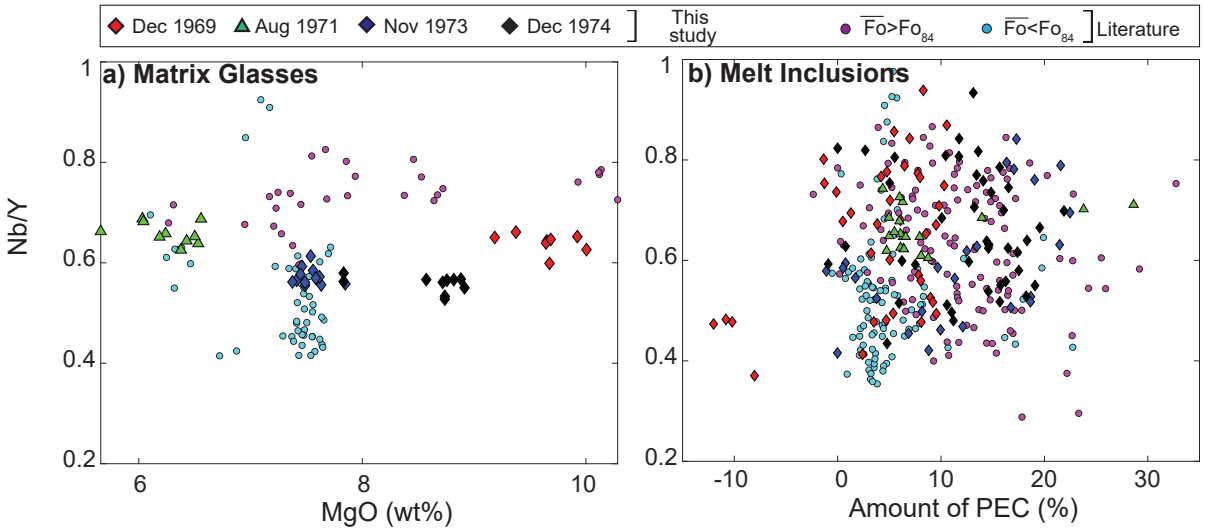


Figure 5.3: There is no correlation between Nb/Y and MgO in matrix glasses **a)**, or between Nb/Y ratios and the amount of PEC in melt inclusions **b)**. This demonstrates that Nb/Y ratios are not sensitive to the crystallization of olivine.

Table 5.2: The variability of each ratio in erupted lavas was calculated in two ways: 1) Dividing the range of each ratio in summit whole-rock compositions between 1790–1982 by the mean ratio (Pietruszka and Garcia, 1999a). 2) Dividing the standard deviation of each ratio over this period by the mean ratio.

Measure	Nb/Y	Zr/Y	La/Y	La/Yb	Sm/Yb	La/Sm	Ba/Nb
Variation (Range, %)	57.1	23.8	54.3	55.5	22.7	38.2	18.7
Variation (σ; %)	15.7	6.6	13.8	13.8	5.8	9	5.2

Within a given eruption hosting evolved crystal cargoes (Fig. 5.1d), melt inclusion Nb/Y ratios show limited chemical diversity, centred on the composition of the co–erupted matrix glass (Fig. 5.4b). This supports the hypothesis based on olivine forsterite contents that evolved crystal cargoes consist predominantly of phenocrysts, which grew in the HMM reservoir from the melt which carried them to the site of the eruption. In contrast, melt inclusions from the three rift eruptions investigated in this study (1969, 1973, 1974) are highly diverse, with indistinguishable mean Nb/Y ratios despite statistically significant changes in the mean matrix glass composition (1969 glasses are distinct from 1973–1974 glasses; ANOVA, α=0.05; Fig. 5.4a, c). In fact, of the 17 eruptions with primitive crystal cargoes (Fig. 5.1d), only two of the melt inclusion populations have distinguishable means at α=0.05. A linear regression through the mean melt inclusion and matrix glass composition for eruptions with primitive crystal cargoes shows no trend (R^2=0.00), unlike the excellent correlation observed for eruptions with evolved crystal cargoes (R^2=0.94; Fig. 5.4b–c).

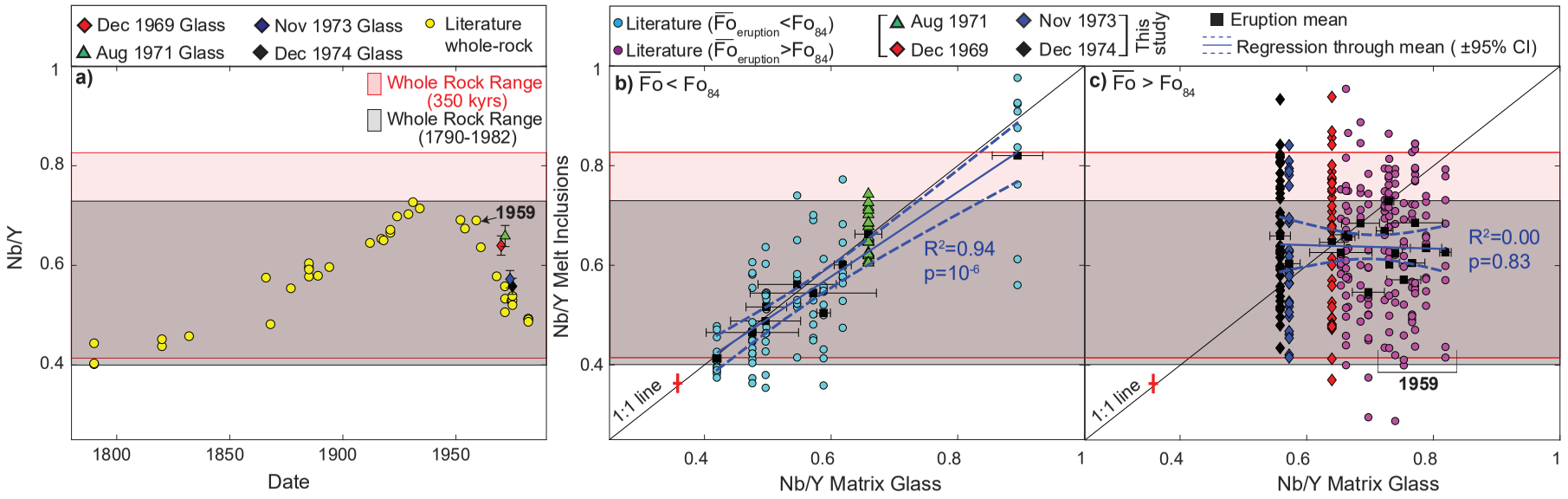


Figure 5.4: a) whole-rock data from summit eruptions display large temporal variations in Nb/Y (Pietruszka and Garcia, 1999b; Pietruszka and Garcia, 1999a). Matrix glasses from the four eruptions analysed in this study follow similar trends, although the 1971 intracaldera eruption lags behind the May 1969 ERZ eruption (error bars show $\pm 1\sigma$ for glass measurements). The grey box shows the range of Nb/Y ratios in whole rock compositions since 1790 (Pietruszka and Garcia, 1999b), and the pink box shows the range of Nb/Y ratios in whole rock compositions over the last 350 kyrs (Quane et al., 2000) **b–c)** Nb/Y ratios of melt inclusions versus co–erupted matrix glasses ($\pm 1\sigma$ glass analyses). Regression lines were calculated for the mean glass and melt inclusion composition of each eruption (95% confidence intervals on the regression are shown with dashed lines). Eruptions with $\overline{Fo}$<Fo$_{84}$ display a strong correlation between the mean Nb/Y ratio of melt inclusions and matrix glasses **(b)**. While the 1961 summit eruption (glass Nb/Y ~0.89) certainly strengthens the observed correlation, the regression is still very good if this eruption is excluded (R^2=0.84, p=10^{-4}). In contrast, there is no correlation between the mean Nb/Y ratios of melt inclusions and matrix glasses from eruptions with $\overline{Fo}$>Fo$_{84}$ **(c)**. In particular, almost all melt inclusions from various episodes of the 1959 Kīlauea Iki eruption have significantly lower Nb/Y ratios than the composition of co–erupted matrix glasses. The red cross on **b–c)** shows the precision for repeated analysis of BCR–2 ($\pm 1\sigma$) in melt inclusions and glasses.

Within a single eruption hosting a primitive crystal cargo, melt inclusion heterogeneity exceeds the range of Nb/Y ratios observed in historic summit lavas (1790–1982; Pietruszka and Garcia, 1999b) and a record of erupted lavas spanning 350 kyrs (Quane et al., 2000; Fig. 5.4). Similarly, it has been demonstrated for several Hawaiian volcanoes that Pb isotopes in melt inclusions from a single eruption show diversity comparable to the total observed variation at a given volcano (Sakyi et al., 2012). Extreme melt inclusion variability in basaltic lavas is commonly attributed to the presence of a diverse range of mantle melts within the plumbing system at any given time (Maclennan, 2019,Maclennan, 2008). Basaltic lavas from Iceland and mid oceanic ridges show substantial reductions in trace element variability with forsterite content, tracking the concurrent mixing and fractionation of diverse mantle melts (Maclennan, 2019, 2008; Sobolev and Shimizu, 1993). In contrast, Kīlauean melt inclusions exhibit no obvious correlation between trace element diversity and olivine forsterite contents (Fig. 5.5). Additionally, the presence of remarkably coherent temporal variations in lava geochemistry at widely–spaced eruption sites at Kīlauea suggests that eruptions are tapping a well-mixed reservoir (Garcia et al., 2003; Pietruszka et al., 2018). Melt homogeneity at Kīlauea has been attributed to efficient mixing in storage reservoirs between primary and resident magmas (Gerlach et al., 2002; Pietruszka et al., 2015). Alternatively, the combination of thick lithosphere and high mantle potential temperatures beneath Hawai'i may permit extensive mixing during long ascent paths from the mantle. In particular, supraliquidus ascent may homogenize melts prior to the crystallization of olivine and the entrapment of melt inclusions (Jennings et al., 2017; Putirka, 2005; Wölbern et al., 2006).

Regardless of the exact mechanism producing the relatively homogenous reservoir compositions, the apparent absence of diverse melt compositions within the plumbing system based on erupted lava compositions implies that diverse melt inclusion populations were acquired from many different, well–mixed reservoir compositions over prolonged periods. An approximate estimate of the contribution to the diversity of melt inclusions from reservoir heterogeneity and magma mixing can be obtained from the range of trace element ratios in melt inclusions from the 1971 summit eruption (Fig. 5.4b; Nb/Y=0.6–0.74). This accounts for only 25% of the variation in Nb/Y ratios observed in the 1969 eruption (Fig. 5.4c; Nb/Y=0.37–0.94). Thus, indistinguishable melt inclusion populations with a broad range of melt inclusion trace element ratios in many different primitive eruptions, combined with the lack of relationship with forsterite contents, supports a model in which carrier melts randomly scavenge olivine antecrysts from mush piles containing highly diverse melt inclusion populations just prior to eruption.

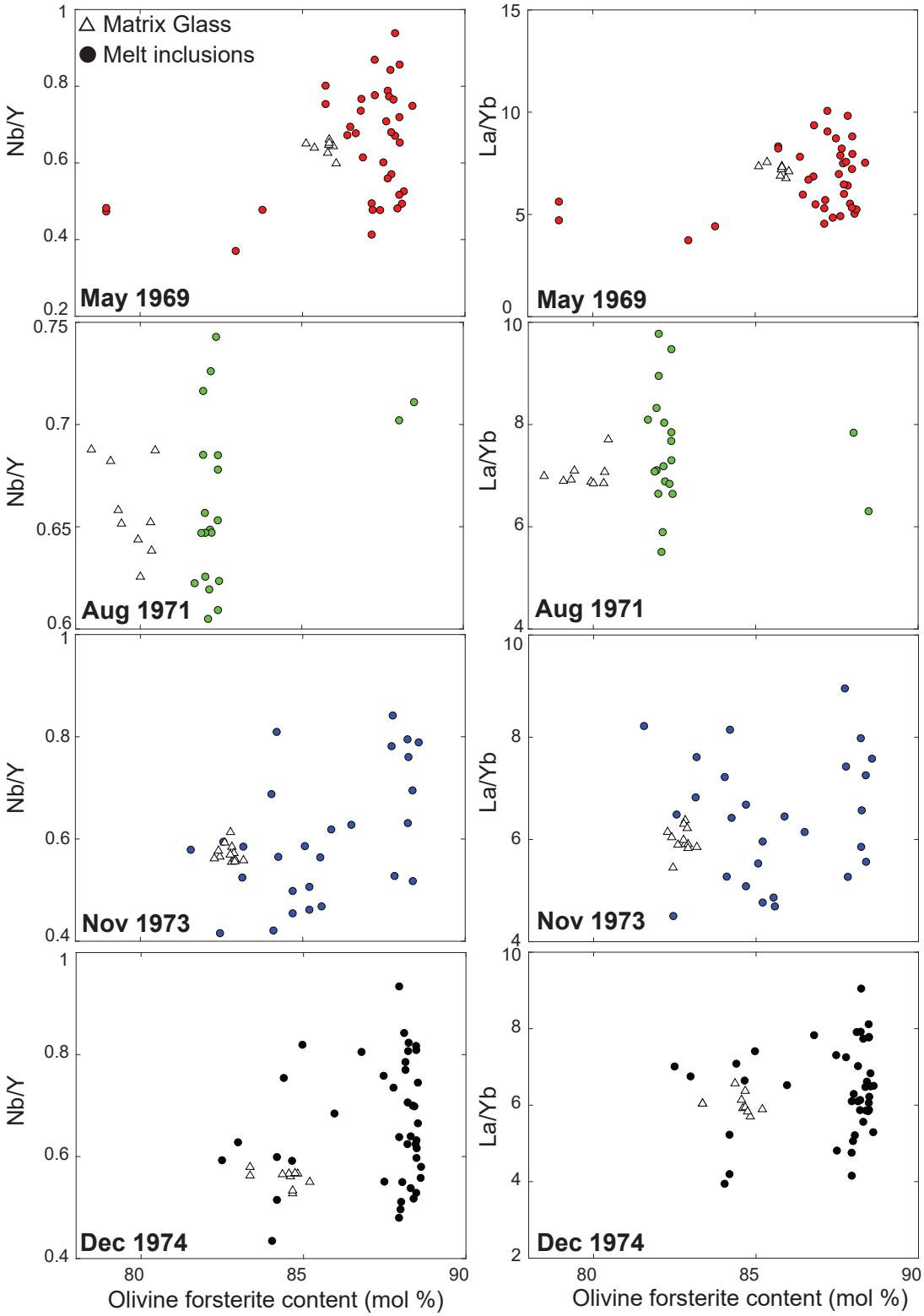


Figure 5.5: Trace element ratios vs. olivine forsterite content for each eruption. The equilibrium olivine composition for each glass chip glass was calculated for K_D=0.3, Fe^{3+}/Fe_T=0.15. Unlike Icelandic melt inclusion records (Maclennan, 2008; Maclennan, 2019), there is no obvious decline in trace element diversity with decreasing forsterite content.

5.3.3 Centurial Storage Times Within Mush Piles

An estimate of the minimum residence times of primitive olivine crystals in mush piles can be obtained by comparing the range of trace element ratios in melt inclusions to erupted lava compositions. Bulk–rock and glass analyses from the 1959 Kīlauea Iki eruption lie close to upper limit of Nb/Y ratios observed since ∼1790 (Fig. 5.4a). Yet, the vast majority of co–erupted melt inclusions have significantly lower Nb/Y ratios (Fig. 5.4c), down to ∼0.4. Melts with these compositions were only present in Kīlauea's plumbing system before ∼1790 (Fig. 5.4a), suggesting that these erupted crystals were stored for at least 170 years. It is highly possible that crystals were stored for considerably longer timescales; the range of Nb/Y ratios in melt inclusion records from the three rift eruptions investigated in this study greatly exceed the range of bulk rock compositions between 1790–1982. In fact, the 1969 eruption displays trace element diversity surpassing the range of erupted lava compositions over a 350 kyr period (Fig. 5.4c).

This study is the first to recognise centurial storage timescales of crystal mushes at Kīlauea. Most previous estimates of timescales are based on the interdiffusion of Fe and Mg within olivine; the relatively high diffusion coefficients of these species means that profiles within individual crystals only record the final processes happening decades to hours before their eventual eruption (Lynn et al., 2017; Rae et al., 2016). Diffusion times reported from modelling of trace element zoning in deformed Kīlauean olivines yield slightly longer timescales (33–238 days for P, and 10 days to 43 years for Cr; Bradshaw et al., 2018). However, the highly disparate timescales obtained from these two different trace elements highlights the difficulty in obtaining storage estimates from olivine trace element contents, due to the uncertainty in experimentally–determined diffusivities (Spandler et al., 2007 vs. Cherniak, 2010). In particular, the presence of sharp, P zones in slowly cooled igneous intrusions suggests that P diffusion may be considerably slower than available experiments, so the storage times of Bradshaw et al. (2018) are very much minimum estimates.

A related question is whether trace elements within olivine–hosted melt inclusions undergo diffusive equilibration with their surrounding melts during centurial storage. While early estimates of diffusion rates for rare earth elements suggest that diffusive re–equilibration may occur over tens to hundreds of years (Spandler et al., 2007), more recent studies calculate diffusivities that are ∼3 orders of magnitude lower (requiring 10^4–10^6 years for 50% re-equilibration of Ce and Yb in a 50 µm melt inclusion within a ∼1 mm olivine at 1300°C; Cherniak, 2010). Evidence for the lack of trace element re–equilibration in our dataset is provided by the similarity of regression lines for incompatible elements defined by matrix glasses and melt inclusions (e.g. Nb vs. La, Nb vs. Ce; Fig. 5.6). These strong correlations are likely produced by different extents of mantle melting (Hofmann et al., 1984).

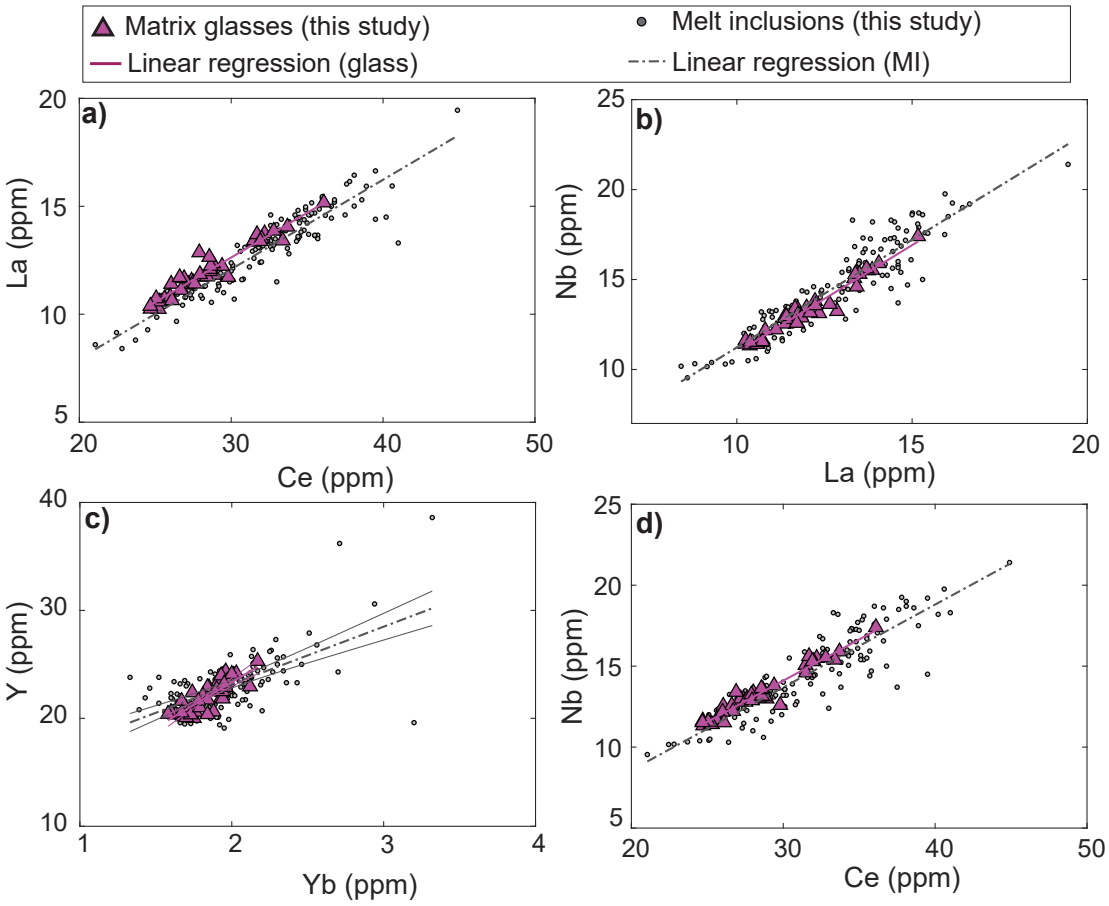


Figure 5.6: Matrix glasses and melt inclusions show strong positive correlations between incompatible elements (e.g. La vs. Ce), due to variations in the extent of mantle melting. If trace elements were undergoing diffusional re–equilibration in melt inclusions, the regression lines defined by the melt inclusions (grey lines) and the glasses (pink lines) would deviate in **b-d)**. This is not observed. 95% confidence intervals are shown for **c)**, as the relatively compatibility of these elements produces weaker correlations.

If trace element re–equilibration was occurring within melt inclusion populations during prolonged mush pile storage, different extents of re–equilibration for different trace elements (and different inclusion and host olivine sizes) would result in melt inclusions defining more scattered correlations with different regression lines compared with matrix glasses. While there are no available experimental estimates for the diffusivities of Nb and Y in olivine, the similar correlations defined by melt inclusions and matrix glasses for Nb vs. Ce and Y vs. Yb (Fig. 5.6) suggests that Nb and Y are also resistant to diffusive re–equilibration during centurial storage. Thus, comparisons of melt inclusion diversity to erupted melt compositions provides the most reliable estimate of storage timescales in long–lived mush–dominated systems crystallizing only olivine.

5.3.4 Disequilibrium Affects Melt Inclusion CO_2 Systematics

The entrainment of hot, primitive antecrysts into cooler, more evolved carrier melts generates thermal disequilibrium, in addition to the major and trace element disequilibrium discussed above. The characteristic conductive cooling time (τ) of an olivine with a radius (l) of 0.5 mm, and a thermal diffusivity (κ) of 5.6×10^{-7} m^2/s (Holt, 1975) is ~0.5 seconds ($\tau = l^2/\kappa$; Turcotte and Schubert, 2002). In contrast, the characteristic diffusional time scale for forsterite contents is ~80 years ($\tau = l^2/D$, where D_{Fo} ~10^{-16} m^2/s; Thomson and Maclennan, 2012). Thus, hot primitive antecrysts (and their melt inclusions) reach thermal equilibrium with cooler, more evolved carrier melts long before major element equilibrium is achieved. Rapid cooling drives post–entrapment crystallization on the inclusion wall. The efficiency of this process is demonstrated by the similarities between MgO contents (which are a proxy for temperature; Helz and Thornber, 1987) of melt inclusions and co–erupted glasses in eruptions with $\overline{Fo}$>Fo_{84} (Fig. 5.7), despite the strong disequilibrium that still exists between olivine forsterite contents and matrix glass Mg#s (Fig. 5.2a).

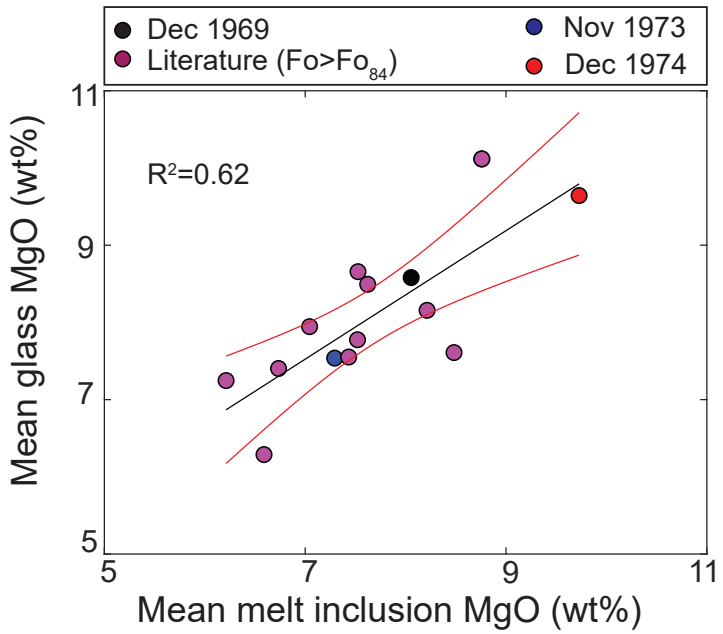


Figure 5.7: There is a strong correlation between melt inclusion and matrix glass MgO contents for eruptions with $\overline{Fo}$>Fo_{84}. This demonstrates the rapidity of post–entrapment crystallization following crystal scavenging.

As the MgO contents of the melt inclusions have rapidly re–equilibrated following entrainment, the degree of olivine–melt disequilibrium (calculated by subtracting the equilibrium forsterite content for the carrier melt from the measured forsterite content) is the best proxy for the temperature difference between entrained olivines and host melts. This parameter strongly correlates with the amount of PEC calculated in Petrolog3 (Fig. 5.8a). The maximum amount of PEC is experienced by the most primitive (and hottest) olivines which are entrained into the most evolved (and coolest) melts. Our hypothesis that post–entrapment crystallization is a direct result of the rapid, thermal re–equilibration following the scavenging of primitive olivines into evolved carrier melts (Sides et al., 2014b)

differs from the common view that PEC is driven by cooling during progressive fractional crystallization (Danyushevsky et al., 2000). Melt inclusions in eruptions with primitive crystal cargoes are hosted by olivine crystals which are significantly out of major element and thermal equilibrium with their carrier melts, and as a result, have experienced large amounts of PEC (up to 30%). It is well established that changes in major element chemistry, combined with a drop in inclusion pressure with increasing PEC favour CO_2 saturation, and the formation of a CO_2–rich vapour bubble (Aster et al., 2016; Maclennan, 2017; Steele-MacInnis et al., 2011). This mechanism accounts for the clear decrease in melt inclusion CO_2 concentrations with increasing amounts of PEC (Sides et al., 2014b) in these eruptions (Fig. 5.8b). Thus, CO_2 contents measured by SIMS or FTIR in melt inclusions (which frequently contain vapour bubbles; Sides et al., 2014b) hosted within entrained antecrystic olivines are far lower than the concentration at the point of entrapment (Aster et al., 2016; Tuohy et al., 2016).

Vapour bubble formation following crystal scavenging can explain the lack of correlation between forsterite content and CO_2 contents at Kīlauea (Tuohy et al., 2016). For example, 57% of olivines with $>Fo_{84}$ record lower pressures than more median CO_2 content of more evolved olivines ($<Fo_{84}$; Fig. 5.8c). This is at odds with conceptual models of the plumbing system, where more primitive melts crystallize at deeper pressures (Helz et al., 2015; Helz et al., 2014; Pietruszka et al., 2018; Tuohy et al., 2016). In fact, 70% of inclusions hosted in olivines with $>Fo_{84}$ record CO_2 concentrations indicating entrapment at <2 km depth (Ryan, 1987; Sides et al., 2014a), which is significantly shallower than the geophysical estimates for the depth of the SC reservoir (Cervelli and Miklius, 2003; Poland et al., 2015). Bubble growth driven by PEC means that reliable barometric estimates can only be gained from analysis protocols accounting for the amount of CO_2 held within the melt inclusion (SIMS or FTIR) and the vapour bubble (e.g. Raman spectroscopy; Hartley et al., 2014). Such PEC-driven bubble growth is particularly problematic at Kīlauea, where the absence of clinopyroxene and plagioclase in most erupted lavas preclude the use of other petrological barometers.

In contrast, the concentration of CO_2 in melt inclusions hosted within evolved crystal cargoes indicate entrapment pressures between ∼8–75 MPa, with most inclusions clustering between 25–50 MPa (Sides et al., 2014a). These pressures encompass geophysical constraints on the depth of the HMM reservoir (pressures of ∼25–50 MPa for storage depths of 1–2 km; Poland et al., 2015 and densities of ∼2600 kg/m^3; Anderson and Poland, 2016). Thus, melt inclusion CO_2 contents in evolved crystal cargoes produce reliable barometric estimates, even though these inclusions contain bubbles. This implies that these bubbles only contain a small fraction of the total CO_2 budget. CO_2–poor bubbles may form during post–eruptive cooling, due to differences between the glass transition temperature and the temperature at which C–diffusion becomes extremely slow (allowing bubble growth, but hindering the diffusion of CO_2 from the melt into the bubble; Anderson and Brown, 1993; Maclennan, 2017; Wallace et al., 2015). The CO_2 budget of melt inclusion vapor bubbles is examined in more detail in Chapter 7.

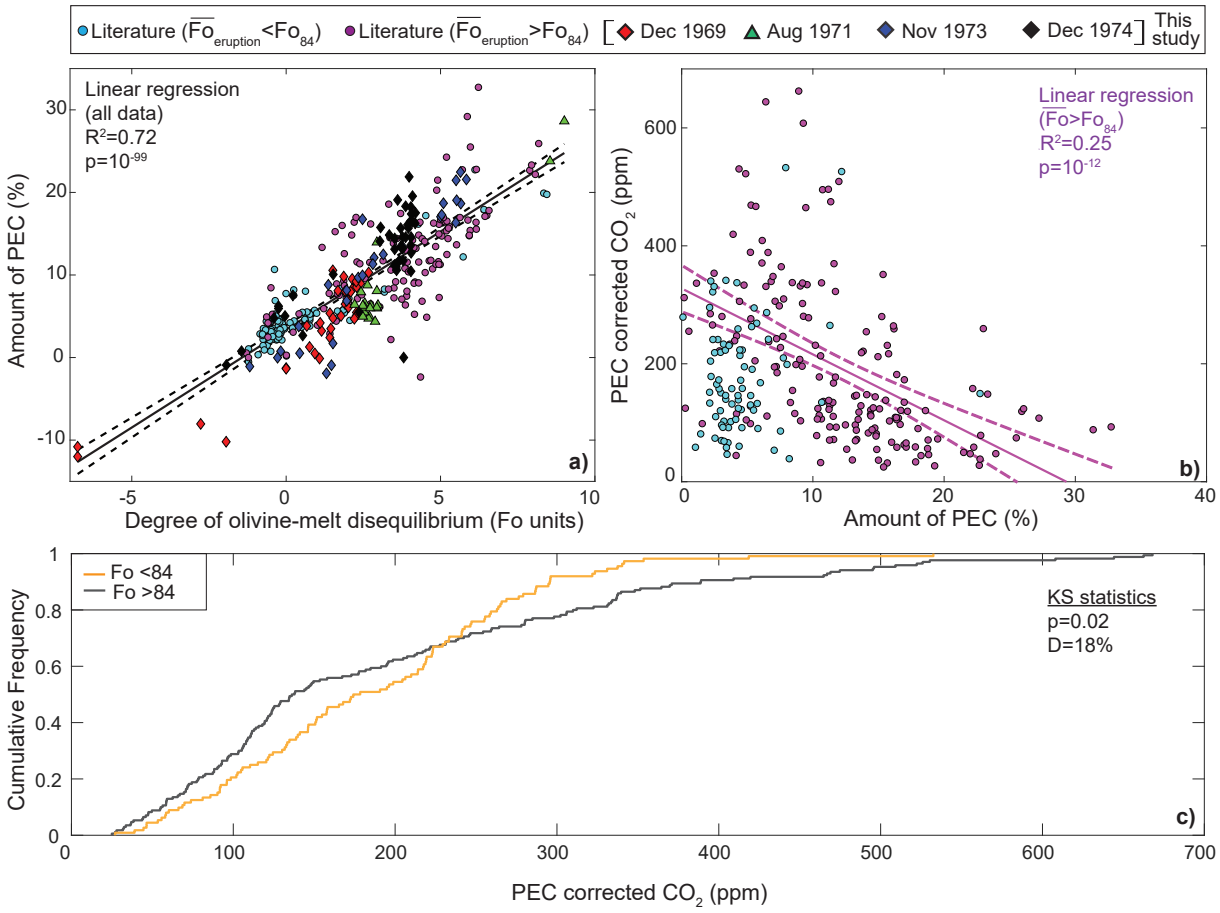


Figure 5.8: a) Degree of olivine–melt disequilibrium versus the amount of post–entrapment crystallization (PEC). Olivine–melt disequilibrium calculated by subtracting the equilibrium forsterite content of the erupted matrix glass (K_D=0.3, Fe^{3+}/Fe_T=0.15; Moussallam et al., 2016) from the olivine forsterite content. A linear regression through all data points is represented by a black line, with 95% confidence intervals indicated by dashed black lines. **b)** Amount of PEC versus melt inclusion CO_2 concentrations. A linear regression through melt inclusions from eruptions with $\overline{Fo}$>Fo_{84} is represented by a purple line, with 95% confidence intervals indicated by dashed purple lines. Amount of PEC calculated in Petrolog3 (Danyushevsky and Plechov, 2011). **c)** Cumulative frequency plot of CO_2 concentrations in melt inclusions from Sides et al. (2014a) subdivided into those hosted by olivines with <Fo_{84} and >Fo_{84}. P values and the test statistics from the two sample Kolmogorov-Smirnov (KS) test are shown. As no CO_2 data was collected in this study for the Mauna Ulu samples, to increase the number of datapoints on panels **b–c)**, all eruptions in Sides et al. (2014a) were used, rather than just those with ≥8 melt inclusions.

5.3.5 Pre–eruptive History of Evolved Crystal Cargoes

The HMM reservoir, supplying intracaldera eruptions, is thought to be replenished from the SC reservoir (supplying extracaldera and rift eruptions (Pietruszka et al., 2018; Fig. 5.9). This geometry explains the lag in Nb/Y ratios in the August 1971 intracaldera eruption products relative to the December 1969 ERZ eruption (Fig. 5.4a). Erupted olivine and melt compositions from the HMM reservoir show restricted major element diversity, due to thermal and chemical buffering at the onset of clinopyroxene fractionation. The

evolved crystal cargoes ($\overline{Fo}$<Fo_{84}) in intracaldera summit eruptions consist predominantly of phenocrysts, shown by the high degree of olivine–melt Fe–Mg equilibrium (Fig. 5.2a) and overlapping melt inclusion and matrix glass trace element ratios (Fig. 5.4b). Low crystal contents of intracaldera eruptions, together with similar whole-rock and glass MgO contents, provide further evidence that melts from the HMM reservoir have not scavenged significant quantities of antecrystic olivines (Garcia et al., 2003). Thus, melt inclusion populations in eruptions hosting evolved crystal cargoes provide a reliable record of the pre–eruptive storage and evolution of their host melts. The high degree of major element equilibrium between olivine and glass compositions limits the amount of PEC experienced by melt inclusions (<10%), resulting in CO_2 entrapment pressures consistent with geophysical constraints on the depths of the HMM reservoir.

5.3.6 Pre–eruptive history of primitive crystal cargoes

The composition of parental melts supplying the SC reservoir changes with time due to variations in mantle source composition and melting conditions (Pietruszka et al., 2015; Pietruszka et al., 2018; Pietruszka and Garcia, 1999b; Pietruszka and Garcia, 1999a; Fig. 5.9). Efficient mixing during ascent from the mantle, and/or following reservoir replenishment, creates a magma batch with limited compositional heterogeneity at any given time (Gerlach et al., 2002; Jennings et al., 2017; Pietruszka and Garcia, 1999b). The injection of hotter mantle melts into the cooler reservoir may create conditions favouring the formation of melt inclusions (Welsch et al., 2012), which trap the restricted range of melt compositions present in the reservoir at any given time. The typical MgO contents of primitive rift zone and extracaldera lavas (∼10 wt% MgO; Pietruszka et al., 2018) requires substantial fractionation of olivine (Clague and Denlinger, 1994) from high MgO mantle melts (∼15–17 wt% MgO; Clague et al., 1991). Over centuries, crystal fractionation combined with rapidly changing reservoir compositions produces a mush pile of olivines hosting chemically diverse melt inclusions. Diffusive re-equilibration of Fe-Mg within the mush pile over centuries (or longer) creates a prominent peak in olivine forsterite contents at ∼$Fo_{87.7}$, while slower diffusion rates for incompatible trace elements preserve melt inclusion diversity (Maclennan, 2008). Prior to eruption, carrier melts scavenge mush-pile olivines (and their diverse melt inclusion populations), explaining the similarity in melt inclusion records in many different eruptions, and the pervasive major and trace element disequilibria between crystal cargoes and their co-erupted glasses. Entrainment of hot, primitive olivines into lower temperature carrier melts drives large amounts of PEC, creating a melt inclusion record which yields spuriously low entrapment pressures from H_2O-CO_2 barometry. Scavenging of mush-pile olivines with a restricted range of forsterite contents due to diffusive re-equilibrium into carrier melts can account for the approximately linear olivine addition trends in whole rock compositions at Kīlauea (projecting back to $Fo_{86-87.5}$; Helz et al., 2015; Helz et al., 2014). The linearity of

these trends has previously been explained by delayed fractionation (Maaløe et al., 1988). However, this explanation is inconsistent with the peaked distribution of primitive olivine compositions, and the large degree of trace element disequilibrium between melt inclusions and matrix glasses (Fig. 5.4c). Overall, these findings challenge the common assumption that the most primitive crystals provide the most pristine record of pre-eruptive processing.

5.4 Conclusions

The compositional relationships between melt inclusions, host olivines, and co-erupted carrier liquids at Kīlauea Volcano reveals that primitive crystal cargoes are stored in mush piles for centuries before their eventual eruption in chemically unrelated carrier liquids. The mush pile likely resides at the base of the deeper South Caldera magma reservoir (∼3–5 km depth; Fig. 5.9).

Primitive olivine crystals trap melt inclusions from this reservoir, which experiences cyclic variations in magma chemistry, and settle into extensive mush piles. Melt inclusions erupted in 1959, 1969, 1973, and 1974 exhibit Nb/Y ratios that were last observed in erupted lavas in ∼1790; providing evidence that crystals were stored for almost two centuries (and possibly much longer) before their eruption. Only more evolved olivines, which formed within the shallower (∼1 km) HMM reservoir, are true phenocrysts providing a record of the processes that occurred in the days to weeks prior to the eruption of a given magma batch (Fig. 5.9).

The history of pre–eruptive processes preserved in melt inclusions can be obscured by accumulation and storage of inclusion–bearing crystals in mushes, followed by crystal scavenging by new carrier liquids. This decoupling of inclusions and crystals from their carrier liquids may be commonplace at volcanoes where high melt fluxes create long–lasting magma reservoirs and associated mush piles. While the processes acting to degrade the melt inclusion record following entrapment are well recognised, this study demonstrate that the common assumption that melt inclusions record pre–eruptive processes is flawed in mush–rich systems. However, scavenged melt inclusion records are far from redundant; they provide novel insights into the storage, and subsequent remobilization, of crystals in magmatic mush piles.

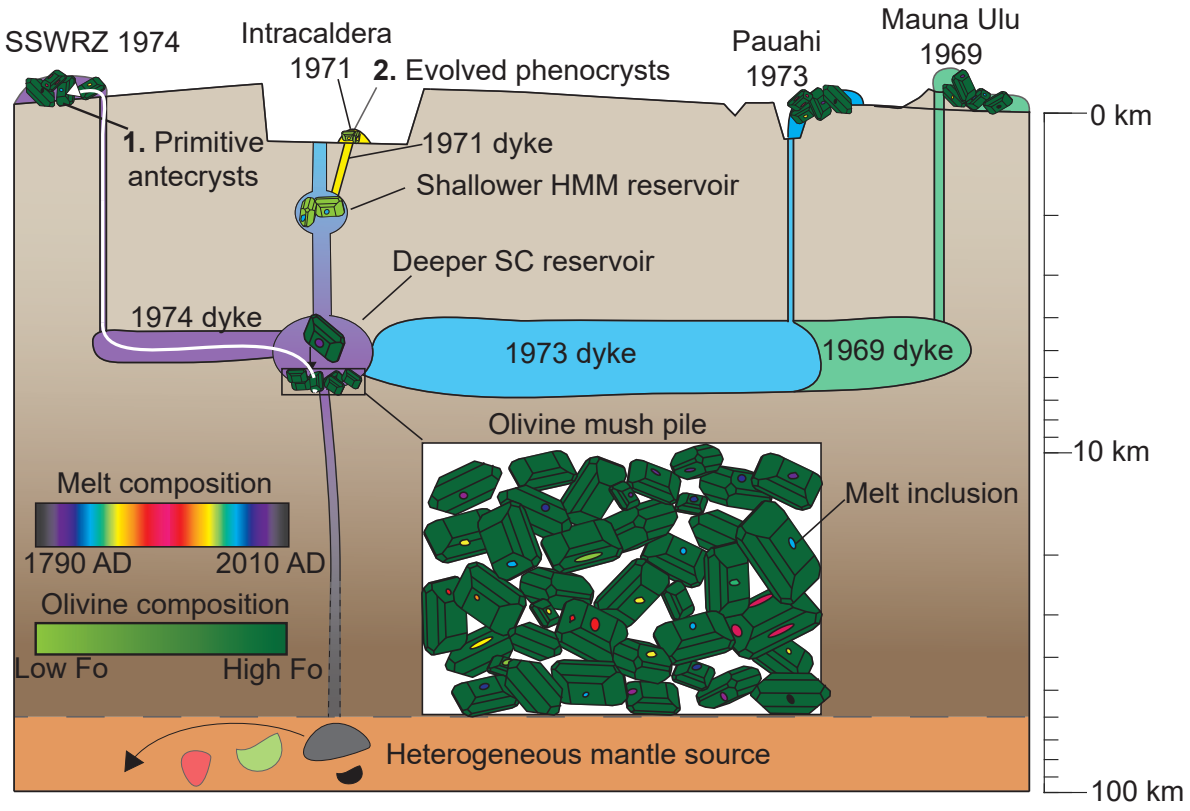


Figure 5.9: Diverse melt compositions are produced by a heterogenous mantle source (Pietruszka et al., 2015; Pietruszka et al., 2018; Pietruszka and Garcia, 1999b; Pietruszka and Garcia, 1999a). Mixing processes on ascent and during reservoir replenishment produce a near homogeneous reservoir composition which changes progressively with time (black-red-black over ∼200 yrs, Fig. 5.4a). At a given time, relatively homogeneous reservoir compositions produce melt inclusions with a narrow range of trace element compositions. Olivines (containing melt inclusions) settle to form extensive mush piles at the base of the SC reservoir (see Chapter 4). Rift zone and extracaldera eruptions are supplied by dykes propagating from the SC reservoir. These erupted liquids scavenge antecrysts from mush piles just prior to eruption, and acquire a melt inclusion record which sampled changing reservoir compositions over centuries to millennia, hosted in a chemically unrelated carrier liquid **(1.)**. In contrast, intracaldera eruptions (e.g. August 1971) are supplied by dykes propagating from the upper HMM reservoir (Pietruszka et al., 2015; Pietruszka et al., 2018). These dykes transport phenocrystic olivines to the surface along with the carrier melts in which these olivines crystallized **(2.)**. Magma transport to each eruption site is shown as a dyke tapping the composition of the reservoir at that point in time (after Pietruszka et al., 2018).

Published as: *Wieser, P.E., Jenner, F.E., Edmonds, M., Maclennan, J. and Kunz, B., 2020, December. Chalcophile elements track the fate of sulfur at Kīlauea Volcano, Hawai'i. GCA.* `https://doi.org/10.1016/j.gca.2020.05.018`
Code available at `https://github.com/PennyWieser/Sulfide_Present_Melting_GCA_Wieser2020`. *Figures reproduced from EarthArxiv under a CC-BY licence.*

6

Chalcophile elements track the fate of sulfur at Kīlauea Volcano, Hawai'i

Abstract

Chalcophile element concentrations in melt inclusions and matrix glasses may be used to investigate low pressure degassing processes, as well as sulfide saturation during crustal fractionation, and mantle melting. Erupted products from Kīlauea Volcano, Hawai'i record three stages of sulfide saturation (in the mantle, crust, and within lava lakes), separated by episodes of sulfide resorption (i.e., sulfide undersaturation) during ascent through the thick Hawaiian lithosphere, and during syn-eruptive degassing. The presence of residual sulfides in the mantle source throughout the melting interval accounts for the high S concentrations of Kīlauean primary melts (1387–1600 ppm). Residual sulfides retain chalcophile elements during melting, decoupling the variability of these elements in high MgO melts from that of lithophile elements. Decompression associated with magma ascent through the thick Hawaiian lithosphere drives an increase in the sulfide concentration at sulfide saturation ($SCSS^{2-}$), resulting in shallow storage reservoirs (∼1–5 km depth) being supplied with sulfide-undersaturated melts. A drop in temperature, coupled with major element changes during the fractionation of olivine, causes the $SCSS^{2-}$ to decrease. Combined with an increase in melt S contents during fractionation, this initiates a second stage of sulfide saturation at relatively high MgO contents (∼12 wt%). Syn-eruptive degassing of S drives the resorption of sulfides in contact with the carrier liquid. The covariance structure of Cu, MgO and Ni contents in melt inclusions and matrix glasses indicates that the dissolution of sulfides effectively liberates sulfide-hosted Cu and Ni back into the melt, rather than the vapour phase. The contrasting behaviour of Cu, Ni, Se and S during sulfide resorption indicates that the chalcophile element signature of the Kīlauean plume is largely controlled by silicate melt-vapour partitioning, rather than sulfide-vapour partitioning. The participation of dense sulfide liquids in shallow degassing processes may result from their direct attachment to buoyant vapour bubbles, or olivine crystals which were remobilized prior to eruption. Sulfide

resorption obscures the textural and chemical record of sulfide saturation in matrix glasses, but not in melt inclusions, which are isolated from this late-stage release of chalcophile elements. The partitioning of S between the dissolving sulfide, melt and the vapour phase accounts for approximately 20% of the total S release into the atmosphere.

6.1 Introduction

Volcanic eruptions emit vast quantities of sulfur (S) and sulfur-loving (chalcophile) elements to the atmosphere, causing perturbations to the global climate system and regional air quality (Robock, 2000; Witham and Oppenheimer, 2004). For example, during the last 35 years, the near-continuous effusion of lava at Kīlauea Volcano, Hawai'i has released globally significant amounts of S to the lower troposphere, culminating in fluxes of >50,000 t/day SO_2 during the lower East Rift Zone eruption in 2018 (Neal et al., 2019). These emissions have serious implications for regional air quality, respiratory health and agricultural productivity across the island (Longo et al., 2010; Nelson and Sewake, 2008; Tam et al., 2016; Whitty et al., 2020).

The concentrations of S and chalcophiles in primary melts entering basaltic systems are predominantly controlled by the behaviour of sulfide during mantle melting (Ding and Dasgupta, 2018). During crystallization in crustal magma chambers, S contents may increase due to the fractionation of S-poor silicate phases, or become buffered by the stabilization of an immiscible sulfide phase (Smythe et al., 2017). Tracking the pre-eruptive evolution of S is non-trivial; erupted lavas have typically lost ∼90% of their original S (Métrich and Mandeville, 2010), and evidence for sulfide fractionation may be obscured by the resorption of sulfides during low pressure degassing (Edmonds and Mather, 2017; Moore et al., 1980). These problems are often circumvented by measuring S contents in melt inclusions (pockets of melt trapped within growing crystals that are less susceptible to degassing than erupted carrier liquids), or through measurements of refractory chalcophile element abundances in quenched matrix glasses (Jenner et al., 2010; Reekie et al., 2019). However, these archives can be degraded by petrological processes; the concentrations of chalcophile elements in melt inclusions may be altered by the secondary growth of sulfide phases post-entrapment (e.g., Hartley et al., 2017). Additionally, S concentrations in melt inclusions at Kīlauea are highly variable within a given sample, possibly due to the mixing of degassed and undegassed melts at depth (identified in submarine glasses by Dixon et al., 1991), or the entrapment of melt inclusions during late-stage degassing (Thornber et al., 2015). The alternative approach, where the concentrations of refractory chalcophile elements in matrix glasses are used as a proxy for S, relies on the assumption that these elements are significantly less volatile than S, so are resistant to low pressure degassing. For example, Se has been used to reconstruct the pre-degassing behaviour of S in subaqueous lavas under the assumption that it behaves identically to S (as available thermodynamic data indicated that SeO_2 would not be stable in

the gas phase; Jenner et al., 2010; Reekie et al., 2019). However, measurements of significant fluxes of Se within volcanic plumes emitted at Kīlauea and other basaltic volcanoes indicate that Se has volatile tendencies, at least in subaerial eruptions (Crowe et al., 1987; Edmonds et al., 2018; Mather et al., 2012). Furthermore, lavas from Antuco, Chile, have recently been shown to have S and Se contents which are significantly lower than mid-oceanic ridge basalts (MORB), supporting the hypothesis that Se degasses at low pressures (Cox et al., 2019).

In this paper, the behaviour of S and other chalcophile elements (Cu, Zn, Mo, Cd, In, Sn, Sb, W, Tl, Bi, Se, As) from the Hawaiian mantle source to the volcanic vent was assessed using a suite of melt inclusions and matrix glasses from Kīlauea Volcano. Previous studies investigating sulfide saturation and chalcophile element behaviour at Kīlauea have been restricted to subaerial lavas which have fractionated beyond olivine control (<6–7 wt% MgO; e.g., those erupted during the 1955 and 1977 eruption; Desborough et al., 1968; Helz and Wright, 1992; Moore et al., 1980). There has been a particular focus in the literature on chalcophile element behaviour in lava lakes formed by the ponding, and subsequent fractionation, of degassed melt in pre-existing pit craters (Greaney et al., 2017; Skinner and Peck, 1969; Fleet and Stone, 1990). Until now, the most primitive glass composition at Kīlauea analysed for chalcophile elements had a MgO content of only 6.1 wt% (Fig. 6.1a; Greaney et al., 2017). In contrast, the spatter and scoria samples investigated in this study span a range of MgO contents (5.7–10.0 wt%; Chapter 5), and were rapidly quenched following eruption, providing new insights into the behaviour of chalcophile elements during mantle melting and fractional crystallization at Kīlauea.

Ratios of chalcophile to lithophile elements in erupted melts (e.g., Pb/Ce, S/Dy, Sb/Pr) are frequently used to gain insight into various aspects of mantle evolution (Jochum and Hofmann, 1997; Hofmann, 1997; Kelley et al., 2013; Newsom et al., 1986; Saal et al., 2002). These studies generally assume that lithophile and chalcophile elements behave similarly during mantle melting, neglecting the complex changes in chalcophile element concentrations with increasing melt fraction that occur when residual sulfides are present in the mantle source. The fate of sulfides during mantle melting for mid-ocean ridge and ocean island basalts remains uncertain (Ding and Dasgupta, 2018). Variations in the concentrations of platinum group elements (PGEs) in lavas across the Hawaiian islands, along with elevated Cu/Pd ratios, have been attributed to variable abundances of residual sulfide in the Hawaiian mantle plume (Bennett et al., 2000). In contrast, Greaney et al. (2017) estimate the chalcophile element concentration of the Kīlauean mantle source from the batch melting equation under the assumption of sulfide-absent melting. As the bulk partition coefficients between the mantle residue and melt (bulk K_D) for chalcophile elements are substantially higher if sulfides are present in the mantle source, sulfide-free melting models will underestimate the concentrations of these elements in the mantle source if residual sulfides are in fact present. Clearly, the fate of mantle sulfides during melting must be

critically evaluated before chalcophile element signatures can be used to assess the presence or absence of recycled materials in the Hawaiian mantle plume (e.g., Greaney et al., 2017).

The point at which sulfides saturate during fractional crystallization in Hawaiian melts is also debated (Greaney et al., 2017; Bennett et al., 2000; Desborough et al., 1968; Dixon et al., 1997; Helz et al., 2017; Tatsumi et al., 1999; Wallace and Anderson, 1998). It has been demonstrated, using the chalcophile element systematics of mid-ocean ridges and oceanic plateaux, that a second stage of sulfide saturation often occurs following ascent of magmas from the mantle and fractional crystallization of these sulfide-undersaturated melts in the crust (Jenner, 2017; Reekie et al., 2019). This second stage of sulfide saturation is driven by an increase in S concentrations during fractional crystallization (as S is incompatible in most silicate minerals), along with a possible decrease in the sulfide (S^{2-}) solubility at sulfide saturation (SCSS), due to dropping temperature and changes in melt chemistry (Smythe et al., 2017). Specifically, the SCSS describes the amount of S^{2-} present in a silicate melt in equilibrium with a sulfide phase (O'Neill, 2020; hereafter $SCSS^{2-}$ for clarity). While PGE fractionation trends in Hawaiian lavas have been attributed to sulfide saturation (Tatsumi et al., 1999), recent Cu measurements in whole-rock and glasses from the Kīlauea Iki lava lake show that Cu behaves incompatibly until ∼2 wt% MgO, leading to suggestions that sulfides only saturate following extensive fractional crystallization (Greaney et al., 2017; Fig. 6.1a). Furthermore, although sulfides are present in eruption pumices and lake samples from Kīlauea Iki with MgO>2 wt%, the wide variability in bulk sulfide composition has been attributed to sulfide formation during late-stage processes such as quenching, rather than during primary sulfide-liquid immiscibility (Stone and Fleet, 1991). The new data presented in this Chapter challenges this dominant view, and instead supports a model where almost all erupting melts at Kīlauea (<12 wt% MgO) were sulfide-saturated prior to the onset of S degassing at shallow pressures (c.f. Ding and Dasgupta, 2018; Skinner and Peck, 1969; Greaney et al., 2017; Helz et al., 2017; Pitcher et al., 2009).

Finally, the effects of syn-eruptive degassing and sulfide resorption on chalcophile element systematics were investigated by comparing the compositions of matrix glasses and melt inclusions at Kīlauea, and undegassed submarine glasses from Lōi'hi volcano. While there is growing evidence that Se degasses during subaerial eruptions (Cox et al., 2019; Mather et al., 2012), until now, Se analyses could only be conducted with laser ablation spot sizes greater than 100 µm (Jenner and O'Neill, 2012b). This prevented in-situ analyses of melt inclusions, making it difficult to pinpoint the timing of Se loss in relation to other volatile species (e.g., S). In this study, Se and As were measured in melt inclusions using a 50 µm diameter laser line scan (Fig. 2.5). This analysis demonstrates that Se and S degas almost concurrently at Kīlauea. Overall, comparisons between matrix glass and melt inclusion compositions allow us to estimate the influence of sulfide saturation, and subsequent resorption on the sulfur outgassing budget of Kīlauean eruptions.

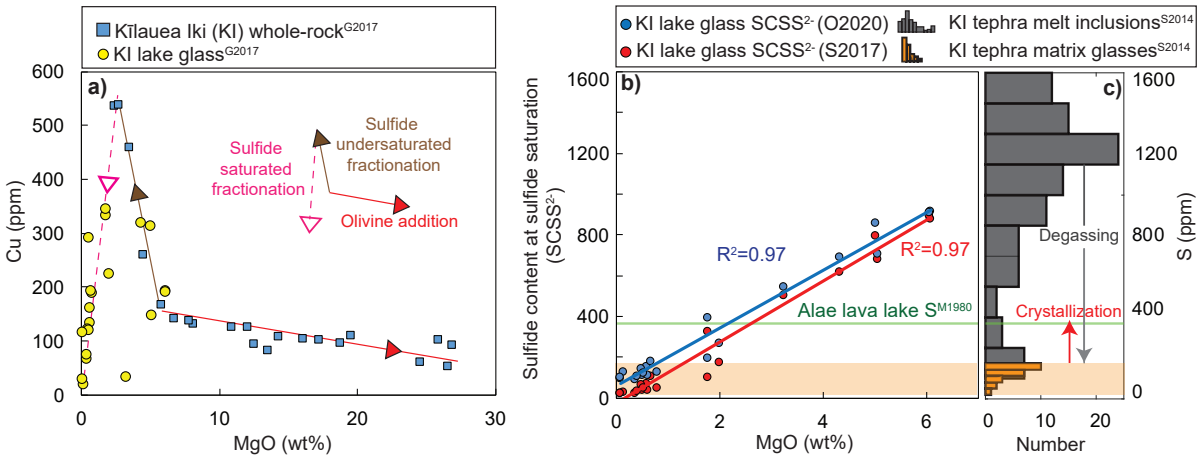


Figure 6.1: Chalcophile element behaviour in the Kīlauea Iki lava lake. **a)** Whole-rock Cu-MgO measurements from Kīlauea Iki (KI) define olivine-addition trends between 27 and 7 wt% MgO. Whole-rock and glass measurements show a rapid increase in Cu between 7 and 2 wt% MgO, followed by a rapid decrease at <2 wt% MgO (Greaney et al., 2017). The approximate vectors producing variability in Cu vs. MgO space are overlain. **b)** Calculated sulfide concentration at sulfide saturation ($SCSS^{2-}$) for the major element compositions of variably evolved glasses from the Kīlauea Iki lava lake (Greaney et al., 2017) using the Smythe et al. 2017 (S2017) and O'Neill, 2020 (O2020) models (with Fe^{3+}/Fe_T=0.1). **c)** Degassing upon eruption causes melt S contents to drop from the high concentrations observed in Kīlauea Iki melt inclusions (PEC-corrected; grey histogram; Sides et al., 2014b) to the low concentrations observed in matrix glasses (Kīlauea Iki scoria; orange histogram and bar; Sides et al., 2014b). These degassed melts have significantly lower S contents than the $SCSS^{2-}$, so are sulfide undersaturated. Major element changes and a drop in temperature associated with extensive crystallization causes a decrease in the $SCSS^{2-}$. The lake became sulfide saturated when the $SCSS^{2-}$ dropped below the S content of the melt, which probably lay between the S content measured in Kīlauea Iki pumices (orange bar; Sides et al., 2014b) and that measured in a fractionated glass from Alae lava lake (green line; Moore et al., 1980).

6.2 Methods and Sample Details

This chapter investigates chalcophile element concentrations in a suite of olivine-hosted melt inclusions and matrix glasses from the same four eruptions discussed in Chapter 5 (1969, 1971, 1973, 1974). To further constrain sulfide occurrence and chemistry at Kīlauea, scoria and lava samples from various locations across the Kīlauean edifice were examined (see Table 2.1). Sample preparation techniques, and details of EPMA, EDS and LA-ICP-MS analyses are presented in Chapter 2. This Kīlauean dataset was also supplemented with chalcophile element analyses of 18 submarine glasses from Lōi'hi Volcano collected using submersibles at water depths of ~980–4700 m (Garcia et al., 1998; Garcia et al., 1993; Pietruszka et al., 2011). Analyses of these Lōi'hi samples were performed by Frances Jenner.

6.3 Results

6.3.1 Glass and Melt Inclusion Chemistry

Matrix glasses from the three Kīlauean rift eruptions (Mauna Ulu, 1969, Pauhi Crater, 1973, and SSWRZ, 1974) are relatively primitive, with 7.4–10 wt% MgO (Fig. 6.2a), and 10.2–11.2 wt% CaO. Their major element systematics, along with the absence of clinopyroxene and plagioclase crystals, indicate that these lavas experienced only olivine (+minor chrome-spinel) fractionation (Wright and Fiske, 1971). The high MgO contents of these glasses relative to the vast majority of subaerial Kīlauea deposits (Helz et al., 2014), combined with their simple fractionation trajectories, makes them suitable for assessment of the behaviour of chalcophile elements during mantle melting. Glasses from the 1971 summit eruption are more evolved than the three rift eruptions (5.7–6.6 wt% MgO, 10.7–11.1 wt% CaO; Fig. 6.2a) and contain small crystals of clinopyroxene. Lōi'hi glasses are variably evolved, with MgO contents between 5.1 and 7.9 wt% MgO. Uncorrected Kīlauean melt inclusions have MgO contents which overlap with the MgO content of their co-erupted erupted matrix glasses (Fig. 6.2a). The amount of post-entrapment crystallization calculated using the Petrolog3 Olivine MI tool (Danyushevsky and Plechov, 2011) at QFM assuming FeO*=11.33 wt% (for consistency with previous studies; Chapter 5; Sides et al., 2014b; Sides et al., 2014a) varies from -12 to 29%. Corrected melt inclusion MgO contents lie between 6.9 and 13.3 wt% (Fig. 6.2b).

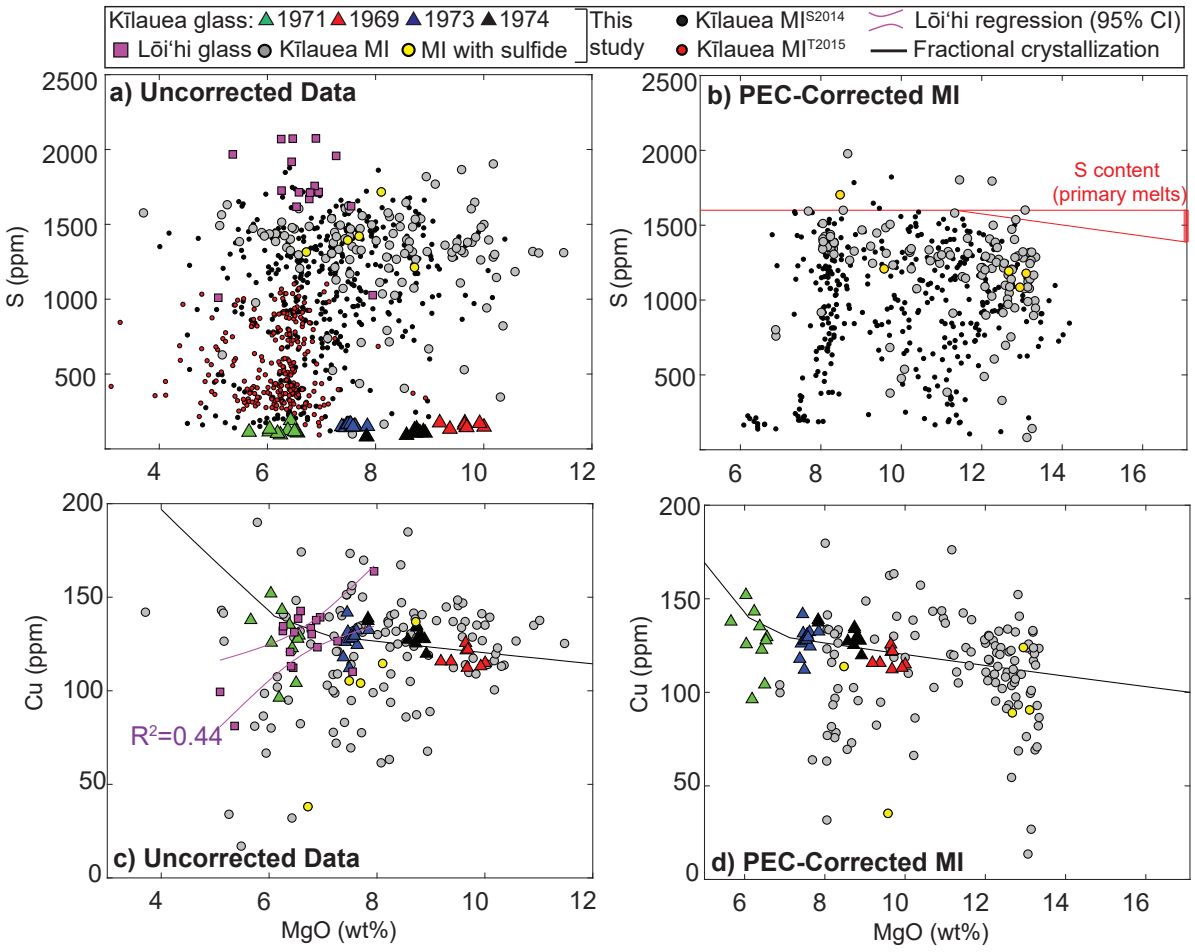


Figure 6.2: Cu, S and MgO systematics. **a)** S concentrations of Kīlauean melt inclusions and subaerial matrix glasses, and submarine matrix glasses from Lōi'hi. Literature melt inclusion data for Kīlauea from Sides et al. (2014b) and Sides et al. (2014a) (black dots) and Thornber et al. (2015) (red dots) are also show. Melt inclusions containing a sulfide (<0.2 vol%) are coloured yellow. **b)** Melt inclusion S and MgO systematics following a correction for post-entrapment crystallization (using the Olivine MI tool in Petrolog3). Estimated S concentrations of primary melts are shown with a vertical red line. The upper limit (1600 ppm) effectively brackets the vast majority of S-rich melt inclusions, while the lower limit (1387 ppm) was calculated by extrapolating back along olivine fractionation trends from 1600 ppm at 11.3 wt% MgO to ~17.1 wt% MgO (Clague et al., 1991) assuming S was entirely incompatible during olivine fractionation. **c)** Kīlauean matrix glasses show a slight increase in Cu contents with decreasing MgO, while Lōi'hi glasses show a decrease in Cu with decreasing MgO. Uncorrected melt inclusions with >10 wt% MgO plot alongside, and slightly above Kīlauean matrix glasses, while more evolved inclusions predominantly plot below matrix glasses. **d)** Following a correction for PEC ($K_{D,\ Cu}^{ol/melt} = 0.1$), melt inclusions form a cluster at ~13–14 wt% MgO, plotting on the fractionation trajectory defined by matrix glasses (black lines), although a number of inclusions lie significantly below this line. The fractional crystallization model for Cu was calculated from the Petrolog3 fractionation path buffered at QFM+0.3 described in the text.

Uncorrected Kīlauean melt inclusion compositions from this study and the literature show variable S contents, from ∼100–1904 ppm (Fig. 6.2a), while melt inclusion compositions corrected for post-entrapment crystallization (assuming S behaves incompatibly during crystallization of olivine) are between 82 and 1978 ppm (Fig. 6.2b). Kīlauean matrix glasses have substantially lower S contents (∼82–190 ppm) than melt inclusions, while submarine Lōi'hi matrix glasses have S contents which slightly exceed those in even the most S-rich Kīlauean melt inclusions (∼1010–2073 ppm; Fig. 6.2a). Melt inclusions with the highest S concentrations have Cl concentrations extending to higher values than erupted matrix glasses, although the correlation between Cl and S for the combined Kīlauean dataset is weak (R^2=0.14; Fig. 6.3a). In contrast, there is a strong correlation between S and Se (R^2=0.90; Fig. 6.3b), and a moderate correlation between S and Bi (R^2=0.35; Fig. 6.3c). Lōi'hi glasses have similar Se, Bi, Cd and Cu concentrations to the most S-rich Kīlauean melt inclusions, but significantly higher Cl, and lower As concentrations (Fig. 6.3a, d).

Kīlauean matrix glasses show a slight increase in Cu with decreasing MgO (Fig. 6.2c), consistent with literature observations of Cu systematics from the Kīlauea Iki lava lake (Greaney et al., 2017; Fig. 6.1a). In contrast, the more restricted sample set of Lōi'hi glasses shows a decrease in Cu with decreasing MgO (R^2=0.44; Fig. 6.2c). Uncorrected Kīlauean melt inclusions show Cu contents which overlap with and extend to significantly lower values than matrix glasses (Fig. 6.2c). Following a correction for post-entrapment crystallization (assuming $K_{D,\ Cu}^{ol/melt} = 0.1$; Greaney et al., 2017), approximately half of melt inclusions with high MgO contents (∼12–14 wt%) lie on the extension of the fractional crystallization trajectory defined by matrix glasses, while the other half plot to significantly lower Cu concentrations. The majority of inclusions with <10 wt% MgO have lower Cu contents than matrix glasses (Fig. 6.2d).

The trace element compositions of matrix glasses from the three rift eruptions which have not fractionated beyond olivine control (MgO>6.8 wt%; Wright and Fiske, 1971) were corrected for the effect of variable olivine fractionation by projecting back to 17.1 wt% MgO (Clague et al., 1991) using the reverse crystallization tool in Petrolog3. For simplicity, all elements except Cu ($K_{D,\ Cu}^{ol/melt} = 0.1$) were assumed to be entirely incompatible in olivine. Fractionation-corrected (FC) glass compositions exhibit strong positive correlations between highly incompatible lithophile elements (e.g., Ba vs. Ce, Ba vs. La; Fig 4a-b). In contrast, more compatible elements such as Yb, as well as Cu, Cd and Pb show weak, or even slightly negative correlations against Ba (Fig. 6.4c-f).

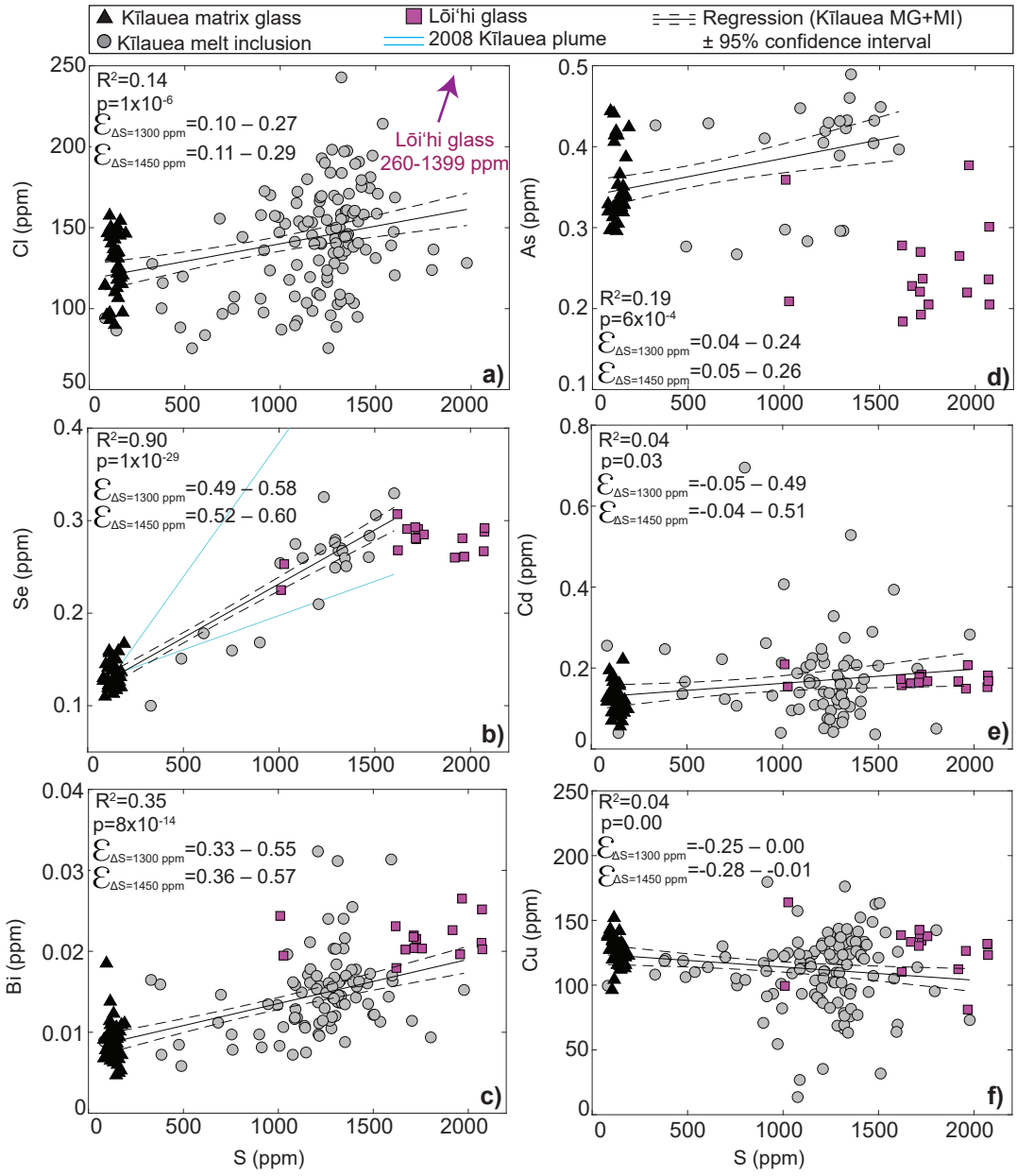


Figure 6.3: Assessing chalcophile element volatility. **a-f)** Plots of various chalcophile elements (and Cl) against S provide insights into elemental volatility. Linear regressions through the combined Kīlauea dataset (matrix glasses and melt inclusions from all 4 eruptions) are shown with 95% confidence intervals. The upper and lower limits of the initial and final concentrations of each element used to calculate emanation coefficients (ε) were estimated from the 95% confidence intervals of the regression lines for S_f=135 ppm, and S_i=1435 ppm and 1585 ppm (ΔS=1300 ppm and 1450 ppm respectively, see Fig. 6.16). PEC-corrected concentrations are shown for melt inclusions, assuming that all elements except Cu ($D_{Cu}^{ol/melt} = 0.1$) are entirely incompatible in olivine. Note, that the y axis in **a)** has been cropped to emphasize the magnitude of Cl variation at Kīlauea, Lōi'hi glasses have Cl concentrations up to 1399 ppm. The range of S/Se ratios observed in the 2008 summit plume are shown in **b)** to demonstrate that the emanation coefficient of Se derived from petrological measurements is consistent with aerosol measurements (Mather et al., 2012). A full comparison of emanation coefficients calculated in this study and those of Mather et al. (2012) is shown in Fig. 6.17.

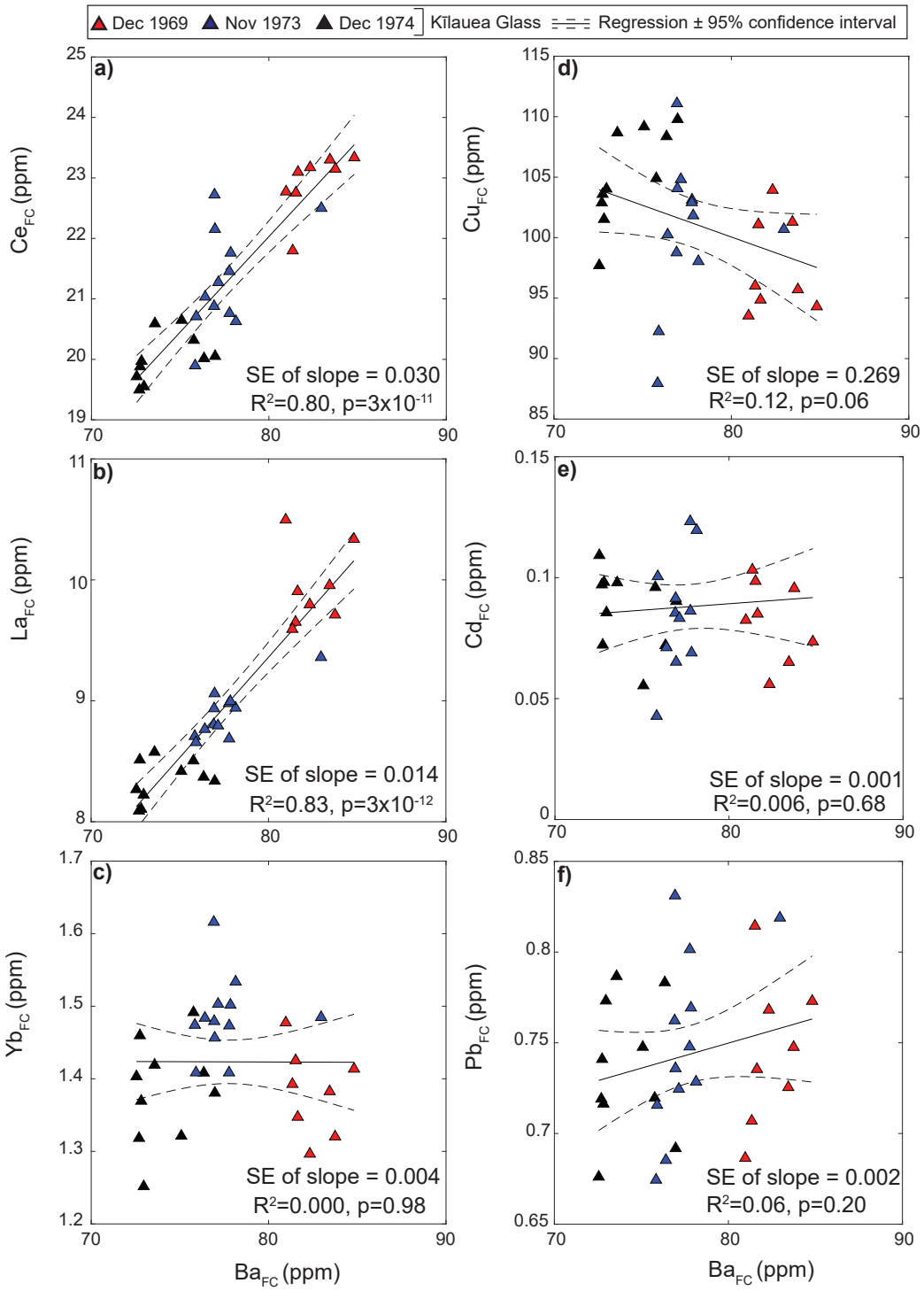


Figure 6.4: Fractionation-corrected trace element concentrations in matrix glasses from the three rift eruptions which have only fractionated olivine (+ minor chromite). **a-b)** Ce and Le show strong positive correlations with Ba. **c-f)** In contrast, Yb, Cu, Cd and Pb show very weak correlations with Ba. Trace element contents were corrected for fractional crystallization (to 17.1 wt% MgO; Clague et al., 1991) assuming all elements except Cu ($^{ol/melt}_{D,\ Cu} = 0.1$) were perfectly incompatible in olivine. The 95% confidence intervals on linear regressions through the data are shown, along with the standard error of the slope (and other statistical measures).

6.3.2 Sulfide Occurrence

Automated BSE-SE mapping identified sulfides in erupted products from seven different subaerial eruptions at Kīlauea (with glass MgO contents ranging from ~6–10 wt%). Sulfides are relatively rare, but were observed in three textural contexts:

1. Included in olivine crystals (Fig. 6.5a), often alongside spinels, and highly variable quantities of melt. Sulfide to melt volume proportions vary from >5% (Figs. 6.5f, g, h) to <0.2% (e.g., ~0.04 vol% in Fig. 6.5e).
2. Within glassy, relatively open embayments with moderate to high S contents (Fig. 6.5c, d). In one instance, the sulfide is attached to the face of the olivine crystal (Fig. 6.5c).
3. In the walls of melt inclusion vapour bubbles and matrix glass vesicles (Fig. 6.5b, 6.6, 6.7).

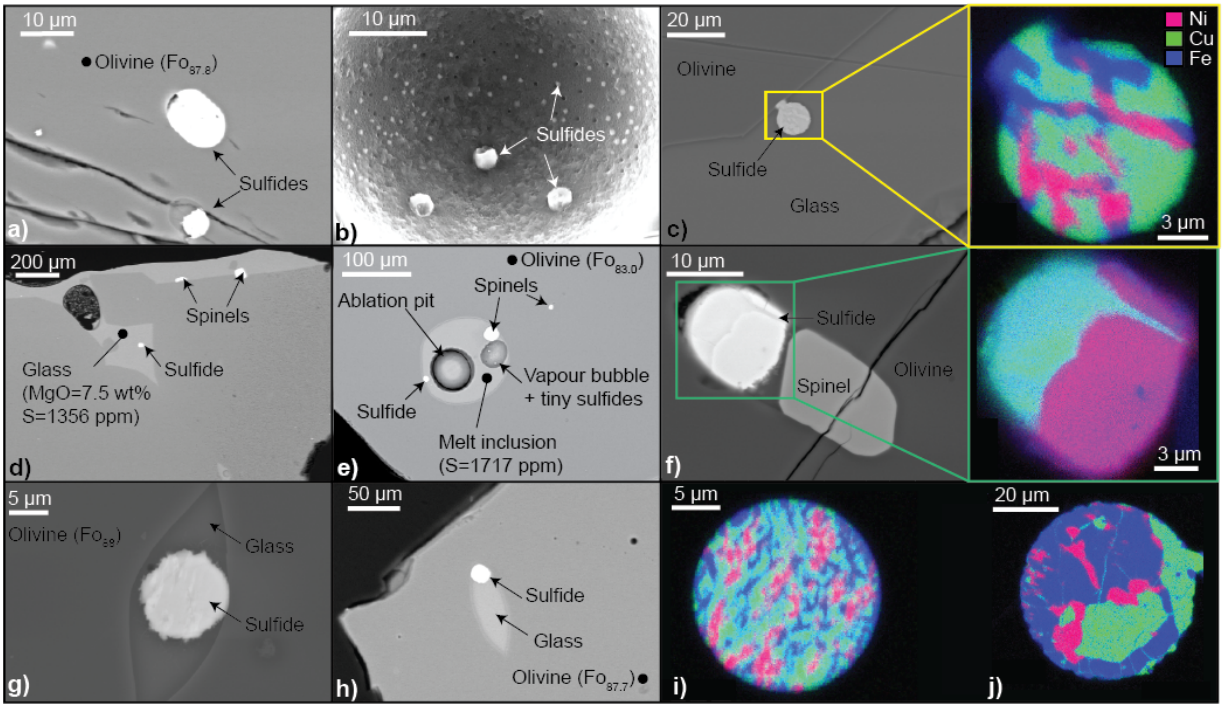


Figure 6.5: Textural and chemical characteristics of Kīlauean sulfides revealed with BSE and EDS mapping. **a)** Sulfides are hosted as inclusions within olivine crystals with high forsterite (Fo) contents. **b)** Sulfides with a bimodal size distribution within the wall of a melt inclusion vapour bubble. **c)** Sulfide attached to an olivine crystal within a relatively open embayment. EDS maps show that this sulfide consists of exsolved Fe, Ni and Cu-rich phases. **d)** Sulfide within an open, but undegassed embayment (S=1356 ppm). **e)** Sulfide within a melt inclusion, which also contains a vapour bubble with tiny <1 µm sulfides embedded in the bubble wall. **f)** Sulfide trapped within an olivine crystal alongside a spinel, and a small amount of melt. EDS maps show that this sulfide has exsolved 2 main phases at a relatively course scale. **g-h)** Sulfides trapped along with small pockets of melt within olivine crystals. **i-j)** EDS maps of sulfides showing fine and coarse exsolution of Cu-Ni-Fe rich phases (BSE images not shown).

Sulfides are roughly spherical to ellipsoidal, with diameters between 3 and 30 µm, except for sulfides in the walls of matrix glass vesicles and melt inclusion vapour bubbles, which have diameters of ∼0.5–3.0 µm (Fig. 6.5b). EDS mapping reveals that sulfides consist of exsolved Cu- and Ni-rich phases, often with a separate Fe-rich phase (Fig. 6.5c, f, i, j). These textures likely result from the exsolution of monosulfide-intermediate solid solution (MSS-ISS) phases from an immiscible sulfide liquid (Czamanske and Moore, 1977; Patten et al., 2012). These findings build on literature reports; sulfide inclusions have been noted in primitive olivines erupted in Kīlauea Iki pumices ($Fo_{88.5}$; Helz, 1987), and within silicate phases and matrix glass from the 1955 and 1977 eruptions of Kīlauea (Desborough et al., 1968; Helz and Wright, 1992; Moore et al., 1980). Interestingly, only three sulfides were found in Kīlauean matrix glasses in comparison to the 14 sulfides found when mapping a roughly equivalent area of olivine crystals. Sulfides within matrix glasses have complex external morphologies (Fig. 6.8) compared with the smooth, spherical morphology of sulfides hosted within olivine crystals, embayments, and melt inclusions (Fig. 6.5). EDS mapping reveals that sulfides with these complex morphologies are predominantly composed of Fe and O, with only small quantities of Cu, Ni and S-rich material (∼1 µm; Fig. 6.8). In contrast, spherical sulfides are O-poor (<4 wt%). Approximately spherical, O-poor sulfides with comparable exsolution textures to those found within Kīlauean olivines and melt inclusions are relatively abundant within Lōi'hi matrix glasses. No texturally complex, O-rich sulfides were observed in Lōi'hi glasses.

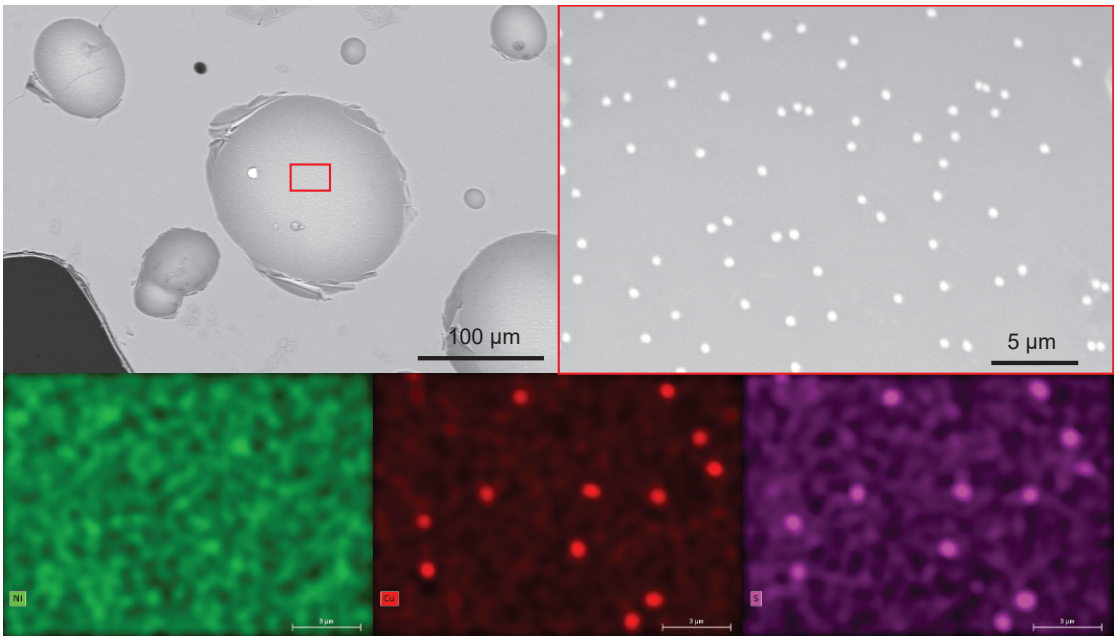


Figure 6.6: Tiny Fe-Cu-rich sulfides within matrix glass vesicles.

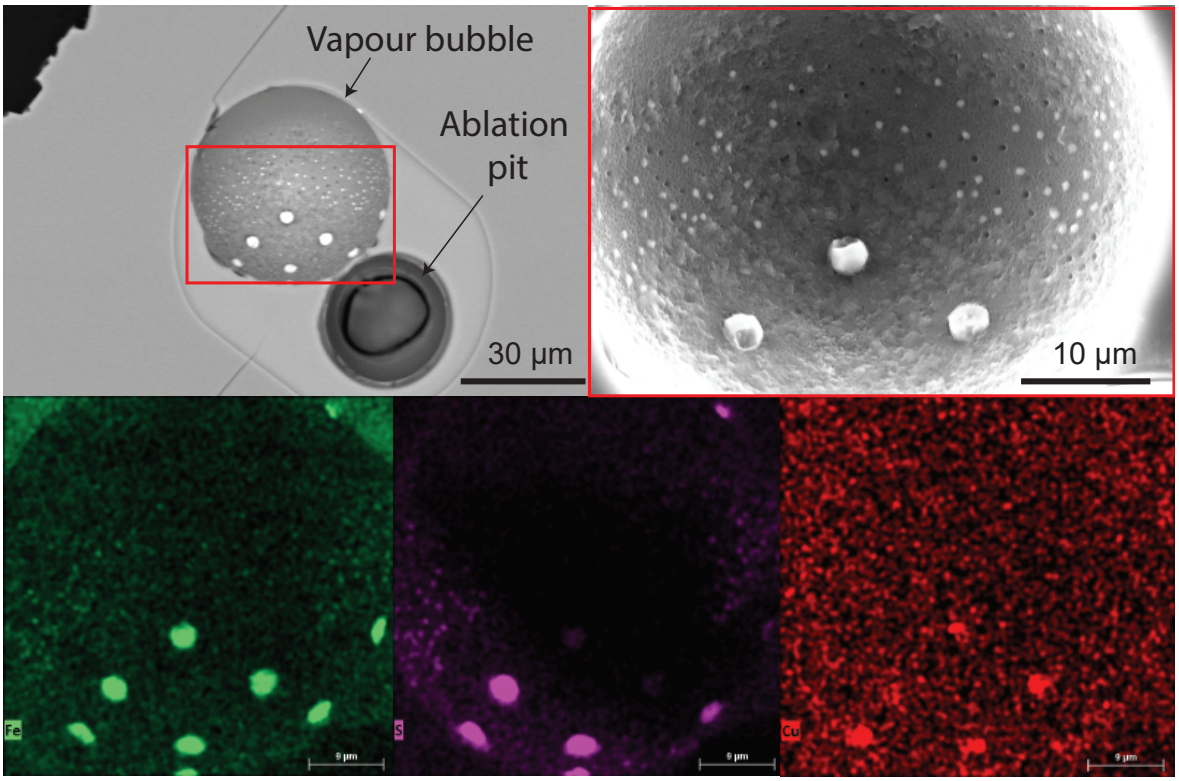


Figure 6.7: Bimodal-sized Fe-Cu rich sulfides within a melt inclusion vapour bubble.

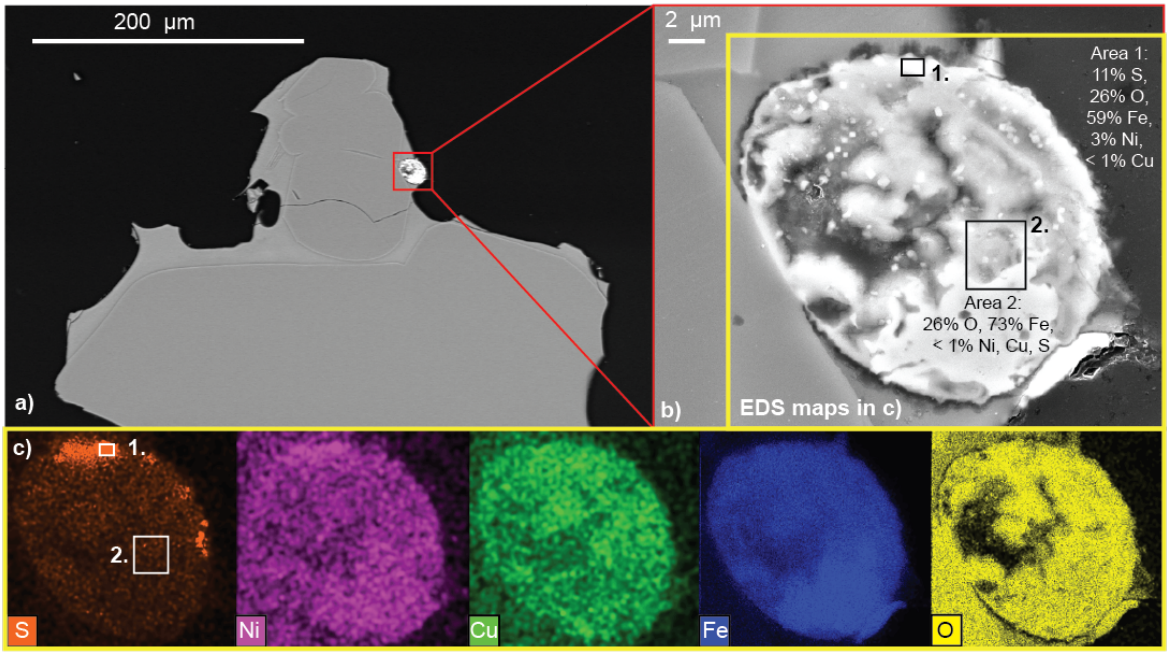


Figure 6.8: Textural and chemical characteristics of resorbed Kīlauean sulfides **a)** A BSE image of a resorbed sulfide attached to an olivine crystal. **b)** BSE image of the sulfide (red square in **a)**, which shows considerable textural complexity compared to the pristine sulfides shown in Fig. 6.5. **c)** EDS maps of the area indicated by the yellow rectangle in b). Most of the resorbed sulfide is very Ni, S and Cu poor, with counts only just above background (e.g., compare area 2 with Fig. 6.5c, f, i, j). Small regions of more S (and Ni)-rich material survive (e.g. area 1). The areas indicated with black rectangles were quantified in Esprit2.1 to give an approximate indication of their composition in wt%. Resorbed sulfides contain considerable quantities of O (∼26 wt%), compared to pristine sulfides which generally contain <4 wt% O.

6.4 Discussion

6.4.1 Sulfides in Kīlauea's Mantle Source

The fate of sulfides during mantle melting can be assessed by comparing the S concentrations of primary Kīlauean melts to models of the sulfide content at sulfide saturation ($SCSS^{2-}$). If residual sulfides are present during mantle melting, the concentration of S^{2-} in the melt is equal to the $SCSS^{2-}$; once sulfides are exhausted, the S^{2-} concentration in melts drops to significantly lower values than the $SCSS^{2-}$ (Ding and Dasgupta, 2018). Thus, if residual sulfides are present throughout the melting interval, the calculated $SCSS^{2-}$ should be approximately equal to the S^{2-} concentrations in primary Kīlauean melts. In contrast, if the mantle has exhausted sulfide, primary melts should have significantly lower S^{2-} concentrations than the $SCSS^{2-}$.

The S content of primary melts at Kīlauea was estimated from PEC-corrected S contents in melt inclusions (this study and Sides et al., 2014a,b). The upper limit was set at 1600 ppm, based on the approximately constant upper limit of S in PEC-corrected melt inclusion data (ignoring a small number of inclusions with significantly higher S; horizontal red line; Fig. 6.2b). As S behaves incompatibly during olivine-only fractionation, a minimum value for the primary S concentration of 1387 ppm was calculated by back-projecting the 1600 ppm observed at ∼11.3 wt% MgO to 17.1 wt% MgO (a reasonable upper limit of the MgO content for Kīlauean primary melts; Clague et al., 1991) assuming S is entirely incompatible in olivine (downward sloping red line; Fig. 6.2b).

For a given pressure, temperature, and melt composition, there are a variety of models which calculate the $SCSS^{2-}$ (e.g., Fortin et al., 2015; Li and Ripley, 2009; Li and Ripley, 2005; Smythe et al., 2017; O'Neill, 2020). However, most experiments used to calibrate $SCSS^{2-}$ models have been performed on FeS liquids, despite the fact that sulfides in basaltic lavas and mantle peridotites contain substantial quantities of Ni and Cu (Kiseeva et al., 2017; Patten et al., 2013; Smythe et al., 2017; Figs. 6.5c, f, i, j). The $SCSS^{2-}$ decreases as the ratio of Fe/(Fe+Ni+Cu) in the sulfide decreases, so $SCSS^{2-}$ models based on experiments with FeS sulfides will overestimate the predicted $SCSS^{2-}$ (Smythe et al., 2017). To account for this, only the two most recent $SCSS^{2-}$ models that include a correction for the Ni and Cu contents of sulfides were used (Smythe et al., 2017; O'Neill, 2020).

The $SCSS^{2-}$ along PT paths for a peridotitic mantle undergoing melting ascending from its solidus to the base of the lithosphere beneath the island of Hawaii were calculated for three different potential temperatures (1450°C, 1550°C, 1650°C; Fig. 6.9a). PT paths were calculated using Melt-PX (Lambart et al., 2016). The pressure at which melting terminated was calculated using estimated lithospheric thicknesses of 90–110 km (Li et al., 2004; Wölbern et al., 2006), assuming 15 km of crust with the density-depth profile of Putirka (2017), and a mantle with ρ=3300 kgm^{-3}. For simplicity, and due to a lack of experimental

data to reliably parameterize major element changes during melting at >3 GPa (Ghiorso et al., 2002), a constant primary melt composition was used for all points along the PT array in $SCSS^{2-}$ models. The primary melt composition was taken from Clague et al. (1991), reducing FeO_T by 3.2% to better fit the liquid line of descent for Kīlauea for the glasses measured in this study. The initial Cu and Ni contents of primary melts were set at Cu_i=100 ppm and Ni_i=900 ppm respectively, and the ratio of Fe^{3+}/Fe_T was set at 0.1 (Fig. 6.10a).

The $SCSS^{2-}$ models of O'Neill (2020) and Smythe et al. (2017) (hereafter O2020 and S2017 for brevity) calculate the composition of the co-existing sulfide. However, in both models (but particularly in the S2017 model), calculated sulfide compositions are more Ni-rich and Fe-poor than the vast majority of literature measurements of sulfide compositions within mantle peridotites and pyroxenites (Fig. 6.9b, see also Fig. 11 of O'Neill, 2020). Consequently, due to the strong influence of the sulfide Fe/(Fe+Cu+Ni) ratio on the $SCSS^{2-}$, model trajectories lie significantly below the range of S contents in primary melts at all pressures (Fig. 6.9c). Interestingly, the S2017 model shows a decrease in the $SCSS^{2-}$ with decreasing pressure due to changes in the sulfide composition, which is the opposite trajectory to that expected from the strong pressure dependency of the $SCSS^{2-}$. The unusual behaviour of the S2017 model, as well as the underprediction of sulfide Fe/(Fe+Cu+Ni) ratios in both models, likely reflects the fact that the parametrizations for sulfide compositions are not suitable for use at the high pressures and temperatures relevant to mantle melting beneath Hawaii. For example, in the S2017 model, sulfide compositions are calculated using the sulfide-silicate partitioning behaviour determined by Kiseeva and Wood (2015) at 1.5 GPa. In the O2020 model, parameterizations for sulfide compositions were obtained by tuning the model to minimise the least squares difference between observed S contents and the SCSS in a dataset of ocean floor glasses (Jenner and O'Neill, 2012a). Due to the absence of constraints on the controls on sulfide compositions at relevant pressures and temperatures, $SCSS^{2-}$ models where the sulfide composition was fixed at 5 wt% Cu, 20 wt% Ni, 33 wt% S, 42 wt% Fe are favoured (Ding and Dasgupta, 2018; yellow square; Fig. 6.9b).

When the sulfide composition is fixed in the S2017 model (solid lines), only melts produced right at the base of the lithosphere (beige bar; Li et al., 2004; Wölbern et al., 2006) for the hottest potential temperatures (T_p=1650°C) have $SCSS^{2-}$ values comparable to the S contents of primary melts (red bar; Fig. 6.9d). In contrast, when the sulfide composition is fixed in the O2020 model, the $SCSS^{2-}$ model trajectories (dashed lines, Fig. 6.9d) largely lie within the field defined by the S contents of primary melts. For a fixed sulfide composition, the differences between the O2020 and S2017 $SCSS^{2-}$ models largely result from their different sensitivities to the Fe^{3+}/Fe_T ratio (which primarily affects the $SCSS^{2-}$ through a decrease in $X_{FeO}^{Sil\,melt}$; O'Neill, 2020). An increase in Fe^{3+}/Fe_T from 0 to 0.2 causes the $SCSS^{2-}$ to increase by only 7% in the S2017 model, but 23% in the O2020 model.

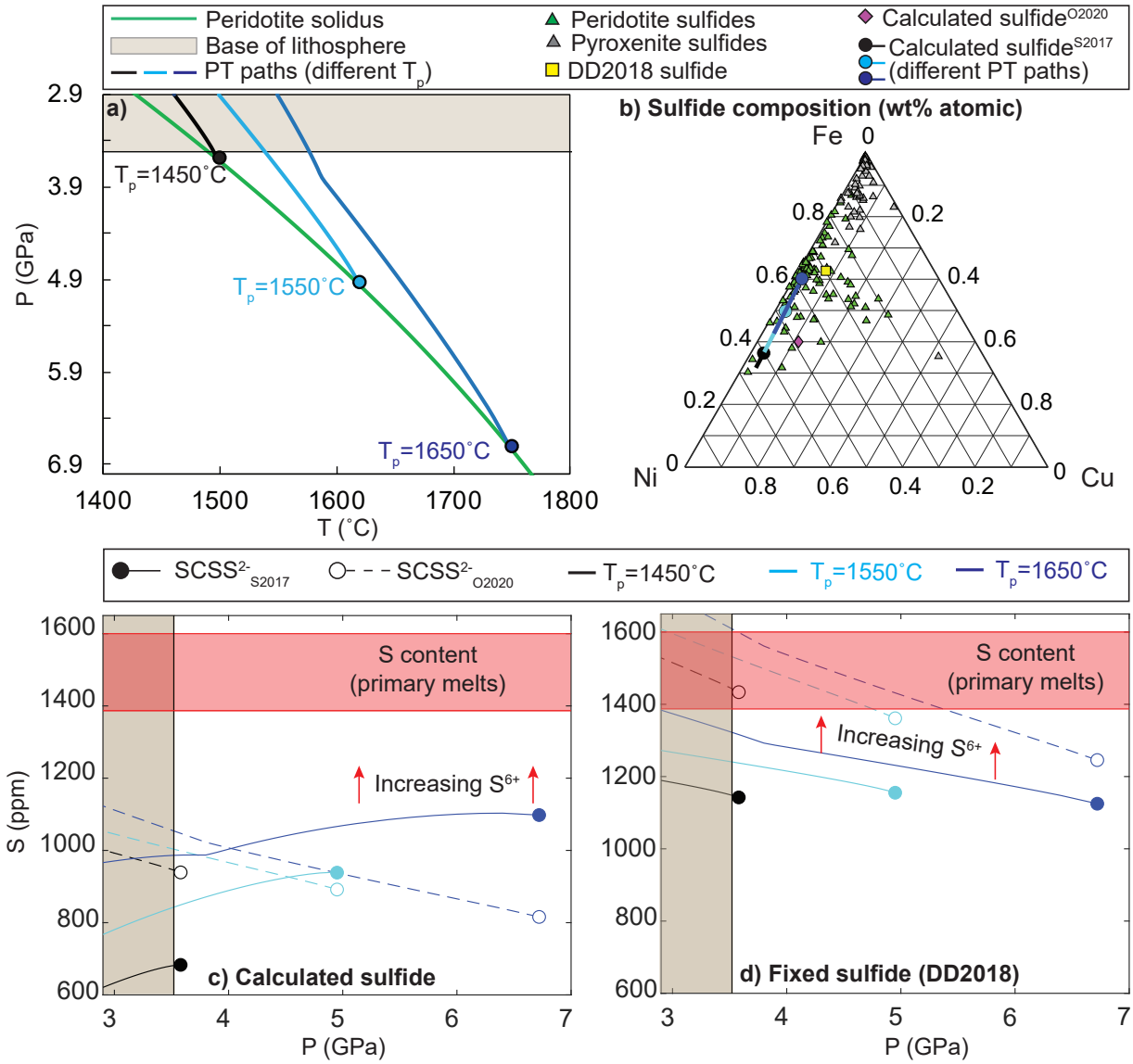


Figure 6.9: Modelling the $SCSS^{2-}$ at PT conditions relevant to mantle melting beneath Hawai'i. **a)** PT paths for an ascending peridotitic mantle undergoing melting for three different potential temperatures (calculated in Melt-PX; Lambart et al., 2016). **b)** Comparison of calculated sulfide compositions from $SCSS^{2-}$ models with measured sulfide compositions in mantle peridotites and eclogites/pyroxenites (Bulanova et al., 1996; Guo et al., 1999; Pearson et al., 1998; Richardson et al., 2001; Westerlund et al., 2006). The sulfide composition in the S2017 model changes along the PT path and deviates from measured sulfide compositions, particularly near the top of the melting column. The calculated sulfide composition from the O2020 model (magenta diamond; which does not change along the PT path) also plots away from the composition of most mantle sulfides. The fixed sulfide composition used in the models shown in **d)** is marked with a yellow square (after Ding and Dasgupta, 2018). **c)** Calculated $SCSS^{2-}$ trajectories following the PT paths in **a)** using calculated sulfide compositions. The decrease in the $SCSS^{2-}$ in the S2017 model with decreasing pressure is an artefact of the change in the composition of the sulfide. As both models predict Fe-poor sulfides compared to measured mantle sulfides, the $SCSS^{2-}$ in both models are anomalously low. **d)** Calculated $SCSS^{2-}$ trajectories using a fixed sulfide composition (yellow square in **b**). Except for melts generated right at the base of the lithosphere from a mantle with T_p=1650°C, model trajectories in the S2017 model plot below the estimated S contents of primary Kīlauean melts. In contrast, the O2020 model predicts $SCSS^{2-}$ values within the range of primary Kīlauean melts. These model differences reflect the increased sensitivity of the O2020 model to Fe^{3+}/Fe_T (set at 0.1 here, Fig. 6.10a).

Given that both models were calibrated on a dataset of reduced melts, it is difficult to critically evaluate these different model sensitivities. However, the fact that both models show $SCSS^{2-}$ values that are less than, or equal to the S contents of primitive Kīlauean magmas demonstrates that the mantle source must remain sulfide saturated throughout the melting interval. If sulfides were exhausted during melting, the S contents of melt inclusions would be lower than modelled $SCSS^{2-}$ values.

Interestingly, the S2017 model trajectories indicate that mantle melts cannot dissolve enough S^{2-} to account for the high S contents observed in primitive melt inclusions, even if the mantle is sulfide saturated (Fig. 6.2, Fig. 6.9). This discrepancy may reflect the elevated oxidation state of Hawaiian melts relative to MORB (Brounce et al., 2017; Moussallam et al., 2019; Moussallam et al., 2016; Cottrell and Kelley, 2011; Berry et al., 2018; red bars, Fig. 6.10a). The speciation of S in basaltic melts undergoes an abrupt transition from S^{2-} and S^{6+} with increasing fO_2 between QFM and QFM+2 (Jugo et al., 2010). S^{6+} species are an order of magnitude more soluble than S^{2-} species in basaltic melts, only forming a separate sulfate phase such as anhydrite at very high melt S contents (∼1.5 wt%, Jugo et al., 2005). Thus, in relatively S-poor melts such as those at Kīlauea (∼1600 ppm), the exponential increase in S^{6+} species with increasing fO_2 drives an exponential increase in the total solubility of S (Jugo et al., 2010). As models of sulfide solubility (e.g., S2017, O2020) only account for S^{2-} species, if S^{6+} species are present, a correction must be applied to $SCSS^{2-}$ model outputs to calculate the total solubility of S (hereafter $SCSS_{Tot}$):

$$SCSS_{Tot} = \frac{SCSS^{2-}}{1 - \frac{S^{6+}}{\Sigma S}} \tag{6.1}$$

For example, if the $SCSS^{2-}$ = 1300 ppm, and Kīlauean melts contained 10% S^{6+}, the $SCSS_{Tot}$ would equal 1444 ppm. Thus, the presence of even a relatively small proportion of S^{6+} species in mantle melts could account for the fact that primary Kīlauean melts have S contents exceeding the solubility limit for S^{2-} species in the S2017 model at pressures and temperatures relevant to melt generation beneath Hawai'i.

At the time of writing, there are no published measurements of S speciation from shield-stage tholeiitic lavas at Kīlauea. Early submarine alkalic lavas have S^{6+}/S_T ratios of 0.09–0.24 (determined by X-ray absorption near-edge structure- XANES; Jugo et al., 2010), although these lavas may be more oxidised than shield stage lavas (Sisson, 2003). Further constraints can be derived from other Hawaiian volcanoes: XANES measurements of submarine basalts from Mauna Kea and Lōi'hi show S^{6+}/S_T ratios up to ∼0.08 (Brounce et al., 2017) and 0.31 respectively (Jugo et al., 2010). However, there is a lack of consistency between different studies; S^{6+}/S_T ratios in a set of Lōi'hi glasses have been estimated using SKα peak shifts by Wallace and Carmichael (1994) (green circles) and XANES by Jugo et al. (2010) (magenta circles). The sample with the highest S^{6+}/S_T ratio measured using SKα peak shifts has the lowest S^{6+}/S_T ratio measured by XANES, while the samples with

the lowest S^{6+}/S_T ratios measured by SKα peak shifts have the highest S^{6+}/S_T ratios measured by XANES (Fig. 6.10b). These discrepancies may reflect differences between SKα peak shift and XANES measurements, or the effects of beam damage (Smythe et al., 2017), but are concerning nonetheless.

An alternative approach to estimate the proportion of S^{6+} species utilizes the strong coupling of Fe and S redox states. Jugo et al. (2010) performed experiments on predominantly hydrous basaltic and andesitic melts at 1050°C, 200 MPa, yielding the following relationship:

$$\frac{S^{6+}}{S_T} = \frac{1}{1 + 10^{(2.1-2\Delta QFM)}} \tag{6.2}$$

Nash et al. (2019) performed experiments on basaltic-dacitic compositions at 1300°C, and 1 atmosphere. They attribute differences in the observed transition of S redox relative to Fe redox between their study and that of Jugo et al. (2010) to a strong temperature dependence, which is incorporated in their parameterization (with T in K):

$$\log\frac{S^{6+}}{S^{2-}} = 8\log\frac{Fe^{3+}}{Fe^{2+}} + \frac{8.7436 \times 10^6}{T^2} - \frac{27703}{T} + 20.273 \tag{6.3}$$

However, while the differences in pressure between these two studies (0.1 vs. 200 MPa) are likely negligible (Nash et al., 2019), the speciation transition has been shown to shift by ∼1.5 log units of fO_2 between 0.5 and 1.5 GPa (Matjuschkin et al., 2016). Unfortunately, as experiments investigating the competing effects of pressure and temperature at conditions relevant to mantle melting beneath the thick Hawaiian lithosphere have not been performed, it would be unwise to apply existing low-pressure experimental parametrizations to estimate the S redox state of primary melts.

In summary, $SCSS^{2-}$ models provide strong evidence that the Kīlauean mantle source must remain sulfide saturated throughout the melting interval to account for the high S contents of primitive melt inclusions. To resolve discrepancies between the S2017 and O2020 models, and assess whether primary melts contain S^{6+} species, significantly more experimental work is required to: 1) evaluate the differential sensitivities of the S2017 and O2020 models to the Fe^{3+}/Fe_T ratio, 2) accurately predict mantle sulfide compositions from silicate melt compositions at high pressures and temperatures, and 3) investigate the position of the speciation transition from S^{2-} to S^{6+} at high pressures and temperatures.

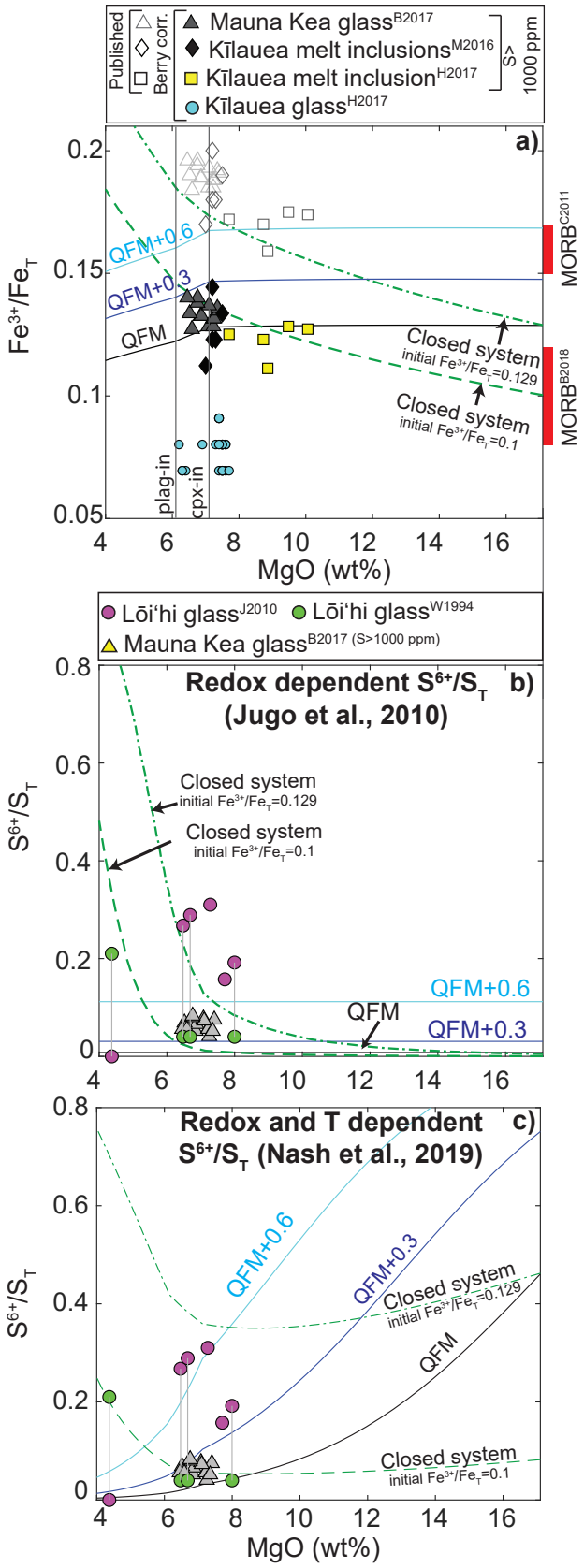


Figure 6.10: Models and observations of S and Fe redox in Hawaiian melts. **a)** Literature measurements of Fe^{3+}/Fe_T in Kīlauean melt inclusions (Moussallam et al., 2016; Helz et al., 2017) and Mauna Kea glasses (Brounce et al., 2017) with S>1000 ppm. Recent debates regarding the interpretation of Mossbauer spectra used for XANES calibration has led to suggestions that a correction must be applied to literature data. Published ratios are shown as hollow symbols, while ratios corrected using the equation of Berry et al. (2018) are shown as filled symbols. Prior to applying this correction, +0.01 was added to the data of Helz et al. (2017) to account for their slight adjustment to the calibration of Cottrell et al. (2009). Values corrected using the Zhang et al. (2018) method would lie in between published and Berry-corrected data. Trajectories from Petrolog3 models are overlain, as well as estimates of the oxidation state of MORB (Berry et al., 2018; Cottrell and Kelley, 2011). **b-c)** Available literature data for S redox from Lōi'hi (Wallace and Carmichael, 1994) and Mauna Kea (Brounce et al., 2017). The fractionation trajectories shown in **a)** were used to calculate the S^{6+}/S_T using the model of Jugo et al. (2010) in part **b)**, and Nash et al. (2019) in part **c)**.

A complementary approach to quantify the longevity of residual sulfide in the Kīlauean mantle source utilizes the differential behaviour of lithophile and chalcophile elements during mantle melting. Lavas erupted at Kīlauea volcano show cyclic variations in trace element and isotope ratios (e.g., Nb/Y, $^{206}Pb/^{204}Pb$; Pietruszka and Garcia, 1999a; Sides et al., 2014b), attributed to variations in melt extent and mantle source heterogeneity (Hofmann et al., 1984; Pietruszka et al., 2018). The suite of eruptions investigated in this study (1969–1974) incorporate some of the most rapid changes in lava chemistry over the past few hundred years (Pietruszka and Garcia, 1999a, Chapter 5), and show chemical variations consistent with changes in extent of melting (Hofmann et al., 1984). Thus, they provide the ideal opportunity to evaluate the longevity of sulfides in the Hawaiian mantle source.

The concentration of chalcophile elements in mantle melts is controlled by the initial concentration in the mantle source (C_i), the melt extent (F), and the bulk partition coefficient between the silicate melt and the mantle residue (which may contain silicate and sulfide phases). The concentrations of two elements with low bulk K_Ds in suites of lavas spanning a range of melt extents are well-correlated (e.g., Ba vs. Ce and La; Fig. 6.4a-b; Hofmann et al., 1984). In contrast, if one element has a high K_D in a residual phase (e.g., Yb in garnet), giving it a bulk K_D close to 1, its concentration will be buffered across a wide range of melt extents. The gradient of a linear regression between this element and a highly incompatible element such as Ba will be ∼0 (e.g., Fig. 6.4c; Hofmann et al., 1984). In the past, such comparisons have been used to demonstrate that residual garnet is present throughout the melting interval at Kīlauea (Hofmann et al., 1984).

Like Yb, many chalcophile elements show poor correlations with Ba (e.g. Cu, Cd, Pb; Fig. 6.4d-f). This implies that chalcophile element concentrations are buffered by the presence of a residual phase during melting in which these elements have a high K_D. Residual sulfide is the most likely candidate, as chalcophile elements have very high K_Ds in sulfides (e.g., $K_{D,\,Cu}^{sulf/melt}$ = 61–729 and $K_{D,\,Pb}^{sulf/melt}$ =7–145 for a wide range of melt FeO contents; Kiseeva and Wood, 2015; $K_{D,\,Cu}^{sulf/melt}$ = 800–4600 and $K_{D,\,Pb}^{sulf/melt}$ =24–170 in basaltic-rhyolitic melts; Li and Audétat, 2015), but low K_Ds in silicates (Lee et al., 2012; Liu et al., 2014). However, it is also worth noting that while $K_{D,\,Cd}^{sulf/melt}$= 12–201 (Kiseeva and Wood, 2015), previous studies have demonstrated that the major host for Cd in the mantle is likely clinopyroxene (Witt-Eickschen et al., 2009).

To demonstrate the variable response of chalcophile and lithophile elements during mantle melting, the concentrations of Cu and Ba in melts produced during melting of a sulfide-bearing mantle were calculated using an adapted version of the modelling approach of Lee et al. (2012). The composition of batch melts calculated at small F steps (termed instantaneous melts, with 3001 steps between F=0 and F=0.3) were pooled to calculate the composition of aggregated melts. The code used for this modelling along with embedded equations is available as a Jupyter notebook at `https://github.com/`

`PennyWieser/Sulfide_Present_Melting_GCA_Wieser2020`. For simplicity, it was assumed that all the S in the mantle was held within sulfides and the concentration of S in mantle melts produced while sulfides were present (S_{melt}) in the residue was 1600 ppm (Fig. 6.2b). The amount of residual sulfide present at each step was calculated assuming that mantle sulfides contain 33 wt% S. The concentration of Ba and Cu in the mantle prior to the onset of melting were set at 6.85 and 20 ppm respectively (Palme and O'Neill, 2014). Unlike the approach of Lee et al. (2012) where P and D in the batch melting equation are assumed to be equal, the non model melting behavoir of sulfides was built into this model (the results converge as the ΔF tends to zero). A constant value of $K_{D,Sil}$ was used, because incorporating non-modal melting of silicates requires accurate estimates of changing mineral modes at high pressures, which is problematic at >3 GPa (Ghiorso et al, 2002). Fixing the value of $K_{D,Sil}$ has negligible effects on modelled Cu concentrations, as $K_{D,\,Sulf}$ is 4–5 orders of magnitude higher than $K_{D,\,Sil}$, and silicate phases have similarly low partition coefficients (Table 6.1). $K_{D,\,Sil}$ was calculated assuming the mantle source contains 59.8% olivine, 21.1% orthopyroxene, 7.6% clinopyroxene and 11.5% garnet (McKenzie and O'Nions, 1991).

Table 6.1: Silicate-melt K_Ds used in mantle melting models. Partition coefficients for Ba are from Gibson and Geist (2010), and those for Cu are from Liu et al. (2014).

Element	Gnt-melt K_D	Cpx-melt K_D	Opx-melt K_D	Ol-melt K_D
Ba	0.00007	0.0004	0.000006	0.000005
Cu	0.03	0.06	0.04	0.05

The partition coefficient of Cu in sulfide varies as a function of temperature and sulfide composition (Kiseeva and Wood, 2015). Assuming a sulfide composition of 20% Ni, 5% Cu (Fig. 6.9b; Ding and Dasgupta, 2018) and a liquid FeO content of 11.3 wt%, $K_{D,\,Cu}^{sulf/melt}$ varies from ∼250 to ∼150 for T=1500°C and 1700°C respectively (Fig. 6.9a; Kiseeva and Wood, 2015). However, previous studies modelling Cu during mantle melting have used values of $K_{D,\,Cu}^{sulf/melt}$ as high as 800 (Lee et al., 2012). To reflect the uncertainty in this parameter, models were run for $K_{D,\,Cu}^{sulf/melt}$ = 200 and 800. Model melt compositions were compared to fractionation-corrected glass compositions from the three rift eruptions of this study which have only fractionated olivine (and minor chrome-spinel; MgO >6.8 wt%, Wright and Fiske, 1971).

At the onset of melting, the presence of residual sulfide in the mantle raises the bulk K_D for Cu, causing aggregated melts to have significantly lower Cu concentrations than melts produced in a sulfide-free mantle (magenta vs. green lines; Fig. 6.11a-d). The concentration of Cu in the melts produced at the onset of melting decreases with increasing initial mantle S contents, as the higher the proportion of sulfide, the higher the bulk $K_{D,\,Cu}$. Rapid changes in Ba (which is highly incompatible) combined with the buffering of Cu by residual sulfide (Fig. 6.11a-d) results in the gradient of Cu vs. Ba being close to zero (Fig. 6.11c-f).

The production of S-rich melts results in the amount of sulfide in the mantle source declining throughout the melting interval. This drives rapid changes in the bulk K_D of Cu until the point at which sulfide is exhausted (black star), after which Cu acts incompatibly (bulk $K_{D,\ Cu}$=0.046). For $K_{D,\ Cu}^{sulf/melt}$= 800, Cu concentrations in aggregated melts peak slightly after the exhaustion of sulfides (Fig. 6.11b, d; Lee et al., 2012). For $K_{D,\ Cu}^{sulf/melt}$= 200, Cu concentrations in aggregated melts remains approximately constant until sulfides are exhausted (black star, Fig. 6.11a, c). In both models, as the point of sulfide exhaustion is approached, there is a rapid change in the trajectory of the gradient vs. Ba. For $K_{D,\ Cu}^{sulf/melt}$= 200, the gradient becomes strongly positive after sulfides are exhausted. For $K_{D,\ Cu}^{sulf/melt}$= 800, the gradient starts increasing (Fig. 6.11f) once sulfides are exhausted, with a delay before the gradient becomes positive (aligning with the prominent peak in Cu vs. F and Cu vs. Ba space; Fig. 6.11b, d). In both models, after the exhaustion of sulfides, melt Cu concentrations gradually approach the compositions of melts produced from a mantle which was sulfide free from the onset of melting (green lines), and the gradients become strongly positive (Fig. 6.11e-f).

The concentration of Cu and the gradient of Cu vs. Ba in fractionation-corrected matrix glasses analysed in this study, along with prior constraints on the extent of mantle melting at Kīlauea, provide insight into the fate of mantle sulfides. Previous studies of trace element abundances in Kīlauean samples have suggested that the mantle source undergoes 5–10% melting (grey box; Fig. 6.11a-b; Bennett et al., 2000; Norman et al., 2002). The range of Ba concentrations observed in the glasses investigated in this study are consistent with melt extents between F=0.08 and 0.095 (for Ba_i=6.85; Palme and O'Neill, 2014). In models where sulfides are exhausted very early (e.g., S_i = 50 ppm; solid magenta line), Cu concentrations produced at the melt extents relevant for Kīlauea (F=0.05–0.1) are similar to those expected from melting of a mantle source which was sulfide-free throughout the melting interval (solid green vs. solid magenta line; Fig. 6.11a-b). As Cu is relatively incompatible in mantle silicate phases, this model exhibits a strong positive correlation between Cu and Ba for the range of Ba concentrations in Kīlauean glasses (Fig. 6.11e-f). Even the upper bound of the 95% confidence interval of the gradient of Cu vs. Ba in the fractionation-corrected glass compositions is ∼30–50× lower than predicted by this model (black rectangle, Fig. 6.11e-f). In contrast, the observed range of fractionation-corrected glass Cu concentrations (light pink bar; Fig. 6.11a-b; triangles on Fig. 6.11c-d) are only ∼2–3× lower than predicted in this model. Changing the initial concentration of Cu in the source cannot resolve these discrepancies in both the gradient and the concentration of Cu. Sulfides are also exhausted within the melting interval at Kīlauea if S_i = 100 ppm. For $K_{D,\ Cu}^{sulf/melt}$=200, models with S_i = 100 ppm display positive gradients for Cu vs. Ba and overestimate the Cu concentrations of primary melts (Fig. 6.11c, **e**). For $K_{D,\ Cu}^{sulf/melt}$=800, the model with S_i = 100 ppm passes through the observed gradients, but overpredicts melt Cu contents (Fig. 6.11b, d).

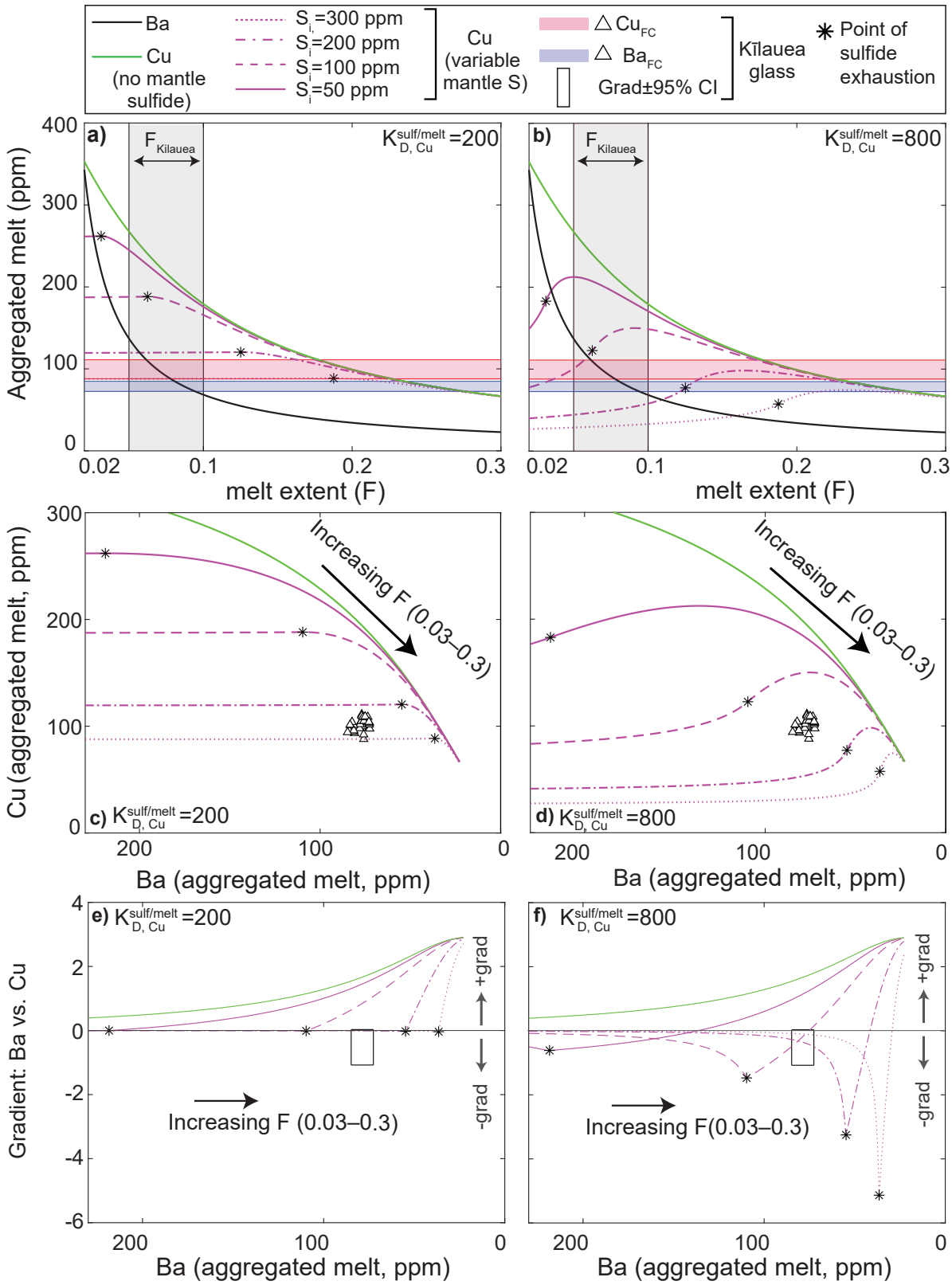


Figure 6.11: (Caption next page.)

Figure 6.11: Models of Cu and Ba contents in aggregated fractional melts with changing melt extents (F) and initial mantle S contents (S_i) assuming Cu_i = 20 ppm. **a-b)** Changes in the Cu contents of aggregated melts with increasing F for two different values of $K_{D,\,Cu}^{sulf/melt}$. Ba rapidly decreases with increasing melt extents (black line). If there are no sulfides in the mantle source, Cu shows a less dramatic increase (green line). The magenta lines show the evolution of Cu for four different S_i values. The point at which sulfides are exhausted (black star) moves to progressively higher F values as S_i increases. The light pink and light blue bar show the range of Cu and Ba concentrations in fractionation-corrected Kīlauean glasses (taken to represent primary melts) from the three rift eruptions which have not fractionated beyond olivine control. In **a)**, Cu concentrations in melts produced at F=0.05–0.1 with S_i= 200–300 ppm bracket the range of primary melt Cu contents, while in **b)**, models with S_i= 100–200 bracket the range of observed values. **c-d)** Cu concentrations in aggregated melts plotted against Ba to aid visual assessment of the changing gradients following sulfide exhaustion. **e-f)** The gradient of Ba vs. Cu in the model vs. the Ba concentration of aggregated melts. The black rectangle shows the range of Ba concentrations in fractionation-corrected glasses, and the 95% confidence interval on the observed gradient of Cu vs. Ba (see Fig. 6.4d).

It could be argued that a model with S_i = 150 ppm and $K_{D,\,Cu}^{sulf/melt}$=800 would recreate observed Cu and Ba concentrations without exhausting sulfide. However, the calculated gradient for this model only passes through the very bottom of the observed 95% confidence interval. Additionally, based on the Kiseeva and Wood (2015) parameterization, $K_{D,\,Cu}^{sulf/melt}$ is very unlikely to be as high as 800. For the more realistic models with $K_{D,\,Cu}^{sulf/melt}$=200, the observed gradients and concentrations of Cu are only recreated in models where sulfides are present in the mantle source throughout the melting interval incorporated by the three primitive eruptions investigated in this study. Overall, the gradient of Cu vs. Ba provides a far more robust measure of the presence or absence of sulfide than absolute concentrations, as it is far less sensitive to the choice of poorly constrained parameters such as mantle Cu contents (Cu_i).

Based on the assumption that sulfides were present throughout the melting interval, the minimum S concentration of the Kīlauean mantle source may be estimated from the S concentration of primary melts (S_{prim}) and the extent of melting (F) using the equation S_{min}= S_{prim}×F. Assuming melt extents between F=0.08 and 0.095 (based on Ba concentrations), and primary S concentrations of 1600 ppm, the mantle source contains a minimum of ∼130–150 ppm S. Placing further constraints on the source S content is challenging; for low values of $K_{D,\,Cu}^{sulf/melt}$ (e.g., 200), once sulfides are residual throughout the melting interval, the gradient between Cu and Ba provides no further discriminatory power (all models have gradients of ∼0; Fig. 6.11e-f), and Cu concentrations in the melts are invariably a trade-off between S_i and Cu_i. More precise constraints on the S concentration of the Kīlauean mantle source will require better constraints on the concentrations of other chalcophile elements in the mantle, as well as sulfide-melt partition coefficients (which likely vary as a function of T, P and sulfide composition), so that inversions can be performed for more than one chalcophile element.

6.4.2 Sulfide Systematics During Magma Ascent and Fractionation

Due to the increase in the $SCSS^{2-}$ with decreasing pressure, a melt that is sulfide-saturated in the mantle will generally become sulfide-undersaturated during its ascent towards the surface (Mavrogenes and O'Neill, 1999). This process was modelled by calculating the $SCSS^{2-}$ for primary melts with the adjusted composition of Clague et al. (1991) ascending along the olivine liquidus (39.16°C/GPa; Putirka, 2008) for two mantle potential temperatures (T_p=1450°C and 1650°C). For each potential temperature, the trajectory of the hottest melt formed at the onset of melting and the coolest melt formed at the base of the lithosphere was modelled (after Matthews et al., 2016; Fig. 6.12a). In **b** the decrease in the $SCSS^{2-}$ with decreasing pressure in the S2017 model is an artefact of changes in the calculated sulfide composition (as in Fig. 6.9c). Using a fixed sulfide composition (after Ding and Dasgupta, 2018), the S2017 and O2020 models both show similar trajectories until ∼1 GPa, where the $SCSS^{2-}$ in the O2020 model decreases, while the S2017 model continues to increase (Fig. 6.12c). The paucity of experimental data collected between atmospheric pressure (100 kPa and 1 GPa; Smythe et al., 2017) makes it difficult to verify the validity of these different trajectories (O'Neill, 2020). However, regardless of the exact choice of SCSS model or potential temperature, this analysis demonstrates that dropping pressures cause the $SCSS^{2-}$ to exceed the S content of primary melts (Fig. 6.12c). Thus, sulfide saturated primary melts become sulfide undersaturated during their ascent through the thick Hawaiian lithosphere into shallow crustal storage reservoirs at 1–5 km depth (Cervelli and Miklius, 2003; Poland et al., 2015). The probable presence of S^{6+} species in primary melts (Fig. 6.10b-c) will shift the $SCSS_{Tot}$ to higher S contents than the $SCSS^{2-}$ models shown in Fig .6.12, resulting in melts becoming sulfide undersaturated at even higher pressures during their ascent. Similarly, if melts were to ascend along an adiabatic gradient instead of the olivine liquidus, the temperature decrease upon ascent would be smaller, resulting in higher values of the $SCSS^{2-}$, and the onset of sulfide undersaturation at higher pressures.

Sulfide-undersaturated primary melts supplied to shallow crustal storage reservoirs at Kīlauea may experience a second phase of sulfide saturation during crystal fractionation. Recent work has concluded that the majority of erupted melts at Kīlauea are sulfide-undersaturated until ∼2 wt% MgO (Ding and Dasgupta, 2018; Greaney et al., 2017; Helz et al., 2017). However, this view is difficult to reconcile with the ubiquitous presence of sulfides in the relatively primitive eruption products investigated in this study (Fig. 6.5), unless sulfides form during late stage processes such as quenching, rather than primary sulfide immiscibility (Stone and Fleet, 1991). The hypothesis that sulfides form upon quench was assessed by comparing bulk sulfide compositions measured using EDS mapping to the predicted sulfide compositions from $SCSS^{2-}$ models. Sulfides formed through primary sulfide immiscibility will progressively evolve towards more Cu-rich and Ni-poor compositions with

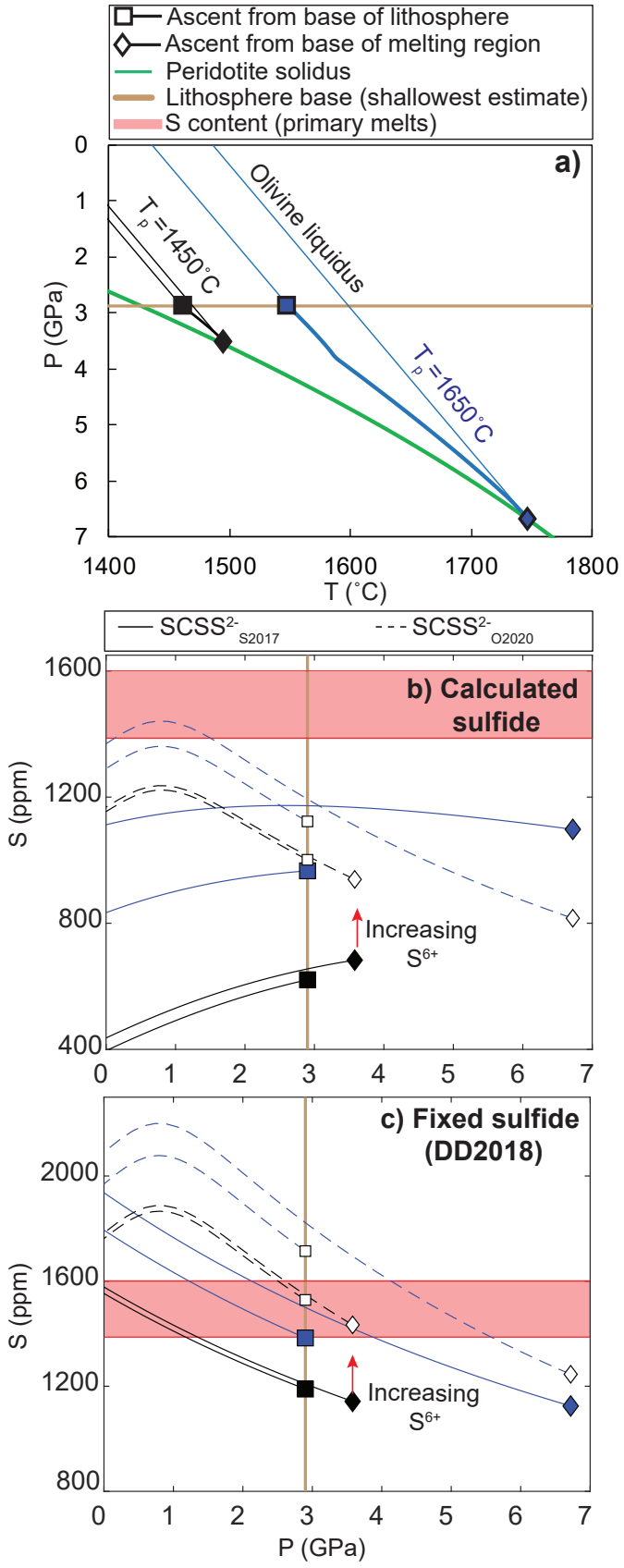


Figure 6.12: Modelling the $SCSS^{2-}$ during the ascent of melts from the mantle into shallow crustal storage reservoirs. **a)** PT paths tracking the ascent of mantle melts generated at bottom and top of the melting column along the olivine liquidus (39.16°C/GPa; after Matthews et al., 2016). **b-c)** Calculated $SCSS^{2-}$ trajectories for these ascent paths, using the adjusted primary melt composition of Clague et al. (1991) for calculated (**b**) and fixed sulfide compositions (**c**). As in Fig. 6.9, the decrease in the $SCSS^{2-}$ with decreasing pressure in the 2017 model is an artefact of the changing sulfide composition. Similarly, calculated sulfide compositions are far more Fe-poor than measured sulfides, leading to anomalously low $SCSS^{2-}$ values. In **c)**, all modelled trajectories except for the lowest T_p (1450°C) in the S2017 model exceed the S concentrations of primary melts (red bar) at low pressures. The presence of even a very small amount of S^{6+} would mean that the $SCSS_{Tot}$ for this model would also exceed the S contents of primary melts. These models indicate that upon ascent, Kīlauean magmas become sulfide-undersaturated. The beige line marks the shallowest estimate for the base of the lithosphere beneath Kīlauea (Li et al., 2004; Wölbern et al., 2006).

increasing fractional crystallization. Conversely, sulfides formed during quench-induced segregation and cooling will show extreme compositional variability (Stone and Fleet, 1991; Fleet and Stone, 1990). The sulfide compositions predicted by $SCSS^{2-}$ models were calculated for Petrolog3 fractionation paths from the adjusted primary melt composition of Clague et al. (1991) at 1 kbar. The mineral models of Danyushevsky (2001) were used for olivine, clinopyroxene and plagioclase. Melt Ni concentrations were modelled assuming Ni_i=900 ppm, using $K_{D,\ Ni}^{ol/melt}$ from Beattie et al. (1991), $K_{D,\ Ni}^{cpx/melt} = 2.6$ from Mysen (1978), and $K_{D,\ Ni}^{plag/melt} = 0$. Melt Cu concentrations were modelled assuming Cu_i=100, using $K_{D,\ Cu}^{ol/melt} = 0.1$, $K_{D,\ Cu}^{cpx/melt} = 0.21$ (Greaney et al., 2017) and $K_{D,\ Cu}^{plag/melt} = 0.14$ (Bougault and Hekinian, 1974).

To assess changes in sulfide chemistry during fractionation (and to compare measured sulfide compositions to those predicted by $SCSS^{2-}$ models), the MgO content of the melt at the time of formation for each Kīlauean sulfide was estimated. Sulfides hosted in matrix glasses or embayments were allocated an equivalent melt MgO content equal to that of the host glass. For sulfides hosted in olivine crystals and melt inclusions, the forsterite content of the host olivine was compared to olivine compositions from the Petrolog3 model, and the sulfide was assigned the liquid MgO content at which the measured olivine composition fractionated.

Contrary to the observations of Stone and Fleet (1991) that bulk sulfide compositions from Kīlauea Iki are highly variable, bulk sulfide compositions measured in this study show coherent changes in Cu and Ni with decreasing melt MgO contents, and relatively little chemical variability (Fig. 6.13a-b). Furthermore, the Ni and Cu contents of the sulfides fall between the calculated sulfide compositions from the S2017 and O2020 $SCSS^{2-}$ models. Coherent variations in sulfide compositions have also been reported for sulfides in samples from the 1955 eruption (Helz and Wright, 1992). It is plausible that scatter in previously reported sulfide compositions from Kīlauea results from the analytical challenges associated with obtaining bulk compositions from EPMA spot analyses of exsolved sulfides. Thus, it is highly probable that observed sulfides in Kīlauean are the result of primary sulfide fractionation.

Our hypothesis that sulfides form during primary sulfide saturation is supported by the presence of sulfides trapped within the cores of olivine crystals (Fig. 6.5a), often associated with small pockets of melt and spinels (Fig. 6.5f-h). These textural associations cannot be explained by quenching processes, or the formation of sulfides following melt inclusion entrapment (e.g. Hartley et al., 2017), as there is simply not enough Cu, Ni and S in these small pockets of melt to form sulfides of the observed sizes after the melt inclusion became a closed system. Only sulfides hosted in melt inclusions where the volume ratio of the sulfide to melt is very low could have grown following melt inclusion entrapment (e.g., ∼0.04%, Fig. 6.5e, yellow squares on Fig. 6.13). The attachment of sulfides to olivine crystals (e.g., Fig. 6.5c, f) suggests that sulfides may have a stronger affinity for

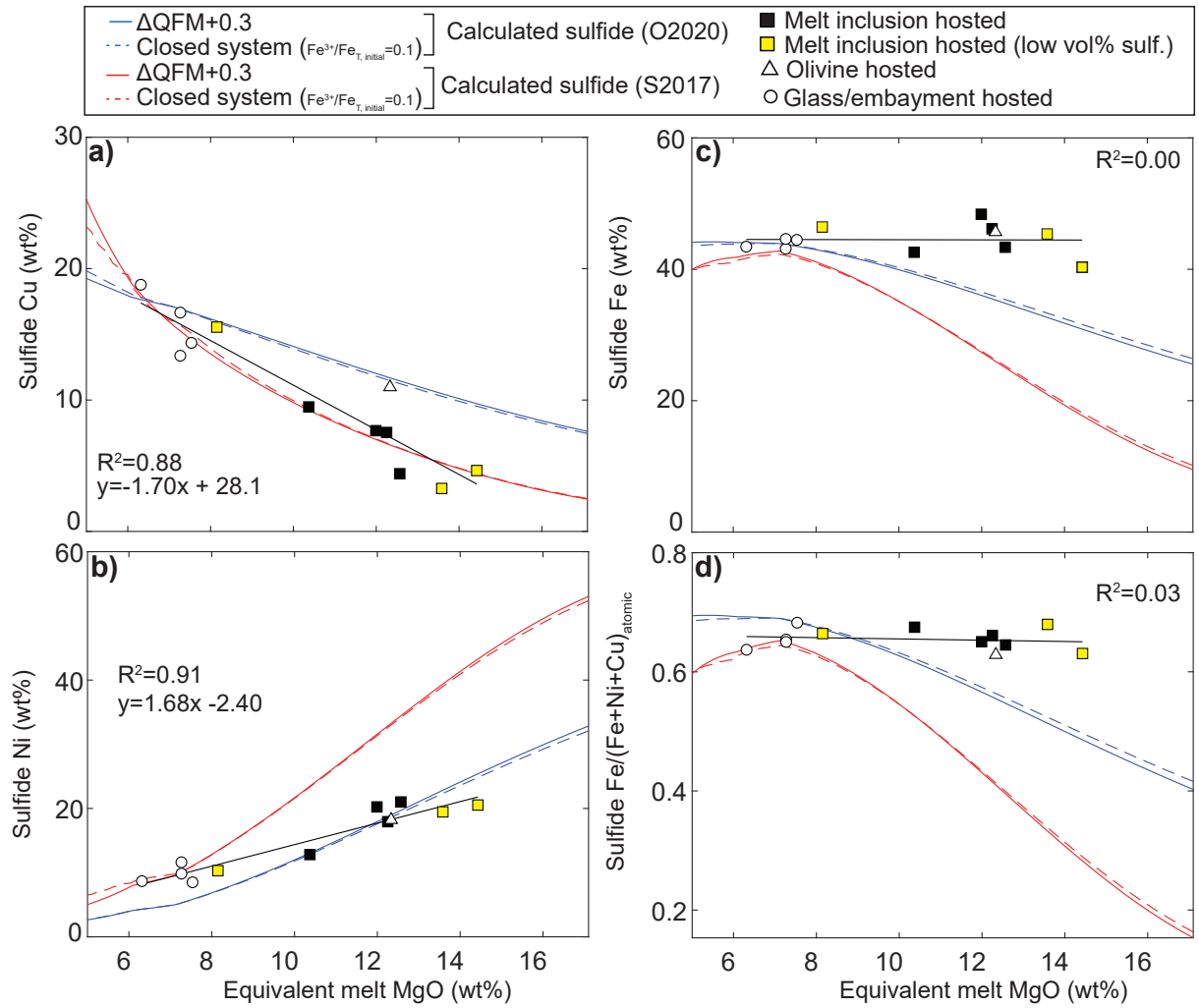


Figure 6.13: Comparison of measured sulfide compositions to those calculated from SCSS^{2-} models. Bulk sulfide compositions were obtained from EDS maps (quantified by analysing sulfide standards whose compositions were determined by EPMA in the same analytical session). Equivalent melt MgO contents for each sulfide were allocated from glass MgO contents, or olivine Fo contents. Modelled sulfide compositions were calculated for Petrolog3 fractionation path described in the text. Closed system and buffered models yield very similar calculated sulfide compositions (dashed vs. solid lines). Sulfides which could plausibly have grown following their entrapment in melt inclusions (based on volume proportions <0.2%) are coloured yellow.

nucleation or attachment to silicate minerals than the silicate melt. The attachment of sulfides to the boundary layer of a growing crystal likely accounts for their incorporation as inclusions. In fact, this process may even trigger the formation of melt inclusions containing sulfides in a similar mechanism to that proposed for inclusions containing chrome-spinels (Maaløe and Hansen, 1982). Overall, these chemical and textural observations of sulfides are consistent with their formation through primary sulfide saturation during differentiation, followed by their subsequent entrapment within growing crystals (often alongside spinels and silicate melt; Nadeau et al., 2010). The occurrence of sulfides hosted within highly

primitive olivine crystals (Fo_{87-88}) alongside very small quantities of melt (Fig. 6.5a, h, g) suggests that sulfides saturated at ∼12 wt% MgO.

This second stage of sulfide saturation was investigated by comparing fractionation trajectories for S (assuming S is incompatible in silicate phases) with $SCSS^{2-}$ models for each Petrolog3 fractionation path. The $SCSS^{2-}$ is sensitive to melt composition (particularly the FeO content), oxidation state (Fe^{3+}/Fe_T), temperature, pressure and the composition of co-existing sulfides (Smythe et al., 2017; O'Neill, 2020). During fractional crystallization at Kīlauea, olivine is the only silicate phase on the liquidus until 6.8 wt% MgO (Wright and Fiske, 1971). Over this fractionation interval, melt FeO contents remain approximately constant. Although $SCSS^{2-}$ models predict an increase in the ratio of Fe/(Fe+Cu+Ni) in sulfides with progressive fractionation, this ratio remains remarkably constant in measured bulk sulfide compositions (Fig. 6.13d). Thus, this parameter was fixed at 0.646 in all models. Use of calculated, rather than fixed sulfide compositions, results in spuriously low $SCSS^{2-}$ values (Fig. 6.14). As magma storage (and fractionation) at Kīlauea is restricted to a narrow range of depths (∼1–5 km; Cervelli and Miklius, 2003), changing pressures during fractionation have a negligible effect on the $SCSS^{2-}$.

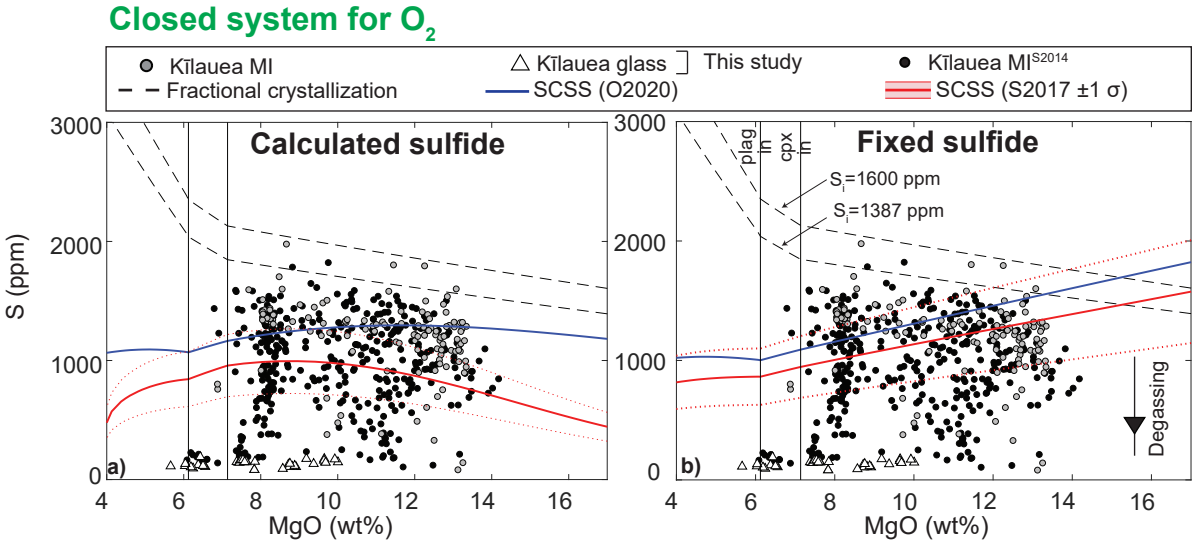


Figure 6.14: $SCSS^{2-}$ models for the closed system model (initial Fe^{3+}/Fe_T=0.1). Using the calculated sulfide composition from the O2020 and S2017 model results in an $SCSS^{2-}$ that is significantly lower than measured melt inclusion S contents.

Changes in melt redox state during fractionation are less certain. Due to an absence of measurements of Fe^{3+}/Fe_T in Kīlauean melts with >10 wt% and <7 wt% MgO (Fig. 6.10a), it is difficult to determine whether melts follow a redox buffer, or act as a closed system for oxygen. Additionally, the re-interpretation of Mössbauer spectra in glass standards which are integral to XANES calibrations (Berry et al., 2018; Zhang et al., 2018) has resulted in significant uncertainty regarding the oxidation state of Kīlauean melts.

Literature data utilizing the calibration of Cottrell et al. (2009) prior to the emergence of this Mössbauer-focused debate are well matched with models buffered at QFM+0.6 to 0.7, or closed system models for Fe^{3+}/Fe_T=0.129 (Fig. 6.10a). However, following the application of the Berry et al. (2018) correction:

$$\frac{Fe^{3+}}{Fe_T}(\text{Corrected}) = \frac{\frac{Fe^{3+}}{Fe_T}(\text{Published}) - 0.065}{1 - 0.065} \tag{6.4}$$

Published data is best matched with models buffered at QFM to QFM+0.3, or closed system models with initial Fe^{3+}/Fe_T=0.1 (Fig. 6.10a). The Zhang recalibration yields Fe^{3+}/Fe_T ratios between published values and those corrected using Equation 6.4. However, other than subtle changes in the MgO content at which clinopyroxene and plagioclase begin to crystallize, the closed system and buffered model show very similar major element systematics. Consequently, the $SCSS^{2-}$ trajectories for models with different redox conditions are very similar, with subtle differences resulting from the different sensitivities of the S2017 and O2020 model to the Fe^{3+}/Fe_T ratio.

$SCSS^{2-}$ models (Fig. 6.15a-b) intercept fractionation trajectories for S at high MgO (∼13–17 wt% MgO). Below ∼12 wt% MgO, the calculated $SCSS^{2-}$ is significantly lower than the measured S contents in melt inclusions, even accounting for the upper 1σ error envelope on the S2017 parameterization (red dotted line). This discrepancy indicates that Kīlauean melts likely contain S^{6+} species, which increase the total solubility of S (Equation 6.1). Several different corrections were performed to account for the presence of S^{6+}. The first, and most simplistic, assumes that the proportion of S^{6+} remains constant throughout the fractionation interval at Kīlauea. Based on available S-redox measurements in submarine glasses from Mauna Kea and Lōi'hi (Jugo et al., 2010; Brounce et al., 2017; Wallace and Carmichael, 1994), this proportion may range from 0–30% (Fig. 6.10b-c). The S2017 $SCSS_{Tot}$ model with 30% S^{6+} and the O2020 model with 20% S^{6+} predict the onset of sulfide saturation at ∼12 wt% MgO (consistent with textural observations; Fig. 6.13), and approximately recreate the upper observed limit of S contents in melt inclusions at lower MgO contents (Fig. 6.15c-d).

The proportion of S^{6+} can also be estimated from the experimental parameterizations of Jugo et al. (2010) and Nash et al., 2019 (Equations 6.2-6.3). ΔQFM values for the Jugo et al. (2010) parameterization, and Fe^{2+}/Fe^{3+} ratios for the Nash et al. (2019) parameterization were calculated from Petrolog3 outputs, and melt temperatures were calculated using the geothermometer of Helz and Thornber, 1987. Unlike the subtle differences in $SCSS^{2-}$ models, the proportion of S^{6+}, and by extension, the $SCSS_{Tot}$, is highly sensitive to redox changes during fractionation. Closed system models show a gradual increase in the Fe^{3+}/Fe_T ratio during olivine-only fractionation (due to the removal of Fe^{2+}-rich olivine; Carmichael and Ghiorso, 1986; Moussallam et al., 2016; Fig. 6.10). As clinopyroxene and plagioclase begin to fractionate, this ratio increases more rapidly per unit decrease in MgO.

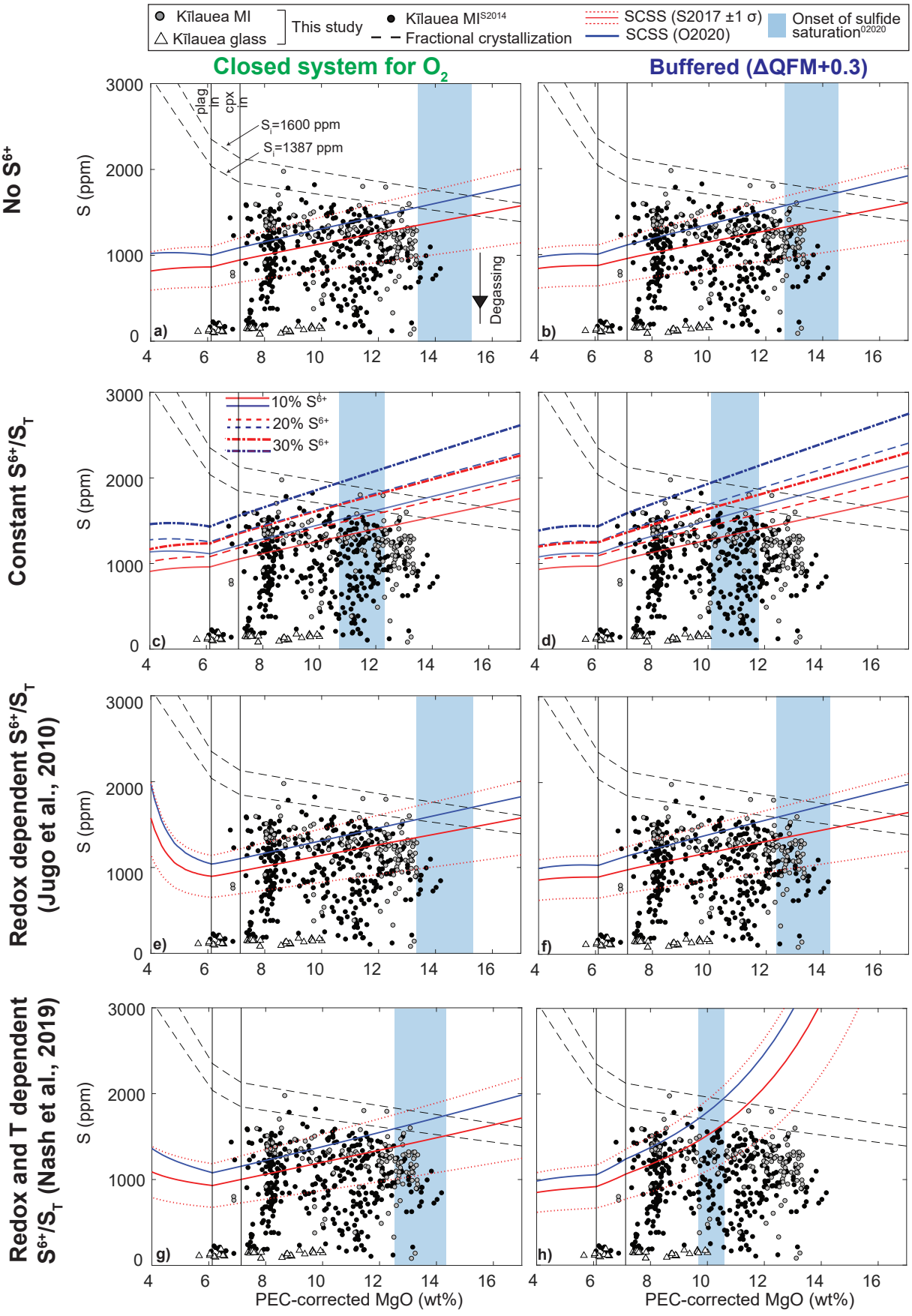


Figure 6.15: (Caption next page.)

Figure 6.15: Comparison of models for sulfide solubility during fractionation (for a specified sulfide composition of Fe/(Fe+Ni+Cu)=0.646) with PEC-corrected melt inclusion compositions. **a-b)** In models only accounting for S^{2-} species, the $SCSS^{2-}$ intercepts the fractionation trajectory for S at high MgO contents (blue bar shows interception for O2020), and underpredicts the S contents of most melt inclusions with <12 wt% MgO. The closed system and buffered model show very similar trajectories, and the O2020 and S2017 are within error of one another (the red dotted lines indicate the published 1 uncertainty on the S2017 model). **c-d)** $SCSS_{Tot}$ trajectories for constant proportions of S^{6+} during differentiation (10%, 20% and 30%). The S2017 model with 30% S^{6+} , and the O2020 model with 20% S^{6+} predict the onset of sulfide saturation at 10–12 wt% MgO (inline with textural observations, Fig. 6.13), and approximately bracket the upper limit of melt inclusion S contents. **e-f)** $SCSS_{Tot}$ trajectories following a correction for S^{6+} using the parameterization of Jugo et al. (2010; Equation 6.2). The closed system and buffered model differ substantially following the onset of plagioclase fractionation (see Fig. 6.10b-c). **g-h)** $SCSS_{Tot}$ trajectories following a correction for S^{6+} using the parameterization of Nash et al. (2019; Equation 6.3). As in **e)**, the closed system model shows a sharp increase in S solubility during plagioclase fractionation. In the buffered model, the strong temperature dependence on the proportion of S^{6+} results in very high estimates of S solubility at high MgO contents.

In contrast, the buffered model exhibits a constant Fe^{3+}/Fe_T ratio during olivine-only fractionation, followed by a slight decrease at lower MgO contents (Fig. 6.10a).

The proportion of S^{6+} predicted by the Jugo et al. (2010) model for the closed system fractionation path with initial Fe^{3+}/Fe_T=0.1 is negligible until the onset of plagioclase fractionation at ∼6 wt% MgO. The closed system fractionation path starting at higher initial Fe^{3+}/Fe_T ratios (=0.129) is offset to higher S^{6+}/S_T ratios, but still predicts <10% S^{6+} during olivine (+minor chromite) fractionation. In the buffered model, by definition, the proportion of S^{6+} predicted by Jugo et al. (2010) remains constant at 0.8% (QFM), 3% (QFM+0.3), and 11% (QFM+0.6). Due to the dependency of the Nash et al. (2019) model on both temperature and Fe^{3+}/Fe_T, the proportions of S^{6+} follow significantly more complex trajectories. In the three buffered models the Fe^{3+}/Fe_T ratio is constant during olivine-only fractionation, so there is a rapid decrease in the S^{6+}/S_T ratio because of dropping temperatures. A slight drop in Fe^{3+}/Fe_T ratios during crystallization of plagioclase and pyroxene causes a kink in the downward trajectory of these curves. In contrast, the closed system models show an almost constant S^{6+}/S_T ratio during olivine-only fractionation, because of the competing effects of dropping temperatures and increasing Fe^{3+}/Fe_T ratios. During crystallization of plagioclase and pyroxene, increasing Fe^{3+}/Fe_T ratios overwhelm the effect of dropping temperatures, so the S^{6+}/S_T ratio increases rapidly. Based on the paucity of S-redox measurements in the literature, and the prominent differences between measurements in the same samples by different studies (e.g., cyan vs. green dots; Fig. 6.10c), it is difficult to assess the validity of these different model outputs. For simplicity, the $SCSS_{Tot}$ was calculated for a fractionation path buffered at QFM+0.3, and for a closed system with initial Fe^{3+}/Fe_T=0.1), to demonstrate the sensitivity of total sulfur solubility to S^{6+}/S_T ratios.

In the closed system model with initial Fe^{3+}/Fe_T=0.1, the $SCSS_{Tot}$ calculated using the Jugo et al. (2010) or Nash et al. (2019) parameterization only deviate outside of the 1σ uncertainty of the $SCSS^{2-}$ after the onset of plagioclase fractionation at ∼6 wt% MgO (Fig. 6.15e-g). The upkick towards higher S contents is most pronounced in the Jugo et al. (2010) parameterization (Fig. 6.15e), because of the competing effects of increasing Fe^{3+}/Fe_T and dropping temperatures in the Nash et al. (2019) parameterization. Due to the low and constant proportion of S^{6+} (3%) in the model buffered at QFM+0.3 using the Jugo et al. (2010) parameterization, the $SCSS_{Tot}$ and the $SCSS^{2-}$ are almost identical. In contrast, the $SCSS_{Tot}$ calculated using the Nash et al. (2019) parameterization deviates substantially from $SCSS^{2-}$ models at high MgO contents (where high S^{6+}/S_T ratios are predicted due to high temperatures). The most significant deviation between these four $SCSS_{Tot}$ models occurs at MgO contents >14 wt% (e.g., Fig. 6.15h vs. Fig. 6.15e, f, g), and following the onset of plagioclase fractionation at ∼6 wt% MgO (e.g., Fig. 6.15e, g vs. Fig. 6.15f, h). The absence of published Fe^{3+}/Fe_T and S^{6+}/S_T ratios for melt inclusions with these low and high MgO contents, as well as the absence of published S data for low MgO content melt inclusions, makes ground truthing these different model scenarios challenging.

Despite the differences between $SCSS_{Tot}$ models, all six predict that the onset of sulfide fractionation occurs at relatively high MgO contents (≫2 wt% MgO; Wallace and Anderson, 1998; cf. Greaney et al., 2017), supporting textural and chemical observations that the vast majority of erupted Kīlauean melts were sulfide-saturated at depth. Based on the absence of constraints for changes in S redox state with differentiation, models using constant S^{6+} proportions, which recreate available textural and chemical constraints regarding the onset of sulfide saturation at Kīlauea (Fig. 6.13, Fig. 6.15c-d), are favoured. These findings further support the inference that mantle melting occurred in the presence of residual sulfides, as melts generated in a mantle which had exhausted sulfide require large amounts of fractionation to intercept the $SCSS_{Tot}$ following ascent to low pressures (Liu et al., 2014).

6.4.3 Sulfide Saturation in Lava Lakes

The prevalent view at Kīlauea that sulfides only saturate following extensive fractionation is not supported by models of sulfide solubility, or textural observations of sulfide occurrence. This discrepancy may result from the focus of previous studies on chemical trajectories defined by samples collected from lava lakes (e.g., Greaney et al., 2017; Pitcher et al., 2009; Stone and Fleet, 1991). A comparison of the S contents of melt inclusions and matrix glasses clearly demonstrates that basaltic melts at Kīlauea degas >90% of their S during subaerial eruptions (∼1600 ppm to ∼135 ppm; Fig. 6.1c; Fig. 6.2a-b). Kīlauea Iki and Alae lava lakes formed by the ponding of S-poor melt within existing pit craters, followed by extensive fractionation (Wright et al., 1976). As the erupted melts filling these lava lakes have similar MgO contents to those examined in this study, it is reasonable to assume

that these magmas were sulfide-saturated prior to their ascent to the surface. However, extensive degassing upon eruption would have caused the S content of the melt to fall well below the $SCSS_{Tot}$, driving sulfide resorption (Edmonds and Mather, 2017; Moore et al., 1980; Reekie et al., 2019). Subsequent fractionation within these lava lakes may then have proceeded under sulfide-undersaturated conditions.

The onset of sulfide saturation within lava lakes was modelled by calculating the $SCSS^{2-}$ using the major element compositions of variably evolved glasses from the Kīlauea Iki lava lake (Fig. 6.1b; Greaney et al., 2017). For simplicity, the amount of S^{6+} in the fractionating lava lake was assumed to be negligible, as extensive degassing of S upon eruption causes a significant drop in the Fe^{3+}/Fe_T ratio (Fig. 6.10a, Moussallam et al., 2016). The evolution of S during progressive fractionation within the lake is uncertain; while the crystallization of silicate minerals drives melt S contents up, the presence of vesicles within lake lava samples and observations of gas release along drill holes suggests that lava lakes continued to lose volatiles during differentiation (Helz and Wright, 1983; Peck, 1978; Wright et al., 1976). To incorporate this uncertainty, the intercerption of regression lines for the calculated $SCSS^{2-}$ vs. MgO with the range of S contents in degassed glasses from Kīlauea Iki pumices (orange histogram; Fig. 6.1b; Sides et al., 2014b), and the S content measured in Alae lava lake (green line; Moore et al., 1980; Fig. 6.1b) were evaluated. These models predict that a third stage of sulfide saturation at Kīlauea will occur at ∼2 wt % MgO, which is consistent with observations that Cu suddenly decreases below 2 wt% MgO in the Kīlauea Iki lava lake (Fig. 6.1a; Greaney et al., 2017). This third stage of sulfide saturation has been attributed to the uptake of Fe^{3+} in Fe-Ti oxides (Greaney et al., 2017) driving S reduction in a mechanism similar to the "magnetite crisis" in arc basalts (Jenner et al., 2010). However, the modelling presented here successfully predicts the onset of sulfide saturation without incorporating changes in redox state (Fig. 6.1b). Instead, the decrease in the $SCSS^{2-}$ is largely driven by changes in the major element concentration of the melt, with a contribution from dropping temperatures. Overall, while lava lakes provide useful insights into the mechanism and timing of sulfide saturation in extensively degassed melts, they are clearly not representative of the fractionation path of undegassed melts within crustal storage reservoirs at Kīlauea.

6.4.4 Degassing of Chalcophile Elements

Aerosol measurements at Kīlauea reveal that, in addition to conventionally volatile elements (e.g., CO_2, H_2O, S, Cl and F), the volcanic plume also contains considerable quantities of chalcophile elements (Edmonds et al., 2018; Mather et al., 2012). The extent to which an element degasses is represented by the emanation coefficient (ε), which quantifies the proportion of an element lost during degassing:

$$\varepsilon = \frac{[X]_i - [X]_f}{[X]_i} \tag{6.5}$$

Where $[X]_i$ and $[X]_f$ are the concentrations of element X in the initial undegassed and final degassed melt respectively (Edmonds et al., 2018; Lambert et al., 1985). Previous petrological work investigating chalcophile element degassing at various Hawaiian volcanoes utilized suites of variably degassed submarine glasses to estimate emanation coefficients (Norman et al., 2004). They observed degassing trends for S (ε=0.86–0.92), Re (ε=0.5–0.74), Bi (ε=0.44–0.45), and Cd (ε=0.19–0.27). However, as Norman et al. (2004) compare glasses from different Hawaiian islands (Ko'olau and Moloka'i), it is difficult to deconvolve the effects of degassing from variations in the original chalcophile contents of these melts.

In this study, emanation coefficients were evaluated by comparing chalcophile element concentrations in melt inclusions (which are variably degassed) and matrix glasses (which have extensively degassed; Fig. 6.3). However, such comparisons rely on the assumption that melt inclusions are genetically related to their matrix glasses. Lithophile trace element ratios in olivine-hosted melt inclusions from the three rift eruptions investigated in this study show considerable overlaps, despite statistically significant changes in the composition of the co-erupted matrix glass. This indicates that these melt inclusions were trapped from a variety of magma batches present within Kīlauea's plumbing system over centuries, and subsequently brought to the surface in an unrelated magma batch (Chapter 5, see also Tuohy et al., 2016). Only the 1971 summit eruption contains a crystal cargo that crystallized from the carrier liquid, permitting a direct comparison between melt inclusions and co-erupted glasses. Fortunately, the presence of residual sulfides in the mantle source means that chalcophile element concentrations do not differ as much as lithophile element concentrations between different magma batches (Fig. 6.4). Thus, degassing can be assessed by comparing the matrix glasses and melt inclusions, considering the data from all four eruptions together.

Emanation coefficients were calculated using Equation 6.5. $[X]_f$ was calculated from regression line of a given element [X] against S at S=135 ppm (the average S content of degassed matrix glasses). The value of $[X]_i$ calculated from the regression lines is sensitive to the amount of S degassed (ΔS); to incorporate this uncertainty, $[X]_i$ was calculated from the regression lines at S=1435 ppm and S=1585 ppm (ΔS=1300 ppm and ΔS=1450 ppm respectively). The uncertainty on the emanation coefficient for a given ΔS was estimated using the 95% confidence intervals of the regression (Fig. 6.16).

The concentrations of many chalcophile elements in melt inclusions and matrix glasses overlap (Loewen, 2013), making it difficult to accurately assess the emanation coefficient, and determine whether a given element is degassing (Fig. 6.3d-f). Several possible criteria to robustly assess whether an element shows petrological evidence for degassing were considered. The first criterion is based on the fact that gaseous observations indicate that Cl partially degasses at Kīlauea (Edmonds et al., 2009). Melt inclusion Cl contents overlap with and extend to higher values than matrix glasses, with the most S-rich (least degassed) inclusions generally having higher Cl contents (Fig. 6.3a). A chalcophile element was deemed to show

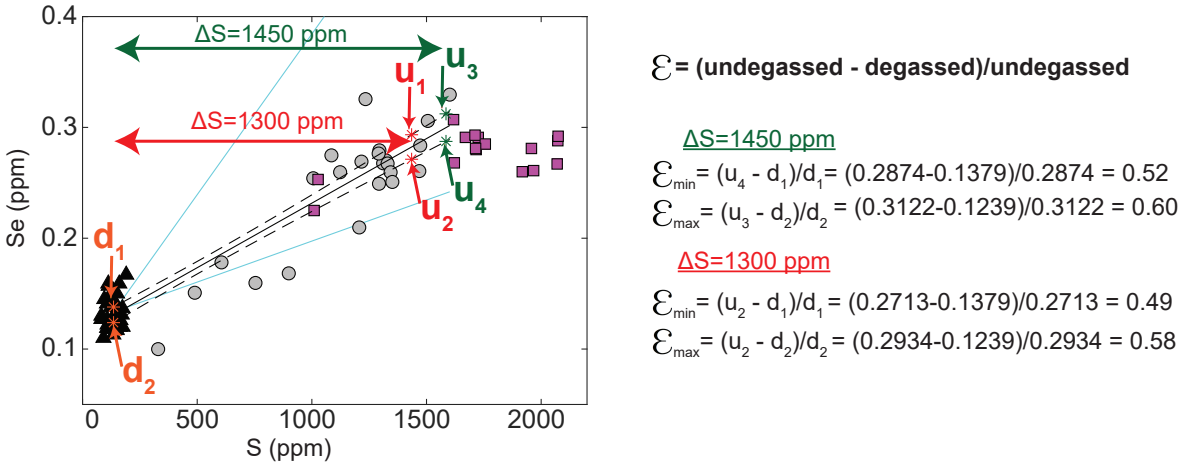


Figure 6.16: The upper and lower bounds of the 95% confidence interval on the regression of a given element against S were used to estimate an upper and lower bound on the emanation coefficient for each ΔS value.

evidence for subaerial degassing if a regression line between that element and S exhibits a higher R^2 value than Cl vs. S (R^2=0.14). This criterion classifies Se (R^2=0.90), Bi (R^2=0.35) and As (R^2=0.19) as degassed (Fig. 6.3).

The second criterion is based on a comparison of mean concentrations of chalcophile elements in PEC-corrected melt inclusions and matrix glasses from the 1971 summit eruption (where melts trapped within crystals and the co-erupted matrix glass have similar trace element signatures; Chapter 5) using the ANOVA test. The small diameter of melt inclusions from this eruption meant that As and Se could not be measured. An element was classified as degassed if $p<0.05$. This criterion only classifies Bi as degassed ($p=9\times10^{-4}$), with no distinguishable differences between matrix glasses and PEC-corrected melt inclusion compositions for Cu (p=0.08), Zn (p=0.66), Mo (p=0.77), Cd (p=0.27), In (p=0.90), Sn (p=0.28), Sb (p=0.21), W (p=0.60), or Tl (p=0.16), despite the fact that aerosol measurements indicate that these elements are present in the volcanic plume at Kīlauea (Mather et al., 2012).

The third criterion involves a comparison of the concentrations of chalcophile elements in Kīlauean and Lōi'hi glasses. Lōi'hi glasses were erupted at water depths of ∼1000–4700 m (Pietruszka et al., 2011), so remain largely undegassed with respect to H_2O and S (Fig. 6.3a). For certain elements (e.g., Se, Bi, Cd), Lōi'hi glasses plot with the least degassed Kīlauean melt inclusions, supporting the hypothesis that these elements have degassed from Kīlauean matrix glasses during subaerial eruptions. However, As concentrations in Lōi'hi glasses are lower than in Kīlauean melt inclusions (Fig. 6.3d), suggesting that Lōi'hi and Kīlauea magmas may have slightly different chalcophile element signatures (perhaps attributable to differences in the mantle source, or the fact that Lōi'hi glasses have experienced clinopyroxene fractionation).

To reconcile the lack of petrological evidence for degassing of many chalcophile elements which are detected in volcanic plumes, the expected change in the concentration of each chalcophile element for ΔS=1300 ppm using the X/S ratios measured in the 2008 summit plume were calculated (Mather et al., 2012). For many elements, this change is far smaller than the median analytical precision of in-situ melt inclusion measurements estimated from the 2σ variation in the LA-ICP-MS signal during melt inclusion ablation (from Iolite). For example, the 2σ variation is $\sim$411$\times$ larger than the predicted loss of Cu during degassing ($\sim$7$\times$ for As and Zn, $\sim$9$\times$ for Bi, $\sim$10$\times$ for Cd, $\sim$23$\times$ for Pb, $\sim$23$\times$ for Tl, 367$\times$ for Mo, and $>$1000$\times$ for Tl). It is perhaps unsurprising that the only element that shows unambiguous petrological evidence for degassing is Se, where the analytical precision is only $\sim$0.15$\times$ the expected loss during degassing.

While the degassing of most chalcophile elements is obscured by analytical noise and natural variability in melt compositions, a crucial finding of this study is that S and Se exhibit a strong positive correlation in melt inclusions and glasses, indicating that these elements are degassing concurrently (Fig. 6.3b, R^2=0.90). Extensive degassing of Se during subaerial eruptions is consistent with aerosol measurements at Kīlauea (Crowe et al., 1987; Edmonds et al., 2018; Mather et al., 2012) and whole-rock analyses of lavas from Antuco, Chile (Cox et al., 2019). However, in subaqueous eruptions (e.g., MORB and oceanic plateau basalts), Se is thought to be less volatile than S and is often used to reconstruct the behaviour of S prior to degassing (Brenan, 2015; Jenner et al., 2012; Jenner et al., 2010; Jenner et al., 2015; Reekie et al., 2019; Patten et al., 2013). The preservation of high Se contents in Lōi‘hi glasses erupted at depths $>$1000 m indicates that the onset of Se degassing takes place at pressures of $<$0.1 kbar. Experimental work assessing the volatility of Se is ambiguous. During preparation of glass reference materials, Se is retained while S is lost (Jenner et al., 2009; Jochum et al., 2006). Yet, experiments on sulfides in the Se-S system (Helmy and Fonseca, 2017), and on chondritic meteorites (Wulf et al., 1995), demonstrate that Se has a similar volatility to S. Thus, although the exact cause of Se degassing at Kīlauea is beyond the scope of this study, these results show that the assumption that Se is less volatile than S may be invalid at low pressures. As metal emissions for Se at arc volcanoes are elevated above those at Kīlauea (Edmonds et al., 2018), it seems likely that Se degasses during subaerial eruptions in a wide variety of tectonic settings.

6.4.5 Sulfide Resorption During Magma Degassing

The strong partitioning of S into the gas phase during ascent and eruption causes melt S contents to drop below the $SCSS_{Tot}$, destabilizing sulfide liquids (Edmonds and Mather, 2017; Gerlach and Nordlie, 1975; Fig. 6.1, Fig. 6.15a). At hotspot volcanoes, emanation coefficients calculated from aerosol measurements of volcanic plumes have been shown to broadly correlate with sulfide-silicate melt partition coefficients (Edmonds et al., 2018). This,

along with literature observations of sulfides attached to bubbles, has led to suggestions that chalcophile elements held within sulfides are directly transferred to the gas phase during sulfide resorption (Mungall et al., 2015; Nadeau et al., 2010). Alternatively, the quantity of chalcophile elements released into the gas phase may depend on the three-way partitioning between sulfide, melt and vapour (Edmonds et al., 2018).

The near-absence of sulfides in matrix glasses from subaerial eruptions at Kīlauea, but presence of sulfides as inclusions in silicate minerals and within undegassed embayments, is convincing evidence that sulfides in contact with the degassing melt resorb (Fig. 6.5; Gerlach and Nordlie, 1975; Moore et al., 1980; Reekie et al., 2019). Further evidence is provided by the presence of resorbed features (∼20 µm in size) in degassed matrix glasses, which predominantly consist of Fe and O, with small regions of Cu-S rich material (∼1 µm; Fig. 6.8). Their chemistry and texture is highly indicative of the breakdown of sulfides to form Fe-oxide phases (e.g., magnetite) which are metal poor (Berlo et al., 2014; Edmonds and Mather, 2017; Nadeau et al., 2010). Only sulfides which are isolated from the degassing melt, including those trapped within olivine crystals, melt inclusions, and S-rich embayments, survive syn-eruptive degassing (Fig. 6.5).

However, differences in chalcophile element concentrations in melt inclusions and matrix glasses do not support a model where sulfide breakdown releases chalcophile elements "almost quantitatively" into the gas phase Mungall et al., 2015). Firstly, there is no correlation between sulfide-melt K_Ds and the emanation coefficients estimated in this study from comparisons of melt inclusion and matrix glass concentrations (Fig. 6.3; Fig. 6.17). Emanation coefficients for Cd, Bi and S calculated in this study are remarkably similar to those estimated by Norman et al. (2004) and overlap with those calculated from the X/S ratios in the 2008 plume for Cu, Ni, Cd, and Se (Mather et al., 2012; Fig. 6.17). These published emanation coefficients also show no correlation with sulfide-melt K_Ds.

A comparison of Cu (and Ni) contents in melt inclusions and matrix glasses provides further insights into elemental partitioning between sulfides, melt, and vapour. A significant proportion of melt inclusions have lower Cu contents than matrix glasses (Fig. 6.2c; Loewen, 2013). These compositional differences between melt inclusions and matrix glasses are most obvious in the 1971 summit eruption (where trace element ratios indicate that olivine crystals grew in their carrier melts; Chapter 5). Raw and PEC-corrected Ni and Cu contents of these melt inclusions follow trajectories consistent with the removal of sulfides with compositions estimated from the regression lines in Fig. 6.13a-b (see caption, Fig. 6.18a). In contrast, matrix glasses mostly plot along the sulfide-free fractional crystallization trajectory (red line; Fig. 6.18a). Although the melt inclusion record in the other three eruptions is complicated by the fact that host olivines trapped a diverse range of melt compositions present in the plumbing system over centuries, when these three eruptions are considered together, melt inclusions form a wedge towards lower Cu and Ni contents that is bracketed by fractionation lines for predicted sulfide compositions at ∼8 and ∼12 wt% MgO (Fig. 6.18b).

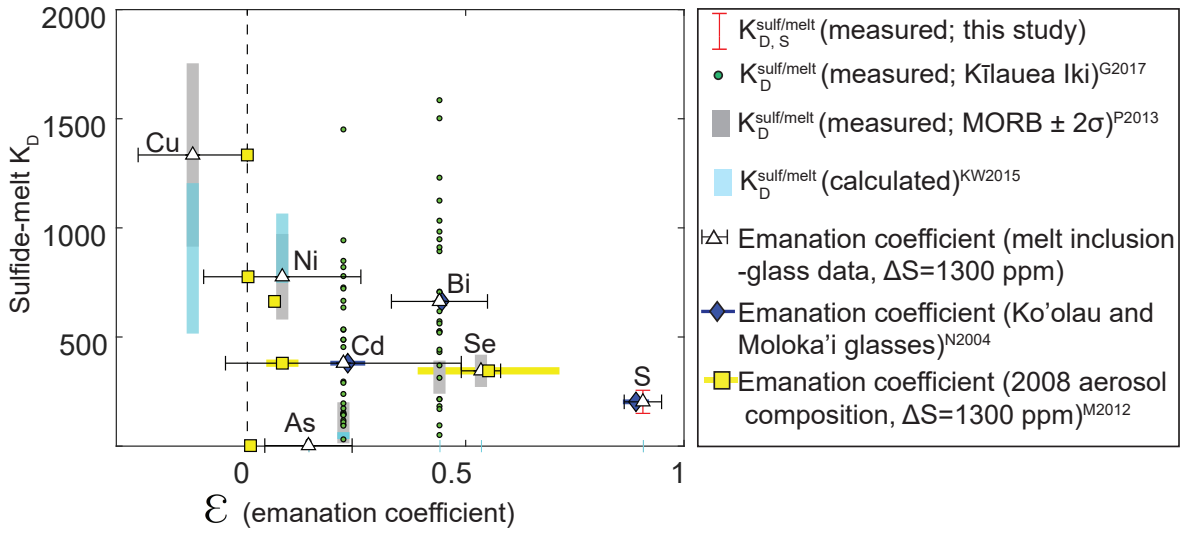


Figure 6.17: Comparison of emanation coefficients and sulfide-liquid partition coefficients. Emanation coefficients from this study (white triangles and error bars) were calculated from the regression line of each element versus S (see Fig. 6.3, 6.5). Due to its compatible behaviour during PEC and fractionation, the emanation coefficient for Ni was calculated using a regression for uncorrected melt inclusion data. Emanation coefficients were calculated from X/S ratios from the 2008 plume (Mather et al., 2012), with the numerator ($[X]_i$-$[X]_f$) calculated from $\frac{X}{S} \times \Delta S_degassed$ and the denominator ($[X]_i$) calculated from $[X]_f + \frac{X}{S} \times \Delta S_{degassed}$, where $[X]_f$ is the average composition of the 1971 matrix glass (most similar in major element composition to the 2008 summit eruption), for ΔS=1300 ppm. Emanation coefficients from Norman et al. (2004) are also overlain. Measured sulfide-silicate partition coefficients from Kīlauea Iki lava lake samples are shown in green (Greaney et al., 2017). The range of measured partition coefficients for MORBs are shown with a grey bar (mean $\pm 2\sigma$; Patten et al., 2013). The light blue bar shows the range of partition coefficients calculated from Kiseeva and Wood (2015) for compositions with MgO contents between 6 and 14 wt% MgO (using the regressions shown in Fig. 6.13 to estimate the Ni and Cu composition in the sulfide, and the geothermometer of Helz and Thornber, 1987 to obtain T). The partition coefficient of S was calculated using the range of measured S concentrations in sulfides, assuming melt S contents of 1387–1600 ppm. There is no correlation between sulfide-liquid partition coefficients and emanation coefficients defined using petrology, or aerosol chemistry.

Differences between the trajectory of melt inclusions and glasses in Ni-Cu space could be interpreted in two ways. Firstly, Fe-loss associated with PEC may have triggered the growth of a sulfide, sequestering melt inclusion Ni and Cu from the melt inclusion (Danyushevsky et al., 2002a; Métrich et al., 1999; Savelyev et al., 2018). As Kīlauean liquids undergoing only olivine (+ minor chromite) fractionation have near-constant FeO contents (∼11.33 wt%), the extent of Fe-loss is inversely proportional to the measured FeO content of the melt inclusion. The absence of correlations between melt inclusion Ni, Cu and S concentrations and melt inclusion FeO contents suggests that the trajectories towards lower Ni and Cu contents do not result from sulfide saturation following Fe-loss. Even without extensive Fe-loss, PEC could drive sulfide saturation because of the crystallization of S-poor olivine, combined with a drop in the temperature of the melt. However, there is also no correlation between raw or corrected melt inclusion S, Cu and Ni contents and the amount of PEC calculated in

Petrolog3. Finally, transmitted light observations reveal that only a very small proportion (∼5%) of melt inclusions contain sulfide blebs (Fig. 6.5e, letter "S" on Fig. 6.18). While some sulfides were inevitably lost during grinding to expose the centre of each melt inclusion, this would only account for the loss of approximately half of the sulfides formed during PEC, which doesn't explain why the vast majority of inclusions with low Cu and Ni contents don't contain sulfides. Although a few of the inclusions containing sulfides have relatively low Cu and Ni contents, others plot near matrix glasses (inclusions marked with an "S" on Fig. 6.18b), suggesting that some sulfides within melt inclusions may have been co-entrapped.

An alternative explanation for the trajectory towards lower Ni and Cu contents is that olivine crystals grew and incorporated pockets of melt over a period in which sulfide liquids were progressively forming, and depleting the melt of Ni and Cu. In order to produce the higher Cu and Ni concentrations of matrix glasses compared with melt inclusions, the resorption of sulfides upon eruption must have released almost all of the Ni and Cu held within sulfide liquids back into the melt. If the Cu (and Ni) entered the gas phase directly, matrix glasses would plot with the most Cu and Ni depleted melt inclusions (Fig. 6.18a). The low emanation coefficients of Ni and Cu from aerosol measurements (0.15 and 0.01% respectively; Mather et al., 2012; Fig. 6.17) support a model in which sulfide-hosted Ni and Cu are released back into the melt during resorption of sulfides upon eruption (e.g., Fig 5), causing matrix glasses to follow a silicate-only fractionation trajectory. In contrast, melt inclusions would be isolated from this late-stage release of Ni and Cu, preserving the chemical trajectories of sulfide fraction prior to the onset of degassing. The fact that matrix glasses lie on a silicate-only fractionation trajectory has implications for the mechanism, and efficiency of sulfide mobilization upon eruption. The high density of sulfide droplets should result in their fractionation from the melt once they grow to a critical size. The involvement of sulfides in volcanic degassing has previously been attributed to the attachment of sulfide melts onto vapour bubbles, producing a compound drop with elevated buoyancy (Edmonds and Mather, 2017; Mungall et al., 2015). Interestingly, sulfide globules attached to the faces of olivine crystals were also observed (Fig. 6.5c). The remobilization of settled olivine crystals (Chapters 4 and 5) upon eruption could provide an additional mechanism by which fractionated sulfides can participate in syn-eruptive degassing.

Chalcophile systematics in Lōi'hi glasses further support the assertion that the different trajectories defined by Cu, Ni and MgO in Kīlauean matrix glasses and melt inclusions are the result of sulfide fractionation, followed by sulfide resorption during low pressure degassing. Unlike Kīlauean glasses, Lōi'hi glasses show a positive correlation between Cu and MgO (Fig. 6.2c; R^2=0.44) and Cu and Ni (Fig. 6.18a; R^2=0.4), which is indicative of sulfide fractionation. In fact, the trajectory of these glasses in Ni vs. Cu space is remarkably similar to that defined by the 1971 melt inclusions (Fig. 6.18a). Furthermore, abundant sulfides (0.3–10% vol) have been reported in Lōi'hi xenoliths (Roedder, 1983), and relatively

abundant, spherical sulfides were observed within Lōi‘hi matrix glasses, providing strong textural evidence that Lōi‘hi magmas were sulfide-saturated. Textural and chemical evidence for sulfide saturation is preserved in Lōi‘hi matrix glasses due to the lack of syn-eruptive degassing of S in subaqueous eruptions; these samples provide a vital analogue for the evolution of sulfides within Kīlauean melts before the onset of syn-eruptive degassing.

The behaviour of Se allows further investigation of the relationship between sulfide resorption and chalcophile element degassing. In the previous section, the excellent correlation between S and Se (Fig. 6.3b) was interpreted as concurrent degassing of these elements. However, the compound drop theory suggests that Se could be released directly from sulfides into the gas phase (Mungall et al., 2015). Thus, the possibility was investigated that the S-Se trajectory defined by melt inclusions and matrix glasses records the removal of Se and S from the melt into the sulfide phase, followed by direct transfer from the sulfide to the gas phase during sulfide resorption. The chemical trajectories associated with the removal of sulfides with 30 wt% S, and Se contents calculated from the likely range of $K_{D,\ Se}^{sulf/melt}$ (271–1012; Brenan, 2015; Patten et al., 2013) were modelled, and compared with the subset of melt inclusion and glasses with Se data. While sulfide removal with $K_{D,\ Se}^{sulf/melt}$=271 approximately recreates the observed trajectories, the low Se concentrations of matrix glasses require removal of >0.4 wt% sulfide (Fig. 6.18c). Removal of this quantity of sulfides is inconsistent with observed trends in Cu vs. S space for the same subset of melt inclusions and glasses (for $K_{D,\ Cu}^{sulf/melt}$=628–1754; Fig. 6.18d). Consequently, as the combined systematics of Cu, Se and S cannot be recreated by the removal of sulfide liquids, the excellent correlation of S and Se must result from syn-eruptive degassing from the silicate melt. This is further supported by the fact that Lōi‘hi glasses, which contain visible sulfides, still have Se concentrations plotting close to the least degassed melt inclusions at Kīlauea (Fig. 6.3b).

These observations provide new insights into the relative importance of vapour-sulfide, vapour-melt, and sulfide-melt partitioning in controlling the chalcophile element budget of volcanic plumes. It seems probable that sulfide resorption releases chalcophile elements into the silicate melt-vapour system, with the partitioning between these two phases depending on element volatility (Fig. 6.19d). This is best demonstrated by comparing the behaviour of Cu and Se. The spread of melt inclusion Ni and Cu contents relative to matrix glasses indicate that approximately 0.1% sulfide resorption may occur upon eruption (Fig. 6.18a-b). While resorption of ∼0.1 wt% sulfide leads to the release of relatively large quantities of Cu (∼50 ppm; Fig. 6.18a-b), the high Cu contents of matrix glasses indicate that almost all of this Cu ends up back in the melt, because of the relatively low volatility of Cu in Kīlauean melts (X/S ratios measured in the 2008 Kīlauean plume indicate that only ∼0.01% of Cu degasses; Mather et al., 2012; Fig. 6.17). In contrast, even if all the Se released from the resorption of 0.1 wt% sulfide liquid entered the gas phase (∼0.08 ppm), a similar quantity of Se would also have to directly degass from the melt (Fig. 6.18c). Given that there is no evidence that sulfide-hosted Cu enters the gas phase directly, it seem likely that Se released from sulfides first enters the melt, then partitions along with S into the vapour phase (Fig. 6.18c).

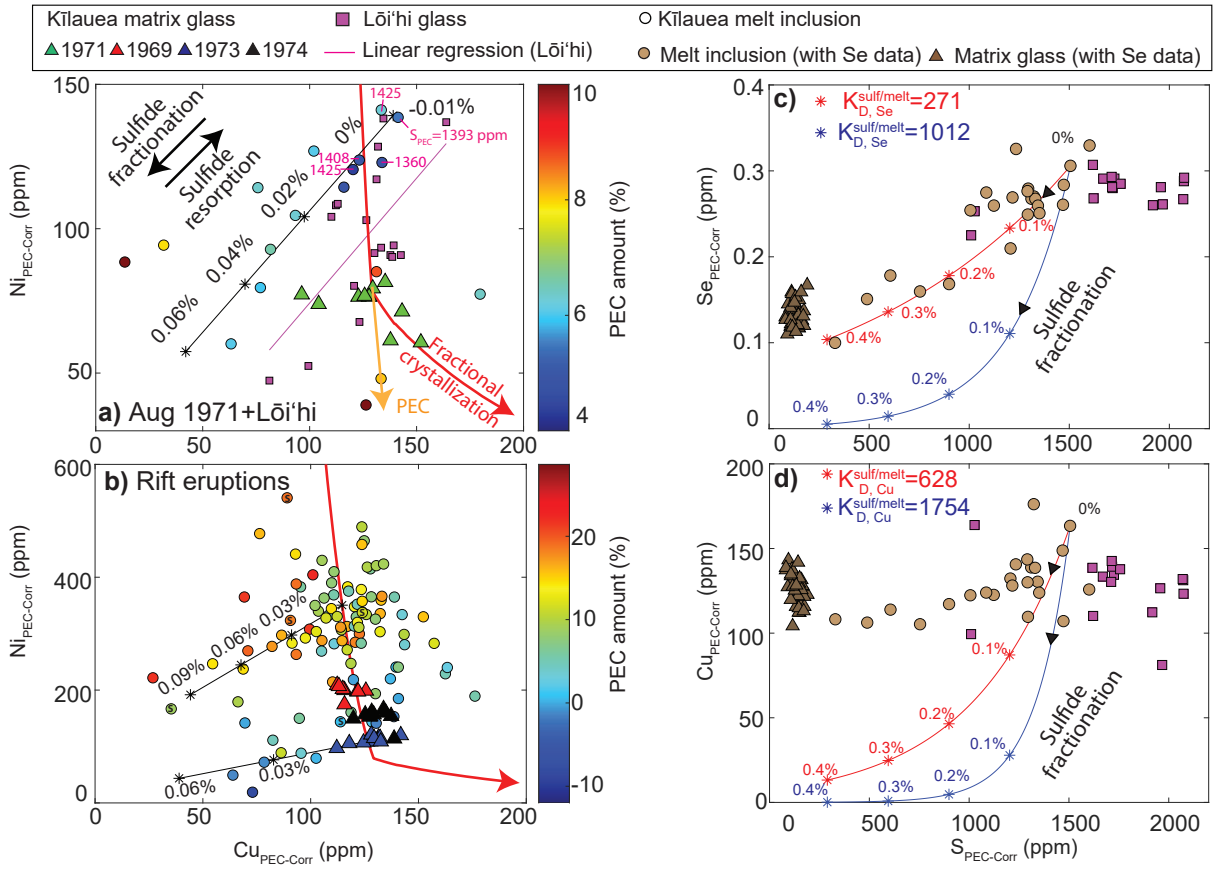


Figure 6.18: Differentiating sulfide resorption and degassing. **a)** Cu-Ni systematics for the 1971 summit eruption (where melt inclusions and carrier melts show a clear genetic relationship; Chapter 5). Matrix glasses largely plot along the sulfide-free fractional crystallization trajectory. Melt inclusion compositions corrected for post-entrapment crystallization follow two trajectories; that of silicate-only fractionation (red line), and decreasing Cu and Ni concentrations indicative of sulfide fractionation (black line). The black lines represent the removal of a sulfide composition calculated from the regression lines in Fig. 6.13 for MgO = 8.4 wt% (the mean PEC-corrected melt inclusion MgO content for this eruption). A linear regression through the composition of matrix glasses from Lōi'hi follows a remarkably similar trajectory. **b)** Cu-Ni systematics for matrix glasses and melt inclusions from the three rift-zone eruptions are bracketed by fractional crystallization and sulfide fractionation trends (lower and upper sulfide removal trend for ∼7 and 12 wt% MgO). Melt inclusions containing a sulfide are marked with an "S". **c)** Models of the trajectory for sulfide fractionation in Se. vs. S space for different values of $K_{D,\ Se}^{sulf/melt}$. While sulfide fractionation for the lower limit of published estimates for the $K_{D,\ Se}^{sulf/melt}$ pass through melt inclusion data, fractionation of large quantities (∼0.4 wt%) of sulfide are required to recreate the low Se concentrations of matrix glasses. **d)** Fractionation of this quantity of sulfides is inconsistent with observed Cu-S concentrations in the subset of matrix glass and melt inclusion compositions with Se data. The minimum value for $K_{D,\ Se}^{sulf/melt}$ (=271) is calculated as the mean minus 2σ from Patten et al. (2013), and the maximum (=1012) is from the parametrization of Brenan (2015) for FeO=11.33 wt%. The maximum $K_{D,\ Cu}^{sulf/melt}$ (=1754) is from Patten et al., 2013 - mean $+2\sigma$), and the minimum (=628) was calculated from the parameterization of Kiseeva and Wood (2015) for the sulfide composition calculated from the regressions in Fig. 6.13 for 14 wt% MgO, and temperatures from Helz and Thornber (1987).

Sulfide resorption upon eruption provides a significant, but previously unquantified flux of S to the atmosphere during Kīlauean eruptions. Resorption of 0.1 wt% sulfide corresponds to the release of 300 ppm of S (as measured sulfides contain ∼30 wt% S). This represents an additional source of error when using the "petrological method" in basaltic systems to quantify total S release (in addition to uncertainty in erupted lava volumes). This source of error can be circumvented if the Cu-Ni-S systematics of melt inclusions are carefully evaluated when choosing S concentrations to compare to co-erupted matrix glasses. The best constraint on the S release during eruptions is provided by melt inclusions with Cu concentrations overlapping those in co-erupted matrix glasses. In the 1971 summit eruption, these melt inclusions have PEC-corrected S concentrations between 1360–1425 ppm. Accounting for the incomplete degassing of basaltic melts (1971 matrix glasses have average S contents of 121 ppm), these measurements suggest that ∼1240–1300 ppm of S was released. In more primitive eruptions, melt inclusions with Ni and Cu systematics similar to matrix glasses have PEC-corrected S contents of ∼1600 ppm, so the S release upon eruption could reach 1465 ppm (accounting for the average glass S content of 135 ppm). SO_2 emissions at Kīlauea have been used to calculate lava effusion rates (Sutton et al., 2003; Sutton et al., 2001) using much lower estimates of S release from C/S ratios measured in volcanic gases (e.g., 861 ppm – Greenland, 1984; Greenland et al., 1988; 745 ppm – Sutton et al., 2003). The significantly higher estimates of S release calculated here highlight the importance of detailed petrological work to accurately constrain lava effusion rates.

6.5 Conclusions

Chalcophile element behaviour at Kīlauea Volcano, Hawai'i, is predominantly controlled by three separate stages of sulfide saturation, combined with the effects of sulfide resorption and degassing upon ascent to the site of eruption. The decoupled variability of chalcophile and lithophile elements during mantle melting in primitive samples (>6.8 wt% MgO) indicates that the concentrations of chalcophile elements in Kīlauea's mantle source are buffered by the presence of residual sulfides (Fig. 6.19a). These residual sulfides (and the possible presence of non-negligible proportions of S^{6+} species) are responsible for the high S contents of primary Kīlauean melts (1387–1600 ppm). The increase in sulfide solubility with decreasing pressures as melts ascend through the thick Hawaiian lithosphere results in crustal magma chambers being supplied with sulfide-undersaturated melts (Fig. 6.19b). The inclusion of sulfides within primitive olivine crystals, combined with models of sulfide solubility during fractional crystallization, indicates that a second stage of sulfide saturation within the crust occurs after relatively small amounts of crystal fractionation (∼12 wt% MgO; Fig. 6.19c).

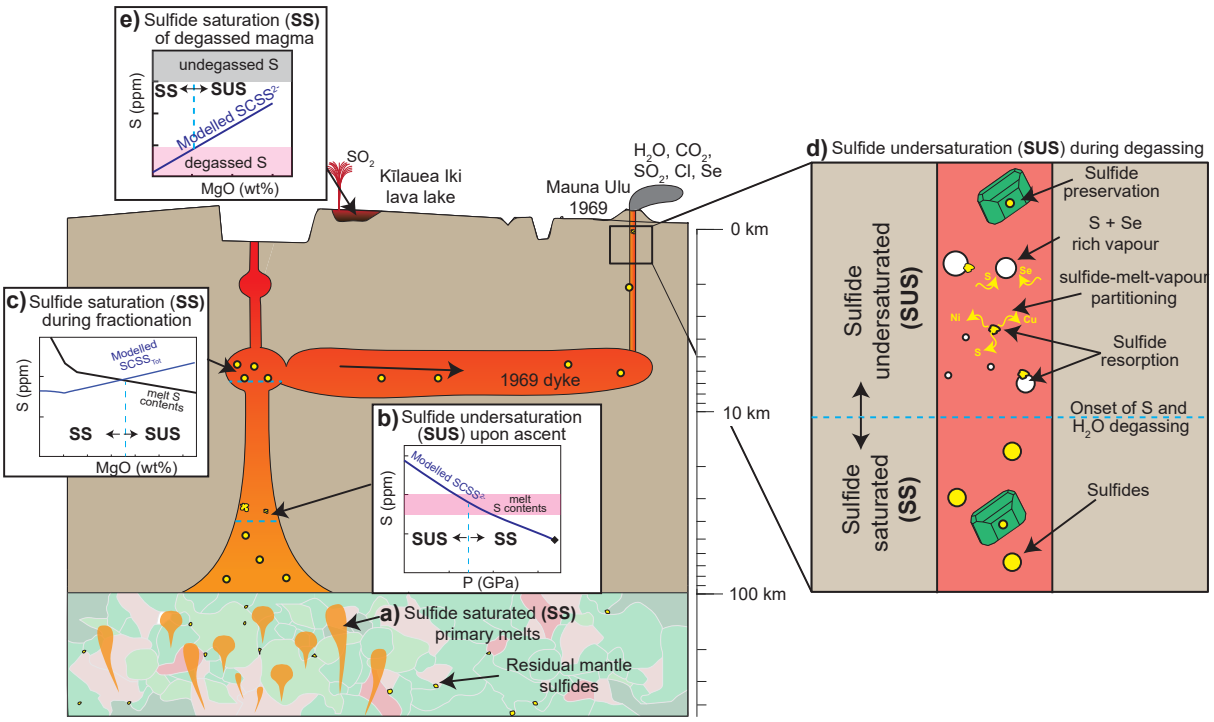


Figure 6.19: Summary diagram of processes affecting chalcophile element concentrations at Kīlauea. **a)** Residual sulfides are present in the mantle source throughout the melting interval of the eruptions analysed in this study (∼F=0.05–0.1), buffering the concentrations of chalcophile elements relative to lithophile elements during changes in melt extent. The presence of residual sulfides accounts for the high S contents of primary melts (1387–1600 ppm). **b)** Upon ascent through the thick Hawaiian lithosphere, the increase in the $SCSS^{2-}$ with decreasing pressure results in melts becoming sulfide undersaturated (SUS). **c)** During fractionation in crustal magma chambers, decreasing temperatures, major element changes, and an increase in melt S contents during crystal fractionation drives the melts towards sulfide saturation once more (∼12 wt% MgO). **d)** At low pressures as magma ascends towards the site of eruption, S partitions strongly into a vapour phase. This causes sulfides to resorb, releasing their chalcophile element load (S, Ni, Cu, Se etc.) back into the melt. These elements then partition between the melt and vapour phase, resulting in volatile elements such as S and Se mostly partitioning in the gas phase, and more refractory elements such as Ni and Cu remaining in the melt. **e)** The lava filling the Kīlauea Iki lava lake was S-poor (and therefore sulfur undersaturated) due to extensive degassing upon eruption. Extensive amounts of cooling and fractionation were required to reach sulfide saturation from such a S-poor melt.

Syn-eruptive degassing causes melt S contents to drop below the $SCSS_{Tot}$, driving the resorption of sulfides which are in contact with the degassing melt (Fig. 6.19d). This releases Cu, Ni, S and other chalcophile elements back into the vapour-melt-(sulfide) system. Elements with high vapour-melt partition coefficients enter the gas phase (e.g., S, Se), while elements with lower vapour-melt partition coefficients (e.g., Ni, Cu) predominantly remain in the melt. The resorption of sulfides, and the release of their chalcophile element budget back into the melts, obscures the textural and chemical record of sulfide saturation in matrix

glasses. The coincidence of Cu-MgO and Cu-Ni systematics in matrix glasses with the trends predicted from sulfide-undersaturated fractionation demonstrates that the vast majority of immiscible sulfide liquids participated in the degassing process; perhaps due to their attachment to buoyant vapour bubbles, or remobilized olivine crystals. Fortunately, the chalcophile element systematics within melt inclusion populations (which are isolated from the late stage release of chalcophile elements into the melt), along with the preservation of visible sulfides within olivine crystals and undegassed embayments, faithfully record the fractionation of sulfides.

Previous studies investigating chalcophile element systematics have focused on lava lakes, formed through the ponding and fractionation of degassing melt within pre-existing pit craters. This has led to suggestions that sulfide saturation at Kīlauea only occurs after significant amounts of crystal fractionation (∼2 wt% MgO). Instead, this study demonstrates that the loss of S to the gas phase upon eruption resulted in previously sulfide-saturated magmas becoming sulfide undersaturated once more. Due to their low S contents, these melts reach a third phase of sulfide saturation following significant amounts of cooling and fractionation (Fig. 6.19e). This phase is unique to the fractionation path taken by degassed melts, and is not representative of the evolution of undegassed melts in crustal magma chambers.

In review as: *Wieser, P.E., Lamadrid, H., Maclennan, J., Edmonds, M., Matthews, S., Iacovino, K., Jenner, F.E., Gansecki, C., Trusdell, F., Lopaka, R.L., Ilyinskaya, E.,. Reconstructing Magma Storage Depths for the 2018 Kīlauean Eruption from Melt Inclusion CO_2 Contents: The Importance of Vapour Bubbles. Geophysics, Geochemistry, Geosystems.*

7

Reconstructing Magma Storage Depths for the 2018 Kīlauean Eruption from Melt Inclusion CO_2 Contents

Note, this Chapter was written before receiving reviewer reports. Please refer to the final published version.

Abstract

The 2018 lower East Rift Zone (LERZ) eruption and the accompanying collapse of the summit caldera marked the most destructive episode of activity at Kīlauea Volcano in the last 200 years. The eruption was extremely well-monitored with continuous geodetic data capturing the caldera collapse and an extensive real-time lava sampling campaign. This multi-parameter dataset provides an exceptional opportunity to determine the reservoir geometry and magma transport paths supplying Kīlauea's LERZ. The forsterite contents of olivine crystals, together with the degree of major element disequilibrium with carrier melts, indicates that two distinct crystal populations were erupted from Fissure 8. Melt inclusion entrapment pressures reveal that more evolved olivines ($<Fo_{81.5}$) crystallized at ∼2 km depth within the shallower Halema'uma'u reservoir, while more primitive olivines ($>Fo_{81.5}$) crystallized within the deeper South Caldera (SC) reservoir at ∼3–5 km depth. Melt inclusions in primitive olivines experienced extensive post-entrapment crystallization following their incorporation into cooler, more evolved melts. This favoured the growth of a CO_2-rich vapour bubble, containing up to 99% of the total melt inclusion CO_2 budget (median=93%). Measurements of CO_2 in only the glass phase of the inclusion would underestimate entrapment depths by up to a factor of 60 (median factor of 12) and fail to recognize the contribution of magma supplied from the SC reservoir. Overall, this work demonstrate that Raman measurements of bubbles, along with careful choice of a suitably-calibrated H_2O-CO_2 solubility model, is vital to place accurate constraints on the depths of magma storage regions supplying volcanic eruptions.

7.1 Introduction

The 2018 lower East Rift Zone (LERZ) eruption was the largest and most destructive in the last 200 years of activity at Kīlauea Volcano, Hawai'i (Neal et al., 2019), accompanied by extremely high co-eruptive fluxes of SO_2 (up to 200 kt a day; Kern et al., 2020) and lava effusion rates (100-300 m^3/s, Neal et al., 2019; Patrick et al., 2019a). Before the onset of this new eruptive episode in May 2018, Kīlauea had been erupting near-continuously for 35 years on the middle East Rift Zone at Pu'u 'Ō'ō cone and surrounding vents, located approximately ~20 km east of Kīlauea's summit (1983–2018), and ~24 km uprift of the 2018 eruption site (Fig. 7.1b). From 2008 to 2018, a persistently active lava lake was also present within Halema'uma'u (HMM) pit crater, located in the south west area of Kīlauea's summit caldera (Fig. 7.1b).

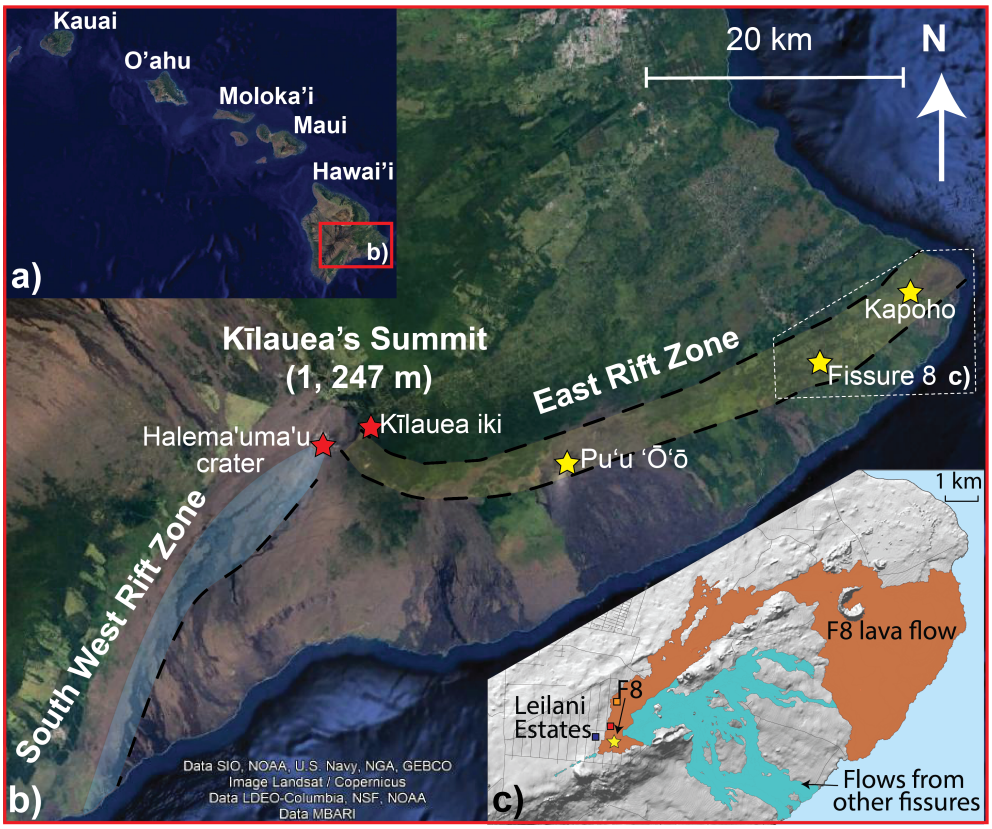


Figure 7.1: Map of Kīlauea Volcano **(b)**, located on the southwest of the island of Hawai'i **(a)**. Two prominent rift zones radiate from Kīlauea's summit caldera **(b)**. The 2018 eruption occurred within the Leilani Estates subdivision on the lower East Rift Zone (LERZ; expanded region in **c)**. The lava flows from F8 are colored deep orange, while flows from Fissures 1–7, and 9–24 are colored light blue. Sample locations are marked with squares (blue=May, 2018, red=July, 2018, orange=Aug, 2018). Base maps for **a)** and **b)** are from Google Earth, and the map in **c)** is adapted from Patrick et al. (2019a).

The 2018 eruption was preceded by swarms of lower-crustal earthquakes at ∼6–12 km depth beneath Kīlauea's summit area on March 7th, April 11th, and April 18th, 2018 (Flinders et al., 2020), interpreted to result from a short-term increase in magma supply. On March 13th, 2018, inflation was recorded by tiltmeters located at Kīlauea's summit. Inflationary ground deformation also began at Pu'u 'Ō'ō, suggesting that excess magma was accumulating beneath this vent (Neal et al., 2019). The pressurization at these two locations continued throughout March and April, demonstrated by the rise of the lava pond at Pu'u 'Ō'ō, and overflows of the summit lava lake in mid-late April. On April 30th, the crater floor at Pu'u 'Ō'ō collapsed, followed by an eastward migration of seismicity along the rift zone, consistent with the propagation of a dyke (Neal et al., 2019). A hazard notice released early in the morning of May 1st warned the residents of Lower Puna to be alert, as a large area along the ERZ east of Pu'u 'Ō'ō was at risk from a new outbreak of lava. Following the appearance of ground cracks in the Leilani Estates subdivision (Fig. 7.1c) on May 2nd, lava reached the surface just before 5 pm on May 3rd (Neal et al., 2019). Over the next few days, multiple fissures opened, preceded by gas emissions and ground cracking. In all, 24 fissures opened between the 3rd and 27th of May 2018.

Activity between the 3rd and 9th of May, classified as Early Phase 1 by Gansecki et al. (2019), was characterized by the eruption of spatter mounds and sluggish, slow-moving lava flows. This relatively evolved magma (mean SiO_2=51 wt% and mean MgO=4 wt%; Lee et al., 2019; Gansecki et al., 2019) is thought to have formed by differentiation within LERZ storage reservoirs over decades to centuries (Neal et al., 2019). Throughout May, the compositions of erupted melts and crystals became increasingly primitive as summit-derived magma flushed out the LERZ storage reservoirs (with the exception of the involvement of a more andesitic composition erupted in mid to late May; Gansecki et al., 2019). The eruption of hotter, less viscous lava led to the generation of fast-moving lava flows on May 18th, which reached the coast five days later (Neal et al., 2019, Fig. 7.1c). By May 28th, activity had localized at Fissure 8 (F8), with the effusion of fast-flowing magma as a channelized flow (Patrick et al., 2019). Activity ended abruptly on August 4th, by which time F8 had erupted ∼1.5 km^3 of lava (Kauahikaua and Trusdell, 2020).

Despite the abundant geophysical and geochemical observations made during the LERZ eruption, the source of the magma erupted at F8 from late May-August 2018 has not yet been established. It is generally accepted that two main reservoirs are located beneath Kīlauea's summit. The shallower Halema'uma'u (HMM) reservoir is recognised as an inflation source located beneath the eastern rim of the HMM crater, and is thought to be centred at ∼0.5–2 km depth (Anderson et al., 2019; Cervelli and Miklius, 2003; Baker and Amelung, 2012; Fiske and Kinoshita, 1969), while the deeper South Caldera (SC) reservoir manifests as an inflation source located beneath the southern portion of the caldera, at ∼3–5 km depth (Baker and Amelung, 2012; Poland et al., 2015). The 2018 LERZ eruption was accompanied

by large-scale subsidence of the caldera floor centred around the HMM crater (500 m in certain locations; Neal et al., 2019), which has been attributed to magma withdrawal from the underlying HMM reservoir to feed the effusion of lava from F8 (Anderson et al., 2019). However, recent estimates of the total SO_2 emissions requires the erupted volume to be approximately twice the modelled volume loss from the HMM reservoir, suggesting that a second magma source was involved (Kern et al., 2020).

Additionally, the erupted crystal cargo from F8 contained some of the most primitive olivines (Fo_{88-89}) observed at Kīlauea since 1974, which formed in liquids with 13–14 wt% MgO (Gansecki et al., 2019). These crystals also contain prominent kink bands (Gansecki et al., 2019), indicating that their crystal lattices have been deformed (see Chapter 4). Previous work has suggested that highly forsteritic, deformed olivines are derived from the deeper, SC reservoir at 3–5 km depth (Helz et al., 2014; Helz et al., 2015, Chapters 4 and 5), or Kīlauea's deep rift zones at 6–9 km depth (Clague and Denlinger, 1994; Vinet and Higgins, 2010). Alternatively, Lynn et al. (2017) suggest that highly forsteritic olivines from the Keanakāko'i Tephra may originate from deeper crustal storage reservoirs, perhaps located near the base of the volcanic pile at ∼8-10 km depth.

This study utilizes the strong pressure dependence on the solubility of CO_2 and H_2O in silicate melts to determine the pressures at which pockets of melt, also known as melt inclusions, were trapped within olivine crystals. Through prior constraints on the density profile of the crust, entrapment pressures from F8 melt inclusions erupted in late May, mid-July and early August 2018 can be converted into entrapment depths. In turn, these depths can be compared to geophysical estimates of the depths of the main magma storage regions at Kīlauea to determine the source(s) of magma erupted at F8.

7.2 Melt Inclusion Entrapment Pressures

7.2.1 The Importance of Vapour Bubbles

In relatively dry systems like Kīlauea where melts contain <1 wt% H_2O (Dixon et al., 1991; Sides et al., 2014a; Sides et al., 2014b; Tucker et al., 2019; Wallace and Anderson, 1998), the solubility of CO_2 in silicate melts is most sensitive to pressure and the major element composition of the melt. In comparison, variations in melt H_2O contents between 0–1 wt% have relatively little influence, except at very low CO_2 concentrations (Fig. 7.2; Newman and Lowenstern, 2002; Dixon et al., 1991). However, a considerable problem with melt inclusion barometry in water-poor systems is that estimation of the initial CO_2 content of a melt inclusion at the point of entrapment is not straightforward. Following entrapment, the host crystal may experience a period of cooling, leading to the post-entrapment crystallization (PEC) of olivine on the walls of the melt inclusion (Roedder, 1984; Danyushevsky et al., 2000; Anderson and Brown, 1993). The precipitation of denser olivine from the silicate

melt, combined with the differential thermal contraction of the melt phase and the host olivine, causes the internal pressure of the melt inclusion to drop, driving the growth of a vapour bubble (Roedder, 1979; Anderson, 1974; Anderson and Brown, 1993). Combined with a reduction in the solubility of CO_2 associated with major element changes during PEC, these processes drive the partitioning of CO_2 from the melt phase into the bubble (Steele-MacInnis et al., 2011; Sides et al., 2014b; Maclennan, 2017; Aster et al., 2016). An additional phase of bubble growth is caused by the differential thermal contraction of the melt inclusion and the host olivine during syn-eruptive cooling from high magmatic temperatures (∼1150° C at F8; Helz and Thornber, 1987; Gansecki et al., 2019) to the glass transition temperature (∼725°C; Ryan and Sammis, 1981).

Unfortunately, the vast majority of published volatile contents in melt inclusions globally, and at Kīlauea, only measured CO_2 in the glass phase, using techniques such as secondary-ion mass spectrometry (SIMS), or Fourier transform infrared spectroscopy (FTIR; Bennett et al., 2019; Ruth et al., 2018; Sides et al., 2014b; Sides et al., 2014a). Given that recent work has shown that ∼40–90% of the total CO_2 budget of melt inclusions may be held within the vapour bubble (Wallace et al., 2015; Rasmussen et al., 2020; Moore et al., 2015; Hartley et al., 2014), entrapment pressures from studies neglecting vapour bubble carbon must be viewed as minimum estimates (Anderson and Brown, 1993; Ruth et al., 2018).

7.2.2 Reconstructing Vapour Bubble CO_2

Several approaches have been used to explore the contribution of vapour bubbles to the CO_2 budget of Hawaiian melt inclusions. Anderson and Brown (1993) theoretically reconstruct vapour bubble CO_2 by assuming that the melt and vapour bubble were in chemical equilibrium at high magmatic temperatures prior to syn-eruptive quenching. Specifically, they calculated melt inclusion internal pressures from glass CO_2 contents, and used these pressures to determine the molar volume of CO_2 in vapour bubbles using the CO_2 equation of state (EOS). They converted molar volumes into CO_2 concentrations assuming that bubbles occupied 0.5 vol% of the melt inclusion prior to quenching, and added these values to measurements of glass CO_2 concentrations. Riker (2005) used a similar method to reconstruct bubble carbon for melt inclusions from the 1859 eruption of Mauna Loa. However, instead of using a fixed bubble volume, they account for the differential amounts of cooling and PEC experienced by erupted crystals, and calculate the bubble volumes prior to quench-induced expansion as a function of the drop in temperature (ΔT) between the melt inclusion at the point of entrapment and eruption (VB vol% = 0.0162 ΔT - 0.0016). More recently, Tucker et al. (2019) theoretically reconstructed bubble carbon contents for a large suite of melt inclusions from several Hawaiian volcanoes, including 167 from Kīlauea. However, instead of estimating the size of the vapour bubble prior to syn-eruptive quenching as in Anderson and Brown (1993) and Riker (2005), they used observed bubble volumes

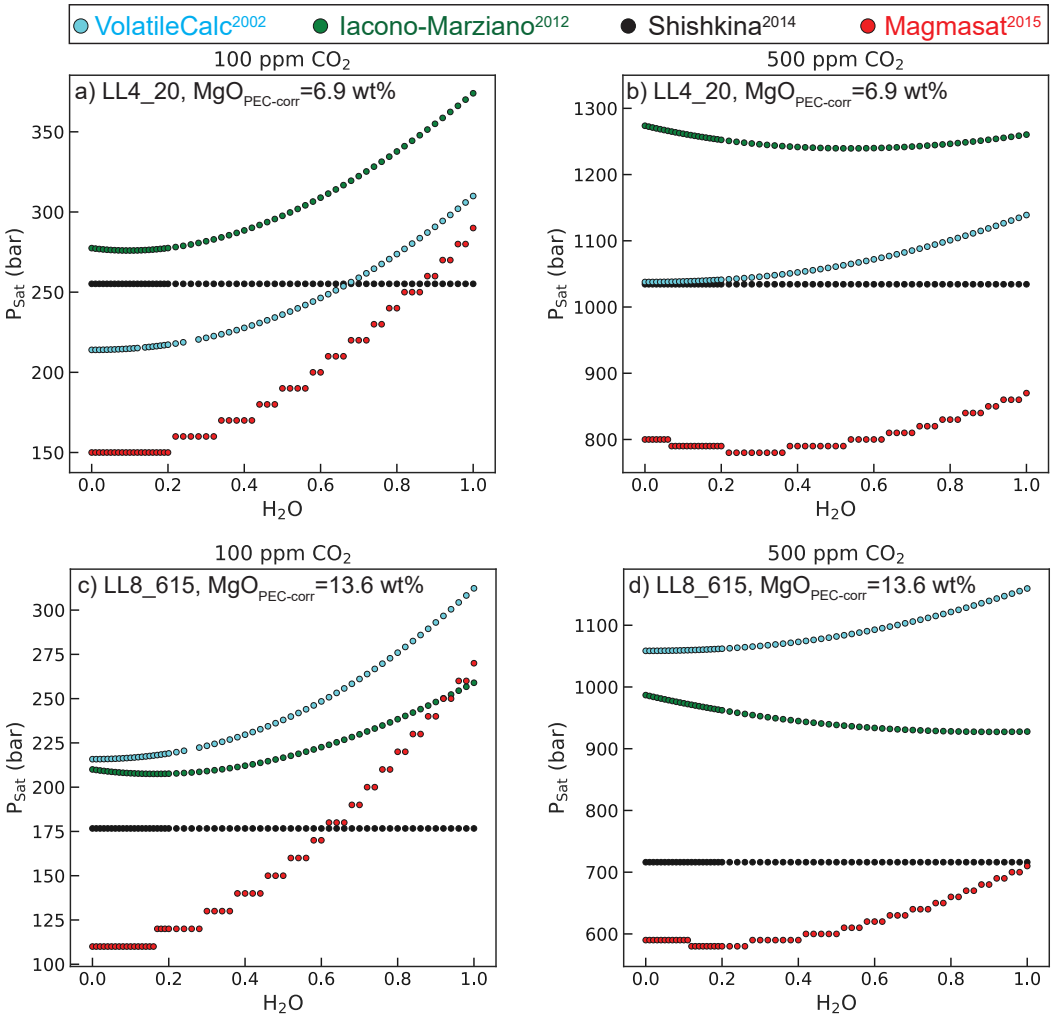


Figure 7.2: Sensitivity of saturation pressures from four different solubility models to melt inclusion H_2O contents at a fixed CO_2 content (100 and 500 ppm) for a PEC-corrected major composition representative of low-Fo **(a-b)** and high-Fo melt inclusions **(c-d)**. Saturation pressures obtained from the Shishkina et al. (2014) model do not vary for H_2O contents < 1 wt%. Magmasat shows the greatest sensitivity, which is particularly pronounced at low CO_2 contents. Regardless of the model, the differences in the saturation pressure between 100 and 500 ppm CO_2 are substantially larger than the variation between 0–1 wt% H_2O. The stepped behaviour to the Magmasat model reflects the calculation step of the way MELTS is called in VESIcal (Iacovino et al., 2020).

to convert CO_2 densities obtained from the EOS into bubble CO_2 concentrations. This approach is problematic because expansion of the bubble during syn-eruptive cooling and quenching continues until the glass transition temperature, while CO_2 diffusion through the melt into the bubble may effectively cease at a higher temperature. Thus, the final stages of bubble expansion will occur without concurrent CO_2 diffusion from the glass into the bubble, meaning that the EOS method will overpredict the amount of CO_2 in the bubble (Anderson and Brown, 1993; Maclennan, 2017; Rasmussen et al., 2020).

The total amount of CO_2 within melt inclusions can also be determined using experimental homogenization techniques, where crystals containing melt inclusions are heated to magmatic

temperatures. This drives the dissolution of the olivine rim precipitated during PEC, which changes the chemistry and volume of the melt inclusion so that CO_2 held within the vapour bubble dissolves back into the melt. Following rapid quenching, the glass phase of these rehomogenized melt inclusions can be analyzed by SIMS or FTIR (Esposito et al., 2012; Rasmussen et al., 2020; Skirius et al., 1990; Tuohy et al., 2016; Wallace et al., 2015). However, experimental homogenization can lead to H_2O loss, excess dissolution of olivine on the walls of the melt inclusion, and loss of mineral and melt inclusion zoning, which degrades the overall utility of the melt inclusion record (Rasmussen et al., 2020; Tuohy et al., 2016). Additionally, it is not always possible to fully dissolve the original bubbles, and new bubbles containing CO_2 may nucleate upon quench (Wallace et al., 2015; Tuohy et al., 2016; Skirius et al., 1990; Rasmussen et al., 2020).

Most recently, the density of CO_2 in vapour bubbles have been measured directly using Raman Spectroscopy (Taracsák et al., 2019; Esposito et al., 2011; Steele-MacInnis et al., 2011; Moore et al., 2018; Moore et al., 2015; Hartley et al., 2014; Aster et al., 2016; Esposito et al., 2011). The Raman spectrum of CO_2 consists of two peaks nominally at 1285 cm^{-1} and 1388 cm^{-1} at 1 bar, resulting from the interaction of a symmetrical stretching mode and an active bending mode in the CO_2 molecule by a process known as Fermi resonance (Rosso and Bodnar, 1995; Lamadrid et al., 2017; Fermi, 1931). Hence, collectively, these peaks are referred to as the Fermi diad (FD), and the distance between the peak centres is the Fermi diad splitting (Δ). However, while it is well accepted that Δ correlates with CO_2 density (ρ_{CO_2}), there are a number of different parameterizations for this relationship in the literature (Wang et al., 2019; Rosso and Bodnar, 1995; Lamadrid et al., 2017; Kawakami et al., 2003, and refs. within). The diversity of published densimeters reflects different instrument hardware, as well as the choice of analytical conditions (Lamadrid et al., 2017). Thus, the approach used by a number of studies where a densimeter is chosen from the literature to convert measurements of Δ to ρ_{CO_2} on a different Raman instrument from the one used to calibrate the densimeter results in large systematic uncertainties in the absolute density of CO_2 (e.g., Venugopal et al., 2020; Taracsák et al., 2019; Hartley et al., 2014). For example, a measured FD splitting of 102.8 cm^{-1} yields ρ_{CO_2}=0.0281 g/cm^3 using the densimeter of Wang et al. (2019), but ρ_{CO_2}=0.1397 g/cm^3 using the densimeter of Kawakami et al. (2003). For a bubble volume of 5% (the 80th percentile of bubble volume proportions at Kīlauea from Tucker et al., 2019), these different densimeters predict vapour bubble CO_2 contents of 520 ppm vs. ∼2590 ppm respectively. For a melt inclusion with SiO_2=49 wt%, and H_2O=0.5 wt%, these CO_2 contents correspond to entrapment pressures of ∼1.1 kbar vs. 4.7 kbar (Newman and Lowenstern, 2002), and entrapment depths of ∼4 km vs. ∼18 km respectively for a crustal density of 2.7 g/cm^3. This demonstrates that the development of an instrument-specific calibration is essential to even be able to differentiate between lower and upper crustal storage at ocean island volcanoes, let alone fingerprinting the involvement of different reservoirs identified by geophysical techniques.

An additional source of error affecting both Raman measurements and EOS methods using measured bubble volumes arises during the conversion of ρ_{CO_2} into the equivalent amount of CO_2 in ppm held within the vapour bubble ($[CO_2]^{VB}$):

$$[CO_2]^{VB} = 10^6 \times \frac{\rho_{CO_2} V_{VB}}{\rho_{MI} V_{MI}} \tag{7.1}$$

Where V_{VB} and V_{MI} are the volume of the vapour bubble and melt inclusion respectively, and ρ_{MI} is the density of the silicate melt (calculated here using DensityX; Iacovino and Till, 2019). Total CO_2 contents are obtained by summing the equivalent amount of CO_2 in the vapour bubble with the concentration of CO_2 measured in the melt phase ($[CO_2]^{MI}$) by SIMS or FTIR:

$$[CO_2]^{Tot} = [CO_2]^{VB} + [CO_2]^{MI} \tag{7.2}$$

The volumes of the vapour bubble and melt inclusion are typically determined from 2D transmitted light images, estimating the length of the third, unmeasurable dimension from the major and minor axes of the plan view of the inclusion. Tucker et al. (2019) simulate this process by randomly intersecting ellipses and show that the smallest errors are achieved by calculating the third axis as the arithmetic mean of the two measured axes of the ellipse. However, this approach is still associated with a 1σ error of -47 to +37% (Tucker et al., 2019). Although important, it is worth noting that this random error is entirely overwhelmed by the systematic error of up to a factor of 4 in literature datasets which have arbitrarily chosen a literature densimeter. In this study, to mitigate the systematic error associated with Raman calibration, the relationship between Δ and ρ_{CO_2} was determined for the specific instrument and acquisition conditions used in this study through the analysis of synthetic fluid melt inclusions with known CO_2 densities (see Chapter 2). Analysis of both the melt phase (using SIMS) and the vapour bubble (using a calibrated Raman system) yields the first extensive dataset critically evaluating the contribution of vapour bubbles to the total CO_2 budget of specific melt inclusions. Combined with a rigorous examination of the suitability of different CO_2 - H_2O solubility models, these measurements place accurate constraints on entrapment depths of olivine-hosted melt inclusions from the 2018 LERZ eruption. This dataset, combined with quantitative models of bubble growth, also allows assessment of the relative importance of post-entrapment crystallization and syn-eruptive quenching on the partitioning of CO_2 between the melt and vapour phase. In turn, this allows the accuracy of EOS methods as an alternative to direct measurements of ρ_{CO_2} using Raman Spectroscopy to be determined.

7.3 Materials and Methods

7.3.1 Sample Details and Preparation

Three samples erupted at F8 were examined (square symbols; Fig. 7.1c):

1. May-18 (erupted May 30th, 2018, lab code LL4, USGS code KE62–3293; blue symbols), comprising vesicular reticulite and scoria which landed in a bucket placed near the F8 vent (19° 27.7486' N, 154° 54.8636' W).

2. July-18 (erupted Mid-July 2018, lab code LL8, red symbols), from the selvages of a naturally-quenched, and highly vesicular proximal overflow from the F8 channel (<50 m from the vent; 19° 27.879' N, 154° 54.645' W).

3. Aug-18 (erupted Aug 1st, lab code LL7, USGS code KE62–3321F; orange symbols), which was sampled directly from the F8 channel using a metal rod and chain, and rapidly quenched in water. Direct lava sampling took place on a stable channel levee (19° 28.31508' N, 154° 54.51426' W), ∼700 m downstream of the position of the July-18 overflow.

Samples were jaw crushed and sieved into three size fractions (250–840, 840–1000 and >1000 μm). Olivines were picked under a binocular microscope, and individually mounted in CrystalBond^{TM} on glass slides. Melt inclusions were exposed by grinding with 250–3000 grade wet and dry paper, allowing embayments to be avoided, and melt inclusions containing vapour bubbles to be identified. Care was taken to prepare melt inclusions hosted within olivine crystals from all three size fractions. Melt inclusions containing vapour bubbles were photographed before the melt inclusion was breached during grinding. For larger melt inclusions, this required two images, one where the bubble was in focus, and one where the melt inclusion outline was in focus. The outline of the bubble and melt inclusion were drawn around in ImageJ, and a best fit ellipse was fitted to each. Volumes were calculated by assuming that the third (non-measurable axis) was equal to the arithmetic mean of the two measured axes of the ellipse (Tucker et al., 2019). Several melt inclusions contained large spinel crystals that were likely co-entrapped. The volume of these spinels (assuming a cuboid shape, with the third dimension also equal to the arithmetic mean of the visible dimensions) was subtracted from the volume of the melt inclusion. Following these measurements, crystals were ground down with progressively finer wet and dry paper (5000–8000) grade until the vapour bubble was within ∼30 μm of the surface. Depending on the optical quality after these fine grinding stages, melt inclusions were variably polished using 9 µm diamond pastes prior to Raman analysis.

Following Raman analyses, individual crystals were ground down to expose the center of each melt inclusion to maximize the available analyzable area. This exposed the bubble in

approximately half of melt inclusions, allowing examination of bubble walls on a FEI Quanta 650FEG SEM in low vacuum mode prior to the application of any coatings. Crystals were then mounted in epoxy in groups of 20–40, and polished with progressively finer diamond pastes (9, 6, 3, 1, 0.25 µm). Following the application of a gold coat, the concentrations of H_2O and CO_2 (as well as MgO and SiO_2 for normalization) in melt inclusions and co-erupted matrix glasses were determined using the Cameca IMS-7f GEO at the NERC Ion Microprobe Facility, University of Edinburgh. SIMS analysis was performed prior to EPMA analysis to avoid volatile migration under the electron beam, and to avoid contamination of measured carbon concentrations by a carbon coat. Following SIMS analyses, the Au coat was removed by polishing on a 0.25 µm diamond polishing pad, and a carbon coat was applied for electron microprobe analyzer (EPMA) analyses. Spot analyses of melt inclusions, matrix glasses and host olivines were obtained using a Cameca SX100 EPMA. Further details of Raman, EPMA and SIMS analyses are presented in Chapter 2.

Melt inclusions were corrected for the effects of post-entrapment crystallization using the Olivine MI tool in Petrolog3 (Danyushevsky and Plechov, 2011). This requires the user to specify the initial FeO_T and the host Fo content of each inclusion. FeO_T was set at 11.33 wt% for melt inclusions hosted in olivines with forsterite contents ([Fo=$Mg^{2+}/(Mg^{2+}+Fe^{2+})$ atomic])>79 mol% based on the liquid line of descent at Kīlauea, and for consistency with previous studies (Chapters 5 and 6, Sides et al., 2014a). For olivine crystals with Fo<79 mol%, the initial FeO content was estimated from the relationship between the equilibrium olivine forsterite content and melt FeO_T contents in a MELTS fractional crystallization model (Fig. 7.3).

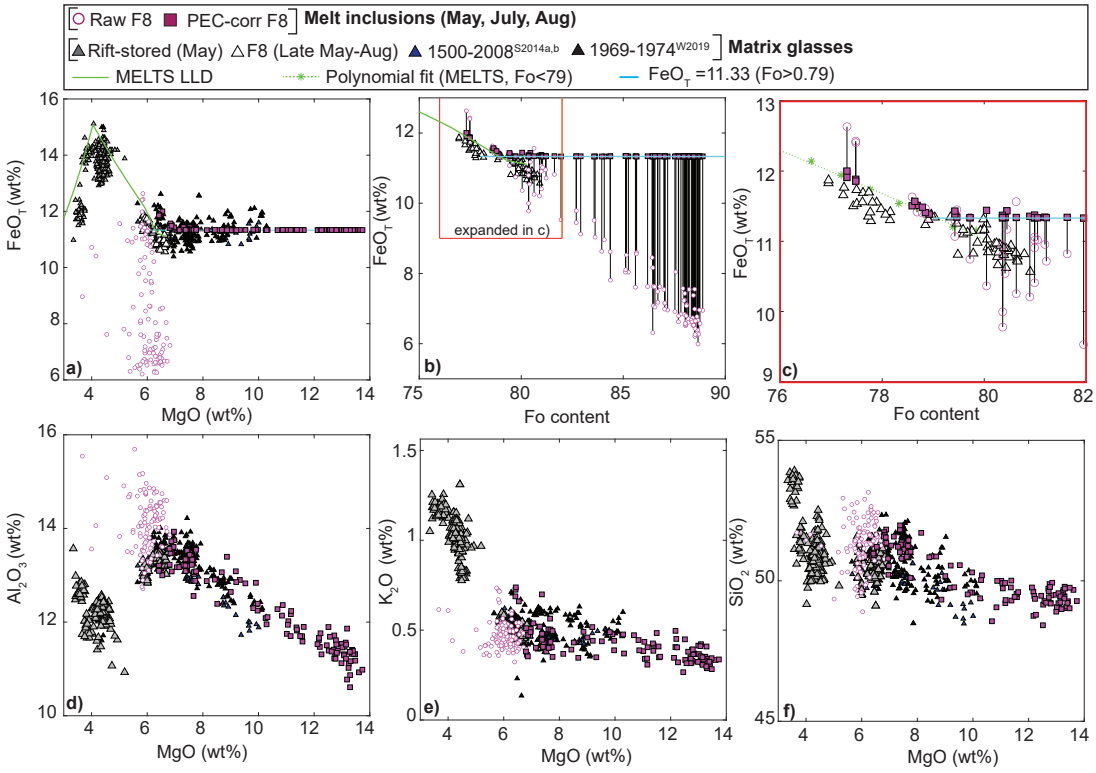


Figure 7.3: Method used to estimate the initial FeO_T contents of inclusions (a required input for Petrolog3 reconstructions). **a)** Based on the near constant FeO_T content of Kilauean glasses at >6.3 wt% MgO, inclusions hosted in olivines with Fo contents >79 was set at 11.33 wt% (cyan line, for consistency with PEC corrections of Sides et al. 2014a, b and Chapters 5 and 6). For inclusions hosted in more evolved olivines, a MELTS model was generated that effectively recreates the major element compositions of glasses erupted at F8 in May-August (black triangles), as well as the more evolved melts erupted at other fissures in Leilani Estates with <6.8 wt% MgO. The Mg# of the liquid line of descent from MELTS was used to calculate the equilibrium Fo content at each model step (using K_D=0.33). To account for slight noise in the model outputs from MELTS in Fo vs. FeO_T space **(b)**, and the finite calculation step in the model, a 2nd order polynomial was fitted between Fo_{68-79} (dashed green line) in **c)**. This polynomial was used to predict the FeO_T content of each melt inclusion based on the host Fo content (black lines in **b** and **c**). **d-e)** Major element plots show that the PEC correction brings melt inclusion data back in line with available glass data for Kilauea.

7.4 Results

F8 melt inclusions are hosted in olivine crystals with a wide range of core compositions (Fo_{77-89}; Fig. 7.4a). Core compositions in all three samples show a peak at ~Fo_{88-89} (Fig. 7.4b-d), which lies significantly above the equilibrium field calculated from the Mg# [where Mg#=$Mg^{2+}/(Mg^{2+}+Fe^{2+})$, atomic] of co-erupted matrix glasses, even considering a wide-range of experimentally-determined values for olivine-melt Fe-Mg partitioning (black lines, Fig. 7.4a; K_D=0.270–0.352, Roeder and Emslie, 1970; Matzen et al., 2011). Fourteen melt inclusions from May-18, but only six melt inclusions from July-18 and 1 from Aug-18 are hosted in olivines which lie within the equilibrium field. F8 olivines have some of the

highest Fo contents ever reported at Kīlauea (Fig. 7.4a, Fig. 7.4b-d. vs. Fig. 7.4e-f), but relatively low carrier melt Mg#s (51–57 mol%; assuming $Fe^{3+}/Fe_T = 0.15$). In turn, this juxtaposition produces some of the most extreme degrees of olivine-carrier melt Fe-Mg disequilibrium seen at Kīlauea (Fig. 7.4a). Crystals with high forsterite cores show strong normal zoning, while those with core compositions plotting closer to the equilibrium field on Fig. 7.4a are not visibly zoned in rapid EDS acquisitions (Fig. 7.5).

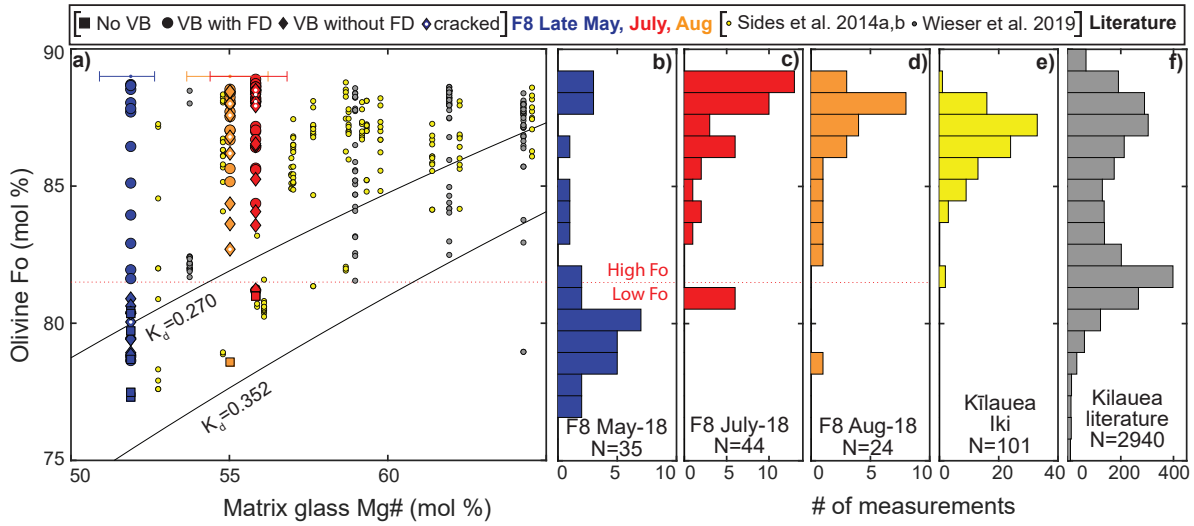


Figure 7.4: Olivine populations and olivine-melt relationships at F8 compared to literature data. **a)** Core olivine forsterite contents versus matrix glass Mg#s for Fe^{3+}/Fe_T=0.15 (Moussallam et al., 2016; Helz et al., 2017). Olivines lying between the black lines (K_D=0.270–0.352) are in equilibrium with their carrier melts considering the range of experimentally-determined Fe-Mg partition coefficients (Roeder and Emslie, 1970; Matzen et al., 2011). F8 olivines have some of the highest Fo contents observed at Kīlauea, yet are hosted in carrier liquids with some of the lowest Mg#s. Data from Chapter 5, Sides et al. (2014b), Sides et al. (2014a). **b-d)** Histograms of olivine Fo contents from this study, **e)** Kīlauea Iki (Sides et al., 2014b; Sides et al., 2014a), and **f)** a compilation of literature analyses from Chapter 5 combined with new measurements from Tucker et al. (2019). The strong bimodality in F8 forsterite contents was used to subdivide melt inclusions into those hosted within high-Fo olivines (>$Fo_{81.5}$) and low-Fo olivines (<$Fo_{81.5}$), with the division marked by the red dotted line.

The majority of F8 melt inclusions exhibit lower FeO contents than co-erupted matrix glasses and the composition of Kīlauean melt inclusions from the literature (grey dots; Chapter 5, Tucker et al., 2019; Sides et al., 2014b; Sides et al., 2014a). Melt inclusion MgO contents are more similar to those of co-erupted matrix glasses (Fig. 7.6a). Following a correction for effects of post-entrapment crystallization, F8 melt inclusions have MgO contents between 6.4 and 13.7 wt%, and FeO contents between 11.3 and 12 wt% (Figs. 7.3, 7.9a). Despite the high degree of Mg# disequilibrium between olivine crystals and their carrier melts (Fig. 7.4a), measured melt inclusion Mg#s (uncorrected for the effects of PEC) mostly lie within, or close to the equilibrium field calculated from the core compositions of

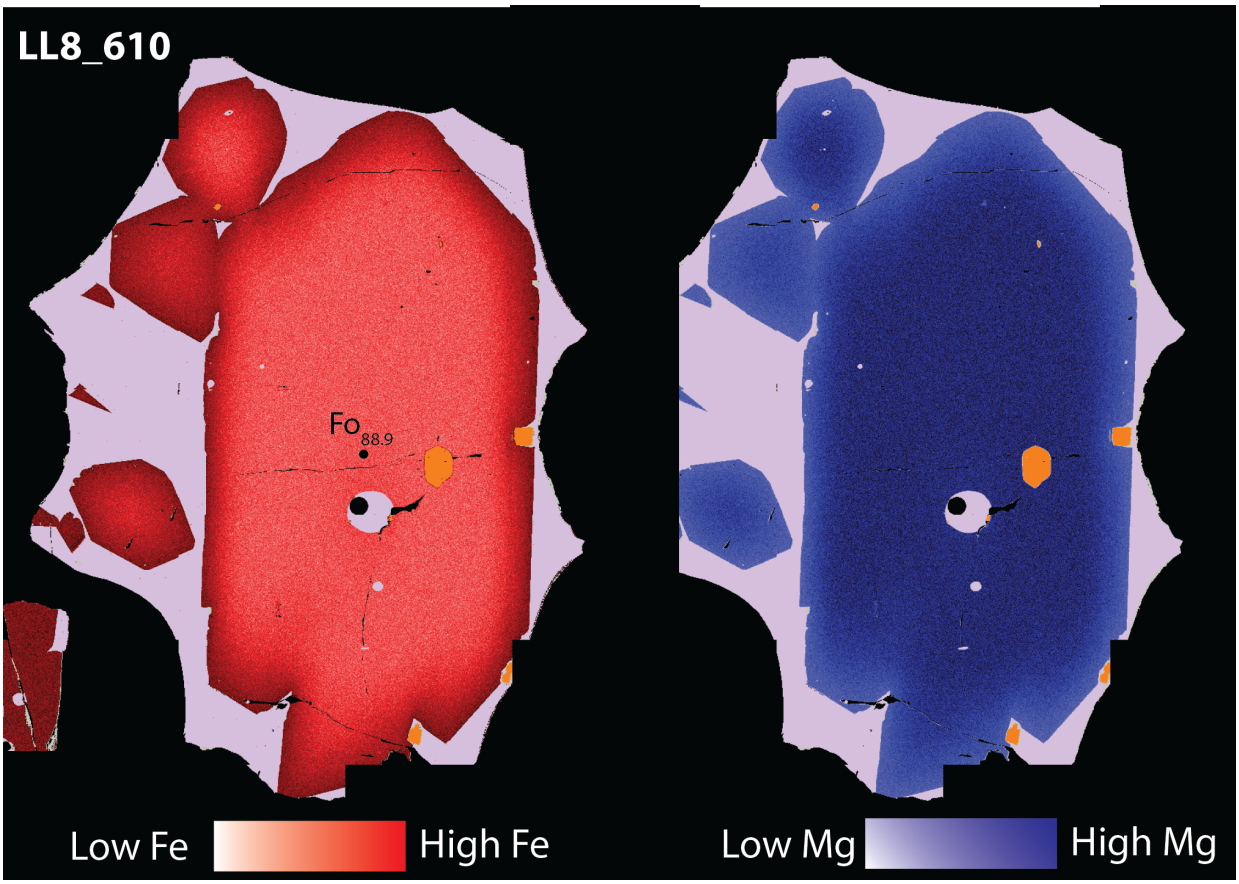


Figure 7.5: EDS maps of Fe and Mg in inclusion LL8_610 showing a prominent, normally zoned rim. Maps collected using Zeiss Mineralogic by Richard Taylor.

.

their host olivines (Fig. 7.6b). The distance from the equilibrium field degree is largest in the July-18 sample, but still less than the vast majority of literature melt inclusions, particularly those hosted in high-Fo olivines (Fig. 7.6b). Melt inclusions hosted in olivine crystals which have the highest degree of disequilibrium with their carrier melts (calculated by subtracting the equilibrium Fo content of the co-erupted matrix glass from the Fo content of each olivine) have experienced the most PEC (Fig. 7.6c) and have the lowest measured FeO contents (Fig. 7.6d). To encapsulate these large variations, F8 melt inclusions were subdivided into those hosted within low- and high-Fo olivines ($<Fo_{81.5}$ and $>Fo_{81.5}$ respectively). Low-Fo olivines are close to, or in major element equilibrium with their carrier melts and have experienced limited PEC, while high-Fo olivines exhibit high degrees of olivine-carrier melt disequilibrium, and have experienced large amounts of PEC (∼10-30%; Fig. 7.4a, Fig. 7.6a, c).

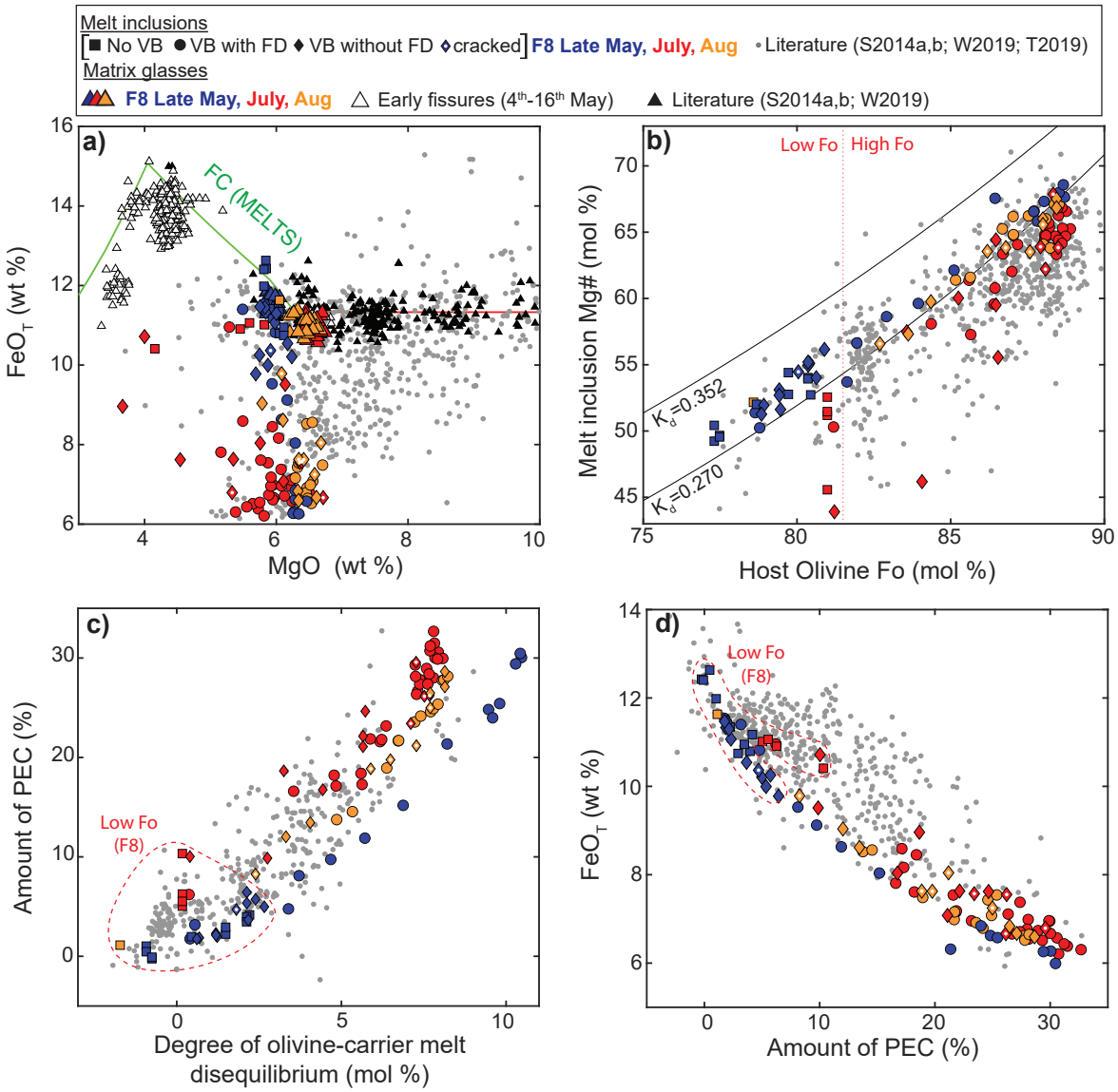


Figure 7.6: Major element systematics for the measured compositions of F8 melt inclusions (uncorrected for the effects of PEC). **a)** F8 melt inclusions have significantly lower FeO contents than liquid line of descent defined by Kīlaean matrix glasses and a MELTS fractionation path following the onset of clinopyroxene and plagioclase fractionation (green line) which recreates glass compositions erupted from earlier, more evolved fissures during the 2018 eruption (white triangles). Despite highly variable FeO contents, the MgO contents of melt inclusions mostly align with those of their co-erupted matrix glasses. **b)** In contrast to the prominent disequilibrium between high-Fo olivine compositions and co-erupted matrix glasses (Fig. 7.4a), melt inclusion Mg#s uncorrected for the effects of PEC (for Fe^{3+}/Fe_T=0.15) plot close to the equilibrium field with their host olivines (particularly melt inclusions from the May-18 and Aug-18 samples). Melt inclusions from previous Kīlauean eruptions (grey dots, Chapter 5, Tucker et al., 2019; Sides et al., 2014b; Sides et al., 2014a) lie much further below the equilibrium field. **c)** The amount of PEC (calculated in Petrolog3; Danyushevsky and Plechov, 2011) is strongly correlated to the degree of ol-melt disequilibrium, calculated by subtracting the equilibrium olivine composition of the co-erupted matrix glass (for K_D=0.3) from the measured Fo content. **d)** The FeO contents of F8 melt inclusions also shows a strong negative correlation with the amount of PEC, lying to lower FeO contents than the vast majority of literature data.

All high-Fo melt inclusions contain a vapour bubble (Fig. 7.6c), 73% (N=53) of which produce a Fermi diad (FD) during Raman analysis. Vapour bubbles which do not produce a FD may contain no CO_2, or CO_2 densities below the detection limit of Raman spectroscopy. While the detection limit will depend on the exact depth of the bubble below the surface, as well as the transparency of the host crystal, the distribution of densities in vapour bubbles which produced a FD indicates that the detection limit lies between 0–0.02 g/cm^3 (green bar in Fig. 7.7c). Nine of the bubbles without a FD are hosted within cracked melt inclusions, which may have resulted in CO_2 loss from the bubble (diamonds with white dots; Fig. 7.6c). In contrast, only 50% (N=15) of low-Fo melt inclusions contain a vapour bubble, and only 20% (N=3) of these produce a FD (Fig. 7.6c). Only 1 of the bubbles without a FD is hosted within a cracked melt inclusion.

Bubble-bearing melt inclusions show a correlation between the volume % of the bubble and the amount of PEC, despite the large random errors associated with measuring bubble proportions from 2D images (grey error bars; Fig. 7.7a). There is a substantial drop in glass CO_2 contents with increasing PEC, and melt inclusions containing vapour bubbles with a FD show significantly lower glass CO_2 contents than bubble-free melt inclusions (Fig. 7.7b, p=10^{-7}; KS test). There is no obvious correlation between the CO_2 density in vapour bubbles and the amount of PEC (Fig. 7.7c, R^2=10^{-6}), the amount of CO_2 in the glass (R^2=0.1) or the volume of the bubble (R^2=0.001). The median and mean proportion of total melt inclusion CO_2 hosted within the vapour bubble is 93% and 87% respectively (black histogram; Fig. 7.7d). This exceeds the proportions calculated by Moore et al. (2015) for melt inclusions from the 1959 and 1960 eruptions of Kīlauea (median=67%, mean=65%; blue histogram). This discrepancy reflects the fact that Moore et al. (2015) did not measure the CO_2 content of the glass in each melt inclusion, so they calculated proportions assuming a glass CO_2 content of 300 ppm (the maximum measured in the same suite of samples by Tuohy et al., 2016). This new data shows the importance of measuring CO_2 in the glass and bubble of a specific melt inclusion; while bubble-free melt inclusions have CO_2 contents up to 300 ppm in the glass phase, those with vapour bubbles producing a FD have median CO_2 contents of only 45 ppm (mean=54 ppm; Fig. 7.7b). In contrast to the highly variable CO_2 contents in melt inclusion glasses, H_2O contents are remarkably constant within a given eruption, despite significant variation in the contents of incompatible elements such as Na_2O, K_2O and Ce (Fig. 7.8a). F8 melt inclusions have lower H_2O contents than most of the Kīlauean melt inclusions measured by Sides et al. (2014a, b), and almost all of those measured by Tucker et al. (2019; Fig. 7.8b).

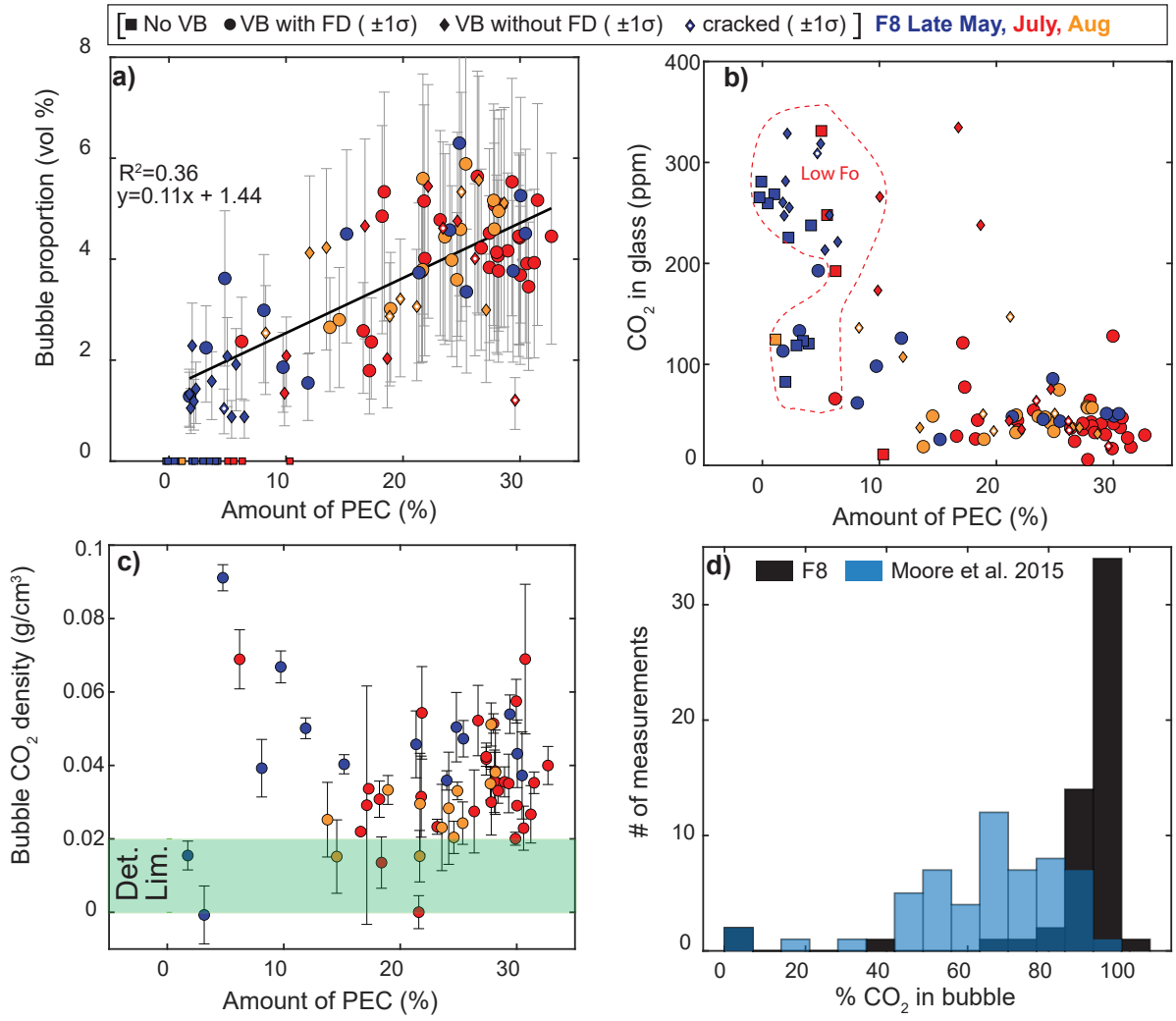


Figure 7.7: Vapour bubble and melt inclusion CO_2 systematics. **a)** There is a positive correlation between the volume proportion of the vapour bubble (VB) and the amount of PEC. Only melt inclusions which have experienced <10% PEC are bubble-free. Error bars show the 1σ errors associated with estimating bubble volume proportions from 2D images (-45% and +37%; Tucker et al., 2019). **b)** With increasing amounts of PEC, the amount of CO_2 within the glass phase of the melt inclusion declines. The highest glass CO_2 contents are observed in melt inclusions with no vapour bubbles (squares), and melt inclusion with bubbles that did not produce a FD (diamonds). In contrast, the vast majority of melt inclusions with low glass CO_2 contents have vapour bubbles which produced a FD (circles), or vapour bubbles without a FD that were hosted within cracked melt inclusions (diamonds with white dots). **c)** There is no correlation between the CO_2 density in vapour bubble measured using Raman Spectroscopy and the amount of PEC. Error bars show the $\pm$ 1σ deviation of three repeated measurements of each vapour bubble. The green bar shows the estimate of the detection limit (Det. Lim.) of Raman analyses in this study based on the distribution of measured bubble densities. **d)** The black histogram shows the proportion of CO_2 held within the vapour bubble for F8 melt inclusions that produced a FD (mean=87%, median=93%). Estimates by Moore et al. (2015) for Kīlauean melt inclusions from the 1959 and 1960 eruptions are also shown.

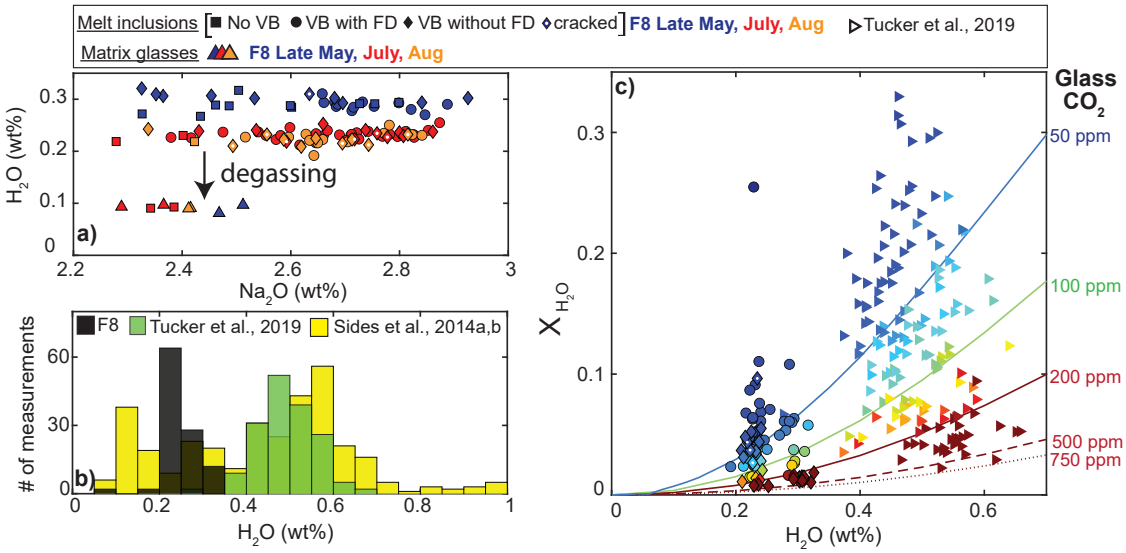


Figure 7.8: H_2O systematics of F8 melt inclusions relative to literature data from Kīlauea. **a)** F8 melt inclusion H_2O contents are remarkably constant within each sample, despite substantial variations in Na_2O. This indicates that melt inclusion H_2O contents were reset by diffusive re-equilibration with their carrier liquid. **b)** F8 melt inclusions have lower H_2O contents than the majority of Kīlauean melt inclusions measured by Sides et al. (2014a,b; yellow histogram), and almost all of the melt inclusions measured by Tucker et al. (2019; green histogram). **c)** Lines for five different melt CO_2 contents (50, 100, 200, 500 and 750 ppm) showing the molar fraction of H_2O in the vapour phase (X_{H_2O}) as a function of melt H_2O content (using VolatileCalc; Newman and Lowenstern, 2002). X_{H_2O} ratios for the co-existing vapour in equilibrium with the measured concentration of CO_2 and H_2O in the melt phase of the bubble-bearing inclusions from this study and Tucker et al. (2019; triangles) are overlain, with symbols colored by the CO_2 content of the glass phase. The relatively low H_2O contents of F8 melt inclusions mean that X_{H_2O} is generally <0.1. However, a number of inclusions from Tucker et al. (2019) with glass CO_2 contents <100 ppm have much higher X_{H_2O} ratios. This causes the CO_2 densities predicted using the EOS method to fall below the trend line defined by F8 melt inclusions on Fig. 7.11a.

7.5 Discussion

7.5.1 Mineral-melt disequilibrium drives the growth of a CO_2-rich bubble

The prominent Mg# disequilibrium between the core compositions of high-Fo olivines from F8 and their carrier melts has been observed in a number of historic eruptions at Kīlauea (Fig. 7.4a; Chapter 5, Tuohy et al., 2016; Sides et al., 2014b; Sides et al., 2014a). Based on major and trace element disequilibrium between melt inclusions and their carrier melts (e.g., Nb/Y ratios), as well as microstructures consistent with deformation of the crystal lattice (similar to high-Fo olivines from F8; Gansecki et al., 2019), Chapters 4 and 5 suggest that primitive olivines are scavenged from long-lived plastically-deforming mush piles at the base of the SC reservoir and placed into cooler, more evolved carrier melts with distinct

trace element signatures just prior to eruption. In contrast, more evolved olivines exhibiting small amounts of olivine-melt disequilibrium (similar to the low-Fo olivines in this study), no lattice distortions, and a high degree of trace element equilibrium are interpreted to have crystallized from their carrier melts as true phenocrysts.

Kīlauean melts with greater than ∼6.8 wt% MgO are saturated in only olivine and minor chrome-spinel (Wright and Fiske, 1971), and show a strong correlation between temperature and the MgO content of the melt (Helz and Thornber, 1987). The remarkably constant FeO contents of these high MgO melts (Fig. 7.6a) means that glass Mg# is strongly correlated with MgO, and therefore temperature. As glass Mg# is closely related to the olivine forsterite content through the Fe-Mg olivine-liquid exchange coefficient, equilibrium olivine forsterite contents are also strongly correlated with temperature. Thus, the difference in Mg# between the measured olivine core composition, and the equilibrium olivine forsterite content calculated from the composition of co-erupted matrix glasses (termed the degree of olivine-melt disequilibrium) is proportional to the amount of cooling experienced by the inclusion prior to syn-eruptive quenching (Chapter 5). The close relationship between the amount of cooling experienced by an inclusion, and the amount of PEC (Danyushevsky et al., 2000) accounts for the excellent correlation between the degree of olivine-melt disequilibrium and the amount of PEC (Fig. 7.6c).

F8 melt inclusions are hosted in some of the most forsteritic olivines erupted at Kīlauea, yet were erupted in some of the most evolved carrier melts (Fig. 7.4a). Consequently, they have experienced some of the largest amounts of cooling following entrapment, and, by extension, some of the largest amounts of PEC ever reported at Kīlauea (up to ∼33%; Fig. 7.6c). The small amounts of cooling (and therefore PEC) experienced by low-Fo olivines, which are close to equilibrium with their carrier melts, likely occurred during fractionation between the formation and eruption of these crystals (Fig. 7.6c). However, progressive fractionation and cooling of a batch of melt cannot account for the peak at $\sim Fo_{88-89}$ in F8 samples (Chapter 5, Maaløe et al., 1988), nor the paucity of olivines with Fo contents in equilibrium with the co-erupted matrix glasses (particularly in the July and Aug samples; Fig. 7.4a). The similarities between the high-Fo olivines from F8 and the samples examined in Chapter 5 (large amounts of olivine-melt disequilibrium, presence of lattice distortions; Gansecki et al., 2019), suggest that cooling was not a gradual process during progressive differentiation of a given magma batch (Maaløe et al., 1988), but occured over short timescales, when primitive olivine crystals residing in hot mush piles were entrained into significantly cooler, more evolved melts (Chapter 5, Sides et al., 2014b).

Melt inclusion MgO and FeO concentrations are strongly affected by the crystallization of olivine on the walls of the melt inclusion (PEC), and subsequent diffusive re-equilibration. Based on the strong coupling between MgO content and temperature in olivine-saturated liquids (Helz and Thornber, 1987), thermal equilibration of a hot olivine crystal with a

cooler carrier melt drives the crystallization of a zoned olivine rim from the melt inclusion, causing the MgO content of the melt inclusion to drop to match that of the carrier melt (Fig. 7.6a). This zoned olivine rim begins to re-equilibrate with the host crystal, and, in turn, the melt inclusion re-equilibrates with the changing rim composition (Danyushevsky et al., 2000). Effectively, the melt inclusion loses FeO by diffusion to achieve Mg# equilibration with the host olivine following the large initial drop in MgO during cooling. As the MgO content of the melt inclusion is a function of the temperature, FeO diffusion is countered by MgO diffusion in the opposite direction, which is sequestered as additional post-entrapment crystallization of olivine on the wall of the melt inclusion.

This FeO-loss process accounts for the negative correlation between melt inclusion FeO contents and the amount of PEC (Fig. 7.6d). For a given amount of PEC, F8 melt inclusions have lower FeO contents and display a smaller degree of Mg# disequilibrium with their olivine host than the vast majority of literature data (Fig. 7.6b, d). It is important to note that in melt inclusions where extensive FeO-loss has occurred, methods calculating the amount of PEC based on the degree of Mg# disequilibrium between the melt inclusion and the host crystal (e.g., Tucker et al., 2019; Neave et al., 2017) will significantly underestimate the true amount of PEC compared to the Petrolog3 method used here where the user specifies an initial FeO_T content. For example, the May-18 melt inclusions with Fo>85 have lost sufficient quantities of FeO by diffusive re-equilibration such that their Mg#s are in equilibrium with the composition of the host olivine. Thus, methods based on Mg# comparisons would indicate that these melt inclusions haven't experienced any PEC. However, their FeO contents lie $\sim$ 4 wt% below the composition of co-erupted matrix glasses, indicating that their compositions have been heavily altered by the PEC process (Fig. 7.6a).

The higher degrees of diffusive FeO-loss for a given amount of PEC for F8 melt inclusions compared to literature data (Fig. 7.6d) indicates that there was a longer time lag between the entrainment of crystals into cooler melts and their eventual eruption. Danyushevsky et al. (2002b) demonstrate that re-equilibration of Fe and Mg between the inclusion and its host can be used to estimate the time lag between the event driving PEC, and the eventual eruption of the crystal. Their Fig. 4c shows that a melt inclusion with a $\sim$50 µm radius which has experienced ΔT=100–150°C, and undergone FeO loss at T=1150–1200°C, achieves 98% equilibrium in $\sim$2 years. These extents of cooling and temperatures of re-equilibration are representative of F8 inclusions. However, Danyushevsky et al. (2002b) assume isotropic diffusion with $D_{Fe,\ Mg}$=$\sim$3–6$\times10^{-17}$ m^2/s at 1150–1200°C, while, in reality, FeO loss will be dominated by diffusion along the fast c-direction in olivine ($D_{Fe,\ Mg}$=$\sim$1–4$\times10^{-16}$ m^2/s for Fo_{80-89}, T=1150–1200°C, and QFM to QFM+0.3; Chakraborty, 2010; Barth et al., 2019). Thus, complete re-equilibration could be achieved almost an order of magnitude faster, in a matter of months. Considering the substantial uncertainties in this method associated with the fact the model of Danyushevsky et al. (2002b) does not account for

diffusional anisotropy, and the fact the degree of re-equilibration is sensitive to the choice of K_D (Fig. 7.6b), the FeO systematics of melt inclusions within high-Fo olivines erupted on May 28th ($\sim$ 70–100% re-equilibration) indicate that entrainment into cooler carrier melts occurred approximately a month to a year prior to eruption.

Given that H_2O in melt inclusions diffusively re-equilibrates with carrier melts over hours to days (Hartley et al., 2015; Gaetani et al., 2012), the timescales inferred from Fe-Mg systematics are more than sufficient for H_2O within F8 melt inclusions to be fully reset. This accounts for the remarkably uniform H_2O contents of F8 melt inclusions in each sample, despite substantial variation in the concentration of other incompatible elements (e.g., Na_2O; Fig. 7.8a). These constant values indicate that F8 carrier melts erupted in late May had H_2O contents of 0.29 wt%, while those erupted in July and August had slightly lower H_2O contents (0.22–0.23 wt%). These carrier melts are relatively H_2O-poor compared to the composition of previously-erupted Kīlauean melts (inferred from published melt inclusion data; Fig. 7.8b). The presence of more H_2O-poor carrier melts in 2018 likely results from the extensive mixing of magmas which had partially degassed their H_2O at the summit lava lake with undegassed melts within the plumbing system between 2008 and 2018 (e.g., Dixon et al., 1991). Because melt inclusion H_2O contents have been reset by late-stage diffusive re-equilibration, they were not corrected for the effects of PEC.

7.5.2 PEC and melt-vapour CO_2 partitioning

It is well recognized that extensive PEC drives the growth of a CO_2-rich vapour bubble (Steele-MacInnis et al., 2011; Sides et al., 2014b; Sides et al., 2014a; Maclennan, 2017). Thus, studies measuring only the CO_2 in the melt phase using SIMS or FTIR will yield spuriously low entrapment depths for melt inclusions which have undergone extensive PEC (Sides et al., 2014b). The concurrent measurements of CO_2 in the melt and bubble phase of a large number of melt inclusions which have experienced a wide range of PEC amounts (Fig. 7.6c-d) in this study provides a unique opportunity to interrogate the various processes causing CO_2 to partition into the vapour bubble.

To investigate the effects of compositional changes in the melt inclusion associated with PEC, the CO_2 solubility model of Shishkina et al. (2014) was used:

$$\ln[CO_2] = 1.15\ln(P) + 6.71\Pi^* - \ 1.345 \tag{7.3}$$

Where $[CO_2]$ is the concentration of CO_2 in ppm, and P is the pressure in MPa. The Π^* term accounts for the compositional dependence on CO_2 solubility, expressed in terms of the cation fractions of 7 major element species:

$$\Pi^* = \frac{Ca^{2+} + \ 0.8K^+ \ + 0.7Na^+ + 0.4Mg^{2+} + 0.4Fe^{2+}}{Si^{4+} + Al^{3+}} \tag{7.4}$$

The change in Π^* during PEC, $\Delta\Pi^*$, was calculated by subtracting the Π^* value of the PEC-corrected major element composition of each melt inclusion from the Π^* value of the measured composition. $\Delta\Pi^*$ becomes progressively more negative with increasing amounts of PEC, showing that CO_2 becomes progressively less soluble (red dots; Fig. 7.9b, see also Maclennan, 2017).

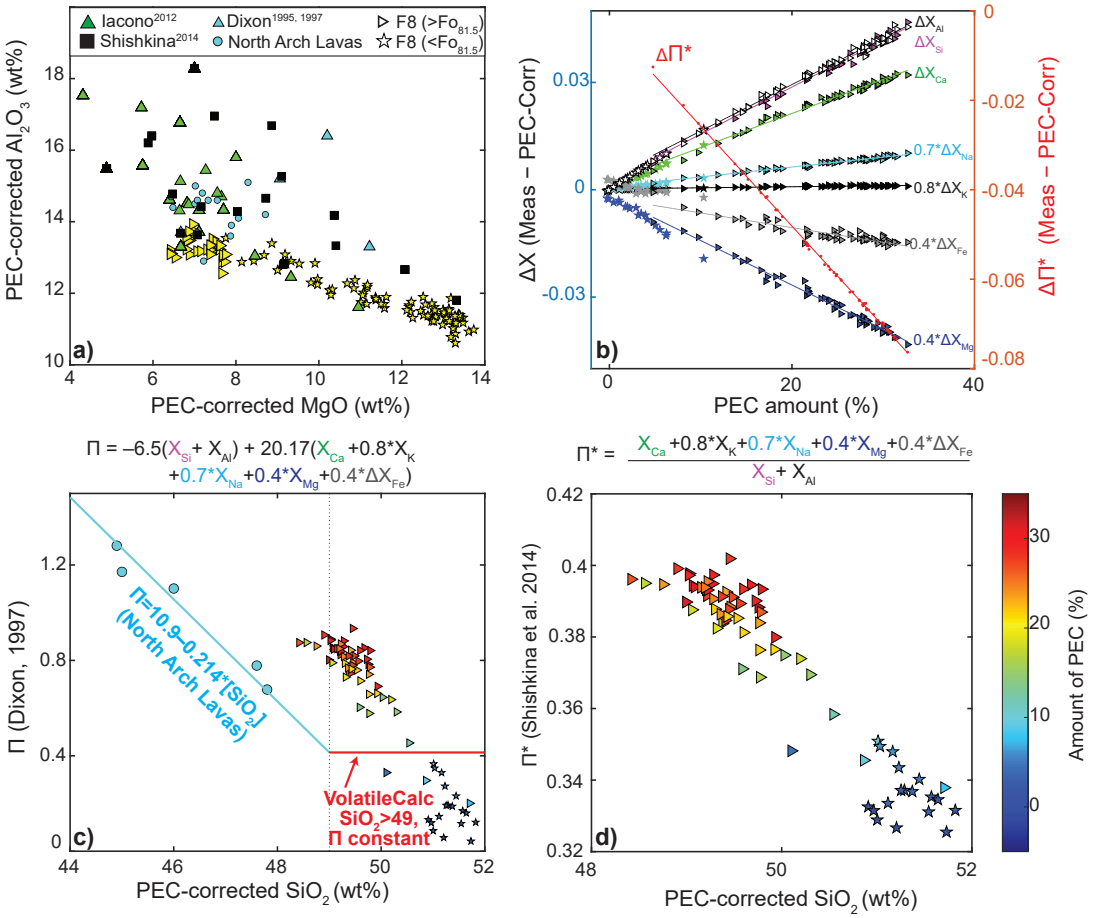


Figure 7.9: Evaluating the compositional sensitivity of CO_2 solubility. **a)** Comparison of the MgO vs. Al_2O_3 systematics of PEC-corrected F8 inclusions to the glass compositions used to calibrate each solubility model. The North Arch lavas which define the simplified Π vs. SiO_2 relationship presented in Dixon (1997) and implemented in VolatileCalc (Newman and Lowenstern, 2002) are also shown (blue circles). The Magmasat dataset (Ghiorso and Gualda, 2015) is not shown, but is almost identical to the calibration dataset shown from Shishkina et al. (2014) and Dixon et al. (1995) for basaltic compositions. **b)** ΔX (triangle and star symbols) and $\Delta\Pi^*$ (red dots; Shishkina et al., 2014) for F8 melt inclusions plotted against the amount of PEC. ΔX and $\Delta\Pi^*$ were calculated by subtracting the values of X and Π^* for PEC-corrected melt inclusions from the values of X and Π^* for measured compositions. For example, inclusion LL8_156 has experienced 33% PEC, and has a PEC-corrected MgO content of 13.5 wt% and a measured MgO content of 5.4 wt%. Thus, ΔX_{MgO} is strongly negative. **c)** The compositional parameter Π of Dixon (1997) calculated for PEC-corrected F8 melt inclusion compositions varies substantially with SiO_2, following an offset trend to that defined by North Arch Glasses Dixon et al., 1997, blue dots and linear regression. VolatileCalc effectively treats all melt inclusions with >49 wt% SiO_2 as if Π is constant (red line). **d)** The compositional parameter Π^* from Shishkina et al. (2014), and therefore the solubility of CO_2, is significantly higher for high-Fo melt inclusions (which have the highest PEC-corrected MgO, and lowest SiO_2 and Al_2O_3 contents). The color of the symbols for F8 melt inclusions in **c)** and **d)** represents the amount of PEC.

Changes in Π^* are dominated by a decrease in X_{Mg}, and increase in X_{Si} and X_{Al} resulting from the crystallization of olivine on the walls of the inclusion. These changes are partially counteracted by an increase in X_{Ca} (as Ca is incompatible in olivine; Fig. 7.9b). To quantify the magnitude of this drop in Π^* in terms of CO_2 partitioning between the melt and bubble, the 8 melt inclusions which have experienced >30% PEC were considered (all of which contain bubbles which produce a FD). The mean Π^* value of the measured compositions of these melt inclusions is 0.33, while the mean Π^* of their PEC-corrected compositions is 0.39 ($\Delta\Pi^*$=-0.068). For P=0.76 kbar (the average entrapment pressure for the PEC-corrected compositions of these melt inclusions calculated using Equation 7.3) CO_2 solubility drops by ∼192 ppm. As melts at Kīlauea are CO_2 saturated at crustal storage depths (Gerlach et al., 2002), all of this CO_2 will enter the vapour bubble.

However, the mean amount of CO_2 measured in the vapour bubbles of these 8 melt inclusions is 657 ppm ($\pm 1\sigma$=231 ppm). This reflects three additional processes which enhance CO_2 partitioning into the bubble during PEC. Firstly, the crystallization of olivine, which contains negligible quantities of CO_2, drives up the total concentration of the CO_2 in the remaining melt by a factor of 1 divided by the amount of PEC. As mentioned above, because Kīlauea melt inclusions are CO_2 saturated (Gerlach et al., 2002), this excess partitions into the bubble. Additionally, the preferential contraction of the melt phase relative to the olivine during thermal re-equilibration, combined with the crystallization of denser olivine on the rim of the melt inclusion, leads to a reduction in the volume of the melt phase. This causes the internal pressure of the melt inclusion, and therefore the CO_2 solubility to decrease further (Equation 7.3). Evidence for these volume changes is provided by the correlation between the amount of PEC and the volume of the vapour bubble (Fig. 7.7a), as well as the observation that all melt inclusions without a vapour bubble have experienced <10% PEC (Fig. 7.6d), while all melt inclusions that have experienced >10% PEC have a vapour bubble.

Overall, changes in melt chemistry, the incompatible behaviour of CO_2, and a drop in the internal pressure of the melt inclusion accounts for the rapid decrease in glass CO_2 contents with increasing PEC (Fig. 7.7b). Concurrent measurements of glass and bubble CO_2 in this study provides the first opportunity to see through these convoluting effects of PEC to robustly determine total CO_2 contents (Fig. 7.10), and therefore entrapment depths of Kīlauean melt inclusions. To account for the uncertainty regarding the amount of CO_2 held within bubbles that did not produce a FD (diamond symbols), particularly those hosted within cracked olivines (diamond symbols with white dot), total CO_2 contents and entrapment depths were only calculated for melt inclusions which had no bubble or a bubble that produced a FD. These total CO_2 were corrected for the effects of PEC (which drives CO_2 contents to higher values than the point of inclusion entrapment).

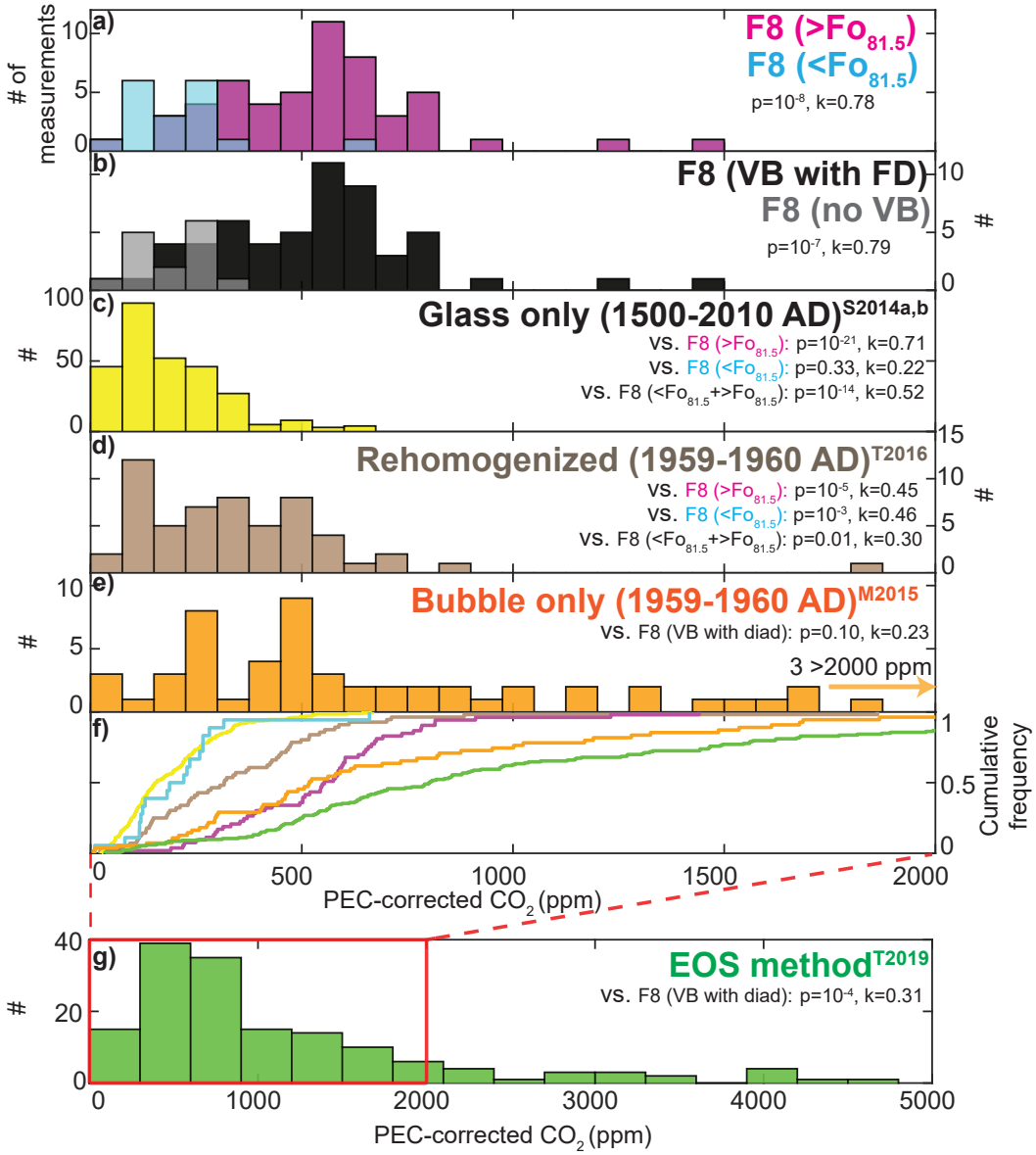


Figure 7.10: Histograms of melt inclusion CO_2 contents from this study and the literature (all corrected for the effects of PEC). **a)** Total CO_2 contents (bubble+glass) for high- and low-Fo melt inclusions are statistically distinguishable at p=0.05 using the Kolmogorov Smirnov (KS) test (p value and test statistic k shown on the figure). **b)** Similarly, melt inclusions which contain a vapour bubble (VB) with a FD have significantly higher total CO_2 contents than bubble-free melt inclusions. **c)** Melt inclusion CO_2 contents from a suite of eruptions at Kīlauea between 1500 and 2008 AD where only the glass phase was measured (Sides et al., 2014a,b). **d)** CO_2 contents of experimentally-homogenized melt inclusions from the 1959 Kīlauea Iki and 1960 Kapoho eruptions (Tuohy et al., 2016). **e)** Bubble CO_2 contents from Moore et al. (2015) in the same suite of samples as in **d)**. For consistency, these bubble CO_2 contents were corrected for PEC using the average amount of PEC reported by Tuohy et al. (2016; 13%). **f)** Cumulative distribution plots for these datasets. **g)** Total inclusion CO_2 contents from Tucker et al. (2019) where the contribution from bubble CO_2 was estimated using the EOS method (excluding inclusions with bubble volumes >8% that the authors suggest were co-entrapped). 35 melt inclusions have CO_2 >1500 ppm. Note the change in x axis scale from plots **a-f)**. For literature data, all melt inclusions are shown, as the highly variably glass Mg#s of these different eruptions means that the Fo=81.5 cut off chosen for F8 samples to classify olivines based on the degree of equilibrium with their carrier melts is not applicable. Additionally, Fo contents were not reported by Moore et al. (2015), and matrix glass Mg#s were not reported in Tucker et al. (2019).

Total CO_2 contents in melt inclusions hosted within high-Fo olivines are offset to significantly higher values compared to those hosted within low-Fo olivines (Fig. 7.10a), indicating that these two olivine populations crystallized at distinct depths within Kīlauea's plumbing system. Unsurprisingly given that ∼90% of CO_2 is held within the vapour bubble (Fig. 7.7d), CO_2 contents in F8 melt inclusions are significantly higher than measurements of just the glass phase by Sides et al. (2014a,b; Fig. 7.10c). F8 melt inclusions are also offset to higher CO_2 contents than experimentally-rehomogenized melt inclusions (Fig. 7.10d), supporting the inference of Tuohy et al. (2016) that the re-appearance of a vapour bubble upon quench in their experiments sequestered some CO_2 from the melt phase. Interestingly, the distribution of total CO_2 contents for F8 melt inclusions which possessed bubbles are indistinguishable (p=0.1) from the CO_2 contribution of just the vapour bubbles in melt inclusions from the 1959 and 1960 eruptions of Kīlauea (Fig. 7.10e; Moore et al., 2015). This demonstrates that in olivine populations which have experienced extensive PEC, measurements of glass CO_2 contents are of subordinate importance to measurements of bubble CO_2 (Fig. 7.7d). In fact, the contribution of CO_2 from the melt phase for the majority of high-Fo melt inclusions from F8 is entirely overwhelmed by the errors on the amount of CO_2 in the bubble associated with estimating bubble volume proportions from 2D images.

However, it is worth noting that analyses of only the CO_2 within vapour bubbles would have failed to identify the population of low-Fo olivines which host almost all of their CO_2 within the glass phase. Thus, future studies should use a small number of SIMS or FTIR analyses to determine the relationship between glass and bubble CO_2 contents and the amount of PEC in different subpopulations of melt inclusions. If the vast majority of CO_2 in a given population is held in the vapour bubble, a limited analytical budget would be better spent accurately measuring bubble volumes to combine with Raman measurements of CO_2 density, instead of precisely quantifying the insignificant amount of CO_2 held within the glass phase using SIMS or FTIR. Importantly, it was also observed that the distribution of total CO_2 contents in bubble-bearing melt inclusions is significantly higher than bubble-free melt inclusions (Fig. 7.10b). This result invalidates the approach of preferentially targeting bubble-free melt inclusions to avoid having to account for CO_2 within the vapour bubbles (e.g., Helo et al., 2011; Esposito et al., 2011) in systems where erupted crystals have experienced extensive PEC prior to eruption. Crucially, analysis of only bubble-free melt inclusions by SIMS or FTIR, or analyses of just vapour bubbles using Raman, would have failed to identify that crystals are supplied from two distinct storage regions within Kīlauea's plumbing system.

7.5.3 Analytical versus theoretical constructions of vapour bubble CO_2

In contrast to the good agreement between estimates of total CO_2 contents from combined SIMS and Raman measurements from F8 and the bubble-only measurements of Moore et al. (2015), the total CO_2 contents estimated by Tucker et al. (2019) using the EOS method are displaced to significantly higher values (Fig. 7.10g). To assess the cause of this discrepancy, the EOS method described by Tucker et al. (2019) was used to calculate CO_2 bubble densities for F8 melt inclusions to compare to Raman measurements. The simplification of the Dixon (1997) solubility model implemented in VolatileCalc (Newman and Lowenstern, 2002) was used to calculate the internal pressure of the melt inclusion based on the measured SiO_2, CO_2 and H_2O contents of the glass phase. The pure CO_2 EOS of Span and Wagner (1996) implemented in Python3 through CoolProp (Bell et al., 2014) was used to determine CO_2 density at this internal pressure and 725°C (the presumed glass transition temperature of Tucker et al. 2019 based on Ryan and Sammis, 1981). The Duan and Zhang (2006) EOS utilized by Tucker et al. (2019) yields identical densities to the fourth decimal place. The more significant source of error involves the choice of the glass transition temperature. This was fixed at 725°C in Tucker et al. (2019) and 825°C in Moore et al. (2015; dashed and solid magenta line; Fig. 7.11a) for simplicity, but in reality, varies as a function of cooling rate and melt viscosity (and, by extension, melt composition; Giordano et al., 2005; Maclennan, 2017). Glass transition temperatures were also calculated for bubble-bearing F8 melt inclusions with the python code MiMIC (Rasmussen et al., 2020, incorporating the model of Giordano et al., 2015) for a cooling rate of 10°C/s. This yields an average temperature of 680°C (dotted magenta line; Fig. 7.11a). Following Tucker et al. (2019), the density obtained from the pure-CO_2 EOS was multiplied by the mole fraction of CO_2 (X_{CO_2}) in the vapour phase determined using the simplification of the Dixon (1997) model implemented in VolatileCalc (Newman and Lowenstern, 2002). This correction neglects the non-ideal mixing of H_2O and CO_2 at magmatic temperatures compared to the use of a mixed H_2O-CO_2 EOS (e.g., Moore et al., 2015), but is likely a reasonable approximation for relatively dry systems such as Kīlauea (Fig. 7.8).

The dominant control of the glass CO_2 content on the internal pressure of the inclusion in relatively dry melts, and the positive relationship between the internal pressure and ρ_{CO_2} from the EOS evaluated at a constant temperature, means that predicted ρ_{CO_2} values increase with increasing glass CO_2 contents (Fig. 7.11a). Predicted CO_2 densities from Tucker et al. (2019) plot on or below the quadratic fit through the EOS predictions for F8 melt inclusions at 725°C (magenta solid line), because of the higher values of X_{H_2O} (and thus lower X_{CO_2}) for a number of melt inclusions which possess high glass H_2O, but low glass CO_2 contents (Fig. 7.8c). However, unlike the predictions from the EOS method, there is no correlation between ρ_{CO_2} measured using Raman spectroscopy and glass CO_2

contents (R^2=0.11). Interestingly, all melt inclusions with >200 ppm CO_2 have vapour bubbles which did not produce a FD (diamond symbols; Fig. 7.11a), indicating that their CO_2 densities were below the detection limit of Raman Spectroscopy (∼0–0.02 g/cm^3; green bar in Fig. 7.7c). It seems implausible that these bubbles could possess the high CO_2 densities predicted by the EOS (ρ_{CO_2} >0.2 g/cm^3) and fail to produce a FD. Furthermore, melt inclusions with ρ_{CO_2} >0.2 g/cm^3 will consist of an outer shell of liquid CO_2, and an inner sphere of vapour CO_2 at room temperature (∼21–22°C). For ρ_{CO_2}=0.4 g/cm^3, this liquid phase will comprise 26% of the radius of the bubble, and the motion of the inner sphere of vapour because of Brownian motion would be readily observable under an optical microscope. No two-phase bubbles were observed in this study, and there are no reports of two-phase bubbles in the Kīlauean literature.

The fundamental tenet of the EOS method used by Tucker et al. (2019) is that CO_2 continues to partition between the vapour bubble and the melt until the bubble stops growing at the glass transition temperature. However, during syn-eruptive quenching, the strong temperature dependence of CO_2 diffusivity means that the diffusion of CO_2 from the melt into the bubble may cease before the bubble reaches its final volume (Anderson and Brown, 1993). Continued bubble growth without concurrent diffusion causes the density of CO_2 within the bubble to drop below that predicted from the EOS (Moore et al., 2015; Maclennan, 2017). Non-equilibrium bubble expansion has been proposed to account for the presence of vapour bubbles in Icelandic melt inclusions with CO_2 concentrations below the detection limit of Raman Spectroscopy (Neave et al., 2014).

The discrepancy between EOS predictions and Raman measurements ($\Delta\rho_{CO_2}$) increases linearly with glass CO_2 content (R^2=0.75. Fig. 7.11b) and decreases with the amount of PEC (Fig. 7.11c). Melt inclusions containing bubbles without a FD lie within the confidence interval of the regression through bubbles which produced a FD if the Raman detection limit (0.02 g/cm^3) is subtracted from CO_2 densities calculated from the EOS (Fig. 7.11b). To investigate these correlations, the relative contribution of bubble growth at high magmatic temperatures during PEC and ascent (where CO_2 diffusion and bubble growth are coupled) compared to bubble growth during quench (where CO_2 diffusion is temperature-limited, and therefore decoupled from the mechanical expansion of the bubble) was assessed. The partitioning of CO_2 between the melt and the vapour bubble was tracked from the point of entrapment to the glass transition temperature using the model of Maclennan (2017; Fig. 7.12). Quench rates of 10°C/s were used based on video footage of the sampling and quenching of the Aug-18 sample; ∼40 s elapsed between the sample being pulled from the channel (∼1150°C) and becoming brittle at the glass transition temperature (∼725°C; Tucker et al. 2019). At these cooling rates, there is negligible transfer of CO_2 from the melt to the bubble during syn-eruptive quenching.

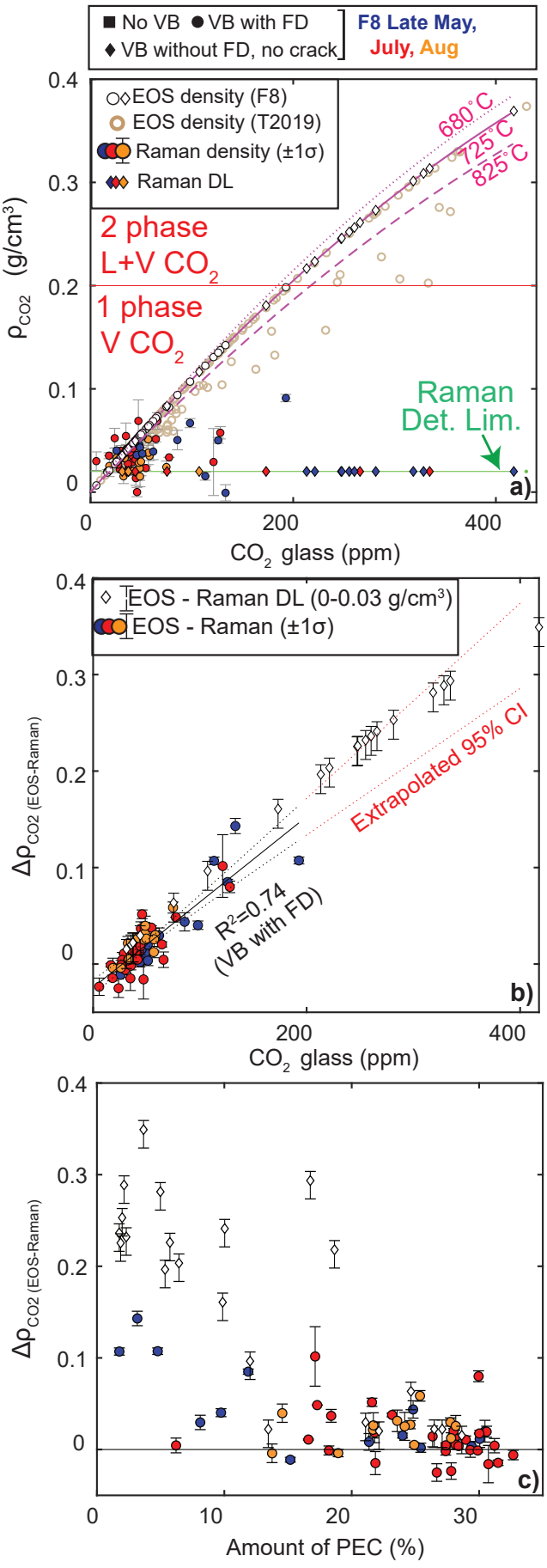


Figure 7.11: Comparisons of bubble densities calculated using the EOS with those measured by Raman Spectroscopy. **a)** Calculated bubble densities for F8 melt inclusions are shown as white circles and diamonds, and those from Tucker et al. (2019) are shown as beige hollow circles. Magenta lines shows quadratic fits through calculated bubble densities for F8 melt inclusions for the EOS evaluated at 680°C, 725°C and 825°C. A number of inclusions with low inclusion CO_2 contents and high H_2O contents from Tucker et al. (2019) lie below this line, because of their lower X_{CO_2} values (Fig. 7.8c). Measured CO_2 densities in this study are shown as colored circles, with error bars showing the 1σ of repeated acquisitions of each bubble. Colored diamonds represent bubbles which did not produce a FD, and were hosted in melt inclusions that weren't cracked. The absence of a diad indicates that their CO_2 concentrations were below the detection limit of Raman spectroscopy, so they are plotted at ρ_{CO_2}=0.02 g/cm^3 (see Fig. 7.7c). **b)** The discrepancy between the predicted and measured CO_2 density, $\Delta\rho_{CO_2}$, correlates strongly with the CO_2 content of the glass. The 95% confidence interval on a linear regression for measured bubble densities is shown with red dotted lines. Bubbles which did not produce a FD lie within error of the extrapolated confidence interval assuming their bubbles contain CO_2 densities of 0.02 g/cm^3 (with an error of 0-0.03 g/cm^3). **c)** Inclusions which have experienced >20% PEC show relatively small discrepancies between predicted and measured CO_2 densities. In contrast, the EOS greatly overpredicts CO_2 densities for those melt inclusions with have experienced <20% PEC.

Two end-member cooling histories were modelled. The red melt inclusion in Figure 7.12a a experiences large amounts of cooling (ΔT=150°C) and PEC at high magmatic temperatures and pressures, representative of the PT path followed by melt inclusions hosted within the most forsteritic olivines. The blue melt inclusion in Figure 7.12b experiences no cooling and post-entrapment crystallization prior to ascent and syn-eruptive quenching, representative of low-Fo melt inclusions which form in carrier melts with similar temperatures to the ones in which they were erupted (Fig. 7.12b).

The high-Fo melt inclusion (red) grows a considerable proportion of its final bubble volume (58%) during PEC at high magmatic temperatures (square to star symbol; Fig. 7.12a). The diffusion of CO_2 into this growing bubble causes the CO_2 content of the melt phase to drop rapidly (Fig. 7.12c). During syn-eruptive quenching, there is no further CO_2 diffusion between the melt and bubble (Fig. 7.12c), and the increase in the bubble volume is relatively minor (accounting for 42% of the final volume; Fig. 7.12a). The relatively small proportional increase in the bubble volume means that ρ_{CO_2} only decreases from 0.10 to 0.06 g/cm^3 during syn-eruptive quenching (Fig. 7.12d). In reality, the proportion of the bubble grown at high temperatures will be substantially greater, as the model of Maclennan (2017) does not account for the FeO-loss process, which greatly increases the amount of PEC for a given ΔT. For example, in models with ΔT=200°C instead of ΔT=150°C, the amount of PEC increases from 18% to 25%, and the proportion of the bubble growth at high temperature increases from 58% to 68%. In turn the bubble density drops from only 0.073 to 0.052 g/cm^3 during syn-eruptive quenching. Considering that high-Fo F8 inclusions have experienced up to 33% PEC, the median 1σ error because of analytical noise estimated from repeated Raman analyses is 0.006 g/cm^3 (17%), and the median X_{H_2O} content of the vapour is 7% (Fig. 7.8c), the reduction in CO_2 density during quench-induced bubble expansion is easily masked by analytical errors and the assumptions involved in the EOS method. Thus, bubble densities in melt inclusions which have experienced extensive PEC are well matched by the EOS method (Fig. 7.11c), as the proportion of bubble growth occurring at temperatures where CO_2 diffusion is temperature-limited is overwhelmed by other sources of error.

In contrast, the low-Fo melt inclusion (blue) grows a very small proportion of its total bubble volume at high temperatures (10%), with 90% of the final bubble volume growing upon quench (Fig. 7.12b). Substantial bubble expansion upon quench without concurrent CO_2 diffusion causes ρ_{CO_2} to drop substantially (Fig. 7.12d). Effectively, the EOS method calculates the density of the bubble at the initiation of the quench stage (ρ_{CO_2}=0.205 g/cm^3; star symbol), while the true bubble density is 10× lower (ρ_{CO_2}=0.021 g/cm^3; circle symbol), close to the detection limit of Raman spectroscopy. Thus, the EOS substantially overestimates ρ_{CO_2} for melt inclusions which have experienced small amounts of PEC and retain high CO_2 contents (Fig. 7.11b, c), because bubble growth in these melt inclusions is dominated by the quenching process, where there is effectively no diffusion of CO_2 into the bubble.

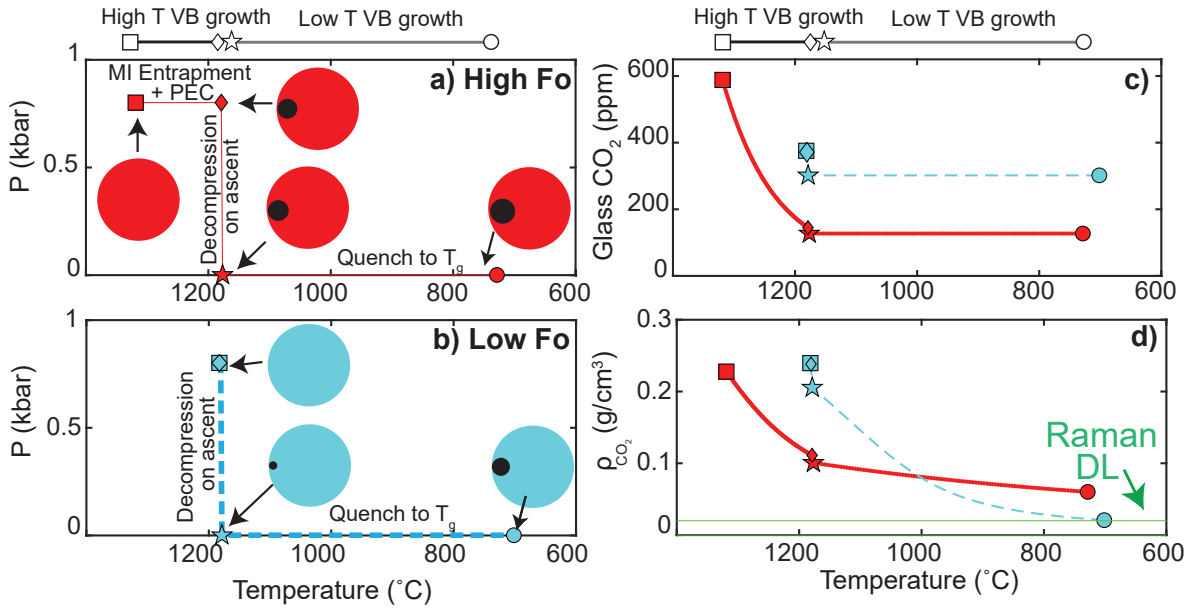


Figure 7.12: Model of CO_2 partitioning between the melt and bubble for PT scenarios representative of inclusions hosted within high- and low-Fo olivines (red and blue colors, respectively). **a)** The red melt inclusion experiences considerable cooling (ΔT=150°C) and post-entrapment crystallization at high temperatures and pressures (square to diamond symbol), driving the growth of a vapour bubble. This high temperature phase of bubble growth is accompanied by CO_2 diffusion from the melt to the bubble, causing the glass CO_2 content to drop substantially **(c)**. This inclusion then ascends to the surface (diamond to star symbol), and experiences a second stage of vapour bubble growth during syn-eruptive quenching (star to circle symbol). **b)** The blue melt inclusion follows an end-member PT path representative of an inclusion hosted within a low-Fo olivine. It experiences no cooling and post-entrapment crystallization at high temperature. A bubble only begins to grow during ascent to the surface, with 90% of the total bubble volume of this inclusion occurs during syn-eruptive quenching (star to circle). At the quenching rates of 10°C/s used in this model, there is negligible CO_2 transfer from the glass to the bubble during this low temperature phase of bubble growth. The large amount of bubble expansion without concurrent CO_2 diffusion causes the density of CO_2 in the vapour bubble to drop close to the detection limit of Raman Spectroscopy (green line, **d**), while the CO_2 of the glass phase remains unchanged **(c)**.

These models suggest that the magnitude of the discrepancy between measured bubble densities and those predicted by the EOS relates to the proportion of the bubble grown during syn-eruptive quenching. In contrast, Tucker et al. (2019) suggest that Raman measurements may underestimate ρ_{CO_2} relative to EOS methods because of the sequestration of significant quantities of CO_2 as thin films of solid carbonate on bubble walls. Carbonate phases have been identified in a number of melt inclusion vapour bubbles from subduction zone settings based on the presence of a distinctive peak in the Raman spectra at ~1090 cm^{-1} (Venugopal et al., 2020; Moore et al., 2015). However, while Moore et al. (2015) report relatively abundant carbonate phases in vapour bubbles from Seguam and Fuego, only four of the 142 Kīlauean vapour bubbles they examined contained carbonates, all of which

were hosted within a single olivine crystal. This suggests that vapour bubble carbonates are significantly less common in H_2O-poor ocean island systems. No carbonate peaks in Raman spectra from F8 bubbles were identified, nor did optical observations made prior to the exposure of bubbles during polishing identify films on bubble walls. Additionally, no carbonate phases were identified during detailed examination of exposed bubble walls using backscatter and secondary electron imaging, and Energy-Dispersive Spectroscopy (EDS) maps on a FEG-SEM. These EDS maps reveal that bubble wall coatings with a "dotted" appearance identified by Tucker et al. (2019; see their Fig. 2F) consist of Fe-Cu sulfides, rather than carbonates (see also Chapter 6, Venugopal et al., 2020; Moore et al., 2015). Finally, even if carbonates in bubble walls remained undetected, the systematic relationship between PEC amounts, CO_2 contents, and the discrepancy between Raman measurements and the EOS would necessitate that only bubbles hosted in melt inclusions which had undergone negligible PEC contain carbonate phases.

7.5.4 Reconstructing Magma Storage Depths

Under the assumption that any reservoir from which a substantial proportion of the crystal cargo was derived must also have supplied melt (in order to entrain these crystals, and carry them to the surface), the depths of the main magma reservoirs supplying F8 can be estimated from melt inclusion entrapment depths. Entrapment pressures were calculated from PEC-corrected total CO_2 and measured H_2O contents using a CO_2-H_2O solubility model, and converted into depths using prior constraints on the density structure of the Kīlauean edifice. As above, we only consider melt inclusions with no vapor bubble, or a vapor bubble which produced a FD.

Literature studies of Kīlauean melt inclusions have mostly used the CO_2-H_2O solubility model of Dixon et al. (1995) and Dixon (1997), implemented in the excel workbook VolatileCalc (Newman and Lowenstern, 2002, e.g., Tuohy et al. 2016; Sides et al. 2014a, b; Moore et al., 2015; Tucker et al., 2019). VolatileCalc uses a simplified relationship for the compositional dependence of CO_2 solubility expressed in terms of just the melt SiO_2 content, rather than the full compositional parameter Π, which accounts for the abundance of seven cations (Dixon, 1997, Fig. 7.9c). In this simplification the parameter $X_{CO_3^{2-}}(P_0, T_0)$, which representing the solubility of CO_2 at 1200°C and 1 bar for a specified fluid CO_2 fugacity in the thermodynamic expression of Dixon et al. (1995), is expressed as:

$$X_{CO_3^{2-}}(P_0, T_0) = 8.7 \times 10^{-6} - 1.7 \times 10^{-7}[SiO_2] \tag{7.5}$$

This simplification derives from the excellent linear correlation between Π and SiO_2 in a suite of lavas with 40–49 wt% from the North Arch Volcanic field (blue regression line; Fig. 7.9c; Dixon, 1997). However, extrapolation of Equation 7.5 to only 51.2 wt% SiO_2 returns a negative value for $X_{CO_3^{2-}}(P_0, T_0)$, which, in turn, predicts that the solubility of CO_2 is

negative at all pressures. To avoid these extrapolation issues, VolatileCalc does not let users enter a SiO_2 content >49 wt%, so most studies simply calculate the CO_2 solubility for melts with >49 wt% SiO_2 using the expression for SiO_2=49 wt% (e.g. Tucker et al., 2019; Sides et al. 2014a, b; Coombs et al., 2006; Rasmussen et al., 2020). Newman and Lowenstern (2002) suggest that this approximation should return accurate entrapment pressures for basaltic compositions with up to 52 wt% SiO_2 contents. However, the simplified compositional parameter used in VolatileCalc is only valid for melt compositions which define the same trajectories in Π vs. SiO_2 space as the North Arch Lavas. F8 melt inclusions which have undergone >10% PEC are offset to substantially higher Π values at a given SiO_2 (Fig. 7.9c), so VolatileCalc underestimates the solubility of CO_2. Additionally, while F8 melt inclusions show a large drop in Π with increasing SiO_2, all but four melt inclusions have SiO_2 >49 wt%, so are treated as if they had the same composition in VolatileCalc (red line; Fig. 7.9c). Thus, VolatileCalc not only underestimates CO_2 solubility, and therefore overestimates entrapment pressures for F8 melt inclusions hosted in high-Fo olivines, it also neglects compositional variations in CO_2 solubility within this suite of melt inclusions (Fig. 7.9c).

To demonstrate the importance of evaluating the suitability of different solubility models, entrapment pressures from VolatileCalc were compared to those from the models of Ghiorso and Gualda (2015), hereafter Magmasat, Iacono-Marziano et al. (2012), hereafter IM-2012, and Shishkina et al. (2014), hereafter S-2014, using the open-source python tool VESIcal (Iacovino et al., 2020). These three models utilize more than a decade of additional experimental constraints compared to the expressions implemented in VolatileCalc for basaltic compositions (Dixon, 1997). By extension, these models are calibrated on a significantly larger compositional range (Fig. 7.9a), so more effectively encapsulate variability in CO_2 solubility as a function of melt composition.

Entrapment pressures for melt inclusions hosted in low-Fo olivines from F8 calculated using VolatileCalc, S-2014, and IM-2012 are statistically indistinguishable using the KS test at p=0.05 (Fig. 7.13a), likely because their major element compositions lie within the calibration range of all four solubility models (Fig. 7.9a). Magmasat returns slightly lower pressures, which are just distinguishable (p=0.039). This may reflect the stronger sensitivity of Magmasat to melt H_2O contents between 0–1 wt% than the other models (Fig. 7.2). It seems likely based on the distribution of H_2O contents in melt inclusions from past Kīlauean eruptions (Fig. 7.8b) that F8 melt inclusions had higher H_2O contents at the time of entrapment. Thus, entrapment pressures calculated in Magmasat using the diffusively re-equilibrated H_2O contents of F8 melt inclusions are likely an underestimate. As only 2 low-Fo melt inclusions have vapour bubbles producing a FD (N=2), the distribution of entrapment pressures calculated using just glass CO_2 contents are indistinguishable from those using total CO_2 contents (dotted vs. solid black lines; Fig. 7.13a).

In contrast, there are substantial differences between the entrapment pressures obtained from different solubility models for high-Fo melt inclusions (>$Fo_{81.5}$), with Magmasat and

S-2014 plotting to significantly lower pressures than IM-2012 and VolatileCalc (both pairs are statistically indistinguishable from one another at p=0.05; Fig. 7.13b). As discussed above, the simplification of the compositional dependence in VolatileCalc means that this model underestimates CO_2 solubility (Fig. 7.9c), and therefore overestimates entrapment pressures for high-Fo melt inclusions. Similarly, Iacono-Marziano et al. (2012) explicitly warn that their semi-empirical model poorly incorporates the compositional effect of melt MgO contents on CO_2 solubility, as the vast majority of melts in their calibration dataset have ∼6–8 wt% MgO. In contrast, high-Fo PEC-corrected melt inclusions have MgO contents ranging from 7.8–13.7 wt% (Fig. 7.9a). Fortunately, the calibration dataset for the S-2014 model incorporates a significantly broader range of basaltic compositions, including melts with MgO contents similar to PEC-corrected high-Fo melt inclusions. As for low-Fo melt inclusions, Magmasat is offset to slightly lower pressures (median offset of 0.1 kbar).

Overall, entrapment pressures from the S-2014 model were favored, as its calibration dataset effectively captures the major element compositions observed in F8 melt inclusions, particularly those with high MgO contents (Fig. 7.9a). Additionally, given that melt inclusion H_2O contents have been reset by diffusional re-equilibration, the fact that entrapment pressures from this model do not vary as a function of H_2O contents between ∼0–1 wt% is a significant advantage (Fig. 7.2). Given that F8 melt inclusions are relatively H_2O-poor compared to the vast majority of literature measurements (Fig. 7.8a-b), reconstruction of melt H_2O contents at the time of entrapment would likely yield similar entrapment pressures from S-2014 and Magmasat.

Entrapment pressures from S-2014 were converted into entrapment depths, using ρ=2400 kg/m^3 for consistency with modelling of the geodetic signals from the 2018 summit collapse by Anderson et al. (2019). Low-Fo melt inclusions yield median entrapment depths of 1.95 km (lower 68%=1.6 km, upper 68% =2.4 km), which align remarkably well with the estimated centroid depth of the HMM reservoir (Anderson et al., 2019, median=1.9 km, lower 68%=1.8 km, upper 68%=2.1 km; cyan bar; Fig. 7.13a). Unlike these barometric estimates from total CO_2 contents (SIMS+Raman) where only inclusions with no bubble or a bubble with a FD were used (because of the uncertainty regarding the amount of CO_2 in bubbles without a FD), for the following discussion of barometric estimates from measurements of only the glass phase and EOS bubble reconstructions, all inclusions (no bubble, bubble with FD, bubble without FD) were considered. This is because studies not using Raman Spectroscopy cannot distinguish between bubbles with and without a FD. Measurements of CO_2 in just the glass phase yield a median entrapment depths of 2.2 km (lower 68%=1.2 km, upper 68% =2.7 km; Fig. 7.13a, 7.14b), showing that measurements of bubble CO_2 are not essential if a population of melt inclusions has experienced limited PEC.

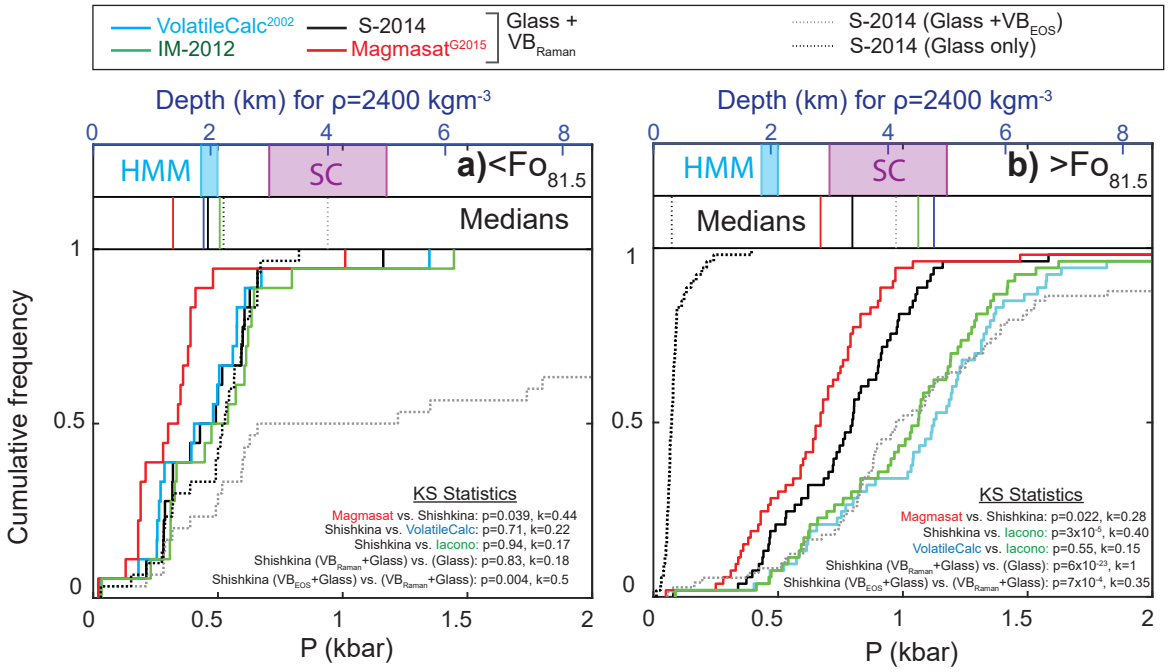


Figure 7.13: Cumulative distribution functions of entrapment pressures from different solubility models (Major elements and CO_2 abundances corrected for the effects of PEC). **a)** Entrapment pressures for melt inclusion hosted in low-Fo olivines ($<Fo_{81.5}$) are statistically indistinguishable for S-2014, VolatileCalc, and IM-2012. Entrapment pressures from Magmasat are offset to slightly lower pressures (just statistically distinguishable at p=0.05 using the KS test). The medians for S-2014 and VolatileCalc align remarkably well with the estimated centroid of the HMM reservoir from Anderson et al. (2019; upper and lower 68% estimates shown with a cyan bar). The distributions of entrapment pressures from the S-2014 model calculated from total carbon contents (bubbles+glass) vs. glass only measurements are indistinguishable. For glass-only measurements (and EOS calculations), all melt inclusions are shown, because studies which do not perform Raman measurements cannot distinguish between bubbles with and without a FD. Entrapment pressures from the S-2014 model with bubble CO_2 contents calculated using the EOS method lie to significantly higher pressures (grey dotted line). **b)** Entrapment pressures calculated for melt inclusions hosted in high-Fo olivines ($>Fo_{81.5}$) using Magmasat and S-2014 are significantly lower than those predicted from IM-2012 and VolatileCalc. All medians plot close to the estimated depth of the SC reservoir (3–5km, Poland et al. 2015, magenta bar). Entrapment pressures from the S-2014 model calculated using only the CO_2 content of the glass (dotted black line) are offset to extremely low pressures, and entrapment pressures calculated from bubble reconstructed using the EOS method are offset to anomalously high pressures.

In contrast, if the CO_2 contents of bubbles in low-Fo olivines are estimated using the EOS method, the median entrapment depth of melt inclusions within low-Fo olivines is 2.8 km (lower 68%=1.2 km, upper 68% =11.4 km; Fig. 7.13a, 7.14c), which would be more consistent with a source from the SC than the HMM reservoir. Crucially, 15 inclusions record entrapment depths >5 km (the base of the SC reservoir) as a result of the fact that the EOS method overestimates bubble CO_2 densities in inclusions which have experienced minimal PEC (Fig. 7.11b-c).

High-Fo melt inclusions have a distribution of entrapment depths (KS test, p=2x10^{-5}) and means (ANOVA, p=3x10^{-4}) offset to higher pressures than low-Fo melt inclusions (Fig. 7.13). The median entrapment depth is 3.4 km (lower 68%=2.0, upper 68%=4.4 km), which align remarkably well with estimates of the depth of the deeper SC reservoir (∼3–5 km depth; Poland et al., 2014; magenta bar; Fig. 7.13b). If bubble CO_2 contents are estimated using the EOS method, the median distribution for all high-Fo melt inclusions is 4.4 km (lower 68%=2.6 km, upper 68% =6.5 km; Fig. 7.13b, 7.14c), with 27 melt inclusions recording entrapment depths >5 km. While still an overestimate compared to the SIMS and Raman measurements made in this study, the discrepancy is smaller than for low-Fo olivines, as a result of the larger proportion of the vapour bubble volume grown at high temperatures in high-Fo melt inclusions. In contrast, the median entrapment depth obtained from measurements of just the CO_2 in the glass phase is only 0.31 km (lower 68%=0.21, upper 68%=0.48 km; Fig. 7.13b, 7.14b).

7.5.5 Summit-Rift Connectivity

Melt inclusion entrapment depths indicate that olivine crystals erupted at F8 crystallized within both the shallower HMM reservoir (low-Fo olivines) and the deeper, SC reservoir (high-Fo olivines). The low degrees of olivine-melt disequilibrium and limited amounts of PEC experienced by melt inclusions hosted within low-Fo olivines indicates that these crystals grew in a melt with a similar temperature to the carrier melt in which they were erupted. In contrast, the high degrees of olivine-melt disequilibrium and large amounts of PEC indicates that high-Fo crystals were mixed into a significantly more evolved (and therefore cooler) carrier liquid than the liquid in which they crystallized. Based on reports of lattice distortions (Gansecki et al., 2019) in F8 olivines, high core forsterite contents, and the distribution of entrapment pressures between 3–5 km (Fig. 7.14a), it seems probable that these olivines grew in the SC reservoir, and then settled into mush piles at the base of this reservoir where they were stored for prolonged periods (likely centuries-millenia; see Chapters 4 and 5). Seismic swarms and the initiation of inflationary tilt in March to April 2018 have been interpreted to record the injection of new melts into the South Caldera reservoir (Neal et al., 2019; Flinders et al., 2020), which may have disturbed the olivine mush pile. These new melts (along with the primitive olivines they scavenged) would then have mixed into the cooler, more evolved melts present within the middle to upper parts of the SC reservoir. Rapid cooling of mush-derived olivines during this mixing event would have initiated large amounts of PEC. The degrees of Mg# re-equilibration (∼70-100%) indicate that crystals were resident in these cooler melts for timescales of approximately a month to a year prior to their eruption at Fissure 8. This is consistent with the time lag between geophysical signals indicating the injection of new magma in March, and the eruption of these crystals between late May and August. The fact that only two melt inclusions record

entrapment depths >5 km rules out models where high forsterite olivines grew in deeper magma storage reservoirs near the base of the volcanic pile (e.g., Lynn et al., 2017), or within Kīlauea's deep rift zones at ∼ 6–9 km (Clague and Denlinger, 1994).

The mechanism by which crystal populations grown in the HMM and SC reservoirs were mixed into a single carrier melt encapsulates an ongoing debate at Kīlauea regarding the geometry of the connection between the rift zone conduit and the summit reservoir system. This connection has been variably described as a Y-shaped feeder system with the SC reservoir feeding both the HMM reservoir and the ERZ conduit with two discrete conduits (Pietruszka et al., 2018; Poland et al., 2015, Model 2, Fig. 7.14d) or a Γ-shaped feeder system with a vertical conduit between the HMM and the SC reservoir, and a single, near-horizontal conduit from the HMM reservoir into the ERZ (Cervelli and Miklius, 2003; Model 3, Fig. 7.14d). Cervelli and Miklius (2003) suggest that the Γ-shaped model is more plausible because a shallow conduit (which is subject to less lithostatic pressure) is more likely to remain open during pauses in eruptive activity than a deep conduit, and because shallow intrusions into the upper ERZ influence both the HMM reservoir and activity at Pu‘u ‘Ō‘ō. However, Poland et al. (2015) favour the Y-shaped model based on earthquake and InSAR observations that dyke intrusions into the ERZ in 2007 and 2011 ascended from a depth of ∼3 km.

In both models, the olivine mush pile at the base of the SC reservoir may have been disturbed by the input of new magma into Kīlauea's summit inferred from geophysical signals (Neal et al., 2019; Flinders et al., 2020). In the Γ-shaped model, crystals sourced from the SC mush pile may have ascended into the HMM reservoir, and then been transported along with more evolved olivines along a shallow rift zone conduit to the site of the eruption. However, the Y-shaped model provides an additional mechanism by which to disturb the SC mush pile. In this geometry, more evolved melts carrying low-Fo olivine crystals within the HMM reservoir would have drained down through the SC reservoir before passing out onto the rift zone, with significant potential for this downward flow and the accompanying collapse of Kīlauea's caldera to erode the SC mush pile. Interestingly, the proportion of crystals which are out of equilibrium with their carrier melts increases substantially between May-August 2018 (Fig. 7.4a), and the degree of re-equilibration between melt inclusions and host crystals decreases (Fig. 7.6b). If the disturbance of the mush pile was solely the result of increased magma supply from the mantle, high-Fo crystals would be expected to be more abundant in the earlier stages of the eruption. In contrast, the erosion and scavenging of high-Fo olivines during the downdraining of melts from the HMM reservoir into the SC reservoir can account for the increase in the proportion of high-Fo olivines with time, similar to the mechanism suggested by Teasdale et al. (2005) for the 1998 eruption of Cerro Azul, Galapagos.

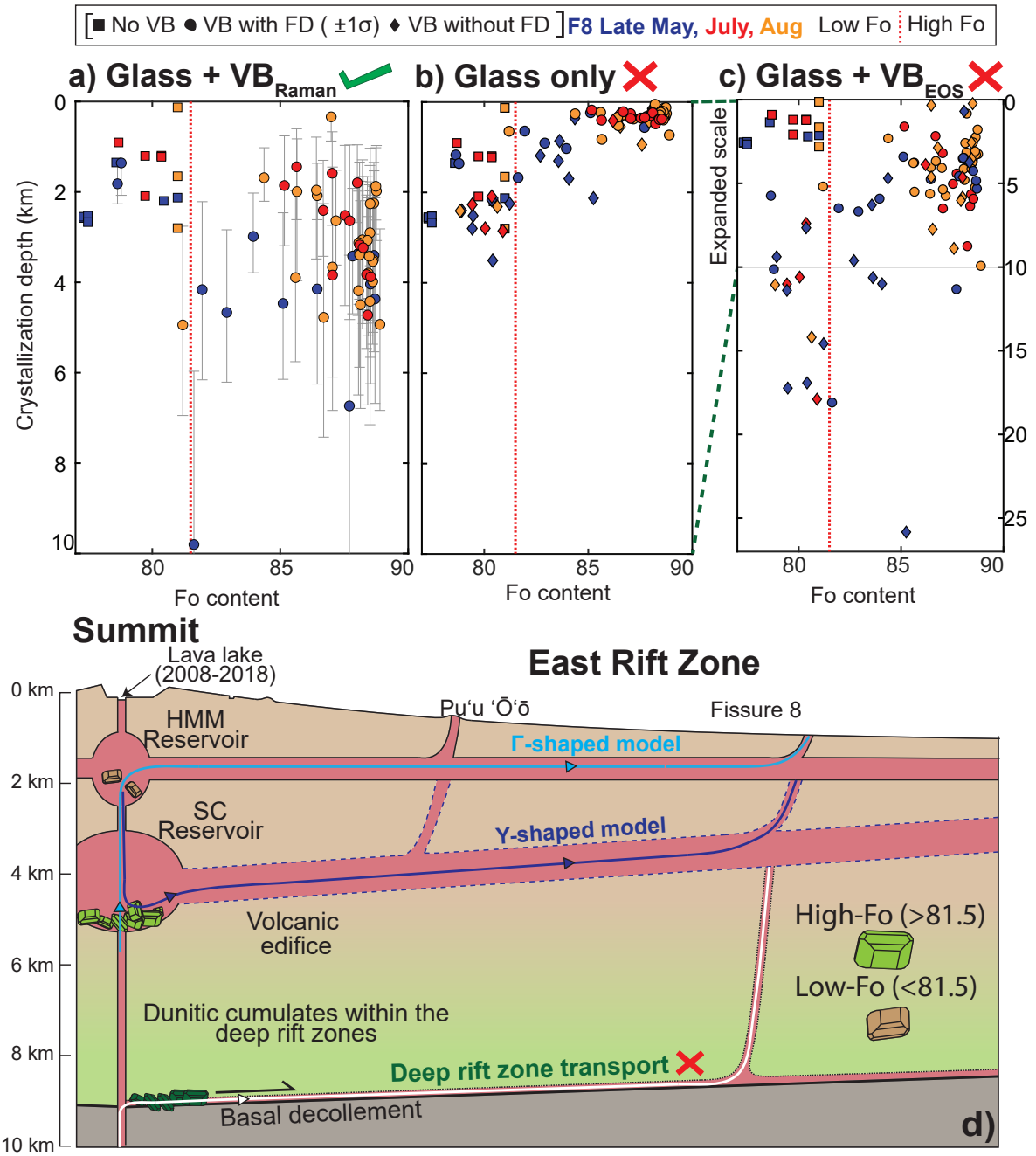


Figure 7.14: Schematic diagram of Kīlauea's plumbing system, with entrapment depths from the S-2014 model for PEC-corrected melt inclusion compositions. **a)** Entrapment depths assuming ρ=2400 kg/m^3 following Anderson et al. (2019). Error bars on bubble-free melt inclusions from SIMS analyses are smaller than the symbol size. Error bars for bubble-bearing melt inclusions were calculated from the minimum and maximum possible total CO_2 content using the 1σ error calculated from repeated Raman analyses of each bubble, and the 1σ estimated by Tucker et al. (2019) associated with calculating 3D bubble volume proportions from 2D images (-48 to 37%). **b)** Entrapment depths estimated from analyses of only the glass phase are anomalously shallow for high-Fo olivines. **c)** Entrapment depths using the EOS method to reconstruct bubble CO_2 contents are anomalously deep, with large numbers of inclusions plotting at >5 km depth (note change in scale). **d)** Cross section showing the three hypothesized magma transport paths supplying rift zone eruptions.

In the May-18 sample, there is no overlap between entrapment depths for melt inclusions within low-Fo olivines (which align with estimated depths of the HMM reservoir) and high-Fo olivines (which align with depths of the SC reservoir; Fig. 7.14a). In contrast, in the July-18 and Aug-18 sample, 36% and 54% of melt inclusions within high-Fo olivines record entrapment depths <2.6 km (the approximate boundary between low- and high-Fo melt inclusions in the May-18 sample). It is plausible based on the large error bars on these entrapment depths (mostly resulting from bubble volume estimates) that many of these melt inclusions crystallized within the SC reservoir. However, another possibility is that these crystals trapped their melt inclusions at shallower depths within the plumbing system. It is possible that remobilized high-Fo crystals from the SC mush pile were transported up into the shallower HMM reservoir. The juxtaposition of these hot crystals with cooler melts within this reservoir may have led to dissolution or rapid growth (Mourey et al., 2020), favouring the formation of embayments. Perhaps due to the mixing with a more primitive melt, growth may have resumed, sealing off melt inclusions recording shallower entrapment depths. It is also possible that the two reservoir systems are significantly more connected than indicated by schematic diagrams such as Fig. 7.14, with frequent cycling of melt and crystals between the two reservoirs, or that the degree of connection increased during the collapse of the summit caldera.

7.6 Conclusion

Detailed investigations of melt inclusion CO_2 systematics from the 2018 eruption of Kīlauea reveals that the crystal cargo erupted at Fissure 8 was derived from both the HMM and SC reservoir. In turn, this suggests that a substantial proportion of the melt erupted at F8 must also have been derived from the SC reservoir, in order to transport these crystals. A substantial source of melt from the SC reservoir supports recent estimates of the total amount of SO_2 emitted from F8, which requires the erupted volume to have been approximately twice that inferred to have drained from the HMM reservoir based on geodetic modelling (Kern et al., 2020; Anderson et al., 2019). Melt inclusions which yield entrapment depths aligned with geophysical estimates of the depth of the SC reservoir (∼3–5 km) host the vast majority of their CO_2 budget in the vapour bubble (∼90%). This is a consequence of the large amounts of PEC experienced by these melt inclusions following their entrainment into cooler, more evolved melts. In contrast, low-Fo olivines host a very small proportion of their CO_2 in the bubble (often below the detection limit of Raman spectroscopy), or are bubble free. The small amount of PEC experienced by these crystals means that almost all of their vapour bubbles grew during syn-eruptive quenching (∼90%), where there was almost no diffusion of CO_2 between the melt and bubble. Thus, the EOS method, which assumes the bubble and melt remain in equilibrium until the bubble stops growing, significantly overpredicts bubble

densities (and therefore entrapment depths) for these melt inclusions (Fig. 7.11b-c, 7.14c). In turn, due to the small amounts of CO_2 in the vapour bubble, estimates of entrapment depths using just melt CO_2 contents for low-Fo olivines are indistinguishable from those where bubble CO_2 was reconstructed using Raman Spectroscopy.

Due to the strong partitioning of CO_2 into the bubble during the extensive PEC experienced by high-Fo melt inclusion, entrapment depths reconstructed using only melt CO_2 contents are, on average, a factor of 12 too low (maximum factor of 60). Reconstructed bubble CO_2 contents using the EOS method overpredict entrapment depths to an extent in high-Fo olivines, but this method is significantly more accurate than for low-Fo melt inclusions where almost all of the bubble grew during syn-eruptive quenching. Overall, this study highlights the importance of measuring bubble densities using Raman Spectroscopy. Analysis of just the glass phase by SIMS or FTIR would have failed to recognize that a significant proportion of the crystal cargo was derived from the SC reservoir (Fig. 7.14b), while theoretical reconstructions using the EOS method of Tucker et al. (2019) would suggest that a substantial fraction of the F8 crystal cargo was derived from deeper depths than the base of the SC reservoir (Fig. 7.14c), requiring the presence of a magma storage reservoir which has not been identified with geophysical monitoring data.

Careful choice of a CO_2-H_2O solubility model is also vital to obtain accurate entrapment pressures, and therefore depths. In particular, like the EOS method, entrapment depths from VolatileCalc (which has been favoured in the literature; Sides et al., 2014a, 2014b; Tucker et al., 2019; Tuohy et al., 2016) indicate that a substantial proportion of the high-Fo F8 crystal cargo ($\sim$50%) must have crystallized at >5 km (Fig. 7.13). This is because the simplified parametrization of the effect of melt composition on CO_2 solubility expressed solely in terms of SiO_2 content used in VolatileCalc underestimates CO_2 solubility, and therefore overestimates entrapment depths for the more primitive (MgO-rich) melt inclusions in high-Fo olivines. Entrapment depths calculated using the Shishkina et al. (2014) model were favoured, because this model is calibrated on a wider variety of basaltic compositions, including melts with MgO contents similar to the PEC-corrected compositions of high-Fo F8 melt inclusions. Entrapment depths calculated using Shishkina et al. (2014) for reconstructed CO_2 contents from SIMS and Raman measurements align remarkably well with the depths of the two main storage reservoirs at Kīlauea based on geophysical constraints. Overall, this study demonstrates that analyses of the CO_2 contents of both the glass phase and vapour bubbles, combined with a critical evaluation of different volatile solubility models, is a powerful tool to accurately constrain magma storage depths.

8

Conclusions and Future Work

This thesis has addressed a number of long-standing debates regarding the storage, chemical evolution and transport of melts and crystals at Kīlauea Volcano, Hawai'i.

Chapter 3 assesses the origin of crystal aggregates, which are a near-ubiquitous textural feature in basaltic lavas worldwide. Kīlauean aggregates were first examined in detail by Schwindinger and Anderson (1989), who used HBF_4 to liberate them from their glassy groundmass, allowing visual examination of attachment geometries. They concluded that aggregates likely formed during physical processes such as crystal settling. However, based on similar visual examinations of olivine aggregates from Reunion, Welsch et al. (2012) suggested that aggregates formed during crystal growth. In this thesis, I use Electron Backscatter Diffraction (EBSD) and energy balance arguments to differentiate between these hypotheses. Unlike optical examinations, EBSD allows the crystallographic relationships between touching grains in large numbers of crystal aggregates to be quantified. To demonstrate the broad versatility of EBSD to differentiate different aggregation mechanisms, chromite aggregates from the Bushveld Complex were also examined in collaboration with Zoja Vukmanovic. Neither olivine nor chromite aggregates show attachment geometries consistent with crystal growth processes such as twinning, epitaxial growth or heterogeneous nucleation. Additionally, I show that heterogeneous nucleation and epitaxial growth are associated with significant energy penalties compared with the continued growth of the pre-existing crystal (although these processes may well be dominant in multi-phase aggregates). Instead, the near-random attachment geometries of chromites indicate that aggregates formed as crystals landed on top of one another after settling to the base of the magma chamber. In contrast, olivine aggregates show a narrower range of geometries, with misorientation axes clustered at [100], and misorientation angles showing three dominant peaks. These attachment geometries, along with different core compositions of attached crystals, indicate that crystals aggregated during late-stage crystal settling or magma transport just prior to their eruption. Since this study was published (Wieser et al., 2019b), Cansu Culha and Jenny Suckale at Stanford have presented numerical models simulating the physical

aggregation of crystals (e.g., Culha et al., 2020, and various virtual conference presentations). Their models of magma ascent within volcanic conduits produce crystal aggregates with very similar distributions of misorientation angles and axes to those presented in this thesis. This demonstrates the potential for integration of quantitative information from EBSD with detailed physical models to gain a greater understanding of volcanic systems.

Chapter 4 investigates the igneous processes responsible for deforming the crystal lattices of a large proportion of Kīlauean olivine crystals. Like olivine aggregates, deformed olivine crystals are near-ubiquitous in a number of volcanic systems worldwide (e.g., West Greenland - Larsen and Pedersen, 2000, Piton de la Fournaise volcano - Welsch et al., 2012, Mull - Westland, 2014, Cerro Azul - Teasdale et al., 2005). These features have been attributed to physical processes such as the plastic deformation of dunitic bodies located within Kīlauea's rift zones (Clague and Denlinger, 1994), collisions of crystals during transport (Natland, 2003), or crystal growth processes (Welsch et al., 2012). Prior to the collection of the EBSD data presented in this thesis, there was little quantitative data to help differentiate these hypotheses. Specifically, I used EBSD to classify the microstructures of deformed olivines, applying techniques developed for examination of deformed olivine crystals within exhumed mantle peridotites. This inter-disciplinary approach revealed that Kīlauean olivines possess subgrain boundaries made of the dislocation types associated with A and E-type fabrics. These fabric types are produced experimentally when relatively anhydrous olivines are deformed at temperatures exceeding 1000°C. Detailed examinations of subgrain sizes, along with calculations performed on published estimates of dislocation densities, reveal that Kīlauean olivines experienced differential stresses of ∼3–12 MPa. The absence of adcumulate textures, high angle grain boundaries, and the broad spatial distribution of deformed grains at a variety of eruption sites around Kīlauea's edifice, are inconsistent with the hypothesis that olivines are deformed within creeping, low melt fraction dunitic bodies in Kīlauea's deep rift zones. This model also cannot account for the occurrence of these features at a number of volcanic systems worldwide which do not possess prominent rift zones. Additionally, the forsterite contents of deformed and undeformed olivine crystals are statistically distinguishable, which is inconsistent with a model where olivines are deformed during crystal-crystal collisions during magma transport processes. Instead, I attribute deformation to gravitational loading within melt-rich cumulate piles with vertical extents of ∼180–720 m located at the base of the deeper South Caldera Reservoir. Mass balance models of Kīlauea's plumbing system, accounting for magma input rates, the volume of olivine fractionated from each volume of melt, and the radii of the SC reservoir inferred from geophysical observations, demonstrates that these thickness's can accumulate within a few centuries (Wieser et al., 2020b).

Chapter 5 compares the major and trace element systematics of erupted olivine crystals to their carrier melts for four of the eruptions examined in Chapter 4 (1969, 1971, 1973, 1974),

as well as an extensive compilation of literature data. The aim of this chapter was to assess whether prolonged storage of olivine crystals within vertically-extensive mush piles convolutes melt inclusion records. I show that a large proportion of Kīlauean olivines erupted in rift zone and extracaldera summit eruptions have high forsterite contents, and exhibit significant Mg# disequilibrium with their co-erupted melts. The distribution of Nb/Y ratios in melt inclusions from 15/17 of these eruptive episodes are indistinguishable, despite substantial temporal variations in the composition of the co-erupted glass. This major and trace element disequilibrium is consistent with the model developed in Chapter 4, where crystals are stored for prolonged periods in vertically-extensive mush piles, before being scavenged by chemically unrelated carrier melts, and carried to the surface. Melts with Nb/Y ratios as low as the most depleted melt inclusions from the 1959 Kīlauea Iki eruption were last erupted $\sim$ 170 years previously, placing a minimum constraint on the residence times of crystals within mush piles. These timescales align remarkably well with those inferred from the mass balance model presented in Chapter 4. This study demonstrates that extreme care is required to link melt inclusion records to eruption-specific measures such as eruption triggering processes, or the fluxes of volatiles released to the atmosphere (Wieser et al., 2019a).

Chapter 6 investigates sulfide saturation at Kīlauea, using SEM mapping to identify sulfides and quantify their chemistry, and LA-ICP-MS to measure chalcophile element concentrations in glasses and melt inclusions from the four eruptions investigated in Chapter 5. Changes in the extent of mantle melting during this time period (1969-1974) provides an opportunity to assess the differential behavoir of chalcophile and lithophile elements during mantle melting. Despite excellent correlations between fractionation-corrected concentrations of highly incompatible lithophile elements (e.g., Ba vs. La), there is no correlation between these lithophile elements and chalcophile elements (e.g., Cu). Along with the estimates of the S and Cu concentrations of primary melts, this indicates that the Kīlauean mantle source was sulfide saturated throughout the melting interval. By modelling changes in sulfide solubility during ascent through the thick Hawaiian lithosphere using the most recent SCSS models, I show that crustal magma chambers are supplied by sulfide-undersaturated melts. Integration of Petrolog3 fractionation trajectories with SCSS models predict that Kīlauean melts become sulfide saturated once more following relatively small amounts of fractional crystallization (at $\sim$12wt% MgO). These models successfully recreate the S contents of Kīlauean melt inclusions, and account for the presence of sulfide inclusions within high forsterite olivine crystals. This work also demonstrates that sulfides in contact with the degassing matrix glass resorb upon eruption, releasing elements such as Ni and Cu back into the melt. This obscures both the textural and chemical record of sulfide saturation in matrix glasses, which explains why previous studies at Kīlauea have suggested that sulfide saturation only occurs at $\sim$2 wt% MgO (Greaney et al., 2017). In particular, I show that the onset of sulfide saturation in degassed melts fractionating within lava lakes (which have

been the focus of most previous studies) is not representative of the fractionation path followed at depth, and instead records a third phase of sulfide saturation. This chapter also examines the petrological evidence for degassing of chalcophile elements during volcanic eruptions. Contrary to examinations of submarine glasses where Se has been shown to be significantly less volatile than S, I suggest that S and Se degas concurrently during subaerial eruptions at Kīlauea. Since the publication of this study (Wieser et al., 2020a), Mason et al. (in review) have performed thermodynamic modelling of the Kīlauean plume, showing that Se speciates as S-Se gas at high magmatic temperatures, supporting this inference.

Chapter 7 examines the CO_2 and H_2O contents of olivine-hosted melt inclusions erupted at Fissure 8 to deduce the geometry of the plumbing system transferring melts from Kīlauea's summit reservoir system to the Lower East Rift Zone during the 2018 eruption. This work is the first to measure CO_2 in both the glass and vapor phase of individual melt inclusions (by SIMS and Raman spectroscopy). These paired measurements reveal that ∼90% of the CO_2 in primitive olivines resides in the vapour bubble. By modelling bubble growth, and changes in CO_2 solubility, I show that CO_2 partitioning into the vapour bubble is driven by extensive post-entrapment crystallization, resulting from the incorporation of hot primitive olivines into cooler more evolved carrier melts. This chapter also compares theoretical reconstructions of bubble densities using the CO_2 equation of state with Raman measurements, and shows that EOS methods vastly overpredict bubble densities within melt inclusions where the vast majority of the bubble volume grew on quench, rather than during PEC. Spurious barometric estimates obtained using EOS reconstructions predict that a substantial proportion of the F8 crystal cargo formed at depths >5 km, requiring magma storage reservoirs which have not been identified geophysically. Similarly, neglecting to measure bubble CO_2 contents underestimates entrapment depths for more primitive olivines by a median factor of 11. Finally, I assess the suitability of different CO_2 - H_2O solubility models, which are used to convert measured volatile contents into entrapment pressures of melt inclusions. The most popular model used at Kīlauea, VolatileCalc, underestimates CO_2 solubility in high MgO F8 melt inclusions, due to the limited compositional range of its calibration dataset. Using the models of Ghiorso and Gualda (2015) and Shishkina et al. (2014), which are calibrated on a much larger dataset of basaltic compositions, I show that depths obtained from melt inclusion volatile contents align remarkably well with the depths of the two main magma storage regions at Kīlauea inferred from geophysical observations.

Overall, this thesis shows that even at exceptionally well-studied volcanoes such as Kīlauea, the application of rapidly-improving microanalytical techniques, combined with critical evaluation of accepted models and methods (e.g., the use of melt inclusions to investigate eruption-specific measures, the near-ubiquitous use of VolatileCalc) can provide novel insights into igneous processes.

8.1 Future Work

This thesis relies on data collected from natural systems using state-of-the-art techniques, and demonstrates the potential of these measurements to quantitatively distinguish hypotheses in volcanology. However, while analytical techniques have advanced substantially, quantitative modelling of igneous processes is fundamentally limited by a paucity of experimental constraints.

For example, the subgrain piezometers used in Chapter 4 were calibrated in the late 1970s based on optical observations of subgrains. In August, Goddard et al. uploaded a preprint presenting recalibrated subgrain size piezometers for quartz and olivine based on EBSD data. However, it is still difficult to know how to apply these methods developed for polycrystalline aggregates to single crystals. Ideally, to improve the accuracy of differential stress estimates presented in Chapter 4, experimental investigation is needed to deduce the best way to estimate stress from individual deformed grains (e.g., optimum transect directions, correction factors accounting for 2D sectioning of subgrain boundaries). Goddard et al. (2020) also warn against extrapolation of their new piezometer to differential stresses below $\sim$ 60 MPa (due to possible changes in the mechanism of subgrain formation). Unfortunately, the range of differential stresses exerted within igneous plumbing systems likely lies below the recommended calibration range.

Additionally, there is little consensus about the temporal evolution of microstructures in crystals subject to time-varying stresses, and long residence times at high temperatures. For example, it is unclear whether the microstructures of olivine crystals record the maximum stress they experienced, or something similar to a time-averaged mean stress (perhaps due to recovery under conditions of lower stress; Goddard et al., 2020; Ross et al., 1980; Wheeler, 2018). Additionally, loading in volcanic mush piles is likely dominated by point contacts of euhedral crystals; such highly heterogenous stress distributions almost certainly convolute piezometry techniques. Ideally, an experimental set up would be designed where a loading force is applied to the top of a touching framework of olivine crystals surrounded by basaltic melt. Removal and re-application of a load would drive the migration of force chains, allowing investigation of time-varying and highly-heterogenous stress distributions. However, it is likely unfeasible to run these experiments for sufficient durations to gain insights into the temporal evolution of microstructures once load is removed. Currently, the best available constraint is the fact that subgrain sizes of deformed olivines resident in the Kīlauea Iki lava lake do not seem to show any correlation with their residence time in the lake, which suggests that annealing takes significantly longer than 20 years (Helz, 1987).

Improvements of the mantle melting models presented in Chapter 6 to place tighter constraints on the amount of S in the Kīlauean mantle source will require a number of additional experimental constraints. Ideally, inversions would be performed for a whole suite of chalcophile elements (instead of just Cu). However, the partitioning behaviour of many

of these elements between silicate and sulfide melts at the high pressures and temperatures relevant to mantle melting beneath Hawai'i are very poorly constrained. Additionally, in relatively oxidised systems such as Kīlauea, more robust melting models will require new experimental parameters of the proportion of S^{6+} species at these conditions. This will be essential to constrain the S content of a sulfide-saturated melt, and therefore, the rate of sulfide consumption during mantle melting. Further work is also needed to improve estimates of the composition of the co-existing sulfide phase during mantle melting.

Chapter 7 demonstrates that Raman analyses of vapor bubbles must be conducted in order to have confidence in melt inclusion entrapment depths in H_2O-poor systems. While some sample sets may not have any CO_2 in the bubble (e.g., low-Fo Kīlauean olivines), at least a subset of each olivine population must be analysed by Raman to confirm this. It is concerning that the vast majority of the studies in the literature using Raman to measure vapour bubbles converted diad splittings into densities using calibration lines developed for a different instrument. As shown in Fig. 2.9, this has led to the publication of large numbers of anomalously high, and thermodynamically-impossible densities. I believe this results from limited collaboration and synergy between fluid inclusion communities (who have been analysing CO_2-rich inclusions for decades, and are well aware of the thermodynamic properties of CO_2 at room temperature), and melt inclusion communities (who are only just realizing the importance of vapor bubbles). Even studies which have appreciated the impossibility of densities between 0.2 and 0.7g/cm^3 at room temperature have explained their results by invoking laser heating, rather than an unsuitable calibration. To my knowledge, there is no evidence in the literature that laser heating of vapour bubbles is important, and significant evidence against this theory (e.g., Dubessy et al., 2012; Rosso and Bodnar, 1995). A related issue is the shortage of standards with known CO_2 densities, as the vast majority of laboratories will not have the expertize or infrastructure to generate their own calibration lines from the compression of pure CO_2 gas. Thus, a series of synthetic or natural CO_2 fluid inclusion standards must be created, measured (ideally on more than one instrument with an in-house gas calibration set up), and distributed to the community. Sadly, a shortage of analytical standards is a problem throughout the Earth Sciences, likely as a function of the fact that current academic hiring/promotion structures do not favour such time consuming community endeavours.

Works Cited

Anderson (1974). Evidence for a picritic, volatile-rich magma beneath Mt. Shasta, California. *Journal of Petrology*, **15**, pp. 243–267.

Anderson, A. T. and Brown, G. G. (1993). CO_2 contents and formation pressures of some Kilauean melt inclusions. *American Mineralogist*, **78**, pp. 794–803.

Anderson, K. R. and Poland, M. P. (2016). Bayesian estimation of magma supply, storage, and eruption rates using a multiphysical volcano model: Kılauea Volcano, 2000–2012. *Earth and Planetary Science Letters*, **447**, pp. 161–171.

Anderson, K. R. et al. (2015). Episodic deflation–inflation events at Kılauea Volcano and implications for the shallow magma system. *Hawaiian Volcanoes: From Source to Surface*, **208**, p. 229.

Anderson, K. R. et al. (2019). Magma reservoir failure and the onset of caldera collapse at Kılauea Volcano in 2018. *Science*, **366**.

Antony, S. (2007). Link between single-particle properties and macroscopic properties in particulate assemblies: role of structures within structures. *Philosophical Transactions of the Royal Society A: Mathematical, Physical and Engineering Sciences*, **365**, pp. 2879–2891.

Arevalo, R., McDonough, W. F., and Piccoli, P. M. (2011). In situ determination of first-row transition metal, Ga and Ge abundances in geological materials via medium-resolution LA-ICP-MS. *Geostandards and Geoanalytical Research*, **35**, pp. 253–273.

Aster, E. M. et al. (2016). Reconstructing CO_2 concentrations in basaltic melt inclusions using Raman analysis of vapor bubbles. *Journal of Volcanology and Geothermal Research*, **323**, pp. 148–162.

Ave'Lallemant, H. G. and Carter, N. L. (1970). Syntectonic recrystallization of olivine and modes of flow in the upper mantle. *Geological Society of America Bulletin*, **81**, pp. 2203–2220.

AvéLallemant, H. G. (1978). Experimental deformation of diopside and websterite. *Tectonophysics*, **48**, pp. 1–27.

Azevedo, S. and Nespolo, M. (2017). Twinning in olivine group revisited. *European Journal of Mineralogy*, **29**, pp. 213–226.

Bachmann, F., Hielscher, R., and Schaeben, H. (2010). Texture analysis with MTEX–free and open source software toolbox. *Solid State Phenomena*, **160**, pp. 63–68.

Bai, Q. and Kohlstedt, D. L. (1992). High-temperature creep of olivine single crystals, 2. Dislocation structures. *Tectonophysics*, **206**, pp. 1–29.

Baker, S. and Amelung, F. (2012). Top-down inflation and deflation at the summit of Kılauea Volcano, Hawai ʻi observed with InSAR. *Journal of Geophysical Research: Solid Earth*, **117**.

Ballmer, M. D. et al. (2013). Double layering of a thermochemical plume in the upper mantle beneath Hawaii. *Earth and Planetary Science Letters*, **376**, pp. 155–164.

Barth, A. et al. (2019). Magma decompression rate correlates with explosivity at basaltic volcanoes—Constraints from water diffusion in olivine. *Journal of Volcanology and Geothermal Research*, **387**, p. 106664.

Beattie, P., Ford, C., and Russell, D. (1991). Partition coefficients for olivine-melt and orthopyroxene-melt systems. *Contributions to Mineralogy and Petrology*, **109**, pp. 212–224.

Bell, I. H. et al. (2014). Pure and pseudo-pure fluid thermophysical property evaluation and the open-source thermophysical property library CoolProp. *Industrial & engineering chemistry research*, **53**, pp. 2498–2508.

Bennett, E. N. et al. (2019). Deep roots for mid-ocean-ridge volcanoes revealed by plagioclase-hosted melt inclusions. *Nature*, **572**, pp. 235–239.

Bennett, V., Norman, M., and Garcia, M. (2000). Rhenium and platinum group element abundances correlated with mantle source components in Hawaiian picrites: sulphides in the plume. *Earth and Planetary Science Letters*, **183**, pp. 513–526.

Bergantz, G. W., Schleicher, J. M., and Burgisser, A. (2017). On the kinematics and dynamics of crystal-rich systems. *Journal of Geophysical Research: Solid Earth*, **122**, pp. 6131–6159.

Berlo, K. et al. (2014). Sulfide breakdown controls metal signature in volcanic gas at Kawah Ijen volcano, Indonesia. *Chemical Geology*, **371**, pp. 115–127.

Berry, A. J. et al. (2018). A re-assessment of the oxidation state of iron in MORB glasses. *Earth and Planetary Science Letters*, **483**, pp. 114–123.

Boioli, F. et al. (2015). Modeling the creep properties of olivine by 2.5-dimensional dislocation dynamics simulations. *Physical Review B*, **92**, p. 014115.

Boudier, F. (1991). Olivine xenocrysts in picritic magmas. *Contributions to Mineralogy and Petrology*, **109**, pp. 114–123.

Bougault, H. and Hekinian, R. (1974). Rift valley in the Atlantic Ocean near 36° 50 N: petrology and geochemistry of basaltic rocks. *Earth and Planetary Science Letters*, **24**, pp. 249–261.

Bradshaw, R. W., Kent, A. J., and Tepley III, F. J. (2018). Chemical fingerprints and residence times of olivine in the 1959 Kilauea Iki eruption, Hawaii: Insights into picrite formation. *American Mineralogist: Journal of Earth and Planetary Materials*, **103**, pp. 1812–1826.

Brandon, D. (1966). The structure of high-angle grain boundaries. *Acta Metallurgica*, **14**, pp. 1479–1484.

Brenan, J. M. (2015). Se–Te fractionation by sulfide–silicate melt partitioning: implications for the composition of mantle-derived magmas and their melting residues. *Earth and Planetary Science Letters*, **422**, pp. 45–57.

Brooker, R. et al. (1999). Solubility, speciation and dissolution mechanisms for CO_2 in melts on the NaAlO2–SiO2 join. *Geochimica et Cosmochimica Acta*, **63**, pp. 3549–3565.

Brough, I., Bate, P., and Humphreys, F. (2006). Optimising the angular resolution of EBSD. *Materials Science and Technology*, **22**, pp. 1279–1286.

Brounce, M., Stolper, E., and Eiler, J. (2017). Redox variations in Mauna Kea lavas, the oxygen fugacity of the Hawaiian plume, and the role of volcanic gases in Earth's oxygenation. *Proceedings of the National Academy of Sciences*, **114**, pp. 8997–9002.

Brugger, C. R. and Hammer, J. E. (2015). Prevalence of growth twins among anhedral plagioclase microlites. *American Mineralogist*, **100**, pp. 385–395.

Bruno, M. et al. (2014). Ab initio calculations of the main crystal surfaces of forsterite (Mg_2SiO_4): a preliminary study to understand the nature of geochemical processes at the olivine interface. *The Journal of Physical Chemistry C*, **118**, pp. 2498–2506.

Bucholz, C. E. et al. (2013). Post-entrapment modification of volatiles and oxygen fugacity in olivine-hosted melt inclusions. *Earth and Planetary Science Letters*, **374**, pp. 145–155.

Buerger, M. (1945). The genesis of twin crystals. *American Mineralogist: Journal of Earth and Planetary Materials*, **30**, pp. 469–482.

Bulanova, G. et al. (1996). Trace elements in sulfide inclusions from Yakutian diamonds. *Contributions to Mineralogy and Petrology*, **124**, pp. 111–125.

Campbell, I. (1978). Some problems with the cumulus theory. *Lithos*, **11**, pp. 311–323.

Cao, Y. et al. (2015). Plastic deformation and seismic properties in fore-arc mantles: a petrofabric analysis of the Yushigou Harzburgites, North Qilian Suture Zone, NW China. *Journal of Petrology*, **56**, pp. 1897–1944.

Carmichael, I. S. and Ghiorso, M. S. (1986). Oxidation-reduction relations in basic magma: a case for homogeneous equilibria. *Earth and Planetary Science Letters*, **78**, pp. 200–210.

Cashman, K. V., Sparks, R. S. J., and Blundy, J. D. (2017). Vertically extensive and unstable magmatic systems: a unified view of igneous processes. *Science*, **355**, eaag3055.

Cervelli, P. F. and Miklius, A. (2003). The shallow magmatic system of Kilauea Volcano. *US Geological Survey Professional Paper*, **1676**, pp. 149–163.

Chakraborty, S. (2010). Diffusion coefficients in olivine, wadsleyite and ringwoodite. *Reviews in mineralogy and geochemistry*, **72**, pp. 603–639.

Chen, Y. et al. (2011). The rate of water loss from olivine-hosted melt inclusions. *Contributions to Mineralogy and Petrology*, **162**, pp. 625–636.

Cherniak, D. (2010). REE diffusion in olivine. *American Mineralogist*, **95**, pp. 362–368.

Clague, D. and Denlinger, R. (1994). Role of olivine cumulates in destabilizing the flanks of Hawaiian volcanoes. *Bulletin of Volcanology*, **56**, pp. 425–434.

Clague, D., Weber, W. S., and Dixon, J. E. (1991). Picritic glasses from Hawaii. *Nature*, **353**, p. 553.

Clague, D. et al. (1995). Petrology of submarine lavas from Kilauea's Puna Ridge, Hawaii. *Journal of Petrology*, **36**, pp. 299–349.

Cody, A. and Cody, R. (1995). Dendrite formation by apparent repeated twinning of calcium oxalate dihydrate. *Journal of crystal growth*, **151**, pp. 369–374.

Cottrell, E. and Kelley, K. A. (2011). The oxidation state of Fe in MORB glasses and the oxygen fugacity of the upper mantle. *Earth and Planetary Science Letters*, **305**, pp. 270–282.

Cottrell, E. et al. (2009). High-precision determination of iron oxidation state in silicate glasses using XANES. *Chemical Geology*, **268**, pp. 167–179.

Cox, D. et al. (2019). Chalcophile element processing beneath a continental arc stratovolcano. *Earth and Planetary Science Letters*, **522**, pp. 1–11.

Crowe, B. M. et al. (1987). Trace element geochemistry of volcanic gases and particles from 1983–1984 eruptive episodes of Kilauea volcano. *Journal of Geophysical Research: Solid Earth*, **92**, pp. 13708–13714.

Culha, C. et al. (2020). Crystal Fractionation by Crystal-Driven Convection. *Geophysical Research Letters*, **47**, e2019GL086784.

Czamanske, G. K. and Moore, J. G. (1977). Composition and phase chemistry of sulfide globules in basalt from the Mid-Atlantic Ridge rift valley near 37 N lat. *Geological Society of America Bulletin*, **88**, pp. 587–599.

Dannberg, J. and Sobolev, S. V. (2015). Low-buoyancy thermochemical plumes resolve controversy of classical mantle plume concept. *Nature Communications*, **6**, pp. 1–9.

Danyushevsky, L. V. (2001). The effect of small amounts of H_2O on crystallisation of mid-ocean ridge and backarc basin magmas. *Journal of Volcanology and Geothermal Research*, **110**, pp. 265–280.

Danyushevsky, L. V., McNeill, A. W., and Sobolev, A. V. (2002a). Experimental and petrological studies of melt inclusions in phenocrysts from mantle-derived magmas: an overview of techniques, advantages and complications. *Chemical Geology*, **183**, pp. 5–24.

Danyushevsky, L. V. and Plechov, P. (2011). Petrolog3: Integrated software for modeling crystallization processes. *Geochemistry, Geophysics, Geosystems*, **12**.

Danyushevsky, L., Sokolov, S., and Falloon, T. J. (2002b). Melt inclusions in olivine phenocrysts: using diffusive re-equilibration to determine the cooling history of a crystal, with implications for the origin of olivine-phyric volcanic rocks. *Journal of Petrology*, **43**, pp. 1651–1671.

Danyushevsky, L., Della-Pasqua, F., and Sokolov, S. (2000). Re-equilibration of melt inclusions trapped by magnesian olivine phenocrysts from subduction-related magmas: petrological implications. *Contributions to Mineralogy and Petrology*, **138**, pp. 68–83.

Davidson, J. et al. (2007). Amphibole "sponge" in arc crust? *Geology*, **35**, pp. 787–790.

Day, J. and Taylor, L. A. (2007). On the structure of mare basalt lava flows from textural analysis of the LaPaz Icefield and Northwest Africa 032 lunar meteorites. *Meteoritics & Planetary Science*, **42**, pp. 3–17.

De Leeuw, N. et al. (2000). Modelling the effect of water on the surface structure and stability of forsterite. *Physics and Chemistry of Minerals*, **27**, pp. 332–341.

Deer, W. A. (1966). An introduction to the rock-forming minerals. Longmann, London, pp. 1–528.

Denlinger, R. and Morgan, J. K. (2014). Instability of Hawaiian volcanoes. *Characteristics of Hawaiian volcanoes*, **1801**, pp. 149–176.

Desborough, G. A., Anderson, A. T., and Wright, T. L. (1968). Mineralogy of sulfides from certain Hawaiian basalts. *Economic Geology*, **63**, pp. 636–644.

Ding, S. and Dasgupta, R. (2018). Sulfur inventory of ocean island basalt source regions constrained by modeling the fate of sulfide during decompression melting of a heterogeneous mantle. *Journal of Petrology*, **59**, pp. 1281–1308.

Dixon, J. E. (1997). Degassing of alkalic basalts. *American Mineralogist*, **82**, pp. 368–378.

Dixon, J. E., Clague, D. A., and Stolper, E. M. (1991). Degassing history of water, sulfur, and carbon in submarine lavas from Kilauea Volcano, Hawaii. *The Journal of Geology*, **99**, pp. 371–394.

Dixon, J. E., Stolper, E. M., and Holloway, J. R. (1995). An experimental study of water and carbon dioxide solubilities in mid-ocean ridge basaltic liquids. Part I: calibration and solubility models. *Journal of Petrology*, **36**, pp. 1607–1631.

Dixon, J. E. et al. (1997). Volatiles in alkalic basalts form the North Arch Volcanic Field, Hawaii: extensive degassing of deep submarine-erupted alkalic series lavas. *Journal of Petrology*, **38**, pp. 911–939.

Dodd, R. and Calef, C. (1971). Twinning and intergrowth of olivine crystals in chondritic meteorites. *Mineralogical Magazine*, **38**, pp. 324–327.

Donaldson, C. H. (1976). An experimental investigation of olivine morphology. *Contributions to Mineralogy and Petrology*, **57**, pp. 187–213.

Dowty, E. (1980a). Computing and drawing crystal shapes. *American Mineralogist*, **65**, pp. 465–471.

Dowty, E. (1980b). Synneusis reconsidered. *Contributions to Mineralogy and Petrology*, **74**, pp. 75–84.

Duan, Z. and Zhang, Z. (2006). Equation of state of the H2O, CO2, and H2O–CO2 systems up to 10 GPa and 2573.15 K: Molecular dynamics simulations with ab initio potential surface. *Geochimica et Cosmochimica Acta*, **70**, pp. 2311–2324.

Dubessy, J. et al. (2012). Instrumentation in Raman spectroscopy: elementary theory and practice. *Raman spectroscopy applied to earth sciences and cultural heritage*, **12**, pp. 83–172.

Eaton, J. P. and Murata, K. (1960). How volcanoes grow. *Science*, **132**, pp. 925–938.

Edmonds, M., Gerlach, T. M., and Herd, R. A. (2009). Halogen degassing during ascent and eruption of water-poor basaltic magma. *Chemical Geology*, **263**, pp. 122–130.

Edmonds, M. and Mather, T. A. (2017). Volcanic sulfides and outgassing. *Elements*, **13**, pp. 105–110.

Edmonds, M., Mather, T. A., and Liu, E. J. (2018). A distinct metal fingerprint in arc volcanic emissions. *Nature Geoscience*, **11**, pp. 790–794.

Ellis, W. (1826). Narrative of a Tour Through Hawaii, Or Owhyhee; with Remarks on the History, Traditions, Manners, Customs, and Language of the Inhabitants of the Sandwich Island. For the author, by H. Fisher, son, and P. Jackson.

Ertel, W., Dingwell, D. B., and Sylvester, P. J. (2008). Siderophile elements in silicate melts—A review of the mechanically assisted equilibration technique and the nanonugget issue. *Chemical Geology*, **248**, pp. 119–139.

Esposito, R. et al. (2012). Application of the Linkam TS1400XY heating stage to melt inclusion studies. *Open Geosciences*, **4**, pp. 208–218.

Esposito, R. et al. (2011). Volatile evolution of magma associated with the Solchiaro eruption in the Phlegrean Volcanic District (Italy). *Journal of Petrology*, **52**, pp. 2431–2460.

Estep, J. and Dufek, J. (2012). Substrate effects from force chain dynamics in dense granular flows. *Journal of Geophysical Research: Earth Surface*, **117**.

Fall, A., Tattitch, B., and Bodnar, R. J. (2011). Combined microthermometric and Raman spectroscopic technique to determine the salinity of H_2O–CO_2–NaCl fluid inclusions based on clathrate melting. *Geochimica et Cosmochimica Acta*, **75**, pp. 951–964.

Faul, U. H. and Gerald, J. D. F. (1999). Grain misorientations in partially molten olivine aggregates: an electron backscatter diffraction study. *Physics and Chemistry of Minerals*, **26**, pp. 187–197.

Faure, F., Trolliard, G., and Soulestin, B. (2003a). TEM investigation of forsterite dendrites. *American Mineralogist*, **88**, pp. 1241–1250.

Faure, F. et al. (2003b). A developmental model of olivine morphology as a function of the cooling rate and the degree of undercooling. *Contributions to Mineralogy and Petrology*, **145**, pp. 251–263.

Fermi, E. (1931). Über den Ramaneffekt des Kohlendioxyds. *Zeitschrift für Physik*, **71**, pp. 250–259.

Fiske, R. S. and Kinoshita, W. T. (1969). Inflation of Kilauea volcano prior to its 1967-1968 eruption. *Science*, **165**, pp. 341–349.

Fleet, M. E. and Stone, W. E. (1990). Nickeliferous sulfides in xenoliths, olivine megacrysts and basaltic glass. *Contributions to Mineralogy and Petrology*, **105**, pp. 629–636.

Flinders, A. et al. (2020). Seismic velocity variations associated with the 2018 lower East Rift Zone eruption of Kılauea, Hawaii. *Bulletin of Volcanology*, **82**, p. 47.

Fortin, M.-A. et al. (2015). The effect of water on the sulfur concentration at sulfide saturation (SCSS) in natural melts. *Geochimica et Cosmochimica Acta*, **160**, pp. 100–116.

Francis, D. (1985). The Baffin Bay lavas and the value of picrites as analogues of primary magmas. *Contributions to Mineralogy and Petrology*, **89**, pp. 144–154.

Gaetani, G. A. et al. (2012). Rapid reequilibration of H_2O and oxygen fugacity in olivine-hosted melt inclusions. *Geology*, **40**, pp. 915–918.

Gallagher, J. et al. (1974). Experimental studies relating to microfracture in sandstone. *Tectonophysics*, **21**, pp. 203–247.

Gansecki, C. et al. (2019). The tangled tale of Kılauea's 2018 eruption as told by geochemical monitoring. *Science*, **366**.

Garbacz, A. and Grabski, M. (1989). Modelling of CSL boundaries distribution in polycrystals. *Scripta Metallurgica*, **23**, pp. 1369–1374.

Garcia, M. O. et al. (1993). An evaluation of temporal geochemical evolution of Loihi summit lavas: results from Alvin submersible dives. *Journal of Geophysical Research: Solid Earth*, **98**, pp. 537–550.

Garcia, M. O. et al. (1998). Petrology and geochronology of basalt breccia from the 1996 earthquake swarm of Loihi seamount, Hawaii: magmatic history of its 1996 eruption. *Bulletin of Volcanology*, **59**, pp. 577–592.

Garcia, M., Pietruszka, A. J., and Rhodes, J. M. (2003). A petrologic perspective of Kılauea volcano's summit magma reservoir. *Journal of Petrology*, **44**, pp. 2313–2339.

Garcia, M. et al. (1996). Petrology of lavas from the Puu Oo eruption of Kilauea Volcano: III. The Kupaianaha episode (1986–1992). *Bulletin of Volcanology*, **58**, pp. 359–379.

Gerding, H. and Nijveld, W. (1936). Raman Spectrum of Gaseous and Liquid Sulphur Dioxide and its Solutions in Water. *Nature*, **137**, pp. 1070–1070.

Gerlach, T. M. and Nordlie, B. E. (1975). The COHS gaseous system; Part I, Composition limits and trends in basaltic cases. *American Journal of Science*, **275**, pp. 353–376.

Gerlach, T. et al. (2002). Carbon dioxide emission rate of Kılauea Volcano: Implications for primary magma and the summit reservoir. *Journal of Geophysical Research: Solid Earth*, **107**, ECV–3.

Ghiorso, M. S. and Gualda, G. A. (2015). An H_2O–CO_2 mixed fluid saturation model compatible with rhyolite-MELTS. *Contributions to Mineralogy and Petrology*, **169**, pp. 1–30.

Ghiorso, M. S. et al. (2002). The pMELTS: A revision of MELTS for improved calculation of phase relations and major element partitioning related to partial melting of the mantle to 3 GPa. *Geochemistry, Geophysics, Geosystems*, **3**, pp. 1–35.

Gibson, S. and Geist, D. (2010). Geochemical and geophysical estimates of lithospheric thickness variation beneath Galápagos. *Earth and Planetary Science Letters*, **300**, pp. 275–286.

Giordano, D., Nichols, A. R., and Dingwell, D. B. (2005). Glass transition temperatures of natural hydrous melts: a relationship with shear viscosity and implications for the welding process. *Journal of Volcanology and Geothermal Research*, **142**, pp. 105–118.

Goddard, R. M. et al. (2020). A subgrain-size piezometer calibrated for EBSD. *Earth and Space Science Open Archive*, p. 28. URL: `https://doi.org/10.1002/essoar.10503878.1`.

Greaney, A. T. et al. (2017). The behavior of chalcophile elements during magmatic differentiation as observed in Kilauea Iki lava lake, Hawaii. *Geochimica et Cosmochimica Acta*, **210**, pp. 71–96.

Greenland, L. (1984). Gas composition of the January 1983 eruption of Kilauea Volcano, Hawaii. *Geochimica et Cosmochimica Acta*, **48**, pp. 193–195.

Greenland, L., Okamura, A., and Stokes, J. (1988). Constraints on the mechanism of eruption, in: The Pu'u O' O Eruption of Kilauea Volcano, Hawai'i: Episodes 1 through 20. *US Geological Survey Professional Paper 1463*, pp. 155–164.

Guggino, S. and Hervig, R. (2011). "Synthesis and Characterization of Five New F-bearing Basalt Reference Materials (Fba Glasses): Quantifying the Fluorine Content of the Basaltic Glass Standards BCR-2G, BHVO-2G. GSA-1G, GSC-1G, GSD-1G, GSE-1G, ML3B-G, KL2-G, and ALV-519-4". In: *AGU Fall Meeting Abstracts*.

Guo, J., Griffin, W. L., and O'Reilly, S. Y. (1999). Geochemistry and origin of sulphide minerals in mantle xenoliths: Qilin, Southeastern China. *Journal of Petrology*, **40**, pp. 1125–1149.

Hammer, J. E., Sharp, T. G., and Wessel, P. (2010). Heterogeneous nucleation and epitaxial crystal growth of magmatic minerals. *Geology*, **38**, pp. 367–370.

Hansen, L. N. and Warren, J. M. (2015). Quantifying the effect of pyroxene on deformation of peridotite in a natural shear zone. *Journal of Geophysical Research: Solid Earth*, **120**, pp. 2717–2738.

Hansen, L. N. et al. (2014). Protracted fabric evolution in olivine: Implications for the relationship among strain, crystallographic fabric, and seismic anisotropy. *Earth and Planetary Science Letters*, **387**, pp. 157–168.

Hansen, S. et al. (2004). Seismic velocity and attenuation structure of the east rift zone and south flank of Kilauea Volcano, Hawaii. *Bulletin of the Seismological Society of America*, **94**, pp. 1430–1440.

Hartley, M. E. et al. (2014). Reconstructing the deep CO_2 degassing behaviour of large basaltic fissure eruptions. *Earth and Planetary Science Letters*, **393**, pp. 120–131.

Hartley, M. E. et al. (2015). Diffusive over-hydration of olivine-hosted melt inclusions. *Earth and Planetary Science Letters*, **425**, pp. 168–178.

Hartley, M. E. et al. (2017). Olivine-hosted melt inclusions as an archive of redox heterogeneity in magmatic systems. *Earth and Planetary Science Letters*, **479**, pp. 192–205.

Hauri, E. (2002). SIMS analysis of volatiles in silicate glasses, 2: isotopes and abundances in Hawaiian melt inclusions. *Chemical Geology*, **183**, pp. 115–141.

Hauri, E. H., Gaetani, G. A., and Green, T. H. (2006). Partitioning of water during melting of the Earth's upper mantle at H_2O-undersaturated conditions. *Earth and Planetary Science Letters*, **248**, pp. 715–734.

Helmy, H. M. and Fonseca, R. O. (2017). The behavior of Pt, Pd, Cu and Ni in the Se-sulfide system between 1050 and 700° C and the role of Se in platinum-group elements fractionation in sulfide melts. *Geochimica et Cosmochimica Acta*, **216**, pp. 141–152.

Helo, C. et al. (2011). Explosive eruptions at mid-ocean ridges driven by CO_2-rich magmas. *Nature Geoscience*, **4**, pp. 260–263.

Helz, R. T. (1987). Diverse olivine types in lava of the 1959 eruption of Kilauea volcano and their bearing on eruption dynamics. *Volcanism in Hawaii*, **1**, pp. 691–722.

Helz, R. T. and Thornber, C. R. (1987). Geothermometry of Kilauea Iki lava lake, Hawaii. *Bulletin of Volcanology*, **49**, pp. 651–668.

Helz, R. T. and Wright, T. L. (1992). Differentiation and magma mixing on Kilauea's east rift zone. *Bulletin of Volcanology*, **54**, pp. 361–384.

Helz, R. T. and Wright, T. L. (1983). Drilling report and core logs for the 1981 drilling of Kilauea Iki lava lake, Kilauea volcano, Hawaii, with comparative notes on earlier (1967-1979) drilling experiences. *Open-File Report 83-326, United States Geological Survey*, pp. 1–68.

Helz, R. T. et al. (2014). Petrologic Insights into Basaltic Volcanism at Historically Active Hawaiian Volcanoes. *US Geological Survey Professional Paper*, **1801**, pp. 237–292.

Helz, R. T. et al. (2015). Evidence for large compositional ranges in coeval melts erupted from Kılauea's summit reservoir. *Hawaiian Volcanoes: from Source to Surface*, pp. 125–145.

Helz, R. et al. (2017). Olivine-melt relationships and syneruptive redox variations in the 1959 eruption of Kılauea Volcano as revealed by XANES. *Journal of Volcanology and Geothermal Research*, **333**, pp. 1–14.

Hofmann, A. W. (1997). Mantle geochemistry: the message from oceanic volcanism. *Nature*, **385**, pp. 219–229.

Hofmann, A. W., Feigenson, M. D., and Raczek, I. (1984). Case studies on the origin of basalt: III. Petrogenesis of the Mauna Ulu eruption, Kilauea, 1969–1971. *Contributions to Mineralogy and Petrology*, **88**, pp. 24–35.

Holcomb, R. T. (1987). Eruptive history and long-term behavior of Kilauea Volcano. *US Geological Survey Professional Paper*, **1350**, pp. 261–350.

Holness, M. B., Farr, R., and Neufeld, J. A. (2017a). Crystal settling and convection in the Shiant Isles Main Sill. *Contributions to Mineralogy and Petrology*, **172**, p. 7.

Holness, M. B., Vukmanovic, Z., and Mariani, E. (2017b). Assessing the role of compaction in the formation of adcumulates: a microstructural perspective. *Journal of Petrology*, **58**, pp. 643–673.

Hughes, C. J. (2013). Igneous petrology. Vol. 7. Elsevier.

Humphreys, F. (2001). Review grain and subgrain characterisation by electron backscatter diffraction. *Journal of Materials Science*, **36**, pp. 3833–3854.

Iacono-Marziano, G. et al. (2012). New experimental data and semi-empirical parameterization of H2O–CO2 solubility in mafic melts. *Geochimica et Cosmochimica Acta*, **97**, pp. 1–23.

Iacovino, K. and Till, C. B. (2019). DensityX: A program for calculating the densities of magmatic liquids up to 1,627 C and 30 kbar. *Volcanica*, **2**, pp. 1–10.

Iacovino, K. et al. (Aug. 2020). VESIcal: An open source thermodynamic model engine for mixed volatile solubility in silicate melts. *Github -https://github.com/kaylai/VESIcal/.*

Jackson, E. D. (1961). Primary Textures and mineral associations in the Ultramafic zone of the Stillwater complex Montana: the petrographic features and origin of the layered chromitites, bronzitites, and harzburgites in the lower part of the Stillwater complex. US Government Printing Office.

Jackson, M., Blundy, J., and Sparks, R. (2018). Chemical differentiation, cold storage and remobilization of magma in the Earth's crust. *Nature*, **564**, p. 405.

Jenner, F. E. and Arevalo Jr, R. D. (2016). Major and trace element analysis of natural and experimental igneous systems using LA–ICP–MS. *Elements*, **12**, pp. 311–316.

Jenner, F. E. and O'Neill, H. S. C. (2012a). Analysis of 60 elements in 616 ocean floor basaltic glasses. *Geochemistry, Geophysics, Geosystems*, **13**.

Jenner, F. E. and O'Neill, H. S. C. (2012b). Major and trace analysis of basaltic glasses by laser-ablation ICP-MS. *Geochemistry, Geophysics, Geosystems*, **13**.

Jenner, F. E. (2017). Cumulate causes for the low contents of sulfide-loving elements in the continental crust. *Nature Geoscience*, **10**, pp. 524–529.

Jenner, F. E. et al. (2012). Chalcophile element systematics in volcanic glasses from the northwestern Lau Basin. *Geochemistry, Geophysics, Geosystems*, **13**.

Jenner, F. E. et al. (2009). Determination of selenium concentrations in NIST SRM 610, 612, 614 and geological glass reference materials using the electron probe, LA-ICP-MS and SHRIMP II. *Geostandards and Geoanalytical Research*, **33**, pp. 309–317.

Jenner, F. E. et al. (2010). The magnetite crisis in the evolution of arc-related magmas and the initial concentration of Au, Ag and Cu. *Journal of Petrology*, **51**, pp. 2445–2464.

Jenner, F. E. et al. (2015). The competing effects of sulfide saturation versus degassing on the behavior of the chalcophile elements during the differentiation of hydrous melts. *Geochemistry, Geophysics, Geosystems*, **16**, pp. 1490–1507.

Jennings, E. S. et al. (2017). Deep mixing of mantle melts beneath continental flood basalt provinces: Constraints from olivine-hosted melt inclusions in primitive magmas. *Geochimica et Cosmochimica Acta*, **196**, pp. 36–57.

Jerram, D. A., Cheadle, M. J., and Philpotts, A. R. (2003). Quantifying the building blocks of igneous rocks: are clustered crystal frameworks the foundation? *Journal of Petrology*, **44**, pp. 2033–2051.

Jochum, K. P. et al. (2006). MPI-DING reference glasses for in situ microanalysis: New reference values for element concentrations and isotope ratios. *Geochemistry, Geophysics, Geosystems*, **7**.

Jochum, K. and Hofmann, A. (1997). Constraints on earth evolution from antimony in mantle-derived rocks. *Chemical geology*, **139**, pp. 39–49.

Jugo, P. J., Luth, R. W., and Richards, J. P. (2005). An experimental study of the sulfur content in basaltic melts saturated with immiscible sulfide or sulfate liquids at 1300° C and 1 GPa. *Journal of Petrology*, **46**, pp. 783–798.

Jugo, P. J., Wilke, M., and Botcharnikov, R. E. (2010). Sulfur K-edge XANES analysis of natural and synthetic basaltic glasses: Implications for S speciation and S content as function of oxygen fugacity. *Geochimica et Cosmochimica Acta*, **74**, pp. 5926–5938.

Jung, H. and Karato, S.-i. (2001). Water-induced fabric transitions in olivine. *Science*, **293**, pp. 1460–1463.

Jung, H. et al. (2006). Effect of water and stress on the lattice-preferred orientation of olivine. *Tectonophysics*, **421**, pp. 1–22.

Karato, S. et al. (2008). Geodynamic significance of seismic anisotropy of the upper mantle: new insights from laboratory studies. *Annu. Rev. Earth Planet. Sci.*, **36**, pp. 59–95.

Katayama, I., Jung, H., and Karato, S.-i. (2004). New type of olivine fabric from deformation experiments at modest water content and low stress. *Geology*, **32**, pp. 1045–1048.

Kauahikaua, J. P. and Trusdell, F. A. (2020). *Have humans influenced volcanic activity on the lower East Rift Zone of Kılauea Volcano? A publication review*. Tech. rep. HVO: US Geological Survey.

Kawakami, Y., Yamamoto, J., and Kagi, H. (2003). Micro-Raman densimeter for CO_2 inclusions in mantle-derived minerals. *Applied spectroscopy*, **57**, pp. 1333–1339.

Keith, H. and Padden, F. (1963). A phenomenological theory of spherulitic crystallization. *Journal of Applied Physics*, **34**, pp. 2409–2421.

Kelley, K. A., Kingsley, R., and Schilling, J.-G. (2013). Composition of plume-influenced mid-ocean ridge lavas and glasses from the Mid-Atlantic Ridge, East Pacific Rise, Galápagos Spreading Center, and Gulf of Aden. *Geochemistry, Geophysics, Geosystems*, **14**, pp. 223–242.

Kern, C. et al. (2020). Quantifying gas emissions associated with the 2018 rift eruption of Kılauea Volcano using ground-based DOAS measurements. *Bulletin of Volcanology*, **82**, pp. 1–24.

Kirby, S. H. and Green, H. (1980). Dunite xenoliths from Hualalai volcano: evidence for mantle diapiric flow beneath the island of Hawaii. *American Journal of Science*, **280**, pp. 550–575.

Kirkpatrick, R. J. (1977). Nucleation and growth of plagioclase, Makaopuhi and Alae lava lakes, Kilauea Volcano, Hawaii. *Geological Society of America Bulletin*, **88**, pp. 78–84.

Kiseeva, E. S., Fonseca, R. O., and Smythe, D. J. (2017). Chalcophile elements and sulfides in the upper mantle. *Elements*, **13**, pp. 111–116.

Kiseeva, E. S. and Wood, B. J. (2015). The effects of composition and temperature on chalcophile and lithophile element partitioning into magmatic sulphides. *Earth and Planetary Science Letters*, **424**, pp. 280–294.

Ko, B. and Jung, H. (2015). Crystal preferred orientation of an amphibole experimentally deformed by simple shear. *Nature Communications*, **6**, p. 6586.

Kohlstedt, D. L. et al. (1976). New technique for decorating dislocations in olivine. *Science*, **191**, pp. 1045–1046.

Kress, V. C. and Carmichael, I. S. (1988). Stoichiometry of the iron oxidation reaction in silicate melts. *American Mineralogist*, **73**, pp. 1267–1274.

Lamadrid, H. et al. (2017). Reassessment of the Raman CO_2 densimeter. *Chemical Geology*, **450**, pp. 210–222.

Lambart, S., Baker, M. B., and Stolper, E. M. (2016). The role of pyroxenite in basalt genesis: Melt-PX, a melting parameterization for mantle pyroxenites between 0.9 and 5 GPa. *Journal of Geophysical Research: Solid Earth*, **121**, pp. 5708–5735.

Lambert, G. et al. (1985). Volcanic emission of radionuclides and magma dynamics. *Earth and Planetary Science Letters*, **76**, pp. 185–192.

Lange, R. A. and Carmichael, I. S. (1987). Densities of Na_2O-K_2O-CaO-MgO-FeO-Fe_2O_3-Al_2O_3-TiO_2-SiO_2 liquids: new measurements and derived partial molar properties. *Geochimica et Cosmochimica Acta*, **51**, pp. 2931–2946.

Larsen, L. M. and Pedersen, A. K. (2000). Processes in high-Mg, high-T magmas: evidence from olivine, chromite and glass in Palaeogene picrites from West Greenland. *Journal of Petrology*, **41**, pp. 1071–1098.

Leal, L. (1980). Particle motions in a viscous fluid. *Annual Review of Fluid Mechanics*, **12**, pp. 435–476.

Lee, C.-T. A. et al. (2012). Copper systematics in arc magmas and implications for crust-mantle differentiation. *Science*, **336**, pp. 64–68.

Lee, R. L. et al. (2019). *Whole-rock chemical analyses of lava samples collected during the 2018 Lower East Rift Zone eruption of Kilauea*. URL: `https://www.sciencebase.gov/catalog/item/5d3279d2e4b01d82ce8791b2`.

Li, C. and Ripley, E. M. (2005). Empirical equations to predict the sulfur content of mafic magmas at sulfide saturation and applications to magmatic sulfide deposits. *Mineralium Deposita*, **40**, pp. 218–230.

Li, C. and Ripley, E. M. (2009). Sulfur contents at sulfide-liquid or anhydrite saturation in silicate melts: empirical equations and example applications. *Economic Geology*, **104**, pp. 405–412.

Li, X. et al. (2004). Rejuvenation of the lithosphere by the Hawaiian plume. *Nature*, **427**, pp. 827–829.

Li, Y. and Audétat, A. (2015). Effects of temperature, silicate melt composition, and oxygen fugacity on the partitioning of V, Mn, Co, Ni, Cu, Zn, As, Mo, Ag, Sn, Sb, W, Au, Pb, and Bi between sulfide phases and silicate melt. *Geochimica et Cosmochimica Acta*, **162**, pp. 25–45.

Lin, F., Bodnar, R., and Becker, S. (2007). Experimental determination of the Raman CH4 symmetric stretching ($\nu 1$) band position from 1–650 bar and 0.3–22° C: Application to fluid inclusion studies. *Geochimica et Cosmochimica Acta*, **71**, pp. 3746–3756.

Liu, X. et al. (2014). Partitioning of copper between olivine, orthopyroxene, clinopyroxene, spinel, garnet and silicate melts at upper mantle conditions. *Geochimica et Cosmochimica Acta*, **125**, pp. 1–22.

Lloyd, A. S. et al. (2013). Volatile loss from melt inclusions in pyroclasts of differing sizes. *Contributions to Mineralogy and Petrology*, **165**, pp. 129–153.

Lloyd, G. E., Farmer, A. B., and Mainprice, D. (1997). Misorientation analysis and the formation and orientation of subgrain and grain boundaries. *Tectonophysics*, **279**, pp. 55–78.

Lockwood, J. P. et al. (1999). Magma migration and resupply during the 1974 summit eruptions of Kilauea Volcano, Hawaii.

Loewen, M. W. (2013). Volatile mobility of trace metals in volcanic systems. *PhD thesis, Oregon State University, Corvallis.*

Lofgren, G. E. (1983). Effect of heterogeneous nucleation on basaltic textures: a dynamic crystallization study. *Journal of Petrology*, **24**, pp. 229–255.

Longo, B. M. et al. (2010). Acute health effects associated with exposure to volcanic air pollution (vog) from increased activity at Kilauea Volcano in 2008. *Journal of Toxicology and Environmental Health, Part A*, **73**, pp. 1370–1381.

Lynn, K. J. et al. (2017). Timescales of mixing and storage for Keanakāko ʻi Tephra magmas (1500–1820 CE), Kılauea Volcano, Hawai ʻi. *Contributions to Mineralogy and Petrology*, **172**, p. 76.

Maaløe, S. and Hansen, B. (1982). Olivine phenocrysts of Hawaiian olivine tholeiite and oceanite. *Contributions to Mineralogy and Petrology*, **81**, pp. 203–211.

Maaløe, S., Pedersen, R. B., and James, D. (1988). Delayed fractionation of basaltic lavas. *Contributions to Mineralogy and Petrology*, **98**, pp. 401–407.

Maclennan, J. (2008). Concurrent mixing and cooling of melts under Iceland. *Journal of Petrology*, **49**, pp. 1931–1953.

Maclennan, J. (2019). Mafic tiers and transient mushes: evidence from Iceland. *Philosophical Transactions of the Royal Society A*, **377**, p. 20180021.

Maclennan, J. (2017). Bubble formation and decrepitation control the CO_2 content of olivine-hosted melt inclusions. *Geochemistry, Geophysics, Geosystems*, **18**, pp. 597–616.

Major, J. J. and Lara, L. E. (2013). Overview of Chaitén Volcano, Chile, and its 2008-2009 eruption. *Andean Geology*, **40**, pp. 196–215.

Marsh, B. D. (1998). On the interpretation of crystal size distributions in magmatic systems. *Journal of Petrology*, **39**, pp. 553–599.

Marske, J. P. et al. (2007). Rapid passage of a small-scale mantle heterogeneity through the melting regions of Kilauea and Mauna Loa Volcanoes. *Earth and Planetary Science Letters*, **259**, pp. 34–50.

Mather, T. et al. (2012). Halogens and trace metal emissions from the ongoing 2008 summit eruption of Kılauea volcano, Hawaii. *Geochimica et Cosmochimica Acta*, **83**, pp. 292–323.

Matjuschkin, V., Blundy, J. D., and Brooker, R. A. (2016). The effect of pressure on sulphur speciation in mid-to deep-crustal arc magmas and implications for the formation of porphyry copper deposits. *Contributions to Mineralogy and Petrology*, **171**, p. 66.

Matthews, S., Shorttle, O., and Maclennan, J. (2016). The temperature of the Icelandic mantle from olivine-spinel aluminum exchange thermometry. *Geochemistry, Geophysics, Geosystems*, **17**, pp. 4725–4752.

Matzen, A. K. et al. (2011). Fe–Mg partitioning between olivine and high-magnesian melts and the nature of Hawaiian parental liquids. *Journal of Petrology*, **52**, pp. 1243–1263.

Mavrogenes, J. A. and O'Neill, H. S. C. (1999). The relative effects of pressure, temperature and oxygen fugacity on the solubility of sulfide in mafic magmas. *Geochimica et Cosmochimica Acta*, **63**, pp. 1173–1180.

McIntire, M. Z., Bergantz, G. W., and Schleicher, J. M. (2019). On the hydrodynamics of crystal clustering. *Philosophical Transactions of the Royal Society A*, **377**, p. 20180015.

McKenzie, D. and O'Nions, R. (1991). Partial melt distributions from inversion of rare earth element concentrations. *Journal of Petrology*, **32**, pp. 1021–1091.

Métrich, N. and Mandeville, C. W. (2010). Sulfur in magmas. *Elements*, **6**, pp. 81–86.

Métrich, N. et al. (1999). Transfer of sulfur in subduction settings: an example from Batan Island (Luzon volcanic arc, Philippines). *Earth and Planetary Science Letters*, **167**, pp. 1–14.

Mishra, R. K. and Thomas, G. (1977). Surface energy of spinel. *Journal of Applied Physics*, **48**, pp. 4576–4580.

Mithen, J. and Sear, R. (2014). Epitaxial nucleation of a crystal on a crystalline surface. *Europhysics Letters*, **105**, p. 18004.

Molist, J. M. (2017). Assessing Volcanic Hazard. *Oxford Handbooks Online*.

Montgomery-Brown, E. K. et al. (2011). Spatiotemporal evolution of dike opening and décollement slip at Kılauea Volcano, Hawai'i. *Journal of Geophysical Research: Solid Earth*, **116**.

Moore, L. R. et al. (2015). Bubbles matter: An assessment of the contribution of vapor bubbles to melt inclusion volatile budgets. *American Mineralogist*, **100**, pp. 806–823.

Moore, L. R. et al. (2018). Volatile contents of primitive bubble-bearing melt inclusions from Klyuchevskoy volcano, Kamchatka: Comparison of volatile contents determined by mass-balance versus experimental homogenization. *Journal of Volcanology and Geothermal Research*, **358**, pp. 124–131.

Moore, R. B. et al. (1980). The 1977 eruption of Kilauea volcano, Hawaii. *Journal of Volcanology and Geothermal Research*, **7**, pp. 189–210.

Morgan, W. J. (1972). Plate motions and deep mantle convection.

Mourey, A. et al. (Aug. 2020). Chalcophile elements track the fate of sulfur at Kılauea Volcano, Hawai'i. *Goldschmidt Abstracts*, **1858**, p. 1. URL: `https://goldschmidt.info/2020/abstracts/abstractView?id=2020003748`.

Moussallam, Y. et al. (2016). The impact of degassing on the oxidation state of basaltic magmas: a case study of Kılauea volcano. *Earth and Planetary Science Letters*, **450**, pp. 317–325.

Moussallam, Y. et al. (2019). Mantle plumes are oxidised. *Earth and Planetary Science Letters*, **527**, p. 115798.

Mungall, J. E. et al. (2015). Transport of metals and sulphur in magmas by flotation of sulphide melt on vapour bubbles. *Nature Geoscience*, **8**, pp. 216–219.

Mysen, B. (1978). Experimental determination of nickel partition coefficients between liquid, pargasite, and garnet peridotite minerals and concentration limits of behavior according to Henry's law at high pressure and temperature. *American Journal of Science*, **278**, pp. 217–243.

Nadeau, O., Williams-Jones, A. E., and Stix, J. (2010). Sulphide magma as a source of metals in arc-related magmatic hydrothermal ore fluids. *Nature Geoscience*, **3**, pp. 501–505.

Naldrett, A. J. (2013). Magmatic sulfide deposits: Geology, geochemistry and exploration. Springer Science & Business Media.

Nash, W. M., Smythe, D. J., and Wood, B. J. (2019). Compositional and temperature effects on sulfur speciation and solubility in silicate melts. *Earth and Planetary Science Letters*, **507**, pp. 187–198.

Natland, J. H. (2003). Capture of helium and other volatiles during the growth of olivine phenocrysts in picritic basalts from the Juan Fernandez Islands. *Journal of Petrology*, **44**, pp. 421–456.

Neal, C. et al. (2019). The 2018 rift eruption and summit collapse of Kılauea Volcano. *Science*, **363**, pp. 367–374.

Neal, C. A. and Lockwood, J. P. (2003). Geologic map of the summit region of Kilauea Volcano, Hawaii. *US Geological Survey Geologic Investigations Series I-2759, 14 p., scale*, **1**, p. 24000.

Neave, D. A. et al. (2014). Crystal storage and transfer in basaltic systems: the Skuggafjöll eruption, Iceland. *Journal of Petrology*, **55**, pp. 2311–2346.

Neave, D. A. et al. (2017). Volatile and light lithophile elements in high-anorthite plagioclase-hosted melt inclusions from Iceland. *Geochimica et Cosmochimica Acta*, **205**, pp. 100–118.

Nelson, S. and Sewake, K. (2008). Volcanic emissions injury to plant foliage. *Plant Disease*, **47**.

Nespolo, M. and Ferraris, G. (2004). The oriented attachment mechanism in the formation of twins-a survey. *European Journal of Mineralogy*, **16**, pp. 401–406.

Newman, S. and Lowenstern, J. B. (2002). VolatileCalc: a silicate melt–H_2O–CO_2 solution model written in Visual Basic for excel. *Computers & Geosciences*, **28**, pp. 597–604.

Newman, S., Stolper, E. M., and Epstein, S. (1986). Measurement of water in rhyolitic glasses; calibration of an infrared spectroscopic technique. *American Mineralogist*, **71**, pp. 1527–1541.

Newsom, H. et al. (1986). Siderophile and chalcophile element abundances in oceanic basalts, Pb isotope evolution and growth of the Earth's core. *Earth and Planetary Science Letters*, **80**, pp. 299–313.

Norman, M. D., Garcia, M. O., and Bennett, V. C. (2004). Rhenium and chalcophile elements in basaltic glasses from Ko'olau and Moloka'i volcanoes: Magmatic outgassing and composition of the Hawaiian plume. *Geochimica et Cosmochimica Acta*, **68**, pp. 3761–3777.

Norman, M. D. et al. (2002). Olivine-hosted melt inclusions in Hawaiian picrites: equilibration, melting, and plume source characteristics. *Chemical Geology*, **183**, pp. 143–168.

O'Neill, H. (2020). The thermodynamic controls on sulfide saturation in silicate melts with application to Ocean Floor Basalts. *https://doi.org/10.1002/essoar.10503096.2*.

Palme, H. and O'Neill, H. (2014). Cosmochemical estimates of mantle composition. *Treatise on Geochemistry*, pp. 1–39.

Park, J. et al. (2007). Comparative velocity structure of active Hawaiian volcanoes from 3-D onshore–offshore seismic tomography. *Earth and Planetary Science Letters*, **259**, pp. 500–516.

Patrick, M. et al. (2019a). Eruptions in sync: Improved constraints on Kılauea Volcano's hydraulic connection. *Earth and Planetary Science Letters*, **507**, pp. 50–61.

Patrick, M. et al. (2019b). Cyclic lava effusion during the 2018 eruption of Kılauea Volcano. *Science*, **366**.

Patten, C., Barnes, S.-J., and Mathez, E. A. (2012). Textural variations in MORB sulfide droplets due to differences in crystallization history. *The Canadian Mineralogist*, **50**, pp. 675–692.

Patten, C. et al. (2013). Partition coefficients of chalcophile elements between sulfide and silicate melts and the early crystallization history of sulfide liquid: LA-ICP-MS analysis of MORB sulfide droplets. *Chemical Geology*, **358**, pp. 170–188.

Pearson, D. et al. (1998). Sulphide inclusions in diamonds from the Koffiefontein kimberlite, S Africa: constraints on diamond ages and mantle Re–Os systematics. *Earth and Planetary Science Letters*, **160**, pp. 311–326.

Peck, D. L. (1978). Cooling and vesiculation of Alae lava lake, Hawaii. *US Geological Survey Professional Paper*, **935A**, A1–A33.

Philpotts, A. R., Shi, J., and Brustman, C. (1998). Role of plagioclase crystal chains in the differentiation of partly crystallized basaltic magma. *Nature*, **395**, p. 343.

Pietruszka, A. J. and Garcia, M. O. (1999a). A rapid fluctuation in the mantle source and melting history of Kilauea Volcano inferred from the geochemistry of its historical summit lavas (1790–1982). *Journal of Petrology*, **40**, pp. 1321–1342.

Pietruszka, A. J. and Garcia, M. O. (1999b). The size and shape of Kilauea Volcano's summit magma storage reservoir: a geochemical probe. *Earth and Planetary Science Letters*, **167**, pp. 311–320.

Pietruszka, A. J. et al. (2011). Excesses of seawater-derived ^{234}U in volcanic glasses from Loihi Seamount due to crustal contamination. *Earth and Planetary Science Letters*, **304**, pp. 280–289.

Pietruszka, A. J. et al. (2015). Two magma bodies beneath the summit of Kılauea Volcano unveiled by isotopically distinct melt deliveries from the mantle. *Earth and Planetary Science Letters*, **413**, pp. 90–100.

Pietruszka, A. J. et al. (2018). An Isotopic Perspective into the Magmatic Evolution and Architecture of the Rift Zones of Kılauea Volcano. *Journal of Petrology*, **59**, pp. 2311–2352.

Pitcher, L. et al. (2009). Fractionation of the platinum-group elments and Re during crystallization of basalt in Kilauea Iki Lava Lake, Hawaii. *Chemical Geology*, **260**, pp. 196–210.

Poirier, J.-P. (1975). On the slip systems of olivine. *Journal of Geophysical Research*, **80**, pp. 4059–4061.

Poland, M. (2015). Preface. *Hawaiian Volcanoes: from Source to Surface*, pp. xi–xiii.

Poland, M. P., Miklius, A., and Montgomery-Brown, E. K. (2015). Magma supply, storage, and transport at shield-stage Hawaiian Volcanoes. *US Geological Survey Professional Paper*, **1801**, pp. 179–234.

Prior, D. J. et al. (1999). The application of electron backscatter diffraction and orientation contrast imaging in the SEM to textural problems in rocks. *American Mineralogist*, **84**, pp. 1741–1759.

Prior, D. (1999). Problems in determining the misorientation axes, for small angular misorientations, using electron backscatter diffraction in the SEM. *Journal of Microscopy*, **195**, pp. 217–225.

Pritchard, M. et al. (2019). Thoughts on the criteria to determine the origin of volcanic unrest as magmatic or non-magmatic. *Philosophical Transactions of the Royal Society A*, **377**, p. 20180008.

Putirka, K. D. (2005). Mantle potential temperatures at Hawaii, Iceland, and the mid-ocean ridge system, as inferred from olivine phenocrysts: Evidence for thermally driven mantle plumes. *Geochemistry, Geophysics, Geosystems*, **6**.

Putirka, K. D. (2008). Thermometers and barometers for volcanic systems. *Reviews in Mineralogy and Geochemistry*, **69**, pp. 61–120.

Putirka, K. D. (2017). Down the crater: where magmas are stored and why they erupt. *Elements*, **13**, pp. 11–16.

Quane, S. et al. (2000). Magmatic history of the East Rift Zone of Kilauea Volcano, Hawaii based on drill core from SOH 1. *Journal of Volcanology and Geothermal Research*, **102**, pp. 319–338.

Rae, A. S. et al. (2016). Time scales of magma transport and mixing at Kılauea Volcano, Hawai'i. *Geology*, **44**, pp. 463–466.

Randle, V. and Engler, O. (2000). *Macrotexture, Microtexture and Orientation Mapping.*

Rasmussen, D. et al. (2020). Vapor-Bubble Growth in Olivine-Hosted Melt Inclusions. *American Mineralogist*.

Reekie, C. et al. (2019). Sulfide resorption during crustal ascent and degassing of oceanic plateau basalts. *Nature Communications*, **10**, pp. 1–11.

Richardson, S. et al. (2001). Archean subduction recorded by Re–Os isotopes in eclogitic sulfide inclusions in Kimberley diamonds. *Earth and Planetary Science Letters*, **191**, pp. 257–266.

Riker, J. (2005). "The 1859 Eruption of Mauna Loa Volcano, Hawai'i: Controls on the Development of Long Lava Channels". PhD thesis. University of Oregon.

Robock, A. (2000). Volcanic eruptions and climate. *Reviews of geophysics*, **38**, pp. 191–219.

Roedder, E. (1984). Fluid inclusions. *Reviews in mineralogy: Mineralogical Society of American, v. 12*.

Roedder, E. (1979). Origin and significance of magmatic inclusions. *Bulletin de Mineralogie*, **102**, pp. 487–510.

Roedder, E. (1983). Geobarometry of ultramafic xenoliths from Loihi Seamount, Hawaii, on the basis of CO_2 inclusions in olivine. *Earth and Planetary Science Letters*, **66**, pp. 369–379.

Roeder, P. and Emslie, R. (1970). Olivine-liquid equilibrium. *Contributions to Mineralogy and Petrology*, **29**, pp. 275–289.

Ross, J. V., Lallemant, H. G. A., and Carter, N. L. (1980). Stress dependence of recrystallized-grain and subgrain size in olivine. *Tectonophysics*, **70**, pp. 39–61.

Ross, J. V. (1957). Combination twinning in plagioclase felspars. *American Journal of Science*, **255**, pp. 650–655.

Rosso, K. and Bodnar, R. (1995). Microthermometric and Raman spectroscopic detection limits of CO_2 in fluid inclusions and the Raman spectroscopic characterization of C02. *Geochimica et Cosmochimica Acta*, **59**, pp. 3961–3975.

Rowland, S. K. and Munro, D. C. (1993). The 1919–1920 eruption of Mauna Iki, Kilauea: chronology, geologic mapping, and magma transport mechanisms. *Bulletin of Volcanology*, **55**, pp. 190–203.

Ruth, D. C. et al. (2018). Crystal and melt inclusion timescales reveal the evolution of magma migration before eruption. *Nature Communications*, **9**, p. 2657.

Ryan, M. P. (1988). The mechanics and three-dimensional internal structure of active magmatic systems: Kilauea Volcano, Hawaii. *Journal of Geophysical Research: Solid Earth*, **93**, pp. 4213–4248.

Ryan, M. P. and Sammis, C. G. (1981). The glass transition in basalt. *Journal of Geophysical Research: Solid Earth*, **86**, pp. 9519–9535.

Ryan, W. B. et al. (2009). Global multi-resolution topography synthesis. *Geochemistry, Geophysics, Geosystems*, **10**.

Saal, A. E. et al. (2002). Vapour undersaturation in primitive mid-ocean-ridge basalt and the volatile content of Earth's upper mantle. *Nature*, **419**, pp. 451–455.

Sakyi, P. A. et al. (2012). Inherited Pb isotopic records in olivine antecryst-hosted melt inclusions from Hawaiian lavas. *Geochimica et Cosmochimica Acta*, **95**, pp. 169–195.

Savelyev, D. P. et al. (2018). Immiscible sulfide melts in primitive oceanic magmas: Evidence and implications from picrite lavas (Eastern Kamchatka, Russia). *American Mineralogist*, **103**, pp. 886–898.

Schwindinger, K. R. (1999). Particle dynamics and aggregation of crystals in a magma chamber with application to Kilauea Iki olivines. *Journal of Volcanology and Geothermal Research*, **88**, pp. 209–238.

Schwindinger, K. R. and Anderson, A. T. (1989). Synneusis of Kilauea Iki olivines. *Contributions to Mineralogy and Petrology*, **103**, pp. 187–198.

Shea, T. et al. (2019). Phosphorus and aluminum zoning in olivine: contrasting behavior of two nominally incompatible trace elements. *Contributions to Mineralogy and Petrology*, **174**, p. 85.

Shishkina, T. et al. (2010). Solubility of H_2O-and CO_2-bearing fluids in tholeiitic basalts at pressures up to 500 MPa. *Chemical geology*, **277**, pp. 115–125.

Shishkina, T. et al. (2014). Compositional and pressure effects on the solubility of H2O and CO2 in mafic melts. *Chemical Geology*, **388**, pp. 112–129.

Sides, I. et al. (2014a). Eruption style at Kılauea Volcano in Hawai 'i linked to primary melt composition. *Nature Geoscience*, **7**, p. 464.

Sides, I. et al. (2014b). Magma mixing and high fountaining during the 1959 Kılauea Iki eruption, Hawai 'i. *Earth and Planetary Science Letters*, **400**, pp. 102–112.

Sisson, T. (2003). Native gold in a Hawaiian alkalic magma. *Economic Geology*, **98**, pp. 643–648.

Skinner, B. J. and Peck, D. L. (1969). An immiscible sulfide melts from Hawaii. *Economic Geology Monogram*, **4**, pp. 310–322.

Skirius, C. M., Peterson, J. W., and Anderson (1990). Homogenizing rhyolitic glass inclusions from the Bishop Tuff. *American Mineralogist*, **75**, pp. 1381–1398.

Smythe, D. J., Wood, B. J., and Kiseeva, E. S. (2017). The S content of silicate melts at sulfide saturation: new experiments and a model incorporating the effects of sulfide composition. *American Mineralogist*, **102**, pp. 795–803.

Span, R. and Wagner, W. (1996). A new equation of state for carbon dioxide covering the fluid region from the triple-point temperature to 1100 K at pressures up to 800 MPa. *Journal of physical and chemical reference data*, **25**, pp. 1509–1596.

Spandler, C., O'Neill, H. S. C., and Kamenetsky, V. S. (2007). Survival times of anomalous melt inclusions from element diffusion in olivine and chromite. *Nature*, **447**, p. 303.

Sparks, S. et al. (2019). Formation and dynamics of magma reservoirs. **377**.

Sperl, M. (2006). Experiments on corn pressure in silo cells–translation and comment of Janssen's paper from 1895. *Granular Matter*, **8**, pp. 59–65.

Špillar, V. and Dolejš, D. (2015). Heterogeneous nucleation as the predominant mode of crystallization in natural magmas: numerical model and implications for crystal–melt interaction. *Contributions to Mineralogy and Petrology*, **169**, p. 4.

Spilliaert, N. et al. (2006). Melt inclusion record of the conditions of ascent, degassing, and extrusion of volatile-rich alkali basalt during the powerful 2002 flank eruption of Mount Etna (Italy). *Journal of Geophysical Research: Solid Earth*, **111**.

Steele-MacInnis, M., Esposito, R., and Bodnar, R. J. (2011). Thermodynamic model for the effect of post-entrapment crystallization on the H_2O–CO_2 systematics of vapor-saturated, silicate melt inclusions. *Journal of Petrology*, **52**, pp. 2461–2482.

Stock, M. J. et al. (2016). Late-stage volatile saturation as a potential trigger for explosive volcanic eruptions. *Nature Geoscience*, **9**, pp. 249–254.

Stone, W. E. and Fleet, M. E. (1991). Nickel-copper sulfides from the 1959 eruption of Kilauea Volcano, Hawaii: Contrasting compositions and phase relations in eruption pumice and Kilauea Iki lava lake. *American Mineralogist*, **76**, pp. 1363–1372.

Stünitz, H., Gerald, J. F., and Tullis, J. (2003). Dislocation generation, slip systems, and dynamic recrystallization in experimentally deformed plagioclase single crystals. *Tectonophysics*, **372**, pp. 215–233.

Sutton, A. J., Elias, T., and Kauahikaua, J. (2003). Lava-effusion rates for the Pu'u'O'o–Kupaianaha eruption derived from SO_2 emissions and very low frequency (VLF) measurements. *US Geol Surv Prof Pap*, **1676**, pp. 137–148.

Sutton, A. et al. (2001). Implications for eruptive processes as indicated by sulfur dioxide emissions from Kılauea Volcano, Hawai 'i, 1979–1997. *Journal of Volcanology and Geothermal Research*, **108**, pp. 283–302.

Tam, E. et al. (2016). Volcanic air pollution over the Island of Hawai'i: Emissions, dispersal, and composition. Association with respiratory symptoms and lung function in Hawai'i Island school children. *Environment international*, **92**, pp. 543–552.

Taracsák, Z. et al. (2019). High fluxes of deep volatiles from ocean island volcanoes: Insights from El Hierro, Canary Islands. *Geochimica et Cosmochimica Acta*, **258**, pp. 19–36.

Tarduno, J. A. et al. (2003). The Emperor Seamounts: Southward motion of the Hawaiian hotspot plume in Earth's mantle. *Science*, **301**, pp. 1064–1069.

Tatsumi, Y., Oguri, K., and Shimoda, G. (1999). The behaviour of platinum-group elements during magmatic differentiation in Hawaiian tholeiites. *Geochemical Journal*, **33**, pp. 237–247.

Teasdale, R. et al. (2005). 1998 Eruption at Volcán Cerro Azul, Galápagos Islands: I. Syn-Eruptive Petrogenesis. *Bulletin of volcanology*, **67**, pp. 170–185.

Thompson, R. and Gibson, S. (2000). Transient high temperatures in mantle plume heads inferred from magnesian olivines in Phanerozoic picrites. *Nature*, **407**, p. 502.

Thomson, A. and Maclennan, J. (2012). The distribution of olivine compositions in Icelandic basalts and picrites. *Journal of Petrology*, **54**, pp. 745–768.

Thornber, C. R. et al. (2015). Petrologic testament to changes in shallow magma storage and transport during 30+ years of recharge and eruption at Kılauea Volcano, Hawai ‘i. *Hawaiian Volcanoes: From Source to Surface*, **208**, p. 147.

Thybo, H. and Artemieva, I. M. (2013). Moho and magmatic underplating in continental lithosphere. *Tectonophysics*, **609**, pp. 605–619.

Tilling, R. I. (1987). Fluctuations in surface height of active lava lakes during 1972–1974 Mauna Ulu eruption, Kilauea volcano, Hawaii. *Journal of Geophysical Research: Solid Earth*, **92**, pp. 13721–13730.

Tilling, R. I. and Dvorak, J. J. (1993). Anatomy of a basaltic volcano. *Nature*, **363**, pp. 125–133.

Tordesillas, A., Walker, D. M., and Lin, Q. (2010). Force cycles and force chains. *Physical Review E*, **81**, p. 011302.

Toriumi, M. (1979). Relation between dislocation density and subgrain size of naturally deformed olivine in peridotites. *Contributions to Mineralogy and Petrology*, **68**, pp. 181–186.

Trusdell, F. A. (1991). “1840 Eruption of Kilauea Volcano: Petrologic and Volcanologic Constraints on Rift Zone Processes”. PhD thesis. University of Hawaii at Manoa.

Tucker, J. M. et al. (2019). A high carbon content of the Hawaiian mantle from olivine-hosted melt inclusions. *Geochimica et Cosmochimica Acta*, **254**, pp. 156–172.

Tuohy, R. M. et al. (2016). Magma transport and olivine crystallization depths in Kılauea’s east rift zone inferred from experimentally rehomogenized melt inclusions. *Geochimica et Cosmochimica Acta*, **185**, pp. 232–250.

Turcotte, D. L. and Schubert, G. (2002). Geodynamics. Cambridge university press.

Turnbull, D. and Vonnegut, B. (1952). Nucleation catalysis. *Industrial & Engineering Chemistry*, **44**, pp. 1292–1298.

USGS (2019a). Summit and Lower East Rift Zone (LERZ) Brief Overview of Events April 17 to October 5, 2018. https://www.usgs.gov/media/files/k-lauea-volcano-2018-summit-and-lower-east-rift-zone-lerz, pp. 1–33.

USGS (2019b). Volcano Alert. *https://volcanoes.usgs.gov/vhp/archive$_s$earch.html?obs = hvo.*

Valade, S. et al. (2019). Towards global volcano monitoring using multisensor sentinel missions and artificial intelligence: The mounts monitoring system. *Remote Sensing*, **11**, p. 1528.

Vance, J. A. (1969). On synneusis. *Contributions to Mineralogy and Petrology*, **24**, pp. 7–29.

Veksler, I. V. et al. (2018). Chemical and textural re-equilibration in the UG2 chromitite layer of the Bushveld Complex, South Africa. *Journal of Petrology*, **59**, pp. 1193–1216.

Venugopal, S. et al. (2020). Melt inclusion vapour bubbles: the hidden reservoir for major and volatile elements. *Scientific Reports*, **10**, pp. 1–14.

Vinet, N., Flemming, R. L., and Higgins, M. D. (2011). Crystal structure, mosaicity, and strain analysis of Hawaiian olivines using in situ X-ray diffraction. *American Mineralogist*, **96**, pp. 486–497.

Vinet, N. and Higgins, M. D. (2010). Magma solidification processes beneath Kilauea volcano, Hawaii: A quantitative textural and geochemical study of the 1969–1974 Mauna Ulu Lavas. *Journal of Petrology*, **51**, pp. 1297–1332.

Vinet, N. et al. (2015). Quantification and origin of the intracrystalline deformation of olivine from basalts of the Andean Southern Volcanic Zone: A multidisciplinary study. *Congreso Geologico Chileno XIV*.

Vogt, J. H. L. (1921). The physical chemistry of the crystallization and magmatic differentiation of igneous rocks. *The Journal of Geology*, **29**, pp. 318–350.

Wallace, P. J. and Anderson, A. T. (1998). Effects of eruption and lava drainback on the H_2O contents of basaltic magmas at Kilauea Volcano. *Bulletin of Volcanology*, **59**, pp. 327–344.

Wallace, P. J. and Carmichael, I. S. (1994). S speciation in submarine basaltic glasses as determined by measurements of S Kα X-ray wavelength shifts. *American Mineralogist*, **79**, pp. 161–167.

Wallace, P. J., Kamenetsky, V. S., and Cervantes, P. (2015). Special Collection: Glasses, Melts, and Fluids, as Tools for Understanding Volcanic Processes and Hazards. Melt inclusion CO_2 contents, pressures of olivine crystallization, and the problem of shrinkage bubbles. *American Mineralogist*, **100**, pp. 787–794.

Wanamaker, B. J. and Kohlstedt, D. L. (1991). The effect of melt composition on the wetting angle between silicate melts and olivine. *Physics and Chemistry of Minerals*, **18**, pp. 26–36.

Wang, W. et al. (2019). Raman spectroscopic densimeter for pure CO_2 and CO_2-H_2O-NaCl fluid systems over a wide PT range up to 360° C and 50 MPa. *Chemical Geology*, **528**, p. 119281.

Wang, X. et al. (2011). Raman spectroscopic measurements of CO_2 density: Experimental calibration with high-pressure optical cell (HPOC) and fused silica capillary capsule (FSCC) with application to fluid inclusion observations. *Geochimica et Cosmochimica Acta*, **75**, pp. 4080–4093.

Welsch, B., Hammer, J., and Hellebrand, E. (2014). Phosphorus zoning reveals dendritic architecture of olivine. *Geology*, **42**, pp. 867–870.

Welsch, B. et al. (2012). Dendritic crystallization: A single process for all the textures of olivine in basalts? *Journal of Petrology*, **54**, pp. 539–574.

Westerlund, K. et al. (2006). A subduction wedge origin for Paleoarchean peridotitic diamonds and harzburgites from the Panda kimberlite, Slave craton: evidence from Re–Os isotope systematics. *Contributions to Mineralogy and Petrology*, **152**, p. 275.

Westland, J. A. (2014). "The field relationships and mineral chemistry of mafic and ultramafic intrusions in the Loch Uisg area, Isle of Mull". PhD thesis. University of Glasgow.

Wheeler, J. (2018). The effects of stress on reactions in the Earth: sometimes rather mean, usually normal, always important. *Journal of Metamorphic Geology*, **36**, pp. 439–461.

Wheeler, J. et al. (2009). The weighted Burgers vector: a new quantity for constraining dislocation densities and types using electron backscatter diffraction on 2D sections through crystalline materials. *Journal of microscopy*, **233**, pp. 482–494.

Wheeler, J. et al. (2001). The petrological significance of misorientations between grains. *Contributions to Mineralogy and Petrology*, **141**, pp. 109–124.

Whitty, R. C. et al. (2020). Spatial and Temporal Variations in SO_2 and $PM_{2.5}$ Levels Around Kılauea Volcano, Hawai'i During 2007–2018. *Frontiers in Earth Sciences*, **8**, p. 36.

Wieser, P. E. and Jenner, F. E. (2020). Chalcophile Elements: Systematics and Relevance. *Encylopedia of Geology*.

Wieser, P. E. et al. (2019a). Crystal scavenging from mush piles recorded by melt inclusions. *Nature Communications*, **10**, pp. 1–11.

Wieser, P. E. et al. (2019b). To sink, swim, twin, or nucleate: A critical appraisal of crystal aggregation processes. *Geology*, **47**, pp. 948–952.

Wieser, P. E. et al. (2020a). Chalcophile elements track the fate of sulfur at Kılauea Volcano, Hawai'i. *Geochimica et Cosmochimica Acta*, **282**, pp. 245–275. URL: `https://doi.org/10.1016/j.gca.2020.05.018`.

Wieser, P. E. et al. (2020b). Microstructural constraints on magmatic mushes under Kılauea Volcano, Hawaii. *Nature Communications*, **11**, pp. 1–14.

Wilkinson, J. and Hensel, H. (1988). The petrology of some picrites from Mauna Loa and Kilauea volcanoes, Hawaii. *Contributions to Mineralogy and Petrology*, **98**, pp. 326–345.

Witham, C. S. and Oppenheimer, C. (2004). Mortality in England during the 1783–4 Laki Craters eruption. *Bulletin of Volcanology*, **67**, pp. 15–26.

Witt-Eickschen, G. et al. (2009). The geochemistry of the volatile trace elements As, Cd, Ga, In and Sn in the Earth's mantle: New evidence from in situ analyses of mantle xenoliths. *Geochimica et Cosmochimica Acta*, **73**, pp. 1755–1778.

Wölbern, I. et al. (2006). Deep origin of the Hawaiian tilted plume conduit derived from receiver functions. *Geophysical Journal International*, **166**, pp. 767–781.

Wright, T. L. and Fiske, R. S. (1971). Origin of the differentiated and hybrid lavas of Kilauea volcano, Hawaii. *Journal of Petrology*, **12**, pp. 1–65.

Wright, T. L. and Klein, F. W. (2014). *Two hundred years of magma transport and storage at Kılauea Volcano, Hawai'i, 1790-2008*. Tech. rep. US Geological Survey.

Wright, T. L., Peck, D. L., and Shaw, H. R. (1976). Kilauea lava lakes: natural laboratories for study of cooling, crystallization, and differentiation of basaltic magma. *The geophysics of the Pacific Ocean basin and its margin*, **19**, pp. 375–390.

Wulf, A., Palme, H., and Jochum, K. (1995). Fractionation of volatile elements in the early solar system: evidence from heating experiments on primitive meteorites. *Planetary and Space Science*, **43**, pp. 451–468.

Yamamoto, J. et al. (2007). Paleo-Moho depth determined from the pressure of CO_2 fluid inclusions: Raman spectroscopic barometry of mantle-and crust-derived rocks. *Earth and Planetary Science Letters*, **253**, pp. 369–377.

Yamamoto, J. et al. (2015). Fluid inclusions in mantle xenoliths: A probe for the physical and chemical state of the lithospheric mantle. *Journal of Geography - Chicaku Zasshi*, **124**, pp. 429–443.

Zhang, H. L. et al. (2018). Determination of $Fe^{3+}/\Sigma Fe$ of XANES basaltic glass standards by Mössbauer spectroscopy and its application to the oxidation state of iron in MORB. *Chemical Geology*, **479**, pp. 166–175.

Zhang, S. and Karato, S.-i. (1995). Lattice preferred orientation of olivine aggregates deformed in simple shear. *Nature*, **375**, p. 774.